

Just like I read the Arabian Nights for pleasure, I'm going to play with physics\*...

Richard Feynman

Go riding, climbing, hiking, swimming, surfing, whatever\*, have fun. If you're having fun then you'll keep doing it.

Will Gadd

# University of Alberta

Microfabricated Nickel Based Sensors for Hostile and High Pressure Environments

by

Christopher Michael Bjustrom Holt

A thesis submitted to the Faculty of Graduate Studies and Research  
in partial fulfillment of the requirements for the degree of

Doctor of Philosophy

in

Materials Engineering

Department of Chemical & Materials Engineering

©Christopher Michael Bjustrom Holt

Fall 2013

Edmonton, Alberta

Permission is hereby granted to the University of Alberta Libraries to reproduce single copies of this thesis and to lend or sell such copies for private, scholarly or scientific research purposes only. Where the thesis is converted to, or otherwise made available in digital form, the University of Alberta will advise potential users of the thesis of these terms.

The author reserves all other publication and other rights in association with the copyright in the thesis and, except as herein before provided, neither the thesis nor any substantial portion thereof may be printed or otherwise reproduced in any material form whatsoever without the author's prior written permission.

# Abstract

This thesis outlines the development of two platforms for integrating microfabricated sensors with high pressure feedthroughs for application in hostile high temperature high pressure environments. An application in oil well production logging is explored and two sensors were implemented with these platforms for application in an oil well.

The first platform developed involved microfabrication directly onto a cut and polished high pressure feedthrough. This technique enables a system that is more robust than the wire bonded silicon die technique used for MEMS integration in pressure sensors. Removing wire bonds from the traditional MEMS package allows for direct interface of a microfabricated sensor with a hostile high pressure fluid environment which is not currently possible. During the development of this platform key performance metrics included pressure testing to 70MPa and temperature cycling from 20°C to 200°C. This platform enables electronics integration with a variety of microfabricated electrical and thermal based sensors which can be immersed within the oil well environment.

The second platform enabled free space fabrication of nickel microfabricated devices onto an array of pins using a thick tin sacrificial layer. This technique allowed microfabrication of metal MEMS that are released by distances of 1cm from their substrate. This method is quite flexible and allows for fabrication to be done on any

pin array substrate regardless of surface quality. Being able to place released MEMS sensors directly onto traditional style circuit boards, ceramic circuit boards, electrical connectors, ribbon cables, pin headers, or high pressure feedthroughs greatly improves the variety of possible applications and reduces fabrication costs.

These two platforms were then used to fabricate thermal conductivity sensors that showed excellent performance for distinguishing between oil, water, and gas phases. Testing was conducted at various flow rates and performance of the released platform was shown to be better than the performance seen in the anchored sensors while both platforms were significantly better than a simply fabricated wrapped wire sensor. The anchored platform was also used to demonstrate a traditional capacitance based fluid dielectric sensor which was found to work similarly to conventional commercial capacitance probes while being significantly smaller in size.

# Preface

The introduction provided in Chapter 1 contains three parts. First it explains the application of sensors in oil well production logging and the need and justification for miniaturization. Second it provides a review of metal MEMS devices that have been fabricated and their current applications. And finally it outlines the requirements for incorporation of MEMS devices with a high pressure feedthrough to enable the use of micro sensors in the high pressure high temperature oil well environment.

The experimental techniques used in this work are explained in Chapter 2 which outlines metal deposition, device patterning, and materials characterization.

In Chapter 3 high pressure feedthroughs will be discussed in detail and a technique developed for cutting, polishing, and fabricating directly onto a high pressure feedthrough will be outlined. Several methods for preparing and then subsequently improving the surface of a cut high pressure feedthrough will be discussed. Patterned electrode and beam structures were then fabricated on these prepared substrates using modified MEMS fabrication techniques.

Chapter 4 reveals a unique substrate free process flow to fabricate released MEMS devices directly onto a vertical array of pins. These pins could be an electrical connector, a circuit board header, or a high pressure feedthrough. The challenges overcome in the development of this process will be outlined as well as a discussion of different methods attempted to achieve this goal. Topics discussed will include sacrificial layer materials selection, thin film adhesion, and electrochemical etching.

Chapter 5 contains characterization of the two sensor systems developed in Chapters 3 and 4 for application in an oil well logging environment. Two phase identification methods were tested with the developed sensor platforms: thermal conductivity measurement, and dielectric constant measurement. The two different architectures of sensors will be compared and their suitability for oil well logging applications discussed.

Chapter 6 is my first author paper published as a conclusion to work conducted in the first two years of my degree on electrocatalytic hydrogenation of bitumen distillate fractions.

Chapter 7 is a summary of the materials development and characterization work that I conducted in order to fabricate nickel iron alloy NEMS devices for magnetic sensor experiments in the Freeman research group. This metal NEMS development work is closely related to the fabrication of metal MEMS sensors onto high pressure feedthroughs but was much simpler due to the ability to conduct fabrication on perfect silicon substrates.

# Acknowledgements

Many people have taught me and helped me through my PhD. Foremost, I thank David Mitlin for guiding my work, giving me freedom to explore ideas, and making my project possible. I have learned so much from you ranging from microscopy to management to materials design and as a result I have a much better understanding of the research world. Almost every week of the last five years I have learned something new or been able to share in an exciting discovery thanks to my research group peers. It is so much fun to explore together and create new ideas. Looking at eggshell membranes with Zhi Li, searching for graphene flowers with Zhanwei Xu, seeing amorphous cluster hopping with Jacob Burgess, and learning to make supercapacitors with Huanlei Wang has been awesome! It has been a great privilege to be part of the world of materials creation and design these last years. My whole group has been so helpful in guiding me, teaching me, and giving advice; thank you Mohsen Danaie, Julian Haagsma, Chris Harrower, Peter Kalisvaart, Reza Mohammadi, Brian Olsen, Babak Shalchi, Xuehai Tan, Ben Zahiri, Elmira Memarzadeh, and Erik Lubner.

Thank you to the summer students that I have worked with who have helped me with my research: Tyler Stephenson, Mike Hazelton, Matt Amyotte, Matt Yachuk, and Allan Beaudry.

Especially I would like to thank Li Zhang for teaching me how experimental design should be conducted in combination with hard work. Colin Ophus, thank you for making research fun! Your general excitement and kindness in helping me when I joined the group will remain a highlight of my time as a student. Your work and accomplishments set a great goal for me to aspire to.

Jaron Van Dijken for setting a great example to follow; it was fun to follow your solar business venture. Thank you John Kwan for showing me the lighter side of graduate life and being a great friend. Thank you Katherine Gagnon for teaching me how to collaborate and letting me see the coolest scientific equipment on campus.

Mark Hartwell, Thank you for supporting my research and always being available to go waterskiing. And thank you Solomon Ssenyange for helping me with my electroplating problems and keeping me up to date with your exciting adventures.

Paul Eaton you set a great example for me to follow in my coming years. It has been extremely exciting to fuse my sensor background with your fouling experience. It has been a great privilege to have the chance to learn from you Murray Gray. I have gained so much from watching you present, listening to your input on my projects, and learning from your experience.

Ray Lemieux, I have truly enjoyed your stories over the last years and have gained much from listening to you. I look forward to working with you over the next year as I start a new company under your MNTorship program.

Mostly importantly, I thank my wonderful family for supporting me throughout my life in my scientific endeavors. And Ashley, you are wonderful, your laughter and happiness has truly enriched my life.

# Contents

1	Introduction.....	1
1.1	Oil Well Sensors .....	1
1.1.1	Fluid Identification Techniques in an Oil Well .....	3
1.2	Metal MEMS .....	6
1.2.1	Metal Micromachining .....	6
1.2.2	Metal Micro Electro Mechanical Systems (MEMS) .....	9
1.2.3	Metal MEMS materials.....	12
1.3	Harsh Environment Sensing .....	14
1.3.1	Feedthrough Integration .....	14
1.3.2	Freestanding Sensors.....	18
1.4	Conclusion.....	20
2	Experimental Techniques .....	22
2.1	Deposition Techniques .....	22
2.1.1	Electrodeposition .....	22
2.1.2	Magnetron Sputtering.....	24
2.1.3	Radio Frequency (RF) Sputtering .....	25
2.1.4	Reactive Sputtering.....	26
2.2	Patterning Techniques .....	26
2.2.1	Photolithography .....	26
2.2.2	Electron Beam Lithography .....	28
2.2.3	Liftoff.....	28
2.2.4	Photo-electroforming.....	29
2.3	Characterization.....	31
2.3.1	Scanning Electron Microscopy .....	31
2.3.2	Energy-dispersive X-ray Spectroscopy .....	32
2.3.3	Optical Profilometry .....	32
2.3.4	X-Ray Diffraction .....	32
3	Fabrication 1: Microfabrication on a High Pressure Feedthrough .....	34
3.1	Fabrication of a High Pressure Feedthrough .....	34
3.2	Cutting of a High Pressure Feedthrough.....	35
3.3	Feedthrough Polishing.....	37

3.4	Glass Surface Modification.....	44
3.4.1	Fox-25Flowable Spin on Glass.....	45
3.4.2	Aremco Silicone Magnesia Low Melting Point Glass.....	48
3.4.3	Aremco LMP Glass.....	50
3.4.4	Lead Borate Solder Glass.....	54
3.4.5	Glass Coating Summary.....	54
3.5	Sensor Device Material Selection .....	57
3.5.1	Feedthrough device over-plating.....	57
3.5.2	Electroplating Chromium .....	57
3.5.3	Electroplating Nickel.....	58
3.6	Diffusion Barrier Coatings .....	59
3.7	Final Implementation .....	65
3.8	Conclusion.....	67
4	Fabrication 2: Phase Change Release Fabrication for Free Standing MEMS69	
4.1.1	Concept for free standing devices using a thick sacrificial layer.....	69
4.1.2	Physical requirements for a sacrificial layer material.....	70
4.2	Material Selection.....	71
4.2.1	Material 1: Sample Mount Epoxy .....	71
4.2.2	Material 2: Crystal Bond.....	73
4.2.3	Material 3: Solder .....	74
4.2.4	Selective Electrochemical Etching of Tin .....	78
4.2.5	Material 4: Indium.....	84
4.2.6	Material 5: Pressed Pure Tin .....	84
4.2.7	Material 6: Melt Cast Pure Tin .....	84
4.2.8	Adhesion of metal devices to Inconel pins.....	85
4.2.9	Sputtered Devices.....	87
4.2.10	Nickel Over-Plate .....	88
4.3	Final Implementation .....	89
4.4	Conclusion.....	90
5	Results and Discussion: Sensor Testing for Oil Well Logging Applications .	91
5.1	Thermal Conductivity Sensor Characterization .....	91
5.1.1	Materials Selection for Thermal Sensing.....	91
5.1.2	Thermal characterization of a fully released nickel beam structure ...	93

5.1.3	Thermal characterization of an anchored nickel beam structure.....	99
5.1.4	Thermal Conductivity Measurement with Miscible fluids.....	100
5.1.5	Thermal Conductivity Measurement with emulsion stabilization.....	102
5.1.6	Effect of current and duty cycle time on heating and cooling behavior.....	103
5.1.7	Sensor Resistance Components.....	112
5.1.8	Thermal Transient Response of Sensor.....	114
5.2	Dielectric constant measurements with a comb style capacitor.....	117
5.3	Conclusion.....	119
6	Electrocatalytic Hydrogenation of 2-cyclohexen-1-one in a High Sulfur Environment Using a Carbon-supported Nanostructured Tungsten Sulfide Catalyst	121
6.1	Abstract.....	121
6.2	Introduction.....	121
6.3	Experimental.....	122
6.4	Results and Discussion.....	125
6.5	Conclusions.....	128
7	Nickel Iron MEMS and NEMS Fabrication.....	129
7.1	Introduction.....	129
7.2	Experimental.....	130
7.3	Results.....	134
7.3.1	XRD.....	134
7.3.2	Average Film Stress.....	136
7.3.3	Magnetic Properties.....	137
7.3.4	Surface Morphology.....	138
7.4	Discussion.....	140
7.4.1	NiFe MEMS Fabrication.....	140
7.4.2	NiFe NEMS Fabrication.....	145
7.4.3	NEMS Resonant Properties.....	146
7.5	Conclusion.....	148
8	Conclusion and Future Work.....	149

# List of Figures

Figure 1.1: Illustration demonstrating difference between conventional production using multiple vertical wells (above) and modern production using a single horizontal well (below). The Grey regions show depletion zones. .... 2

Figure 1.2: a) 3D Copper RF component fabricated with the Polyrata process[68], b) diagram and false colored SEM of probe card springs by FormFactor[69], c-d) SEM images of a nickel gyroscope fabricated using the EFAB process[63]. .... 11

Figure 1.3: a) Illustration of traditionally accepted integration of a MEMS device with a high pressure feedthrough involving wirebonds. b) A higher magnification of the MEMS pressure sensor with gold bond pads wirebonded to the feedthrough pins ..... 15

Figure 1.4: Photograph of the IBM SLT module[98] and a magazine ad highlighting the revolution caused by this integration[99]. .... 16

Figure 1.5: Figures from Schlumberger patent 7392697 that show a method of integrating MEMS sensors with a high pressure feedthrough[12]. a) is an isometric view and b) shows a cross section view of a). .... 16

Figure 1.6: Images of the high temperature SiC based pressure sensor developed by the Glenn research centre. a) A photo of the sensor element and a diagram of the sensor integrated into a high pressure feedthrough using the DCA process[101]. b) shows a cross section SEM image of the DCA between the Contact wire and the SiC sensor[100]. c) Sensor elements integrated with high pressure fittings in the final product that could be used for conducting high temperature tests[100]. .... 17

Figure 1.7: Diagram of flow velocities in a pipe in laminar flow. .... 18

Figure 2.1: Electroplating system used for nickel depositions. a) A schema of the system labeling the critical components. b) A solid model of the electroplating system designed for depositions in this work showing the major components. .... 23

Figure 2.2: a) A schematic of a sputtering machine showing confocal sputtering sources and an inverted rotating feedthrough substrate. b) A detailed diagram showing the magnetron sputtering source. c) A 3D representation of the sputtering chamber showing a co-sputtering configuration. .... 25

Figure 2.3: Diagram of the main components required for optical photolithography exposure. .... 27

Figure 2.4: The lift off procedure showing a) deposition and patterning of the photoresist and b) deposition of a thin material to be patterned by lift off. c) The remaining film after the photoresist is removed. d) A higher magnification of the

deposited film profile that results from shadowing during deposition. This shadowing assists in the lift off process..... 29

Figure 2.5: a) Schematic of photo electroforming showing nickel only electroplating in the exposed areas of substrate. b) SEM micrograph of a released beam structure formed by electroforming. c) Diagram of photoresist and substrate covered with a thin metal seed layer and subsequent electroplating on the seed layer. d) SEM micrograph showing structure of device formed using this technique (photomask used was the same as in b)..... 31

Figure 3.1: a) Fixture used for firing of a high pressure feedthrough. b) photograph of a HCC Ametek high pressure feedthrough before cutting. .... 35

Figure 3.2: A diagram of the belt fed grinding station used by HCC Ametek to try to provide a smooth surface on a high pressure feedthrough. .... 36

Figure 3.3: a) Gravity fed South Bay Technology Saw. b) High speed precision saw by Struers. .... 36

Figure 3.4: a HCC high pressure feedthrough a) cut with a gravity feed slow speed diamond saw. b) cut with a high speed automatic feed diamond saw and c) cut with a high speed SiC wheel. .... 37

Figure 3.5: a) High pressure feedthrough after being cut with a diamond saw at 3000RPM b) after being polished with 600 grit sand paper for 1 minute c) after being polished to 2400 grit SiC paper ..... 38

Figure 3.6: Pictures of a HCC all glass high pressure feedthrough that has been cut with a diamond saw and polished with 4000 grit SiC sandpaper. Notice the large bubbles located at the pins, cracking around the pins and spherical defects on the surface in (b) and (c). The cross section shown in blue is shown Figure 3.12. .... 39

Figure 3.7: SEM images of various feedthroughs, showing the size and extent to which the defects are present across the surface. a) and b) Low magnification images of the glass surface between two metallic pins. c) A large pit next to one of the pins. d) A large ~ 400  $\mu\text{m}$  diameter pit. .... 40

Figure 3.8: SEM images of a feedthrough cut at the interface between two glass frits with higher than normal defect density. a) A cluster of ~50  $\mu\text{m}$  pits present on the feedthrough surface. b) Low magnification image showing large defects. c) 100  $\mu\text{m}$  defects between two metallic pins. d) Numerous defects, ranging in size from 20  $\mu\text{m}$  to ~1000  $\mu\text{m}$ . .... 41

Figure 3.9: a) Scanning electron micrograph of a typical feedthrough surface. b) Filtered image showing dark spots the same size as the defects. c) Size distribution of the filtered image defects showing a high number of smaller defects but a significant number of defects in the 40-60 $\mu\text{m}$  range. .... 42

Figure 3.10: Height profiles of various defects present on the surface of cut feedthroughs. a) A cluster of 100 $\mu$ m sized defects. b) Dense cluster of smaller sized defects. c) Two smaller defects present on the feedthrough surface. d) Shallow defects, all under 60  $\mu$ m in depth. .... 43

Figure 3.11: Representation of two different bubble cross sections. a) Cross section at the top of a bubble showing sharp transition from surface to defect. b) Cross section at the bottom of a bubble showing a much more gentle transition from the flat surface to the defect. .... 43

Figure 3.12: Diagram of defect correction process (schematic from the region marked in blue on Figure 3.6). a) Shows the as cut and polished surface with fine and large cracks and bubbles on the surface, b) shows the surface after a spin on coating and firing of a glass layer and c) shows the surface after a back polish to reveal the feedthrough pins. .... 44

Figure 3.13: Four possible stages of HSQ curing. Note the temperature ranges for each stage, and the associated chemical reactions[141]. .... 46

Figure 3.14: Thick coatings of Fox-25 deposited onto a high pressure feedthrough after curing process of 170°C for 30min and 350°C for 30minutes. .... 47

Figure 3.15: a,b) Optical micrograph of chromium devices fabricated on a high pressure feedthrough coated with a thin layer of cured spin on glass. No cracking is evident, but feedthroughs still have very clear large defects on the surface. c) Image of devices fabricated on a feedthrough with thicker spin on glass showing significant cracking. .... 48

Figure 3.16: Photograph of feedthroughs coated with Aremco Silicone Magnesia Low Melting Point Glass before firing. .... 49

Figure 3.17: Optical micrographs of feedthroughs with chromium devices fabricated on them after surface treatment with Aremco silicone magnesia low melting point glass. Image d) shows three large defects mostly filled with glass and the rough texture of glass in the defect area. .... 50

Figure 3.18: Low magnification SEM micrographs of Aremco low melting point glass melted on a glass slide at 450°C a), 475°C c) and 500°C e), and higher magnification images of the same in b), d), and f). .... 51

Figure 3.19: Very large defects successfully filled with low melting point glass after 1 coating in a) and c) and after two coatings in b) and d). Inset of b) shows a 100 $\mu$ m size feature perfectly filled with glass. .... 53

Figure 3.20: Low magnification scanning electron micrograph overview of a high pressure feedthrough with a large number of defects mostly corrected with a surface treatment with low melting point glass. .... 53

Figure 3.21: a) Cut and polished feedthrough b) PbO based glass melted then polished back c) Spin on glass coated and polished back d) Aremco coating covered and polished back. .... 54

Figure 3.22: a) Cut and polished feedthrough b) PbO based glass melted then polished back c) Spin on glass coated and polished back d) Aremco coating with MgO filler covered and polished back..... 56

Figure 3.23: Results from first chromium electroplating test. a) The feedthrough after two of the beams were electroplated b) the appearance of the Cr under layer before deposition c) the appearance of the device after 100 seconds of electroplating at 20mA d) after extended electroplating for 10 min at 20mA, the surface stress resulted in the bulk of the chromium flaking off of the surface..... 58

Figure 3.24: a) Optical micrograph of a beam electroplated with nickel for 10 minutes at 2mA b) SEM of a beam electroplated with nickel for 20 minutes at 2mA ..... 59

Figure 3.25: Fabrication procedure for anchored devices on a high pressure feedthrough. b) finished feedthrough device with two comb structures and one beam structure. c) finished device with three beam structures..... 60

Figure 3.26: Resistance vs. Temperature calibration graph for a feedthrough with three beam structures. Furnace was heated and cooled three times with resistance and temperature measurements recorded during cycling. .... 61

Figure 3.27: Monomers of the four types of Parylene: a) Parylene N. b) Parylene C. c) Parylene D. d) AF – 4, SF, HT[143]..... 61

Figure 3.28: Chemical stability of Parylene C at room temperature in various solvents. Time of exposure was ~60 hours. All samples were dried, coated with a thin layer of gold and imaged..... 64

Figure 3.29: Implementation of the high pressure feedthrough in a down hole oil well tool. A) The integration of the feedthrough sensor in an inconel housing that surrounds the sensor circuit boards. b) Images of the fabricated circuit boards for interfacing an AD7746 capacitance to digital converter to the sensors. c) Photograph of the finished sensor device soldered to the measuring circuit board. .... 67

Figure 4.1: Free standing devices removed from silicon wafer using scotch tape. Devices were rigid and did not bend much when removed from the tape. This indicated that the devices could work well if fully released on pins. .... 69

Figure 4.2: Process flow for fabrication of fully released devices. a) shows the starting high pressure feedthrough device b) shows filling of the space between the pins with a sacrificial material c) shows what the device looks like after being cut and polished d) After photolithographic patterning of devices. e) After removal of the sacrificial layer. .... 70

Figure 4.3: Problems that can occur during the cutting and polishing step if material properties are not ideal for the sacrificial layer. ....	71
Figure 4.4: Feedthrough with sample mount epoxy sacrificial layer at process step before electroplating and after photolithography.....	72
Figure 4.5: Epoxy remover release issue: a) shows the feedthrough with completed devices electroplated on the pins that is ready for release b) after the assembly is immersed into epoxy remover the epoxy starts to swell and this applies pressure on the electroplated devices c) the devices eventually pop off of the pins due to the swelling epoxy. ....	73
Figure 4.6: Feedthrough with crystal bond melted into the space between the pins. The red plastic is a cup to hold the crystal bond in place as it cools and solidifies. 74	
Figure 4.7: a) Mild steel mold used to hold feedthroughs in place for molten solder to be poured over the pins. b) Feedthrough with a block of solid tin surrounding the pins with microfabricated devices on top.....	75
Figure 4.8: Cutting step of preparing the feedthrough in a gravity fed slow speed diamond saw.....	75
Figure 4.9: SEM images of the nickel electroplated structures on top of the prepared solder surface showing a) a top down view of the devices and b) a higher magnification at a high angle showing the thickness of the electroplated nickel... 76	
Figure 4.10: a) Photo of feedthrough after the majority of the solder has been removed. b) Top down SEM image of the devices coated with a thin layer of solder. c) Magnified section of b showing a section that is partially free from tin. d) EDAX map of tin in for the magnified area e) EDAX map of nickel for the magnified area. ....	77
Figure 4.11: SEM Images of a nickel device fabricated onto a high pressure feedthrough after a failed etching attempt to remove the remaining tin coating the devices.....	78
Figure 4.12: Pourbaix diagrams for nickel (a) and tin (b) in water[148]. ....	79
Figure 4.13: CV at 100mV/s and linear sweep voltammetry at 2mV/s for the Sn electrode in 4M NaOH. Potential is shown vs. MSE and the electrode is 2mm in diameter[150]. ....	80
Figure 4.14: Shows the current response with time as the electrode is held at -1.44V vs. MSE for 2000 seconds in 4M NaOH solution. The transient behavior in a shorter time scale is shown as an inset. The electrode is 2mm in diameter[150]. ....	80
Figure 4.15: CV recorded at a sweep rate of 10mV/s in 1M NaOH at 25°C for a nickel mesh electrode[151]......	81

Figure 4.16: Linear Sweep Voltammetry conducted in 2M NaOH all potentials reported vs Ag/AgCl reference electrode. A) shows a sweep from -0.8V to 0.2V for pure nickel. B) shows a sweep from -1.2V to -0.2V for tin based solder. C) Shows a and b plotted on the same scale showing the dramatically lower currents seen for nickel. Highlighted in all is the selected voltage region for selective electrochemical etching. D) The current drop during a long term electrochemical etch of tin based solder covered nickel devices. .... 82

Figure 4.17: a) high angle SEM of feedthrough after 5.5hour etch b) top down view of same feedthrough c) combined EDX map of partially covered pin red is Ni, blue is Sn, green is Cu. d) EDX map for Ni e) EDX map for Sn ..... 83

Figure 4.18: Photograph of a feedthrough etched overnight at -0.7V vs. Ag/AgCl in 2M NaOH until the current reached zero. .... 83

Figure 4.19: Diagram of the over-plating process. a) The devices after being released and cleaned showing in light blue the released beam and in purple the inconel pins. b) The same device but coated with a thin nickel over-plate (green). c) A magnified view showing the nickel over-plate attaching the beam structure to the Inconel pins. .... 89

Figure 4.20: Finalized fabrication procedure for producing cm scale released Nickel MEMS structures. .... 90

Figure 5.1: Resistance vs. temperature graphs for a sputtered nickel thin film cycled in air (a) and capped by SiO in argon (b)[158]. .... 93

Figure 5.2: a) Resistance with time recorded for the feedthrough as the oil bath temperature was adjusted to 10 different set temperatures. b) Plot of two successive calibrations of the same beam of temperature vs. beam resistance. .... 94

Figure 5.3: Resistance of a released beam vs. time as the current pulsed through the beam is pulsed to a high value then to a low value in a square wave pattern. High current corresponds to the heat section and low current corresponds to the cool section. .... 94

Figure 5.4: Photographs of the experimental setup to test transitions between air, oil and water. A computer controlled linear actuator sets the position and speed of the feedthrough and a hotplate controls the fluid flow and temperature..... 95

Figure 5.5: Figure of beam temperature vs. time with a square wave current. The transition sequence is air, oil water, oil, air. .... 96

Figure 5.6: a) magnified section of an oil to water transition of the sensor. Resistance of the beam is plotted vs time as the beam is pulsed with a square wave current. The orange amplitude is in oil and the green amplitude is in water. Inset (b) shows he last 10 point in a cycle and a thick blue line denoting the value achieved when

taking the average of the last ten acquired data points used in deriving the temperature amplitude. ....	97
Figure 5.7: The calculated amplitude vs cycle number from the data in figure 5.5. The amplitude changes significantly for the three fluids tested. ....	98
Figure 5.8: a) amplitude vs time for the sensor as it moves through the fluids at 3mm/sec. Three stirring speeds and still fluid are plotted. b,c) same plot at a speed of 6mm/sec and 12mm/sec respectively. d) photograph of the fluid stack at each of the three stirring speeds. ....	99
Figure 5.9: Temperature amplitude vs cycle number for three transitions from air to oil to water to oil to air for an anchored nickel beam. On the last transition water was detected as the oil film on the sensor surface broke. ....	100
Figure 5.10: Amplitude of heating and cooling waveform in several different mixtures of IPA and Water tested in three separate trials plotted on the same figure. ....	101
Figure 5.11: Amplitude of heating and cooling waveform in eight different mixtures of partially stabilized emulsions of oil and water. ....	102
Figure 5.12: Test data from a released nickel beam tested in a matrix of five different high currents, five different low currents, and three different pulsing times. a) Measured voltage vs time. b) Set current vs. time. c) Measured resistance vs time. d) Calibrated temperature vs. time. E) Magnified section of current vs. time (b). f) Magnified section of resistance vs. time (c) measurements with the lowest currents resulted in source meter giving incorrect resistance measurements resulting in off scale measurements for resistance and temperature in some plots. ....	104
Figure 5.13: Response overlays of wire at different currents. a) heating at 800mA after cooling at 100mA. b) Cooling at 100mA after Heating at 800mA. c) heating at 350mA after cooling at 50mA and d) Cooling at 50mA after heating at 350mA. .	105
Figure 5.14: a) pulsing current current used to heat and cool a released nickel beam structure. b) the response of that beam resistance to the stimulus current. ....	106
Figure 5.15: Raw data for the a frequency sweep from pulse times of 20ms to 100seconds of a released nickel beam in Air (green), Oil (purple), and water (blue). ....	107
Figure 5.16: Processed data showing the amplitude of the temperature swing vs pulse period for a released nickel beam in air, oil, and water. ....	108
Figure 5.17: The amplitude of the temperature swing vs pulse period for 200 $\mu$ m diameter 2mm long 316 stainless steel wire in air, oil, and water. ....	109

Figure 5.18: The amplitude of the temperature swing vs pulse period for an anchored on feedthrough nickel beam in air, oil, and water. ....	110
Figure 5.19: The amplitude of the temperature swing vs pulse period for an anchored on feedthrough nickel beam coated with 30um of Parylene in air, oil, and water. ....	111
Figure 5.20: Diagram of the different geometries tested for thermal response to current pulsing in this work. ....	112
Figure 5.21: 3D drawing of the fabricated released nickel beam structures showing the different resistances that are measured by the attached 4-wire source meter. ....	114
Figure 5.22: Calculated thermal response of nickel MEMS beams and larger inconel pins when immersed in a high temperature fluid. When $\Theta / \Theta_i$ is -1 the beams/pins are at their initial temperature. When $\Theta / \Theta_i$ reaches 0 they have reached equilibrium with the bath temperature. ....	116
Figure 5.23: Resistance response of anchored and freestanding devices when rapidly plunged into 170°C oil. ....	116
Figure 5.24: a) Cross section of the comb capacitor showing the interdigitated teeth, the expected electric field and the critical dimensions of the comb capacitor. b) A figure showing a coating that is thinner than the expected penetration depth of the electric field. c) A 3D model of the comb capacitor showing the overall dimensions. ....	118
Figure 5.25: The response of the comb capacitor coated with 30um of Parylene to several different mixtures of IPA and water in sequence. The inset is the generated calibration curve of capacitance vs. water content. ....	119
Figure 6.1: Cross-section schematic of the symmetric opposing electrode electrochemical reactor used for the experiments. ....	123
Figure 6.2: A) XPS scans of pre- and post-sulfided electrodes in tungsten binding energy range. B) XPS scan of post-sulfided electrodes in sulfur binding energy range. C) SEM images of various thicknesses of W catalyst on vitreous carbon, after complete sulfiding. ....	126
Figure 6.3: Product yield of cyclohexanone and cyclohexanol versus nominal catalyst thickness after a 90 minute hydrogenation of 2-cyclohexen-1-one under applied potential of - 1.3V versus Ag/AgCl(sat'd). ....	127
Figure 7.1: Process flow for fabrication of micrometer scale devices. Sputtered permalloy is patterned with a HPR 504 photomask and a chemical etch and the patterned devices are released using a XeF <sub>2</sub> dry etch. ....	131

Figure 7.2: Process flow for fabrication of submicrometer scale devices. Sputtered permalloy is patterned with a dual layer PMMA photoresist in a lift off process and then the devices are released using a FeCl saturated BOE solution and a pentane solution transfer. ....	133
Figure 7.3: System used for resonant testing of the NEMS cantilever structures. The inset is a scanning electron micrograph of a released beam 300nm wide and 2µm long. Scale bar is 500nm. ....	134
Figure 7.4: Phase diagram for the Ni-Fe System[199]. ....	135
Figure 7.5: X-ray diffraction of 200nm thick co-sputtered Ni-Fe thin films deposited at a) room temperature and b) 200°C. Indexed peaks are for face centered cubic nickel.....	136
Figure 7.6: Average thin film stress for 200nm thick co-sputtered Ni-Fe thin films measured by an in-situ Multi-beam Optical Stress Sensor.....	137
Figure 7.7: Magnetic hysteresis loops acquired using MOKE of Ni-Fe thin films deposited at a) room temperature and b) 200°C . ....	138
Figure 7.8: Scanning electron micrographs of a 200nm thick Ni <sub>80</sub> Fe <sub>20</sub> thin film with different thermal treatments. a) Film deposited onto a 200°C heated substrate, b) Film deposited onto a room temperature substrate, and c), d) room temperature deposition followed by a 300°C and 200°C two hour anneal respectively. e) A magnified section of a fracture in a 200°C annealed device after release. ....	140
Figure 7.9: Stress model in a thin film including the first two terms of equation 2.1. ....	141
Figure 7.10: End of cantilever images of 200nm thick Ni <sub>80</sub> Fe <sub>20</sub> structures released with XeF <sub>2</sub> deposited at a) 200°C, b) 25°C and annealed at 300°C (c) and 200°C (d). ....	142
Figure 7.11: Released singly clamped cantilever structures fabricated from 200nm thick Ni <sub>80</sub> Fe <sub>20</sub> . Blue circles are drawn to match the radius of curvature of the released structures. These beams curled and then fell over onto the substrate during the release process .....	143
Figure 7.12: Sequence of magnifications of a circle (a,b,c) showing that a large curl radius is hard to notice on a small length scale. d) A thin NiMo beam that is only a few micrometers long showing very little curvature. e) 500 µm long beams made from the same material showing significant curvature.....	144
Figure 7.13: Released Ni <sub>80</sub> Fe <sub>20</sub> structures showing a) longer curved beams touching the substrate and beams less than 50µm long (b) showing very little curvature.	145

Figure 7.14: NEMS devices fabricated from nickel iron thin films. a) A doubly clamped beam, b) a singly clamped cantilever, and c) a lower magnification view of the array of NEMS structures. The structure in the foreground is a wirebond used to electrostatically actuate the devices..... 146

Figure 7.15: Resonant frequency of an array of singly clamped beams ranging from  $4\mu\text{m}$  to  $2\mu\text{m}$  in length. Inset is the frequency response of a  $5\mu\text{m}$  long beam. .... 147

# List of Tables

Table 2.1: Bath composition used in this work for deposition of nickel thin films..	23
Table 3.1: Composition of Aremco low melting point glass as determined by XPS.	50
Table 3.2: Summary of tested planarization materials. ....	56
Table 3.3: Specifications and general properties of Parylene C[144].....	63
Table 3.4: Change in mass of Parylene C samples after exposure to various solvents for 24 hrs. ....	63
Table 3.5: Summary of sensor device material combinations. ....	65
Table 5.1: Temperature Coefficient of Resistance for several metals as bulk measurements and measurements of thin films deposited by sputtering and evaporation[158]. ....	92
Table 7.1: Comparison of the surface tensions of water, isopropyl alcohol, and pentane as reported by Raccurt[195]. ....	132

# 1 Introduction

## 1.1 Oil Well Sensors

Production logging is a global oil-services industry where down-hole information (such as temperature, pressure, phase identification, and fluid flow) is gathered from already producing wells to assess their health and condition[1, 2]. Data gathered from a well can be used to make important decisions on well maintenance and modifications to improve production[3]. The field of well logging has gone through two major revolutions in the last thirty years. The first revolution in this field was the implementation of smart electrical sensors in a down-hole environment in the 1980s. By doing some signal processing down-hole it became possible to acquire readings from several different sensors at one time from a well. The resulting tools were very large and complicated, often tens of meters tall and hundreds of kilograms in weight. In the 1990's, the implementation of then-modern microelectronics allowed these tools to shrink considerably in size and weight (to about 50 Kg). The tools have not fundamentally evolved since then. Micro-machined technology is almost ubiquitous in modern society, comprising many of the core sensors in automobiles, aerospace, home entertainment and biomedical applications. However, such technology has achieved almost no ingress into down-hole sensing. This is due to the inability of conventional micro-machined materials to survive the extremely harsh well environment which combines high temperatures (up to 180 °C), high pressures (up to 100 MPa), and corrosive fluid media. Traditional packaging of MEMS devices using wirebonding is not compatible with this hostile environment and typical MEMS plastic encapsulation techniques are also not suitable. A number of textbooks on packaging of MEMS sensors exist but none address a solution that is compatible with oil well logging applications[4-6]. Some patents by Schlumberger outline methods for implementing MEMS sensors into a down hole tool but are quite complicated and proprietary[7-12]. Developing a platform for integrating MEMS sensors into a down-hole environment could bring about a third major revolution in down hole logging technology and be quite disruptive in the field.

Horizontal well drilling and completion is becoming more and more common. Horizontal well drilling, though more expensive than conventional well drilling, can often provide substantially increased production and reduces the number of wells required per oil reservoir. Figure 1.1 illustrates the advantage of horizontal drilling in reducing the number of wells required to produce from an oil reserve. A standard vertically drilled oil well only has access to petroleum reserves immediately adjacent to the well bore. If a petroleum reserve is spread out horizontally new wells have to be drilled adjacent to the first to gain access to the entire reservoir. Using horizontal

drilling one can access the entire reservoir with only one well instead of multiple vertical conventional wells.

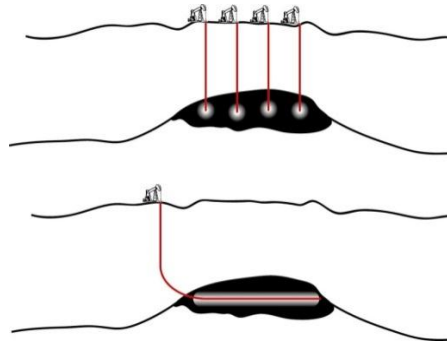


**Figure 1.1:** Illustration demonstrating difference between conventional production using multiple vertical wells (above) and modern production using a single horizontal well (below). The Grey regions show depletion zones.

These horizontal wells have significantly different flow properties compared to vertical wells. Oil, water, and gas phases separate more easily across the well bore in horizontal wells. It then becomes important to have an array of sensors to discretely measure each of these phases. Conventional large production logging tools are only able to measure a single fluid property at the center of the well bore. This single sensor works well in vertical wells but will miss critical information in horizontal wells where an array of sensors are required to get all of the flow information. Currently only two companies (Schlumberger and Sondex – a division of General Electric) have the technology to deploy an array of site-specific sensors across a given well bore and neither of these companies have yet incorporated MEMS sensor technology into their commercially available tools.

The motivation for fabricating multiple MEMS sensor elements onto high pressure feedthroughs is to make a smaller oil well production logging tool capable of measuring multiple fluid properties at a single location in the wellbore. Current tools successfully measure multiple oil well fluid properties but at different locations in the well bore with each sensor only measuring a single parameter at a single location. The existing technology for detecting fluid properties to distinguish oil water and gas in a producing oil well has been established for nearly 25 years and has been focused on using a combination of dielectric constant measurement with differential pressure density to identify the fluids present in an oil well. The techniques using optical and acoustic density are relatively new, being developed in the last five years in order to address needs for fluid identification in highly deviated and horizontal wells.

### 1.1.1 Fluid Identification Techniques in an Oil Well

Below is a list of parameters that are currently used for phase identification in oil well production logging. A short discussion is also included for each method outlining the suitability of the technique for incorporation into a microfabricated platform. The existing commercial technologies for phase identification (water, oil, gas) include the following:

#### Phase ID - Capacitance (Dielectric constant)

The phases of interest have the following dielectric constant (a unitless multiple of the value in a vacuum)

Water = 34-78

Oil = 2-4

Air = 1

The capacitance between two parallel plates of area  $A$  at a distance  $d$  from one another, with a material of dielectric constant  $k$  in between, can be determined from the following equation.

$$\text{Capacitance} = \frac{k\epsilon_0 A}{d} \quad \text{Eq. 1.1}$$

The constant  $\epsilon_0$  is the permittivity of space. The large variation in capacitance values between water and air/oil allows for a good approximation of water content in fluid contacting the sensor. The closer the two electrodes are to one another the larger the capacitance reading and the easier it is to electrically detect changes in the value. Microfabrication is an excellent technique for precisely fabricating a structure with a very small  $d$  value on the order of a few  $\mu\text{m}$ . Current large scale devices compensate for a large electrode spacing by making the sensor quite large and increasing the electrode area. Using microfabrication it is quite possible to shrink the size of this sensor.

#### Phase ID - Differential Pressure Density

The phases of interest have the following densities (psi/m)

Water = 1.4

Oil = 1.2

Gas = 0.0016

Distinguishing liquid and gas is easy using this technique as the difference in density is so large. The variation between oil and water is also significant. Using the difference in pressure between two points on a long tool (oriented vertically) will give a good reading of the density of the fluid. The further the sensors are vertically separated the better the data gathered from this type of sensor. In the case of measurement in a horizontal well this vertical distance is reduced to a low value and sensing density in this fashion is no longer possible. Because of the intrinsic

requirement of this technique to vertically space two sensors from one another, it is not possible to miniaturize this technique.

### **Phase ID - Optical**

The phases of interest have the following optical refractive indices

Water = 1.33

Oil = 1.5

Gas = 1.0004

This detection method uses a specially shaped silica probe that measures the refractive index of a fluid by means of total internal reflection. The intensity of the reflected light from the tip of the probe directly corresponds to the refractive index of the fluid surrounding the tip. The system requires a photo-diode for detection and a light emitting diode for producing the light. There are significant challenges in finding a monochromatic light source and detector that work reliably in the downhole environment. This technique is inherently quite small and only requires a single optical fiber exposed to the wellbore fluid. Schlumberger is the only company to use this technique for phase identification in their downhole tools and they have patented its use[13].

### **Phase ID - Acoustic Density**

This method uses the damping effect of a dense and viscous material on a resonating structure to measure the difference between phases. The density difference between water, oil, and gas is shown in the differential pressure density section. The damping of the resonating structure causes a shift in the structures resonant frequency which can be measured with a piezoelectric driving device and a piezoelectric sensor. By coupling this sensing circuit and driving circuit in a phase locked loop the resonant frequency can be detected with surprisingly high accuracy. This method of density measurement is well established in other fields, such as in bio-detection or micro-fluidics[14] and has recently been incorporated into commercial down-hole sensors[15, 16]. The structures fabricated in this work that are released fully from the substrate would be excellent for this type of fluid identification. Brueckner et al. demonstrated a technique for resonating an electrically conducting free standing beam using a short current pulse through the beam in a strong DC magnetic field[17]. The Lorentz force would start the beam in motion and then the resonating beam in a magnetic field would generate a measurable AC current in the wire that could be detected with an amplifier and an oscilloscope. The frequency of the generated current is at the resonant frequency of the released beam and could be used to determine the density of a fluid. Schlumberger has conducted a significant amount of work on a sensor using this actuation technique but at a larger scale for fluid property measurement at high pressure and temperature[18]. The mechanical requirements for this type of sensor

are met using the freestanding beams developed in this work. This technique lends itself to improvement through microfabrication.

### **Phase ID – Thermal Conductivity**

Thermal conductivity is a technique that was developed in this work that is not currently used in oil well production logging but performs quite well at distinguishing between water, oil and gas. The thermal conductivities are dramatically different for these three materials:

Water = 0.6W/mK

Oil = 0.126W/mK

Gas = 0.024W/mK

The use of an electrically heated wire to measure thermal properties of materials was started in the 1950s by a number of researchers in different fields. The growing availability of precise electronic equipment for measuring current and voltage as well as the use of electrical switching apparatus that allowed for pulse heating and fast switching for voltage measurements from a thermocouple led to the development of these new techniques. This in turn enabled materials property measurement and observations to be conducted at extremely high temperatures.

Ordway conducted experiments observing the crystallization and melting behavior of glass mixtures using a heated platinum wire[19]. Experimental difficulties encountered while operating at temperatures above 1000°C led him to develop a new technique based upon a pulse heated thermocouple. Electrical current was pulsed through the thermocouple 50% of the time and the other 50% of the time the voltage from the thermocouple was measured. Using this technique he was able to control the temperature of a glass sample to within 0.1°C at temperatures ranging from room temperature to above 1000°C[19]. This technique was expanded and refined by Welsh who used a 5% rhodium-platinum/20% rhodium-platinum thermocouple to expand the operating temperature up to 1750°C[20]. In a similar timeframe to this work a pulse heated wire technique for measuring a wire's heat capacity was developed by Pochapsky that pulsed a thin platinum wire with current and measured the resistance change using an oscilloscope[21]. This technique was also used for measuring heat capacity and thermal diffusivity in silver bromide. This technique is frequently used to find the heat capacity and thermal conductivity of liquid samples[22].

Recently a number of MEMS based sensors have incorporated heated wires for both material characterization [23-26] and measurement of flow rates [27-29]. Heated wire flow sensors are quite useful because they are very simple, robust, do not contain moving parts, are sensitive to small flow variations and can measure a wide range of velocities. Most commercial mass flow controllers use a heated wire technique for flow measurement because of these advantages. Thermal based flow

sensors are also used in hostile environments where a spinning turbine structure would not survive. Using microfabricated structures for thermal properties measurement has allowed for an interesting development of a new method called microcalorimetry that allows for extremely high heating and cooling rates of a sample under test. The larger the ratio of surface area to volume for an element the faster it can be cooled by thermal convection[30]. Greve *et al.* made a micro calorimetric sensor from a silicon nitride beam with doped silicon heaters and temperature sensors on top with dimensions of 400 $\mu$ m long, 100 $\mu$ m wide, 400nm thick. They estimated that the thermal mass of their bridge was 30nJ/K and were able to heat their beams from 20°C to 500°C in 30ms by applying a voltage ramp to their heating elements[31].

## **1.2 Metal MEMS**

Traditional MEMS microfabrication materials and methods are not compatible with the down hole oil well environment. Silicon is brittle and has poor fracture toughness, gold wirebonds are fragile and suffer dramatic degradation at high temperatures, and aluminum has poor corrosion characteristics when exposed to H<sub>2</sub>S. Most of the traditional materials used for MEMS device manufacturing are unsuitable for fabrication of a robust sensing platform for an oil well logging environment. The field of metal MEMS addresses many of these limitations.

Many different metal MEMS devices have been demonstrated and the field is well developed. Most initial work involved creating purely physical devices such as tiny gears, springs and levers. This initial work then progressed to exploit a key material property advantage of metals over silicon: electrical conductivity. Silicon micro devices require a separate doping or metallization process step in order to integrate electrical actuation or measurement. Metal devices because they are electrically conducting do not require this extra processing step. Below is a brief outline of metal micro-fabrication followed by a discussion on the development of this field into electrically integrated metal MEMS devices.

### **1.2.1 Metal Micromachining**

The most established manufacturing process for fabricating metal micro structures is called LIGA (A German acronym for lithography, electroplating, and polymer replication). The LIGA process flow involves patterning a thick resist, using X-ray lithography, on an electrically conducting substrate and then electroplating a metal into the lithographically patterned mold. The mold is then removed and the resulting structure can either be used directly or as a template. This process was first reported in 1982 for the application of fabricating metal nozzles for the enriching of uranium[32]. A review of LIGA technology applications by Malek et al. in 2003 identified over 100 different applications in the four categories of fabrication of MEMS and high precision parts, Micro-Opto-Electro-Mechanical Systems

(MOEMS), Microfluidics and bio-MEMS[33]. A book on “LIGA and its applications” is also available and explains some of the history and challenges of this technique[34]. Most successful applications of LIGA involve making two dimensional physical parts with features smaller than can be obtained using precision machining. These parts typically are not used for sensor or electronic applications and are purely physical in their implementation as gears, springs, latches or other moving mechanisms.

Current LIGA fabrication processes requiring X-ray lithography of Polymethyl methacrylate (PMMA) resists are expensive and slow and limit application of this technique. Using intermediate molds with conducting bases can help improve the throughput of this technique creating devices up to 250 $\mu$ m thick but require post processing involving polishing[35]. The use of SU-8 photoresist instead of PMMA can reduce the exposure time required in X-ray lithography by a factor of  $\sim$ 300 resulting in a dramatic decrease in cost per exposure and increase in throughput of an X-ray lithography system[36]. SU-8 can also be used with a conventional UV or deep UV exposure system further reducing the cost of the LIGA process[37]. Unfortunately, UV exposed SU-8 sacrifices the resolution of X-ray lithography and the attainable device aspect ratio is lower and these are the two principle advantages of the LIGA process over traditional machining.

A critical advantage of LIGA and electroforming methods is the improved resolution possible with the technique, this advantage in resolution was quite significant 25 years ago with LIGA being able to provide sub micrometer accuracy and devices several millimeters thick. This advantage has been worn away over the last 25 years as traditional machining has advanced significantly and the gap between LIGA and machining is not as significant. Precision waterjet cutting provides a processing accuracy of approximately 100 $\mu$ m, laser cutting can provide accuracy reaching 50 $\mu$ m, and a combined Laser MicroJet cutting process by Synova has pushed this accuracy to better than 5 $\mu$ m[38]. Laser cutting technology reaching such high accuracies limits applications of LIGA technology to spaces that require sub 5 $\mu$ m features. Meanwhile advances in thermal stability, vibration control, and fabrication of precision ultra-sharp cutting tools have allowed for CNC milling and lathe mechanical machining processes to reach extremely high accuracies of better than 10 $\mu$ m[39].

Traditional LIGA is called a 2.5D process as parts fabricated with this technique are extruded 2D patterns and changes in features through the depth is accomplished by adding layers. Significant work has been conducted towards extending the LIGA style process to produce 3D metal structures by producing a 3D pattern in a photoresist and then electroplating around this structure. Microstereolithography has been used to pattern SU-8 resist in arbitrary 3D patterns, with a resolution of 5 $\mu$ m, which can subsequently be filled with nickel using electroplating[40]. Multiphoton absorption polymerization has also been used to produce resin structures which can be transferred to polydimethylsiloxane (PDMS) creating a mold

that can be used to make 3D structures[41]. Exposing a photoresist in two orthogonal directions can also allow for 3D patterns to be fabricated as demonstrated by a microneedle array[42]. Taking advantage of the collimated nature of the X-ray lithography process and the ability to have a large mask to substrate distance allowed researchers to expose a cylindrical substrate coated with resist to create a spiral pattern that could be used to fabricate electroplated copper microcoils patterned with a pitch of 10 $\mu$ m[43, 44]. These examples of extending the LIGA process to create 3D metal structures show great promise for producing a wide variety of interesting structures beyond the reach of traditional mechanical machining.

Non-lithography based microfabrication techniques are typically serial in nature involving deposition or etching through a physical, chemical, or electrochemical process. Only a few non-lithographic techniques are capable of creating features below 10 $\mu$ m in size of which laser CVD forming[45], Focused Ion Beam fabrication, and electrochemical micro machining[46] are included. These techniques, although very accurate and capable of creating extremely fine featured 3D structures, are typically extremely slow requiring days to fabricate complicated structures in a serial fashion.

Some specific examples of metal microfabricated mechanical structures are expanded upon below including the fabrication of gears, mechanical munition fuzes, and atomic force microscopy probes. These are three examples of where purely mechanical microfabricated structures have been found to be useful.

The performance and cost of LIGA fabricated parts for application as watch gears and precision micro motor parts was compared by the German ANKA institute in 2008. They showed that LIGA fabricated gears could reduce backlash in a motor by 30% compared to precision machined gears, unfortunately the limitation of using a NiCo alloy vs high strength steel reduced the lifetime of these same gears by half[47].

An excellent application of metal micro-mechanical structures in hostile environments can be found in work by CH Robinson et al. to produce all metal ultra-miniature safety and arming devices for munitions fuzes. Munitions fuzes, which include multiple latches, springs and pins, are designed to survive firing from a weapon and subsequently arm warheads after a set acceleration and rotational velocity are reached[48]. It was found that completely removing silicon from the fabrication process was necessary to prevent device failures from impact induced fractures. They used a nickel based LIGA process on a metal substrate and found that the transition to an all metal construction even allowed for re-use of the Fuzes when used without explosives indicating that the devices survived firing, activating, and landing[49]. Similar work has been conducted by multiple military entities to improve the reliability and reduce the cost of weapons triggering mechanisms [50, 51].

Multiple applications in Atomic Force Microscopy (AFM) make use of all metal microfabricated probes. Electroformed nickel probes with a gold coating have been used for AFM based Nanolithography[52]. High resonant frequency probes made from a Titanium/Gold bilayer with a silicon tip[53] provided excellent performance as a scanning probe. A combined electroforming and adhesive transfer process allowed for all metal AFM probes from different metals including gold, copper, and nickel[54]. Metal probes enable additional applications due to their electrical conductivity, are often more robust, and can have higher sensitivity than silicon probes.

### **1.2.2 Metal Micro Electro Mechanical Systems (MEMS)**

More recently, metal MEMS structures that are interfaced with electronics resulting in intelligent structures that can be used as sensors have been created. Fabrication of electroplated structures that are interfaced with electronics involve challenges as the requirement for electrical current to electroplate also means that all of the plated parts must be electrically connected during plating, additional patterning or processing must then be done as an additional step to electrically isolate the plated devices.

When these micro-machined devices are integrated with sensing and driving electronic circuits a much wider list of possibilities is enabled. These applications for electrically interfaced high aspect ratio metal MEMS include high reflectivity movable micro-mirrors, high current micro-relays, high mass accelerometers, and low thermal expansion micro-optical devices[35]. The multi-step processing required to enable complicated multi part metal MEMS devices has limited the number of demonstrations of metal MEMS devices shown in literature. Differential thin film stress and electroplating reliability issues also work against designers who wish to fabricate metal MEMS devices. A recent example of these hardships can be seen in an impressively unsuccessful attempt to make deformable micro mirrors using three different commercial metal micro fabrication processes[55]. Three commercial processes for fabricating electrically interfaced metal MEMS devices exist: MetalMUMPS which offers a single 20 $\mu$ m thick electroplated nickel layer that can be released, Polystrata which provides a multi-layer copper process for fabricating 3D structures and EFAB which allows for up to 50 layers of electroplated nickel to be deposited. These methods relate closely to the microfabricated devices in this work and will be briefly outlined below.

A single layer commercial multi-user nickel MEMS process is offered by a publicly traded European company MEMSCAP called MetalMUMPS. It offers an electroformed nickel process step integrated with signal and oxide isolation layers. The nickel devices are 20 $\mu$ m thick and can be released by 25 $\mu$ m through a KOH etching step[56]. This process is available to educational and industrial clients at a fixed price per 1cm x 1cm die in lots of 15. A number of papers have recently been published based upon this open process involving metal relays[57], gyroscopes[58],

inductors[59, 60], tunable capacitors[61], and a voltage doubler[62]. The residual stress in the nickel layer that these structures are made from limits the structures that can be successfully implemented as long released beams tend to bend considerably[63].

A technique developed by the company Micro-fabrica called Electrochemical FABrication (EFAB) expands typical LIGA processing techniques to allow for truly 3D fabrication through the use of successively electroplated and polished layers. By using up-to 50 layers between 2-45um thick, that can be precisely controlled in 2 dimensions, many different 3D structures are enabled with a demonstrated total device thickness of just over 1mm. This process uses nickel devices surrounded by copper in a layer by layer additive method. At the end of the additive process the copper can be selectively etched away leaving complex freestanding nickel structures. This process is limited by registration between layers and stress gradients in the nickel layers causing device buckling and bending [64-66]. Very complex metal MEMS structures have been demonstrated on the EFAB process including an all nickel micro-gyroscope shown in Figure 1.2c and d[64]. The EFAB technique depends upon a highly selective chemical etch that allows for a significant amount of copper to be etched away while the nickel device remains. Another technique that depends upon this Cu-Ni etch selectivity involves micro-milling a mold in copper followed by electroplating nickel into this mold and then machining this electroplated nickel further. This leaves a 3D nickel part anchored into a copper mold that can be selectively etched away[67].

The Polystrata process by Nuvotronics allows for a multi-layer 3D copper devices using a sacrificial photoresist layer that is removed at the end of the process that serves a very similar function as the copper in the EFAB process[68]. This process flow has gained significant traction for fabrication of Radio Frequency (RF) passive components like combiners, filters and splitters[69]. An example of a 3D radio frequency component almost 1mm thick made using the Polystrata process is shown in Figure 1.2a.

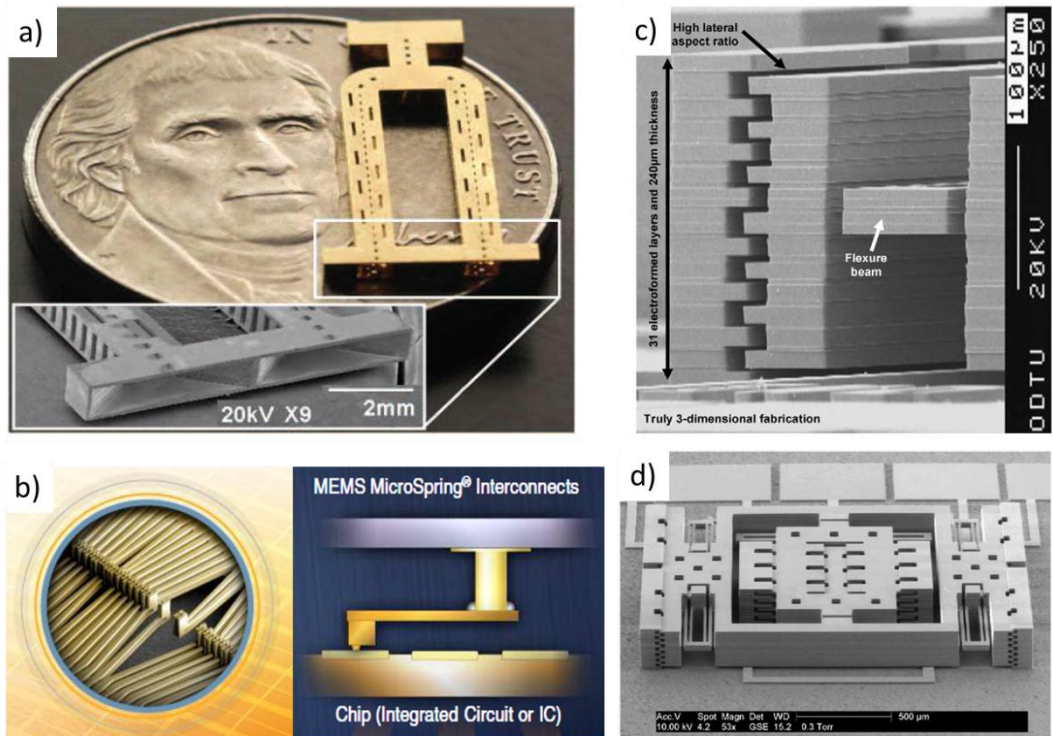


Figure 1.2: a) 3D Copper RF component fabricated with the Polystrata process[69], b) diagram and false colored SEM of probe card springs by FormFactor[70], c-d) SEM images of a nickel gyroscope fabricated using the EFAB process[64].

One significant application for larger metal MEMS devices can be found in the semiconductor probe card manufacturing industry. Probe cards are used by semiconductor manufacturing companies to enable electrical testing of integrated circuits before they are diced and packaged. These probe cards consist of arrays of metal contact springs that make electrical contact with the bond pads of an integrated circuit to connect the circuit to electronic test equipment. A diagram of the contacts and a false colored SEM image of a probe card from FormFactor are shown in Figure 1.2b. Chips that do not pass electrical testing using a probe card can then be thrown out and the cost of packaging defective chips is saved. This probe card market, based upon the implementation of metal micro spring contacts, was approximately \$913 million a year in 2011[70]. A world leader in this technology is Form Factor who is one of the top 10 MEMS manufacturers in the world and specializes almost exclusively in metal MEMS[71-73]. Several other groups have done work in this field. Bong-Hwan Kim et al. produced probe cards consisting of an electroplated Ni-Co beam and tip bonded to an electroplated nickel post using an Au-Sn solder paste and a flipchip bonding process[74]. A number of techniques have been shown in literature to make probe card like structures including: internal differential stress curled nickel beams[75], flip chip bonding of high aspect ratio nickel devices[76], and through wafer electroplating and etching[77]. All of these processes share the use of electroplated metal in their fabrication and involve quite complex fabrication processes involving flip chip

bonding or through wafer etching. Probe cards can also be fabricated using silicon MEMS processing to form silicon probe structures and then coating or patterning onto these structures with 1-20µm of metal to reinforce, improve fracture resistance, and increase electrical conductivity of the probes[78, 79]. One of the simplest techniques for fabricating metal probe cards involved physically bending the probe contacts and annealing the bent beams using electrical current to retain the out of plane shape but this technique only achieved 1mm pitches and produced very rough electrical contact points[80]. These probe card examples demonstrate thicker metal MEMS structures with some depths over 1mm enabled through bonding process steps.

### **1.2.3 Metal MEMS materials**

Many metal MEMS examples in literature are fabricated from nickel or alloys of nickel. The mechanical and materials characterization of nickel electroplated thin films specifically for MEMS applications have been addressed by some research groups. Luo et al. explored the Young's modulus of nickel sulfamate bath electroplated nickel using micro-cantilever structures and showed some dependence of Young's modulus on the bath temperature and plating current density[81]. Son et al. fabricated tensile testing coupons from electroplated nickel and used these to generate stress strain curves and conduct fatigue testing. They found, for their nickel sulfamate bath electroplated nickel, an average yield strength of 480MPa, a tensile strength of 1.2GPa, an elongation of 0.33, and a fatigue strength of 143MPa[82]. The measured fatigue strength of their nickel films was lower than expected. Tensile testing of structures between 50µm and 200µm thick showed no thickness dependence on film mechanical properties[83]. Tungsten has been alloyed with electroplated nickel by adding sodium tungstate to the electroplating bath resulting in a higher ultimate tensile strength of between 1100 and 1400MPa and better thermal stability (maintaining hardness after annealing at temperatures up to 700°C)[84].

One serious problem found in nickel electroforming is caused by incomplete filling of high aspect ratio and complex geometries with the plated metal. Some improvement with respect to this issue has been found by using a low stress nickel chloride bath and implementing ultrasonic agitation either before or during plating[85, 86].

Electroplated nickel has generally been shown to work well for MEMS devices with its combination of low film stress, high strength, rapid deposition rate, good film uniformity/smoothness, and the ease and simplicity of the deposition technique compared to CVD and PVD deposition methods.

Other materials have been used for metal MEMS devices and are discussed below, the development of new materials for micro applications is a developing field and much research has been conducted in this area.

Creep resistant alloys of aluminum were developed by Texas Instruments in the 1990s for application in micro-mirror devices. The mechanisms of creep and fatigue in metal MEMS was discussed in a review by Merlijin et al. where they explained that creep is not significant when the temperature is maintained below  $0.3 T_m$  and fatigue in thin metal films is less significant than what would be expected from bulk material analogs[87]. Fatigue properties of thin film metals are expected to behave significantly differently than bulk materials due to the small number of grains that would span the thickness of the film[87]. Movement of dislocations to the surface of the material results in dislocation pileup resulting in fatigue crack formation. In thin films the quantity of dislocation movement to the surface is lower due to the small number of grains across the thickness of the film making it difficult for dislocation density to reach a level high enough for fatigue cracks to form[88]. This result contrasts with findings by Son et al. [82] which showed lower than expected fatigue strength for electroplated nickel structures, but in this case the microstructure and scale were significantly different than those studied by Texas Instruments in their micro-mirror devices.

Sandia has developed a Molded Tungsten based MEMS process (MOLTUN) that creates free standing devices above a silicon substrate. The process uses PECVD  $\text{SiO}_2$  as a sacrificial layer and a CVD deposited W layer as a structural layer. Devices have a 1 $\mu\text{m}$  lateral resolution, allow for aspect ratios of 5:1, are approximately 1 $\mu\text{m}$  thick and are released by a distance of approximately 1 $\mu\text{m}$ [89]. This process has been used for building ultra-high pressure (GPa) sensor arrays and photonic crystals[90, 91].

One drawback of nickel MEMS devices is the lower hardness and wear-resistance of electroplated nickel vs silicon, ceramic, or high strength steel materials. This limitation has been overcome by the use of metallic glasses as a construction material for micro devices. By using nickel, alumina, or silicon molds fabricated using lithography, bulk metallic glasses can be patterned with a micromolding process to make a wide variety of micro devices with excellent mechanical properties[92, 93].

The Mitlin research group at the University of Alberta has conducted significant work in the field of alloy design for micro and nano-mechanical applications. They developed a methodology and used it to find composition regions in three alloy systems where metallic glasses would form. Then these metallic glass materials were used to fabricate extremely small size and low thickness released metal beams with excellent mechanical properties. The explored alloy systems included Al-Mo[94], Ni-Mo[95], and Cu-Hf[96].

Although high hardness, corrosion resistance, and high strength are possible with metallic glasses, the limitations of being brittle, having poor thermal stability, and possessing a very low Temperature Coefficient of Resistance (TCR) removed metallic glasses as candidates for the sensor platform developed in this work for a downhole phase identification sensor. The surface of a high pressure feedthrough is quite

dynamic during temperature cycling from 20°C to 200°C as the feedthrough glass and the inconel body/pins have different thermal expansion coefficients. The metal coating that bridges the interface between the pins and the glass must have some ductility in order to accommodate this strain without cracking.

### **1.3 Harsh Environment Sensing**

Central to all data acquisition and sensing applications in the oil well environment is a device called a high pressure feedthrough. Feedthroughs are required because electronics and battery systems used for measuring electrical signals from sensors are not able to survive the high pressures seen in an oil well. The high pressure feedthrough allows for the sensor element to be kept in the fluid environment at a higher pressure than the sensor electronics which are protected by a pressure tight housing. By integrating sensors directly into a high pressure feedthrough, electrical connections in the hostile oil well environment can be avoided and the electrical sensing circuits can be more closely integrated with the sensor elements themselves. The idea of this tight integration and the potential increase in sensor durability and decrease in sensor size was the motivation for exploring the possibility of microfabricating sensors directly onto a high pressure feedthrough.

#### **1.3.1 Feedthrough Integration**

An example of MEMS integration into a down hole environment is available in a pressure transducer fabricated by KELLER AG für Druckmesstechnik. They integrate a piezoresistive pressure sensor that is microfabricated out of silicon with a high pressure feedthrough and protect the sensor with an inconel bellows structure. A cut away of one of their sensors is shown in Figure 1.3 where the inconel bellows that physically protects the sensor has been cut away. Inside of the sensor is a firmly mounted silicon chip with a microfabricated pressure sensor membrane. The silicon chip is electrically connected to the high pressure feedthrough with thin gold wirebonds. This delicate system works because the sensor does not need to be in direct contact with the oil wellbore fluid. Pressure is transmitted through the inconel membrane due to elastic deformation and the sensor remains immersed in clean oil during operation. This architecture would not work for a sensor system that needed to be exposed directly to a wellbore fluid. Two aspects of this design need to be altered in order to improve durability: Removal of the delicate wirebonds, and replacement of the brittle silicon sensor element with one based on tougher materials.

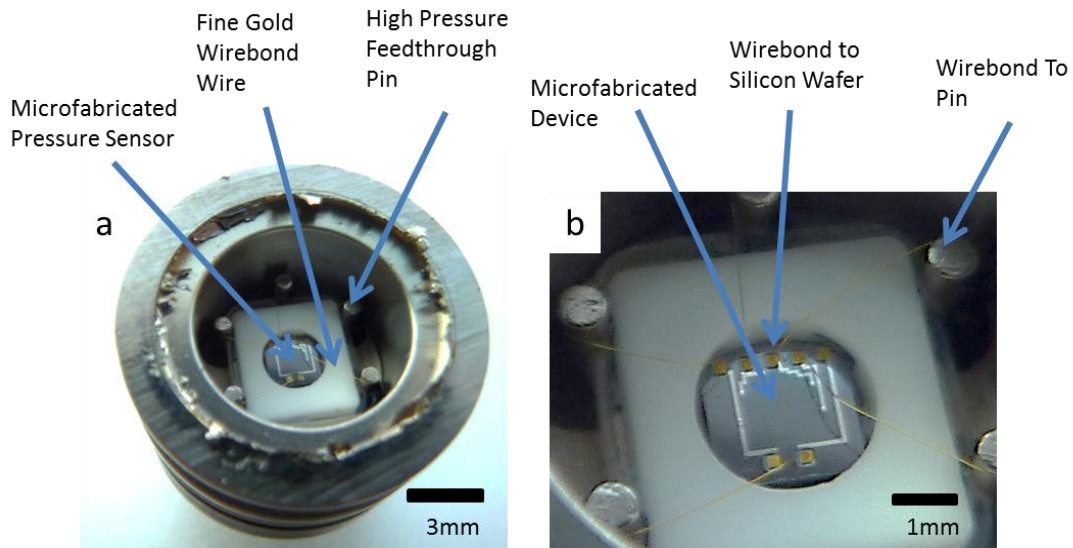


**Figure 1.3: a) Illustration of traditionally accepted integration of a MEMS device with a high pressure feedthrough involving wirebonds. b) A higher magnification of the MEMS pressure sensor with gold bond pads wirebonded to the feedthrough pins**

Three examples showing the removal of wire bonds and a transition to a more durable materials platform will be outlined below. It is interesting that these objectives existed for a different electrical platform in the 1960s. Prior to the 60s electronic transistors were packaged in TO-5 glass sealed hermetic cans where wirebonds attached the individual silicon based transistors to the pins in the TO-5 can packages. The structure was not unlike what is shown in Figure 1.3b where a single silicon chip is glued in the center and wirebonded to the pins in the package. The wire bonds introduced two problems: they slowed production as they had to be manually placed in sequence, and they dramatically reduced reliability. In 1964 IBM removed the need for wirebonding in packaging and allowed for multiple transistors and resistors to be placed in the same packaged module with their Solid Logic Technology (SLT)[97]. SLT allowed for multiple electrical devices to be packaged together dramatically improving the transistor density for computers, lowering timing delays in circuitry, reducing cost, and improving reliability[98]. One of these modules is shown in Figure 1.4 along with an advertisement of the time demonstrating the impact of the technology on computers. This packaging was enabled by the ability to “print” electrical traces and resistors directly onto ceramic substrates with holes for electrical interface pins that could be installed in a later step.

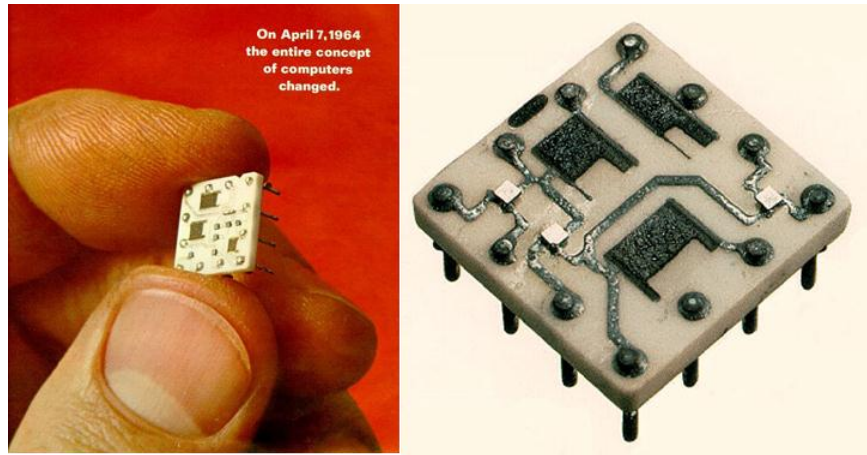


Figure 1.4: Photograph of the IBM SLT module[99] and a magazine ad highlighting the revolution caused by this integration[100].

More recently Schlumberger, realizing the advantages of integrating MEMS sensors with high pressure feedthroughs to enable advanced fluid diagnostics in oil well environments has created a platform for feedthrough integrated MEMS devices based on ceramic printed circuit board technology[12]. Shown in Figure 1.5a is a high pressure feedthrough module that allows for MEMS sensors to be placed in a high pressure oil well environment and Figure 1.5b is a cross section of this device. Marked 142 is where the MEMS devices would be located and 104 is the ceramic feedthrough structure. The building of such a large, custom machined, cylindrical, and multi-layer ceramic element is a very complicated process. The system requires multiple seals and due to the large ceramic component it is not expected to be very robust.

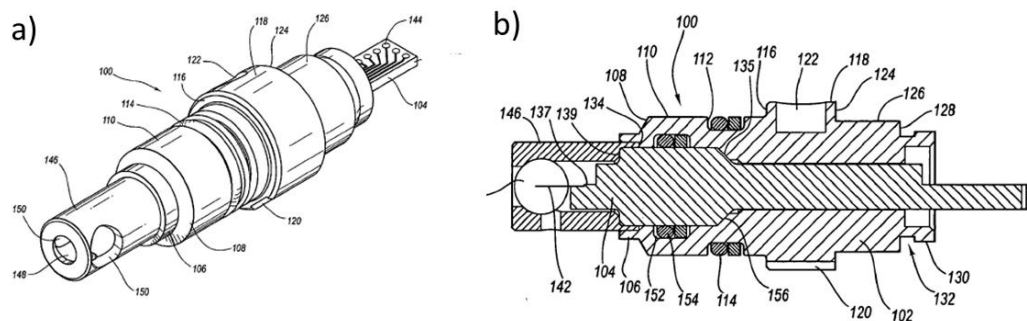
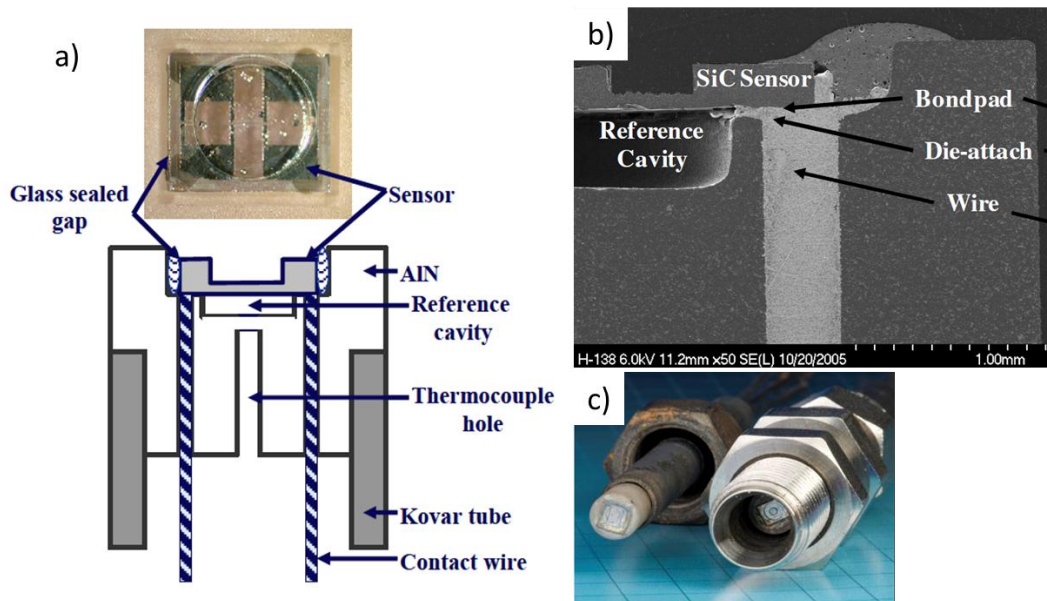


Figure 1.5: Figures from Schlumberger patent 7392697 that show a method of integrating MEMS sensors with a high pressure feedthrough[12]. a) is an isometric view and b) shows a cross section view of a).

The NASA Glenn research centre has a division dedicated to the building of high temperature sensors and electronics for hostile environments for application in deep oil well monitoring, jet engine monitoring, nuclear reactor pressure monitoring, and a potential in situ science mission to Venus (where the surface temperature is 470°C)[101]. They have developed a platform including SiC based Metal Oxide Semiconductor Field Effect Transistors (MOSFETS), Junction Field Effect

Transistors (JFETS), sensors, and packaging that can all survive temperatures of above 500°C[102]. The Glenn centre has patented a Direct Chip Attach (DCA) process for creating a reliable electrical connection between a SiC based pressure sensor and a high pressure feedthrough that can survive high temperatures (600°C) and pressures up to 500psi[101]. This DCA process does not involve wirebonding which was recognized by the researchers to be unsuitable for hostile environments and high temperature operation. Figure 1.6a shows a diagram of a SiC based pressure sensor integrated with a high pressure feedthrough showing the “contact wire” directly attached, with the DCA process, to a SiC sensing element. Figure 1.6b shows a SEM image of the contact wire making direct contact with the SiC sensor die and the low melting point glass used to seal the connection and sensor to the feedthrough. Finally Figure 1.6c shows what the sensor elements look like when integrated with a high pressure fitting in an integrated sensor ready for application. These sensors were tested for 360 hours at 600°C at pressures up-to 500psi and found to function properly with drift less than +/- 20%[101].



**Figure 1.6: Images of the high temperature SiC based pressure sensor developed by the Glenn research centre. a) A photo of the sensor element and a diagram of the sensor integrated into a high pressure feedthrough using the DCA process[102]. b) shows a cross section SEM image of the DCA between the Contact wire and the SiC sensor[101]. c) Sensor elements integrated with high pressure fittings in the final product that could be used for conducting high temperature tests[101].**

The two solutions shown from Schlumberger and NASA for integrating MEMS sensors with a high pressure feedthrough are either extremely complicated and delicate (Schlumberger) or not capable of operating at oil well pressures (NASA). No other wirebond free solutions for MEMS integration with a high pressure feedthrough exist. There remains a demand for a solution that provides a wirebond

free IBM SLT like platform for MEMS sensor integration with a high pressure feedthrough that is simple and robust.

### 1.3.2 Freestanding Sensors

There are several significant advantages to having MEMS sensor elements released from a surface by a significant distance of approximately a centimeter. The best thermal conductivity or thermal flow rate sensors involve released structures with a low thermal mass.

In a flowing liquid there is an advantage of placing the sensors above the surface boundary layer. The flow rate of a fluid at a boundary is zero which results in poor transport of the fluid to be measured across the sensor surface. By placing the sensors farther into the fluid flow a better representation of the bulk liquid is possible and flow rates past the sensor are higher as shown in Figure 1.7.

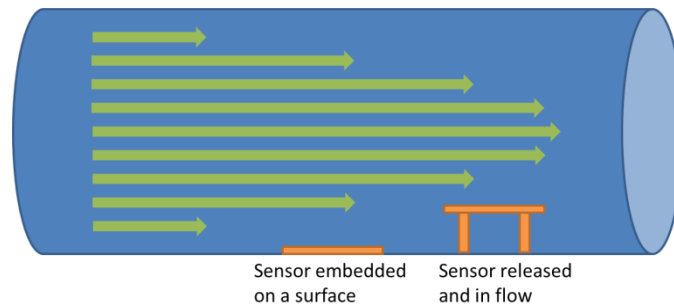


Figure 1.7: Diagram of flow velocities in a pipe in laminar flow.

A second major advantage for having a centimeter scale release of the sensor devices arises in two phase flow measurements with water and oil. Surface wetting of the sensor by oil and water when making two phase measurements can cause issues with a traditional device that is close to a surface. If a flat sensor is covered by a thin film of oil that wets the surface well, it will be difficult for this thin layer to be removed if the sensor is then brought into contact with water. It is possible that the sensor would then only read the presence of oil for the remainder of the logging. Vice-versa, it could also be possible to cover the sensor with water and it would no longer detect an oil environment. The response rate of the sensor when transitioning between water and oil phases depends on this wetting behavior and the flow rate. While this problem can be somewhat mitigated by using a detection technique that can measure some distance above the sensor element like a capacitance sensor, the best case is to have the sensor released and allow for significant flow around the whole sensor element resulting in a washing effect thus reducing the chance of surface wetting based masking.

The third major advantage is dramatically increased sensitivity for thermal measurements due to more thermal contact with the fluid and a reduced thermal mass of the sensing element. When a temperature sensor is anchored to a surface,

not only does the element need to heat itself, but also the surrounding support. If the beam is released, only the beam's thermal mass needs to be heated and the support has little effect on the response rate of the sensor.

These three significant advantages make fabricating a three-dimensional released sensor highly desirable and the larger the release distance the better these advantages become. Releasing MEMS devices a full centimeter from the substrate would make for a fantastic fluid sensor platform. The ability to reach sensors beyond the stationary boundary layer of a surface, the avoidance of sensor masking in mixed oil water flow, and the dramatic decrease in thermal mass allow for a new class of MEMS sensors.

Several examples of thick sacrificial layers exist in the MEMS literature. Maciossek et al. produced several different micro structures with release distances up to 100 $\mu$ m using AZ 4500 series photoresist and electroplated copper[103]. Cui et al. used a 4 $\mu$ m thick sacrificial layer from AZ4562 photoresist to release thick electroplated nickel devices[104]. Another example of a thick sacrificial layer for the fabrication of half-coaxial transmission line filters used a 100 $\mu$ m thick layer of JSR THB-151N photo resist and removed the layer with oxygen plasma ashing. Their removal rate was only 1 $\mu$ m/minute and the removal process caused thermal damage to the devices and left significant residue behind[105].

One major limitation of the etching technique is that most chemical etches are quite slow. In the etch rates for micromachining processing handbook several common etchants are described and their etch rate for a variety of materials are listed. The fastest chemical etches listed, of aluminum in KOH (30% by weight in water) 12,900nm/min and vanadium in Si Iso Etch (126 HNO<sub>3</sub> : 60 H<sub>2</sub>O : 5 NH<sub>4</sub> F). 9,600nm/min would still take an extremely long time to etch through 1cm of material 775min or 1041min respectively[106]. Etching and ashing of sacrificial layers is intrinsically slow when working with thicknesses approaching 1cm.

The freestanding devices developed in this work use a sacrificial tin scaffolding surrounding an array of pins instead of a traditional substrate for supporting MEMS devices. For traditional MEMS manufacturing techniques, the surface quality of the substrate is of utmost importance: Most fabrication is started on a silicon wafer surface that is free from defects and perfectly flat,[107, 108] while other devices start with polished glass or silicon carbide[109-111]. Fabrication on other surfaces such as titanium and creating freestanding structures using soft lithography is also done[112, 113]. If the surface is not flat and free from defects, then yield of the fabrication process will suffer dramatically. Creating a new substrate with a sacrificial layer on a surface that ordinarily would prohibit lithography based fabrication is a new concept that is developed in this work.

## 1.4 Conclusion

This thesis outlines the development of two platforms for integrating microfabricated sensors with high pressure feedthroughs for application in hostile high temperature high pressure environments. A specific application in oil well production logging is explored and two sensors were implemented with these developed platforms for application in an oil well.

The first platform developed, involving microfabrication on a cut and polished feedthrough, is more robust than the wire bonded silicon die technique used for MEMS integration in pressure sensors and therefore allows for direct interface of a microfabricated sensor with a fluid environment which is not currently possible. Two solutions for removing these wirebonds from a hostile environment sensor platform have been developed by NASA and Schlumberger. The NASA solution has only reported operation at pressures of 500psi (not high enough for oil well application) and the Schlumberger solution involves a multilayer machined ceramic circuit board which is complicated, proprietary and may have poor durability. My platform takes up less space than the Schlumberger platform, and provides an extremely simple integration with a high pressure feedthrough. The platform developed within has been pressure tested to 10,000psi and temperature cycled several times from 20°C to 200°C. This platform is simpler than the Schlumberger feedthrough, more robust than the NASA feedthrough, and enables electronics integration with a variety of electrical and thermal based sensors within the oil well environment.

The second platform developed, involving free space fabrication of nickel microfabricated devices onto an array of pins, enables for the very first time microfabricated metal MEMS that are released by distances of 1cm from their substrate. Multiple examples of sacrificial layers and release processes for metal and nonmetal MEMS devices exist, but the largest distances reported are approximately 1mm (Polystrata, EFab) while the majority of examples claiming large release distances involve sacrificial layers of less than 100um. Larger structures can be fabricated using bonding processes but it is difficult to precisely and with good repeatability bond small structures to pins. No examples of MEMS devices with sub 50um features and heights of 1cm were found in literature making the structures fabricated in this work unique.

The released MEMS sensor process flow allows for fabrication to be done on any pin array substrate regardless of surface quality. By fabricating a new surface the problem of MEMS substrate selection is avoided. Being able to place released MEMS sensors directly onto traditional style circuit boards, ceramic circuit boards, electrical connectors, ribbon cables, pin headers, or high pressure feedthroughs greatly improves the variety of possible applications and reduces fabrication costs.

These two developed platforms were then used to fabricate thermal conductivity sensors that showed excellent performance for distinguishing between oil, water, and gas phases. Thermal conductivity sensors are not currently used for phase identification in an oil well, making these sensors unique in the production logging field. Larger macro machined sensors do not respond quickly enough to be used in a flowing environment and use a significant amount of electrical power to heat making their implementation in oil well production logging impossible. Microfabrication enables application of this type of sensor by improving response time and reducing power consumption. Testing was conducted with the two platforms at various flow rates and performance of the released platform was shown to be better than the performance seen in the anchored sensors while both platforms were significantly better than a simply fabricated wrapped wire sensor. The anchored platform was also used to demonstrate a traditional capacitance based fluid dielectric sensor which was found to work similarly to conventional commercial capacitance probes while being significantly smaller in size.

## 2 Experimental Techniques

This chapter outlines basic theory regarding the experimental techniques used to accomplish the goal of fabricating MEMS devices onto high pressure feedthroughs. Deposition, patterning, and characterization are covered in the following three sections.

### 2.1 Deposition Techniques

Predominantly two thin film deposition techniques were used in this body of work: electrodeposition and magnetron sputtering. Both techniques will be covered briefly below. Electrodeposition is an extremely versatile technique allowing films to be grown from sub-nanometer thicknesses to thicknesses over 1mm. Electrodeposition requires an electrically conducting substrate for deposition to take place, somewhat limiting the ability to coat insulating substrates without pretreatment. Sputtering on the other hand will coat almost any solid material that is high vacuum compatible including glass, ceramics, and plastic substrates. Magnetron Sputtering is typically limited to much thinner films (less than 1  $\mu\text{m}$ ) due to its slow deposition rate.

Originally in this project it was expected that only magnetron sputtering would be required to deposit the sensor devices, but electrodeposition was later used to allow for creating thicker ( $\sim 20 \mu\text{m}$  thick) devices.

#### 2.1.1 Electrodeposition

Electrodeposition involves ionic migration, electron transfer, and incorporation. First hydrated metal ions  $M^{z+}$  move towards the cathode through diffusion, convection, and through the applied potential gradient. Once the hydrated ion reaches the cathode surface and enters into the diffusion double layer it loses its hydration shell and adsorbs to the cathode surface where it can be neutralized by electrons provided from an external power supply. This adsorbed atom can diffuse on the surface of the cathode until it is incorporated into the growing film lattice.

For electrodeposition a pair of reactions happens at the two electrodes involved. At the positively biased electrode (counter electrode) a corrosion process occurs where the counter electrode metal is dissolved into solution i.e.  $\text{Ni} \rightarrow \text{Ni}^{2+} + 2 e^-$ . At the negatively biased electrode (working electrode) electrodeposition takes place where ions are reduced into a deposited film i.e.  $\text{Ni}^{2+} + 2 e^- \rightarrow \text{Ni}$ . A potentiostat is used to control the current in this system and therefore the plating rate. By plating at a constant current the growth rate of the thin film is constant and a precise control of the film thickness is possible. In the case of nickel plating, sometimes a secondary reaction of hydrogen evolution can happen at the negatively biased electrode as hydrogen ions are reduced on the electrode to become adsorbed hydrogen atoms and eventually hydrogen gas. This reaction leads to a current efficiency of nickel

plating of less than 100% as some electrons are used to drive the reaction  $2H^+ + 2e^- \rightarrow H_2$ . The current efficiency is typically between 90-100% for nickel plating depending on the plating solution[114]. A basic electroplating system is shown in Figure 2.1a.

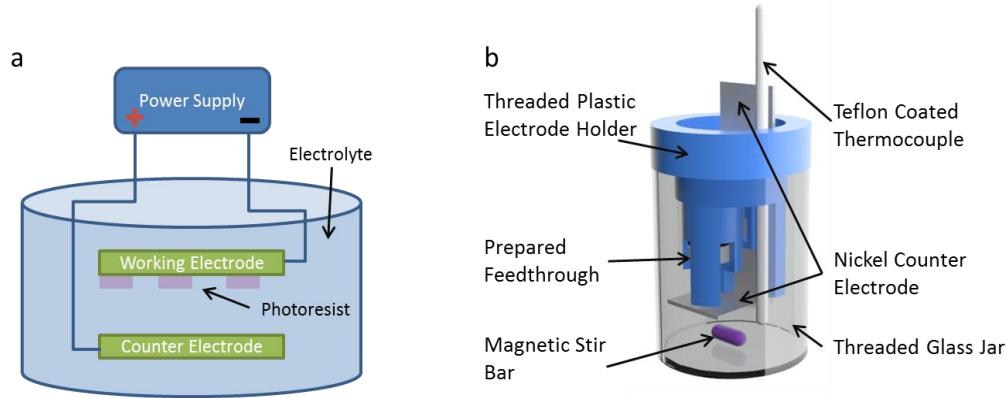


**Figure 2.1: Electroplating system used for nickel depositions. a) A schema of the system labeling the critical components. b) A solid model of the electroplating system designed for depositions in this work showing the major components.**

This system consists of a working electrode where the film will be deposited, a counter electrode that is often anodically dissolved as plating takes place, a solution containing a metal salt, and a power supply. For this work a nickel sulfamate electroplating bath was used with a sacrificial nickel counter electrode. The bath composition was as follows:

**Table 2.1: Bath composition used in this work for deposition of nickel thin films.**

Chemical	Concentration (g/L)
Nickel Sulfamate	320
Boric Acid	38
Nickel Chloride Hexahydrate	22.5
MC-3760 Anti-Pitter	3

Several different plating baths have been developed that are used for different functional applications as coatings ranging from decorative to functional (corrosion protection and mechanical properties improvement) and for electroforming to build structures directly. Nickel sulfamate baths are most commonly used for electroforming applications because they produce deposits with low internal stress and they allow for very high deposition rates[114]. For a practical electroplating system several aspects must be controlled. The spacing between the counter electrode and the working electrode should be kept constant, and the two electrodes should be parallel. If the spacing varies between the two electrodes the deposition rate will be significantly higher where the two electrodes are closer. The counter electrode should be larger than the working electrode. The bath should be

clean and free from particles and organic contaminants. Many commercial electroplating systems have extensive filtration facilities for their baths in order to ensure a clean plating solution, but in our case the plating solution is small enough that a clean fresh bath can be prepared for each deposition and filtration is not required. Gentle agitation is recommended to ensure good ion transport in the solution; in this work the electroplating system used a small magnetic stir bar. Temperature control is very important as plating temperature has a significant effect on film mechanical properties. A temperature controlled hotplate with a Teflon thermocouple is used to keep the bath at a constant 54°C during plating. A rapid prototype electrode holder was fabricated to ensure consistent positioning of the electrodes for electroplating. The holder was manufactured with threads so that it could screw onto a glass jar and allow for quick setup for plating and be replaced with a simple threaded lid for quick storage of the electroplating solution after plating was completed. The finished electroplating apparatus is shown in Figure 2.1b and can be used to quickly plate a single high pressure feedthrough based sensor device.

### **2.1.2 Magnetron Sputtering**

In basic sputtering, a target material is bombarded with argon ions that are generated in a plasma discharge. These accelerated argon ions hit the target surface and initiate a collision cascade that often results in the ejection of a target atom into the deposition chamber. This process is called sputtering. These atoms travel away from the target towards a substrate where they condense and form a thin film of the same material as the target. During this sputtering process, secondary electrons are also produced from the target surface and help to maintain the plasma. A variation in basic sputtering involves introducing a magnetic field above the target material to help trap secondary electrons close to the surface of the target. These trapped secondary electrons increase the probability of a collision between Argon atoms and electrons that would result in an ionization event producing  $\text{Ar}^+$ . This increased ionization efficiency leads to a denser plasma above the target and increased ion bombardment of the target surface. This dramatically increases the deposition rates possible. The increased ionization efficiency allows for the plasma to be maintained at lower operating pressures and at lower voltages[115]. A simplified diagram of the AJA orion 8 magnetron sputtering chamber is shown in Figure 2.2a which is a “sputter up” layout.

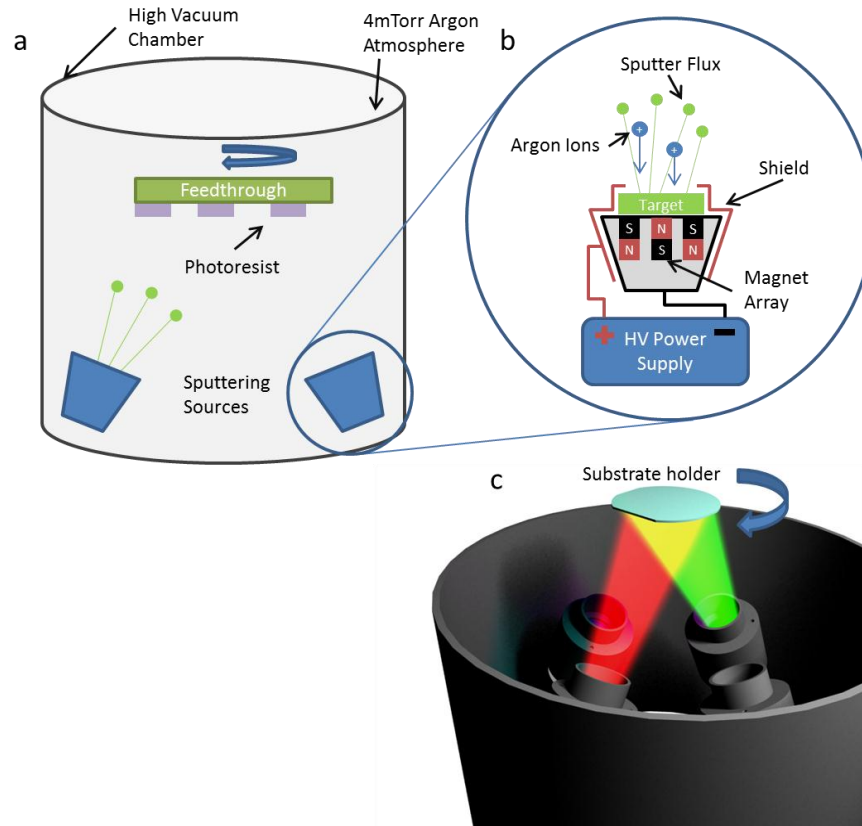


Figure 2.2: a) A schematic of a sputtering machine showing confocal sputtering sources and an inverted rotating feedthrough substrate. b) A detailed diagram showing the magnetron sputtering source. c) A 3D representation of the sputtering chamber showing a co-sputtering configuration.

A substrate is held and rotated above 6 sputtering guns, each equipped with a shutter and computer controlled power supply. The sputtering guns are each aimed at the substrate at an angle of  $10^\circ$  from vertical. A configuration showing 4 sputtering guns is modeled in Figure 2.2c. Figure 2.2b shows a cross section of one of the magnetron sputtering sources, with the magnet array underneath the target, the shield which is held at a grounded potential and the target which is biased negatively using a high voltage power supply. The magnet array is arranged with a single rare earth magnet in the center of the gun with the north side up and a ring of magnets around the perimeter of the gun with the south side up.

### 2.1.3 Radio Frequency (RF) Sputtering

Direct Current (DC) magnetron sputtering can only be used to deposit from electrically conducting targets. When the target is not electrically conducting, a radio frequency (RF) power supply can be used for deposition. The RF power supply varies the voltage applied to the target at a frequency of 13.15MHz allowing for accumulated charge on the surface of the target to be dissipated. The deposition rate obtained with an RF power supply is significantly lower than what is observed with DC sputtering but electrically insulating materials can be deposited. Also in the

application of reactive sputtering, an RF power supply results in significantly less sensitivity to the poisoning effect.

#### **2.1.4 Reactive Sputtering**

Reactive sputtering involves the deposition of materials in the presence of chemically reactive gasses that react with the sputtered material as well as the surface of the target. The reactive gas can include oxygen for depositing oxides, nitrogen for depositing nitrides, or H<sub>2</sub>S for depositing sulfides. In this work oxygen was used as a reactive gas for depositing oxides. By controlling the partial pressure of oxygen during deposition the stoichiometry of the oxide being deposited can be carefully adjusted. For example, it is possible to controllably deposit NbO, NbO<sub>2</sub>, or Nb<sub>2</sub>O<sub>5</sub> by varying the flow rate of oxygen into the chamber while keeping the deposition power constant[116]. Reactive sputtering requires some process optimization to ensure that the target does not become “poisoned” during the deposition. Near the poisoning transition where the oxygen partial pressure is high enough to completely oxidize the sputtering target, the deposition rate drops significantly, the cathode voltage required to maintain the same power increases, and the oxygen partial pressure rises significantly as a result of the reduced sputtering rate. Ideally the system is operated in a region where most of the target remains metallic rather than being oxidized. Three methods used to maintain this condition during reactive sputtering are outlined in a reactive sputtering review by Safi: dramatically increase the chamber pumping speed so that most of the oxygen introduced is consumed by the pump rather than through gettering on the substrate, increasing the distance from the target to the substrate and lowering the deposition rate, and obstructing the reactive gas flow to the target so that the reactive gas is higher in partial pressure at the substrate[117]. In this work the AJA Orion 8 sputtering machine incorporates all of these design considerations and works quite well in providing stable conditions when conducting reactive sputtering.

## **2.2 Patterning Techniques**

### **2.2.1 Photolithography**

Patterning in this project was done using contact optical lithography. Optical lithography depends upon a surface being uniformly coated with a photosensitive material called photoresist. The photoresist is either hardened and resists washing away in a developer when exposed to light (negative) or becomes soluble in a developer when exposed to light (positive). By coating a thin layer onto a surface and then exposing the surface to collimated Ultra Violet (UV) light through a patterned photomask a thin patterned polymer can be placed onto this surface. This process has a close analog in print photography where the negative is similar to the mask and the photographic emulsion on the print is similar to the photoresist[118]. The process of exposing a surface through a mask is shown below in Figure 2.3. Here

collimated light is projected through the mask and the shadowed areas on the substrate are clearly visible. If a positive resist is used these shaded areas will remain after developing and will be protected by a thin polymer layer.

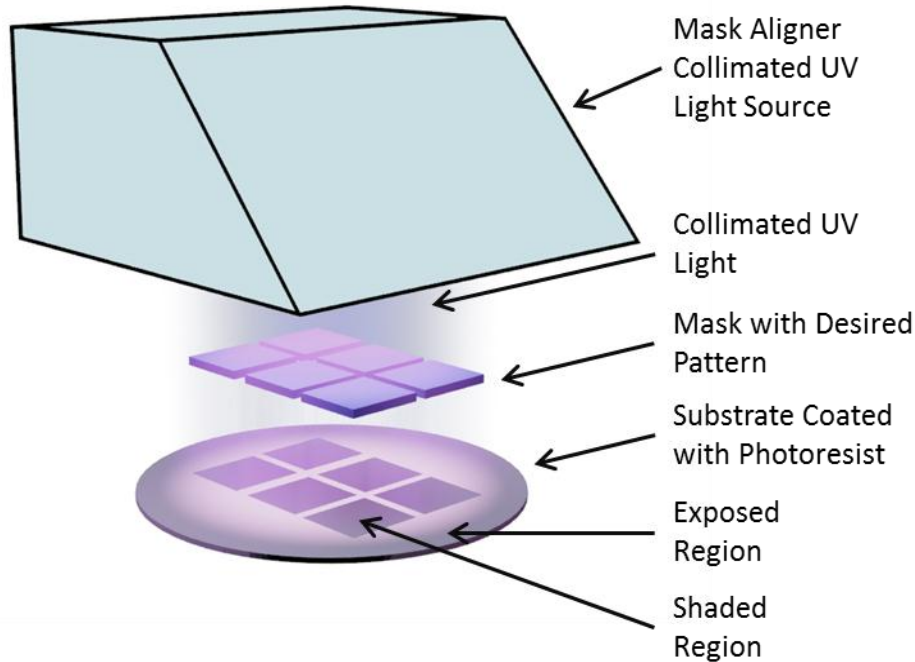


**Figure 2.3: Diagram of the main components required for optical photolithography exposure.**

A simple mask aligner light source is typically made up of a mercury arc lamp light source, a parabolic mirror to produce a collimated light source, filters to isolate the 365nm emission line from mercury, reflectors and lenses to project the light onto the wafer[119]. In this work three types of photoresists were used: AZ4620 (positive resist), HPR 504 (positive resist), and KMPR 1000 (negative resist). AZ4620 and HPR 504 were used for patterning sputtered devices using a lift off process and are approximately 10 $\mu\text{m}$  thick and 1 $\mu\text{m}$  thick, respectively. This thickness can be adjusted slightly by changing the final spin speed during photoresist deposition. These resists can be used for lifting off sputter deposited films less than 500nm thick quite consistently. The KMPR resist is significantly thicker and is ideal for producing molds for electroplating. In this work the KMPR resist is  $\sim 50\mu\text{m}$  thick. Only single mask processes were used and only simple alignment was needed in this body of work. An excellent resource outlining all of the process steps involved in microfabrication lithography can be found in "Microlithography" written by David Elliott[120].

### **2.2.2 Electron Beam Lithography**

Electron beam lithography (EBL) uses a focused electron beam that is moved over a surface to expose a resist instead of light directed through a mask as in photolithography. Because the focused electron beam is very small and can be precisely controlled, very high resolution is possible with this technique. Unfortunately, because the small beam must be steered to every area on the surface where the resist is to be removed (positive resist) or remain (negative resist) sequentially, this technique is only suitable for exposing small areas of a surface. Exposing an entire wafer using this technique would be very difficult, expensive and time consuming. This technique was only used for the fabrication of metallic NEMS in chapter 7 in order to define device structures with dimensions less than  $1\mu\text{m}$ . More information regarding this technique can be found in *Electron-beam technology in microelectronic fabrication* by Brewer[121].

### **2.2.3 Liftoff**

The liftoff technique for patterning deposited thin films is extremely simple and versatile. It involves masking a substrate with photoresist prior to the thin film deposition in all the areas where the thin film deposition is not wanted. Once the photoresist is patterned (Figure 2.4a) the wafer is inserted into a thin film deposition instrument (typically sputtering/evaporation) and the thin film is deposited onto the entire wafer coating both the masked and exposed areas of the substrate (Figure 2.4b). The photoresist typically has to be thicker than the deposited film to achieve reliable lift off of the film. The wafer is then submerged in a bath that dissolves the photoresist and this physically detaches or “lifts off” the film from the photoresist masked areas. Often ultrasonic agitation can be used to help improve the removal of the photoresist which takes with it the deposited film. After liftoff the thin deposited film remains attached to the substrate in all of the areas that were not coated with photoresist (Figure 2.4c). Often some remnants of the sidewall are left behind resulting in a characteristic rough edge on features patterned with this technique[122, 123]. During deposition of the thin film onto the profiled substrate, often shadowing occurs where the thin film deposition flux is interrupted by surface topography. Figure 2.4d shows a typical shadowing effect that would be expected at the edge of a thick photoresist. This shadowing effect can result in the deposited film being quite thin in concave corners and this significantly aids in the lift off process providing a weak spot in the deposited film where it can cleanly break off. Often a two layer photoresist is used in liftoff which provides an overhang that can cause a gap between the deposited film on the substrate and on the photoresist. In this case lift off works quite well and the rough lift off edge can be avoided[120].

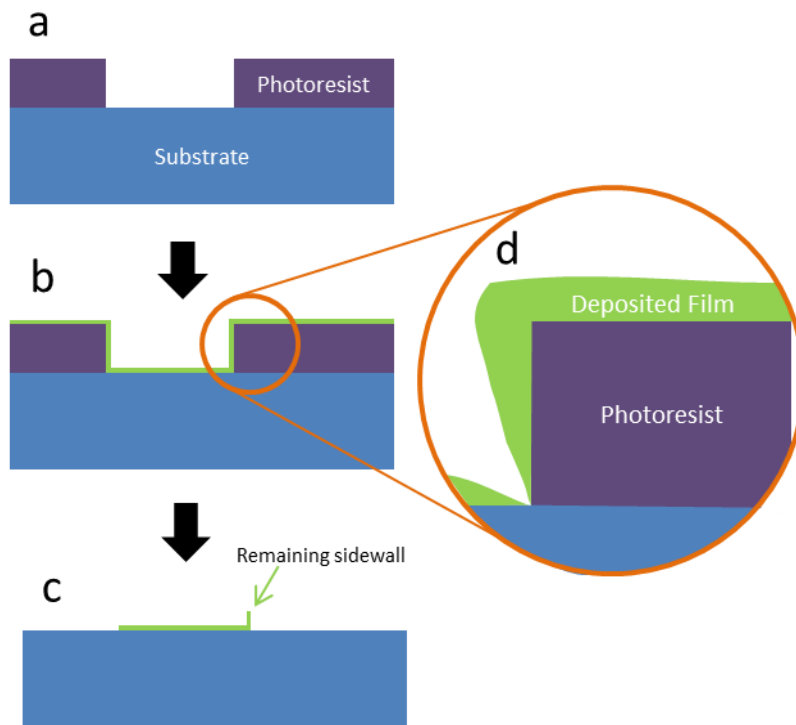


**Figure 2.4:** The lift off procedure showing a) deposition and patterning of the photoresist and b) deposition of a thin material to be patterned by lift off. c) The remaining film after the photoresist is removed. d) A higher magnification of the deposited film profile that results from shadowing during deposition. This shadowing assists in the lift off process.

Lift off removes the need for developing chemical etches for patterning thin films using lithography. Often finding a selective etch that will cleanly remove a thin film is quite difficult or impossible especially when working with corrosion resistant alloy materials. Excellent resources for finding selective etches for pure metals are available, but a good resource for etches of alloy thin films is not readily available. Lift off provides a good solution to this problem. One significant disadvantage to using lift off with a photoresist is that it is often not possible to deposit the thin film onto a heated substrate, as heating the substrate would cause the photoresist to degas and decompose inside of the high vacuum thin film deposition system. This limits lift off techniques to room temperature depositions. It is possible to work around this limitation by using a two-step process of patterning a metal that can be selectively removed and then using this metal as the liftoff layer. This process was used to pattern niobium oxide films deposited at 700°C with a chromium liftoff mask[124].

#### **2.2.4 Photo-electroforming**

Electroforming is a process of fabricating patterned bulk materials through electroplating into or onto a mold which is later removed to release the deposited structures. A number of different molds can be used and in photo electroforming a photoresist material is used as a mold to pattern the deposited material.

An advantage of electroplating is that material is only deposited on surfaces that are electrically connected to the working electrode; one can deposit material quite precisely through masking. Areas covered with photoresist will not receive any deposition flux because the photoresist is an electrical insulator and cannot provide the electrons required to reduce the metal salts in solution. Further, by using a thick photoresist, the electroplated material will remain confined to the photoresist mold as it grows out from the substrate. Figure 2.5a, shows the concept of photoelectroforming into a photoresist mold and Figure 2.5b shows an image of a nickel device produced using this process. If the photoresist is covered with an electrically conducting seed layer, the electroplated material will uniformly grow out from the surface of the photoresist as well as the substrate leading to a plated structure as shown in Figure 2.5c and d. This sidewall structure can sometimes be useful as it allows for out of plane structural support structures to be created. Each of these two methods of electroforming were used in this work with both insulating photoresist used to shape the structures and metalized photoresist used to provide conformal growth around the photoresist. The implementation of photoelectroforming used in this work is similar to that used by Lee and Jiang in that a thick KMPR photoresist was used as the electroforming mask and a nickel sulfamate bath was used for depositing thick nickel layers[125].

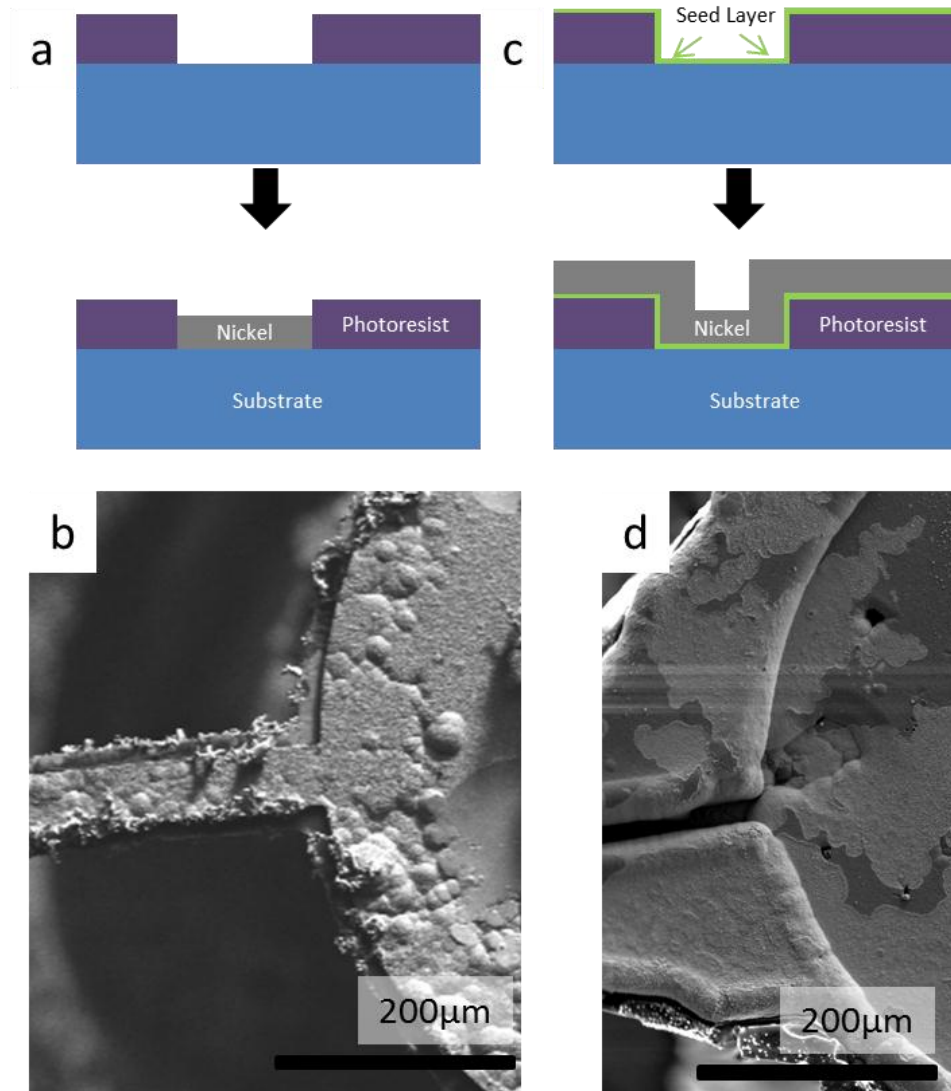


Figure 2.5: a) Schematic of photo electroforming showing nickel only electroplating in the exposed areas of substrate. b) SEM micrograph of a released beam structure formed by electroforming. c) Diagram of photoresist and substrate covered with a thin metal seed layer and subsequent electroplating on the seed layer. d) SEM micrograph showing structure of device formed using this technique (photomask used was the same as in b).

## 2.3 Characterization

### 2.3.1 Scanning Electron Microscopy

Scanning electron microscopy (SEM) involves scanning a highly focused electron beam across the sample rapidly while a detector observes the emission of secondary or backscattered electrons. Each location on the sample that the electron beam scans over will have corresponding amplitude of detected electrons and an image can be reconstructed by a computer. This technique can provide high resolution images of the surface topography of samples. The S-4800 microscope used in this

work can provide images with a resolution of  $\sim 10\text{nm}$  while the S-3000 microscope in this work is limited to a much lower resolution. An interesting history of the development of the SEM can be found in an article by McMullan [126] and a more careful outline of the technique can be found in *Physical Principles of Electron Microscopy: An Introduction to TEM, SEM, and AEM* by Egerton[127].

### **2.3.2 Energy-dispersive X-ray Spectroscopy**

In Energy-Dispersive x-ray Spectroscopy (EDS), a high energy electron beam is focused onto a sample and some of the electrons in the sample are excited into higher orbitals or ejected from the atoms. When a higher energy electron falls into the space made available by the excited electron a characteristic energy x-ray is released. By analyzing the energy spectrum of released x-rays from the sample when it is being bombarded with the electron beam elements can be identified by their characteristic x-ray emission. The relative emission rates for different energy x-rays can be used to quantify the concentration of different elements in the sample. This technique is excellent for both identifying and quantifying the concentrations of elements heavier than Be in an alloy. Although it is possible to detect B, C, N, O, and F in a sample the quantification of these elements is difficult with EDS as the energy of x-ray emission energy from these elements is low and these peaks often overlap making deconvolution difficult. When used in conjunction with an SEM a compositional map can be made of the surface of a material with a spatial resolution of approximately  $1\mu\text{m}$ . More information regarding EDS can be found in the *Handbook of X-Ray Spectrometry* by Grieken and Markowicz[128].

### **2.3.3 Optical Profilometry**

This technique uses interference between a beam of light reflected from a sample and a reference beam as the sample is moved vertically. The interference pattern is recorded with a camera as the sample is moved and a computer algorithm is used to generate a 3D map of the surface with sub 1 nm vertical resolution. The viewing range of the Zygo optical profilometer used in this work is over 10mm with a resolution of  $10\mu\text{m}$  which allows for surface reconstruction of a significant area of a surface allowing for characterization over a wider area than is possible with atomic force microscopy, stylus profilometry, or cross sectional microscopy. More information regarding this technique can be found in a reference by Osten[129].

### **2.3.4 X-Ray Diffraction**

X-ray diffractometry (XRD) uses a collimated single wavelength x-ray source to irradiate a sample. The x-rays interacting with the sample are diffracted by the sample atom's electrons. If these atoms are arranged with long range order the diffracted x-rays can be described by Bragg's law. By rotating an x-ray detector around the sample an intensity reading can be generated for each angle  $2\theta$  between the source and the detector producing a diffraction pattern that can be used to

identify the crystal structure and lattice spacing of the sample. Information regarding the crystalline grain size and local lattice strain can also be derived from an x-ray diffraction pattern by analyzing the shape and position of the diffraction peaks. XRD works quite well for analyzing films thicker than 50nm and uniquely identifying phases present in a sample but does not have a high spatial resolution and is not useful for composition mapping. Further information regarding XRD and analysis of diffraction patterns can be found in *Thin Film Analysis by X-Ray Scattering* by Birkholz[130].

### 3 Fabrication 1: Microfabrication on a High Pressure Feedthrough

#### 3.1 Fabrication of a High Pressure Feedthrough

Hermetically sealed feedthroughs are used in multiple commercial applications where a seal is required between different atmospheres in an electrical system. They are found in sensors, valves, detonators and explosive actuators, aircraft, missile and spacecraft instrumentation, and gyroscopes[131]. The feedthrough used in this work is designed for “Ultra Harsh Environments” including temperatures from  $-65^{\circ}\text{C}$  to  $427^{\circ}\text{C}$  and differential pressures up to 69MPa (10,000psi)[132]. HCC Ametek provides a traditional high pressure feedthrough part number X222012-6-CC40-3 that is shown in Figure 3.1b. Below is a quick summary of knowledge regarding the fabrication of this feedthrough obtained through two visits to the facility where these feedthroughs are manufactured. This part consists of an outer housing made of Inconel X-750 and a single body of “Durock” glass surrounding six 1mm diameter pins that travel from one end to the other of the feedthrough. The “Durock” glass has the approximate composition in mol % of: 84.3%  $\text{SiO}_2$ , 7.2%  $\text{B}_2\text{O}_3$ , 3.6%  $\text{Al}_2\text{O}_3$ , 2.2%  $\text{Na}_2\text{O}$ , 1.4%  $\text{K}_2\text{O}$ , and 1.4%  $\text{CaO}$  (Determined with XPS). This high pressure feedthrough is made by placing the pins, glass and feedthrough body into a graphite jig composed of three parts shown in Figure 3.1a. A base with alignment holes for the body and pins, a sheath to hold everything concentrically and a cap with a weight that is designed to fall a specified compression distance. Five glass frit preforms (shaped like coins with six 1mm holes in them) are dropped into the assembly around the pins and inside of the full body. These glass frit preforms are prepared by physically pressing together a finely ground mixed glass powder with an organic binder in a shaped metal die. Once pressed, the disks are fired at a temperature that causes the binder to burn off and leaving a lightly sintered glass preform. These glass preform disks are kept under pressure from the weighted cap during the firing. The firing process is done in a production belt furnace with a temperature of  $980^{\circ}\text{C}$  and a belt speed of 5cm per minute. The ends of the furnace are open to atmosphere but the chamber is kept under a slight positive pressure of nitrogen bubbled through water called “wet gas”. The hot zone is approximately six feet long and provides a hot time of approximately 30 minutes. Surprisingly the cooling section is not much longer than the hot zone resulting in a rapid quench to room temperature in less than an hour. The thermal expansion coefficient of the glass is less than that of the Inconel body and pins and upon cooling this results in a large compressive force on the glass filler. This force holds the feedthrough together and prevents the pins from pushing out when a large differential pressure is applied across the feedthrough.

The firing procedure causes all of the exposed Inconel surfaces in the feedthrough to oxidize leaving a non-uniform pale green color surface finish. This surface is cleaned by an acid dip and subsequently a thin gold coating is applied to the pins by

electrodeposition. Each of the pins is wrapped with a fine copper wire and connected to an electrode rack. This assembly is dropped into a plating bath and a thin coating is uniformly applied to the pins everywhere except for the areas covered by the wrap wire. The finished product provided by HCC Ametek is shown in Figure 3.1b.

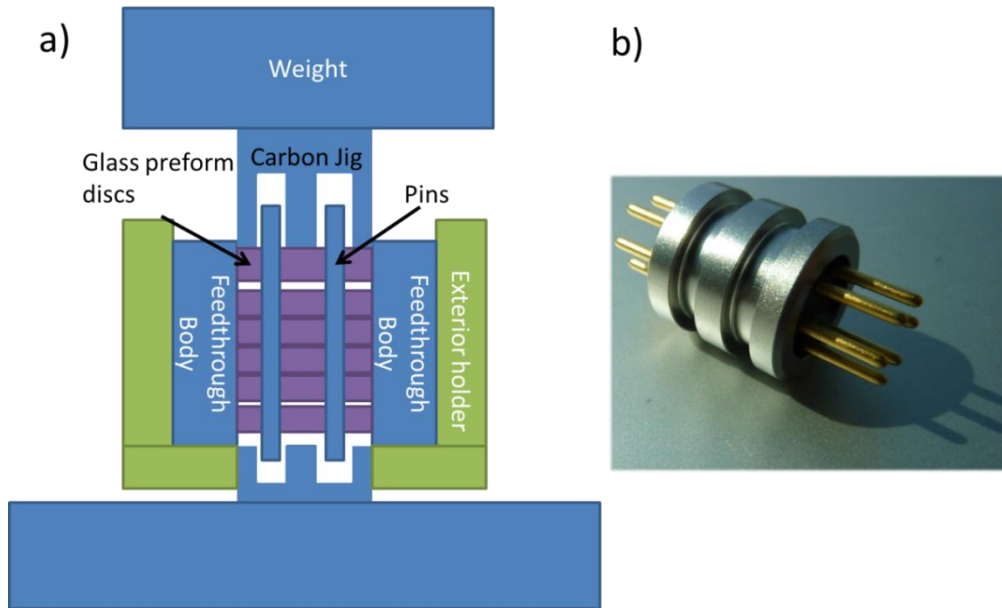


Figure 3.1: a) Fixture used for firing of a high pressure feedthrough. b) photograph of a HCC Ametek high pressure feedthrough before cutting.

### 3.2 Cutting of a High Pressure Feedthrough

Cutting a high pressure feedthrough was significantly more challenging than expected at first. The high pressure feedthrough is composed of two intimately mated dissimilar materials. A ductile and high strength material: Inconel X-750, and a brittle and hard material: “Durock” glass. These two materials would ideally be cut by two different saws a high speed diamond/nickel saw for the glass and a SiC/binder composite wheel for the Inconel. To tackle this problem, four techniques were trialed and optimized for cutting of the high pressure feedthrough to provide the required surface for microfabrication. The first was a large industrial lapping machine that belt fed jig mounted feedthroughs into a high speed tapered grinding wheel shown in Figure 3.2.

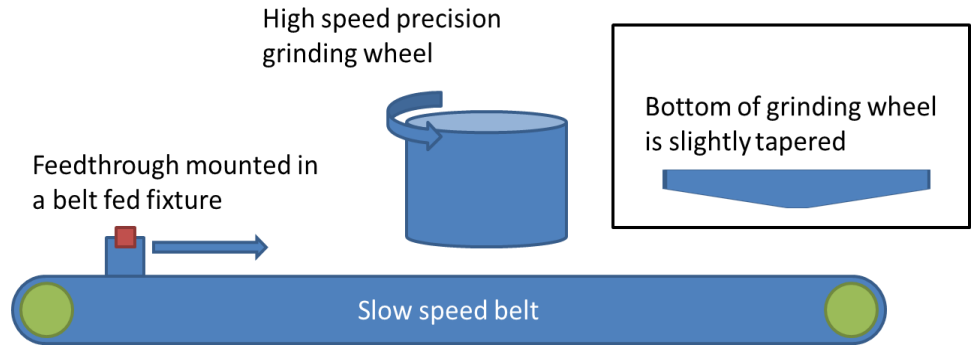


Figure 3.2: A diagram of the belt fed grinding station used by HCC Ametek to try to provide a smooth surface on a high pressure feedthrough.

The next two techniques involved a precision high speed saw (Struers Secotom-10 Figure 3.3b) with a “soft” SiC wheel and with a “hard” diamond saw. The “soft” technique was first recommended by Struers and the “hard” technique was tried after the first failed. The final technique used a slow speed gravity fed diamond wheel saw (South Bay Technology Model-650 Figure 3.3a).

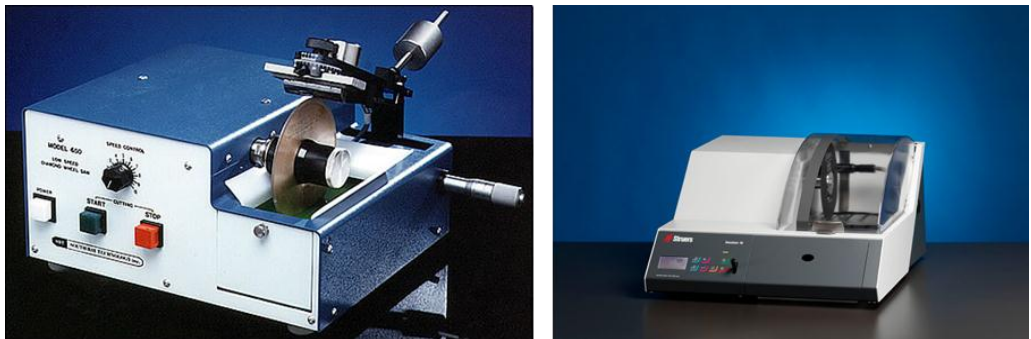


Figure 3.3: a) Gravity fed South Bay Technology Saw. b) High speed precision saw by Struers.

The slow speed gravity fed saw provided the best surface finish of the four techniques used. This surface was almost free from any surface cracking and provided a surface finish that allowed for immediate polishing with 800grit sand paper. Figure 3.4 shows optical micrographs of the feedthrough surface after cutting with the last three techniques. Clear cracking is visible around the pins in b and c where the Struers Secotom saw was used. The belt fed lapping machine caused severe cracking and damage after leveling the surface of the feedthrough and is not shown as this was attempted at HCC Ametek and was unsuccessful.

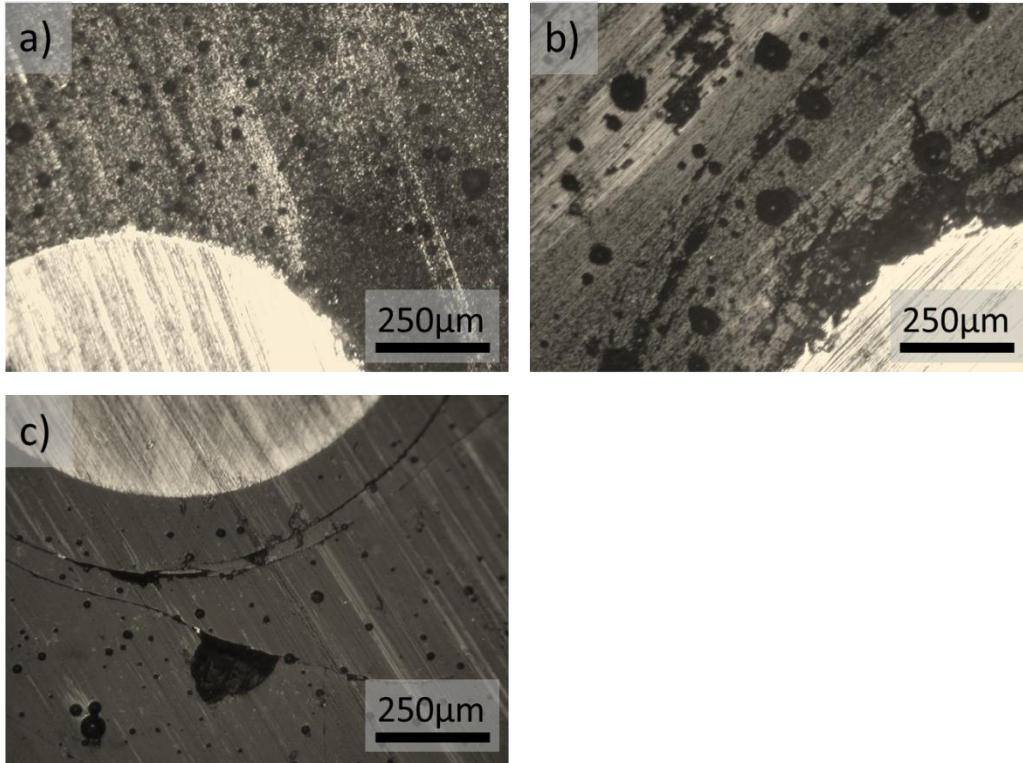
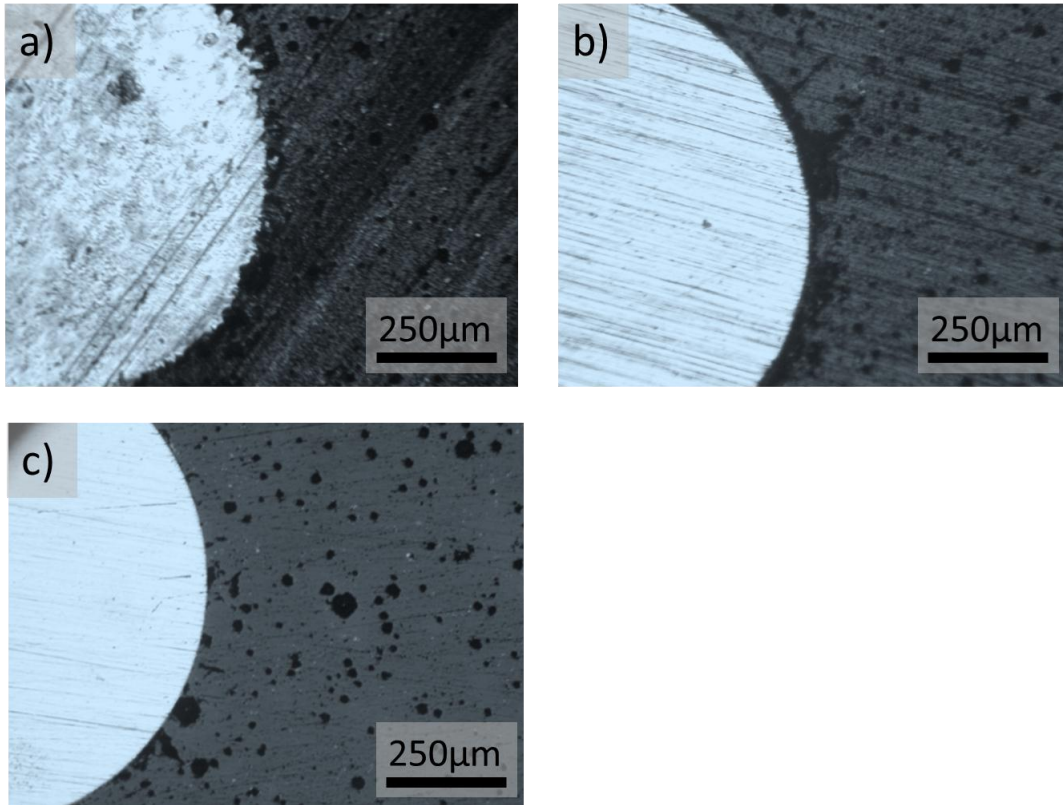


Figure 3.4: a) HCC high pressure feedthrough a) cut with a gravity feed slow speed diamond saw. b) cut with a high speed automatic feed diamond saw and c) cut with a high speed SiC wheel.

### 3.3 Feedthrough Polishing

Subsequent polishing was done with a simple polishing wheel (Allied High Tech MetPrep 3). It was found that grinding with SiC paper with a lower grit than 800 resulted in cracking of the glass on the high pressure feedthrough. This was potentially caused by lateral forces exerted on the feedthrough pins by the polishing wheel causing vibration of the pins in the glass body of the feedthrough. If only 800 grit and above SiC paper are used at a rotational rate of 40rpm, no additional cracks are introduced into the feedthrough surface during polishing. Using 800-1000-1200-2400-4000 papers in sequence, results in a smooth surface only containing fine polishing marks and the intrinsic bubble defects on the surface. The resulting surface is shown in Figure 3.5.



**Figure 3.5: a) High pressure feedthrough after being cut with a diamond saw at 3000RPM b) after being polished with 600 grit sand paper for 1 minute c) after being polished to 2400 grit SiC paper**

Microfabricated devices on this cut and polished feedthrough surface can be produced using a lift off and sputtering technique with good yield if the device feature sizes are kept larger than 50µm. Images of a fabricated beam structure on the high pressure feedthrough are shown in Figure 3.6.

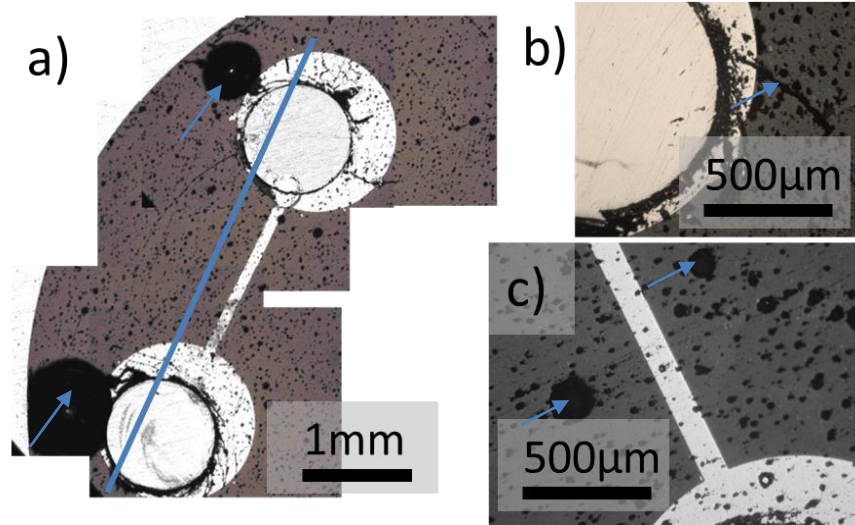
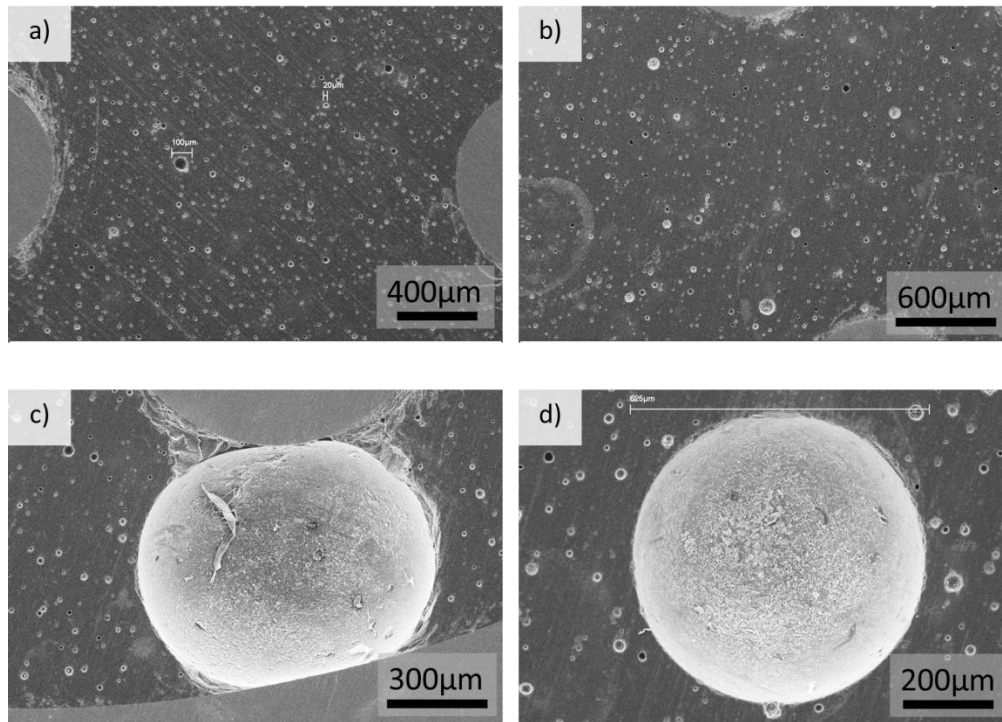


Figure 3.6: Pictures of a HCC all glass high pressure feedthrough that has been cut with a diamond saw and polished with 4000 grit SiC sandpaper. Notice the large bubbles located at the pins, cracking around the pins and spherical defects on the surface in (b) and (c). The cross section shown in blue is shown Figure 3.12.

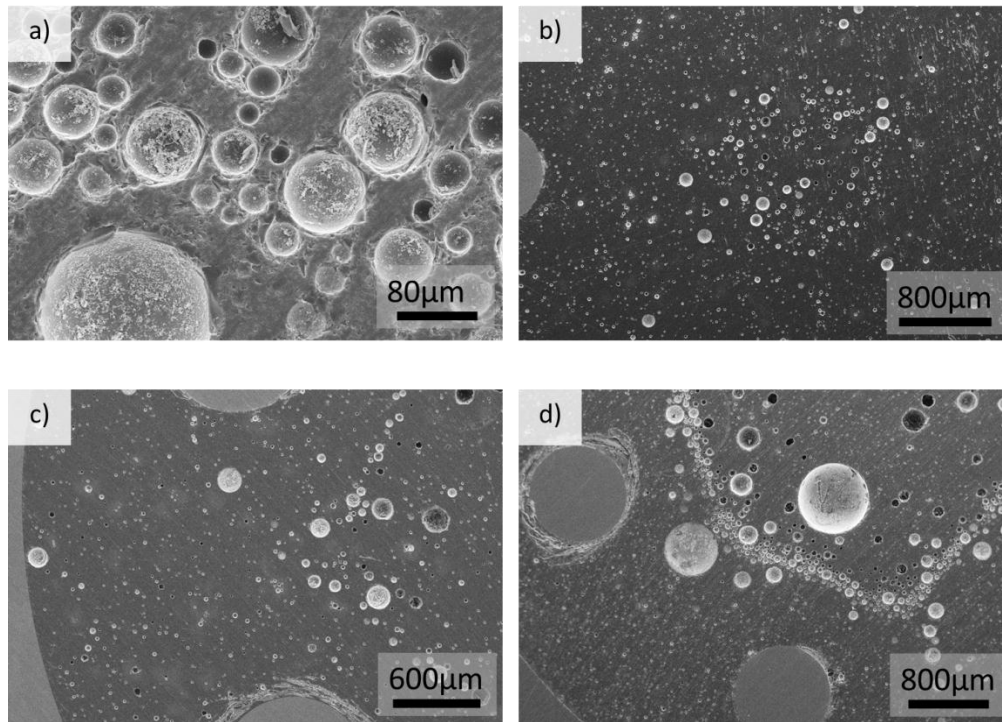
At this point a proof of concept for fabricating electrodes and conductive structures directly onto a high pressure feedthrough was established and further work was undertaken to test and optimize the surface for microfabrication processes.

Figure 3.7 shows several SEM images from the surface of a typical cross sectioned feedthrough. The surface is covered with small craters ranging in size from  $1\mu\text{m}$  to  $500\mu\text{m}$  with the majority of the bubbles being less than  $50\mu\text{m}$  and only a few large craters forming between the pins and the inconel body (Figure 3.7c) These craters occur during cross sectioning of the feedthrough as a result of cutting bubbles in the high pressure feedthrough in half. The glass is filled with many small air pockets as a property of the high pressure feedthrough. According to an engineer at HCC Ametek, the bubbles could act as crack termination points in the glass and are important for the structural integrity of the glass. Discussions with HCC Ametek regarding reduction of the number of bubbles did not yield much success; they modified their process to reduce the number of larger bubbles ( $\sim 500\mu\text{m}$  size) by placing additional weight and compression distance in their firing jig design. They suggested using an enamel or glass to fill the defects. The defects shown in Figure 3.7a) and b) allow for large feature size microfabrication on this surface and generally devices with feature sizes larger than  $50\mu\text{m}$  in size have good yield on this substrate.



**Figure 3.7:** SEM images of various feedthroughs, showing the size and extent to which the defects are present across the surface. a) and b) Low magnification images of the glass surface between two metallic pins. c) A large pit next to one of the pins. d) A large  $\sim 400 \mu\text{m}$  diameter pit.

Some of the feedthroughs showed substantially more defects when cross sectioned and had a surface similar to that shown in Figure 3.8. In these cases several large bubbles were present that were significantly larger than  $100\mu\text{m}$  in size. This feedthrough would not allow for successful microfabrication of devices as the larger bubbles would interfere with the lithography and thin film deposition processes. In cases where the surface has this appearance, re-cutting the feedthrough at a slightly lower depth reveals a surface with fewer bubbles. This suggests that these large bubble regions are spatially confined to a thin layer in the feedthrough. It is expected that this would correlate to a region between two of the pressed glass frits used in fabrication of the feedthrough as shown in Figure 3.8 where more trapped air, as expected at the interface between two frits, is shown in a cross section. This effect at the interface between frits suggests that control over pore configuration in the pre melted frits can have a significant effect on the post melt bubble structure. It would be interesting to further study the effect of frit pressing and firing procedure on bubble structure in the finished feedthrough but this work is difficult to undertake without access to frit pressing equipment or the glass frit precursor material at the supplier. Because of this lack of access work was conducted on a post fabrication surface improvement process.



**Figure 3.8:** SEM images of a feedthrough cut at the interface between two glass frits with higher than normal defect density. a) A cluster of  $\sim 50 \mu\text{m}$  pits present on the feedthrough surface. b) Low magnification image showing large defects. c)  $100 \mu\text{m}$  defects between two metallic pins. d) Numerous defects, ranging in size from  $20 \mu\text{m}$  to  $\sim 1000 \mu\text{m}$ .

In order to better quantify the surface defect distribution of these feedthroughs a thresholding process was conducted in Gwyddion software to highlight the bubble areas in a magnification SEM image of the surface. The SEM image used is shown in Figure 3.9a, the extracted defects from this image are shown in Figure 3.9b. From this mask, the defect distribution on the surface can be seen to mainly consist of bubbles less than  $20 \mu\text{m}$  in radius as shown in Figure 3.9c. There are a small but significant number of defects between  $20 \mu\text{m}$  and  $60 \mu\text{m}$  in radius.

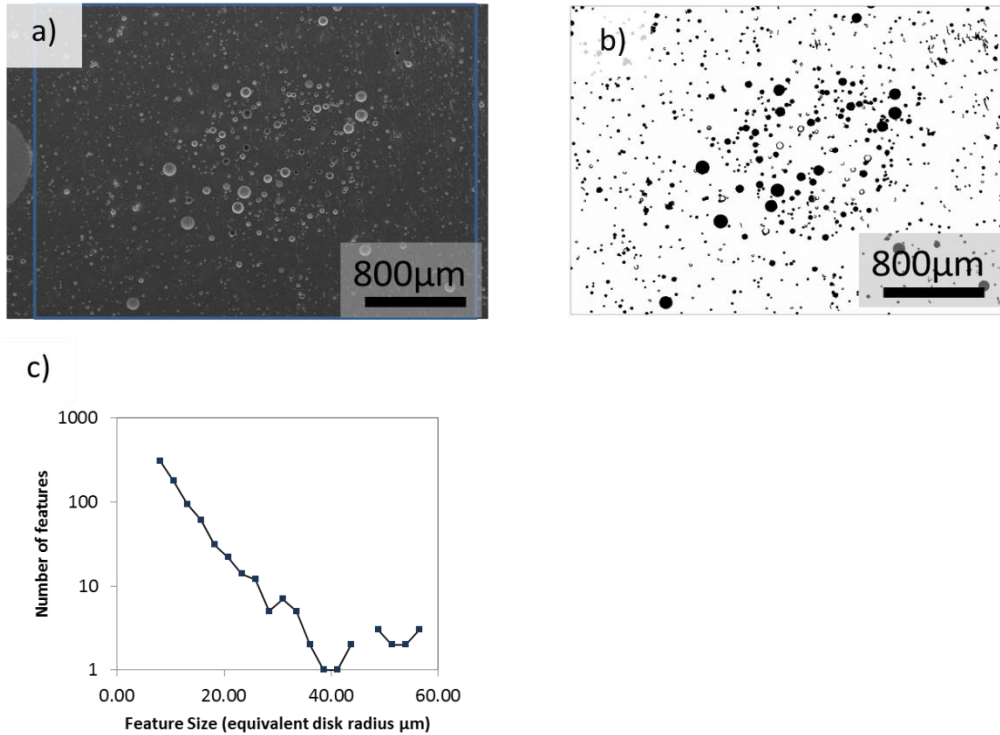


**Figure 3.9: a) Scanning electron micrograph of a typical feedthrough surface. b) Filtered image showing dark spots the same size as the defects. c) Size distribution of the filtered image defects showing a high number of smaller defects but a significant number of defects in the 40-60µm range.**

Surface profilometry was also conducted to confirm the shape and depth of the surface defects using a Zygo Optical profilometer. Results from a feedthrough with a large number of defects are shown in Figure 3.10.

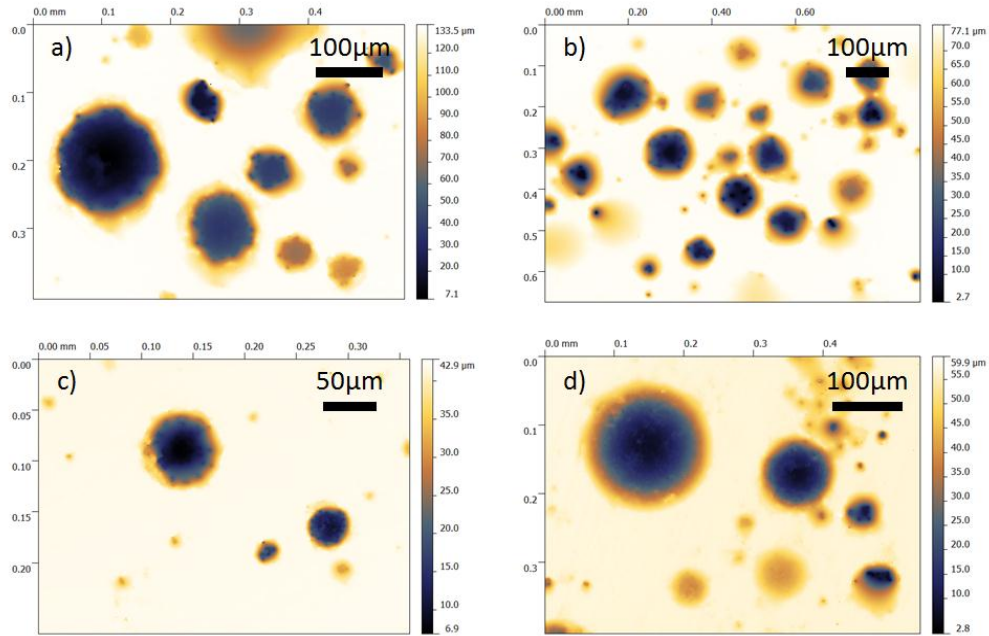


**Figure 3.10: Height profiles of various defects present on the surface of cut feedthroughs. a) A cluster of 100µm sized defects. b) Dense cluster of smaller sized defects. c) Two smaller defects present on the feedthrough surface. d) Shallow defects, all under 60 µm in depth.**

It can be seen that the defects have a hemispherical shape and the depth of the defects correlates with the expected depth profiles of various cross sections of spheres. Some defects are shallow corresponding with a cross section near the bottom of a sphere (Figure 3.11b) and other defects are quite deep with sharp drop offs in height corresponding to a cross section near the top of a sphere (Figure 3.11a). These two types of cross sections can also be seen in the SEM images where defects correlating to a cross section near the top of a sphere appear dark due to the structure obstructing secondary electron emission from the bottom of the sphere and shallow defects correlating to a cross section near the bottom of a sphere appear lighter.

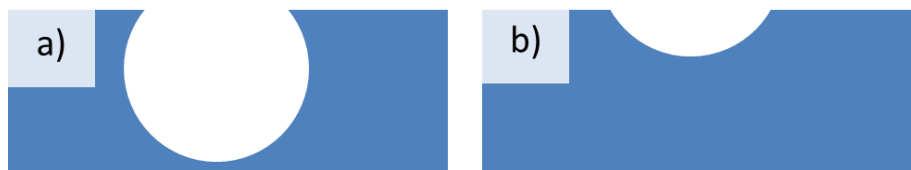


**Figure 3.11: Representation of two different bubble cross sections. a) Cross section at the top of a bubble showing sharp transition from surface to defect. b) Cross section at the bottom of a bubble showing a much more gentle transition from the flat surface to the defect.**

### 3.4 Glass Surface Modification

In order to improve the surface finish of the resulting high pressure feedthrough platform, a process commonly used in multilayer semiconductor manufacturing called planarization was used. It involves depositing a thicker than needed dielectric layer and then back polishing this layer to the required thickness using a precision polishing step. A schematic of this process to fill in the bubble defects on the cut high pressure feedthrough is shown in Figure 3.12. First, the feedthrough is cut and polished to a fine surface finish. Second, a thick layer of electrically insulating filler is spread onto the surface filling the surface accessible defects. Finally, the feedthrough is polished back to leave a surface with most of the defects completely filled. In the figure one bubble is shown almost touching the surface, this bubble would be exposed if the surface was polished back slightly more than level. It is important when polishing back not to remove too much material as this will expose additional bubbles close to the surface and create additional surface defects.

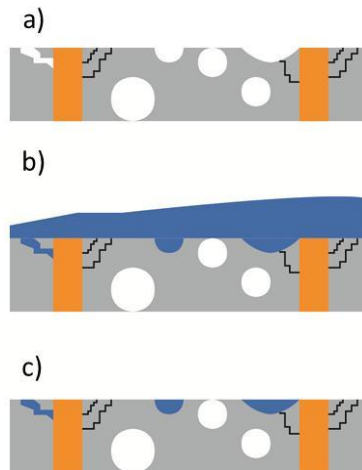


**Figure 3.12: Diagram of defect correction process (schematic from the region marked in blue on Figure 3.6). a) Shows the as cut and polished surface with fine and large cracks and bubbles on the surface, b) shows the surface after a spin on coating and firing of a glass layer and c) shows the surface after a back polish to reveal the feedthrough pins.**

Several different electrically insulating materials were tried to find a solution that could provide surface quality improvements while maintaining surface robustness in temperature cycling. The surface modification should strongly adhere to the glass surface and must not crack, spall or delaminate when cycled between  $-40^{\circ}\text{C}$  and  $200^{\circ}\text{C}$ . The surface coating should be electrically insulating, and should flow into all of the different defect sizes on the surface of the glass.

By repairing these surface defects, yield can be improved in fabrication of electrode devices on the feedthroughs and smaller feature sizes can be patterned on the surface. The majority of the small defects could be repaired with a relatively thin

dielectric layer deposition like spin on glass 100-500nm thick or sputtered or evaporated glass 100nm-5 $\mu$ m thick. The larger defects would require a significantly thicker layer (~100 $\mu$ m thick) in order to fill the entire voids (50-100 $\mu$ m sized defects). Spin on or dip coatings are ideal because they have the potential to preferentially deposit in low lying areas and traps on the surface. The second most attractive option is CVD coating that deposits on all surfaces at approximately the same rate providing isotropic film growth[133]. Physical Vapor Deposition (PVD) coatings like sputtering are least attractive because they deposit a lower amount in shadowed pits on the surface than they do on high lying surfaces. An excellent review of the different deposition techniques that can be used for depositing electrically insulating dielectric films for semiconductor applications can be found in a publication by Amick et al[134].

Spin coating is a common technique for surface planarization because it is simple, can be done at a low temperature, and is effective[135]. Spin coat leveling involves pouring a curable liquid over a spinning substrate to deposit a uniform film over the surface, waiting for a leveling process based on capillary-driven flow and then curing the liquid[136, 137]. Both polymers and spin on glasses have been used to significantly improve the surface finish of microfabricated devices for optical applications[135], and semiconductor planarization[138]. Dip coating has also been used to fill porosity and surface damage with acetate functionalized alumina nanoparticles[139]. Yasseen et al. used a technique very similar to that used in this work for polysilicon surface micromachining involving spin coating of a low melting point glass frit onto a surface followed by melting and back polishing[140]. This technique was used again by Hollar et al. for filling of 50 $\mu$ m deep trenches in a silicon based micro robot fabrication process with good success. Hollar et al. noticed that the molten glass contained small bubbles that could be minimized by heating for a longer time and cycling the pressure of the furnace from 2 Torr to 760 Torr[141].

In this work several materials were tested for effectiveness in filling these surface defects on the high pressure feedthroughs: Fox-25 flowable oxide, Aremco magnesia filled low melting temperature glass with silicone binder, a low melting temperature lead oxide based glass from Gunther, and a low melting temperature glass based on bismuth oxide and zinc oxide from Aremco. Each of these materials was tested and the results from their use as a planarizing dielectric will be briefly outlined below.

#### **3.4.1 Fox-25 Flowable Spin on Glass**

Fox25 flowable oxide available from Dow Corning is a liquid solution of 22.5% hydrogen silsesquioxane (HSQ) in a carrier solvent of volatile methyl siloxane. This liquid has a thin consistency and can easily be spin coated onto a substrate. The spin on glass has an expected thermal expansion coefficient that is quite large (20ppm/ $^{\circ}$ C) and is therefore expected to shrink more during cooling than the

surrounding glass and the Inconel parts after firing. This thermal expansion mismatch can lead to cracking in the HSQ coating layer if it is over a certain thickness. Spin on glass is used for coatings thinner than 1µm as a result of this cracking tendency.

The procedure for curing in a HSQ film is as follows. First at temperatures below 250°C the carrier solvent is evaporated and the HSQ material is left uniformly distributed on the surface. Second at temperatures from 250°C to 350°C there is a process of cage-network redistribution in the HSQ layer. At temperatures from 350°C to 435°C Si-H bonds are broken resulting in hydrogen leaving the film and leaving behind SiO<sub>2</sub> and Si. At temperatures above 435°C the cage structure of the HSQ starts to collapse resulting in a higher density deposited film[142, 143]. This process is outlined in Figure 3.13.

- |   |  |
|---|--|
| <p>1. T = 25°C – 250°C<br/><i>Solvent loss</i></p>  |  |
| <p>2. T = 250°C – 350°C<br/><i>Cage-network redistribution</i></p>                          | $\left\{ \begin{array}{l} 2\text{HSiO}_{3/2} \rightarrow \text{H}_2\text{SiO}_{2/2} + \text{SiO}_{4/2} \\ \text{H}_2\text{SiO}_{2/2} + \text{HSiO}_{3/2} \\ \qquad \qquad \qquad \rightarrow \text{SiO}_{4/2} + \text{H}_3\text{SiO}_{1/2} \\ \text{H}_3\text{SiO}_{1/2} + \text{HSiO}_{3/2} \rightarrow \text{SiO}_{4/2} + \text{SiH}_4 \\ 4\text{HSiO}_{3/2} \rightarrow 3\text{SiO}_{4/2} + \text{SiH}_4 \\ \text{SiH}_4 \rightarrow \text{Si} + 2\text{H}_2 \text{ or cleavage or Si - H} \end{array} \right.$ |
| <p>3. T = 350°C – 435°C<br/><i>Si-H thermal dissociation and network redistribution</i></p> |  |
| <p>4. T &gt; 435°C<br/><i>Collapse of the cage structure</i></p>                            |  |

**Figure 3.13:** Four possible stages of HSQ curing. Note the temperature ranges for each stage, and the associated chemical reactions[142].

The deposition of the HSQ was done with the following procedure: First the feedthrough was cleaned with a five minute sonication in acetone followed by a five minute sonication in isopropyl alcohol and finally rinsed with MiliQ water. Immediately after drying, the feedthrough was placed into a spin coater and a thick pool of Fox-25 was pipetted onto the surface (~100µL/cm<sup>2</sup>). The feedthrough was spun for 15 seconds at 500rpm and then for 15 seconds at 1000rpm. After spin coating the feedthrough was placed into an oven set to 170°C for 30 minutes and then transferred to an oven at 350°C for 30 minutes. The feedthrough was allowed to slowly cool to room temperature after the two baking steps. The resulting coating was smooth and free from cracks when observed under an optical microscope.

Coatings that were deposited at slower spin speeds resulted in a thicker edge bead on the feedthrough that resulted in a thick HSQ layer that subsequently cracked during the curing procedure. Using the fast second step spin removed most of this edge bead and resulted in uniform and thin coatings without any cracking. Some of this cracking observed when thick HSQ layers were deposited on the feedthrough are shown in Figure 3.14.

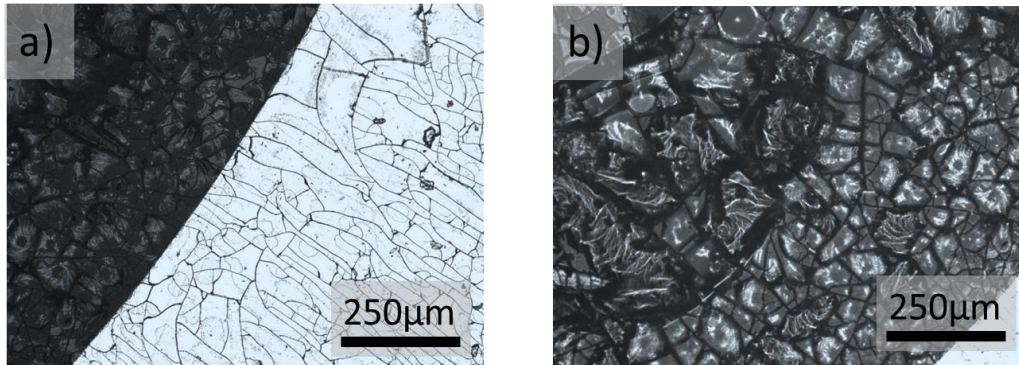


**Figure 3.14: Thick coatings of Fox-25 deposited onto a high pressure feedthrough after curing process of 170°C for 30min and 350°C for 30minutes.**

The thin coatings noticeably changed the appearance of the pits but did not completely fill the pits. Any thicker coatings that were tried resulted in a dramatically cracked surface that did not appear to be an improvement over the original surface. A figure of some devices prepared after a thin spin on glass coating are shown in Figure 3.15a and b and the dramatic cracking observed when using a thick layer of spin on glass is shown in Figure 3.15c.

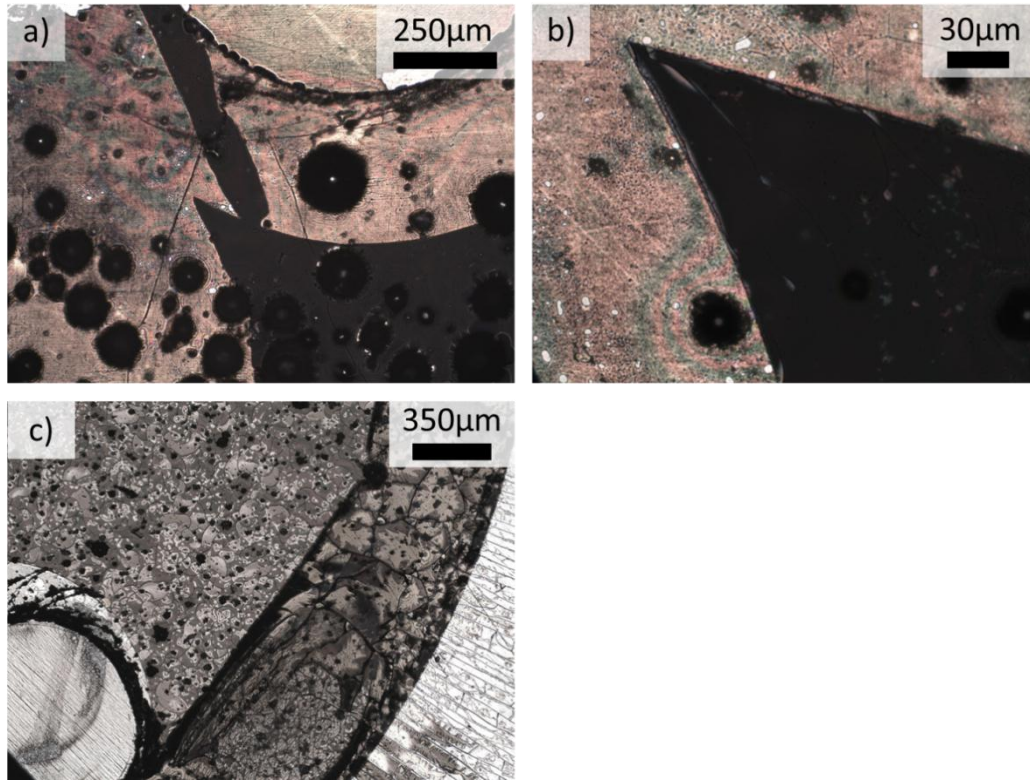


Figure 3.15: a,b) Optical micrograph of chromium devices fabricated on a high pressure feedthrough coated with a thin layer of cured spin on glass. No cracking is evident, but feedthroughs still have very clear large defects on the surface. c) Image of devices fabricated on a feedthrough with thicker spin on glass showing significant cracking.

Spin on glass was not used further for surface modification as it was concluded that it was only suitable for filling defects smaller than  $1\mu\text{m}$  in size (using SEM and optical microscopy) and could not help much with planarizing the larger defects on the feedthrough surfaces for this work.

### 3.4.2 *Aremco Silicone Magnesia Low Melting Point Glass*

This coating is made up of a mixture of silicone, low melting point glass, and a magnesia filler to adjust the thermal expansion coefficient to better work as a corrosion coating for stainless steels and inconel materials ( $\sim 13 \times 10^{-6} \text{K}^{-1}$ ). The silicone base allows the coating to be applied easily and gives a paint-like texture to the coating that can be brushed onto a surface and dry to a sticky film that adheres strongly to this surface. The suggested maximum processing temperature of this coating is within the limit of the high pressure feedthrough and the consistency and adhesion of the suspension allow for easy application via spin coating. This coating was applied at various thicknesses by varying the spin speed used when applying the liquid coating. The feedthroughs were first thoroughly cleaned using an ultrasonic bath of acetone, IPA and MiliQ water in sequence. The coating was then

applied using a spin coater with a two-step process, first a slower spreading step at 500-750rpm and then a faster spreading and drying step at 750-3000rpm. After spin coating the feedthroughs had a uniform coating of the glass material that seemed to form quite well to the feedthrough topography as seen in Figure 3.16.



**Figure 3.16: Photograph of feedthroughs coated with Aremco Silicone Magnesia Low Melting Point Glass before firing.**

These coated feedthroughs were then air dried for 15minutes and then baked at three steps of 100°C for 30 minutes, 260°C for 15 minutes, and finally 450°C for 30 minutes.

The speeds 750rpm-750rpm and 500rpm-3000rpm were selected as two example coatings that worked well and had significantly different thicknesses; the 750rpm final spin speed was many times thicker than the 3000rpm final spin speed coating. Each of these coatings were then back polished using P-4000 grit sand paper until the feedthrough pins and body were exposed and finally devices were patterned onto the surface using a lift off process and sputtering. Optical images of these devices are shown in Figure 3.17. Figure 3.17 a and b show images of the device with the thinner coating of glass and Figure 3.17 c and d show images of the feedthrough with the thicker coating of glass. In both cases a large number of the larger defects appeared to be partially filled in with material. The filled in pits still appear to have a significant roughness. This roughness was caused by the MgO filler material in the glass that was used to adjust the thermal expansion properties of the mixture. The MgO filler does not melt at the maximum processing temperature of 450°C and remains as a rough powder in the molten glass when firing. When cooled this powder remains in the glass and leads to a higher surface roughness after polishing in the filled in defects. A significant number of the defects, especially the smaller defects do not get completely filled in after this process, but a large number of the ~100µm scale defects do get filled in according to SEM observations.

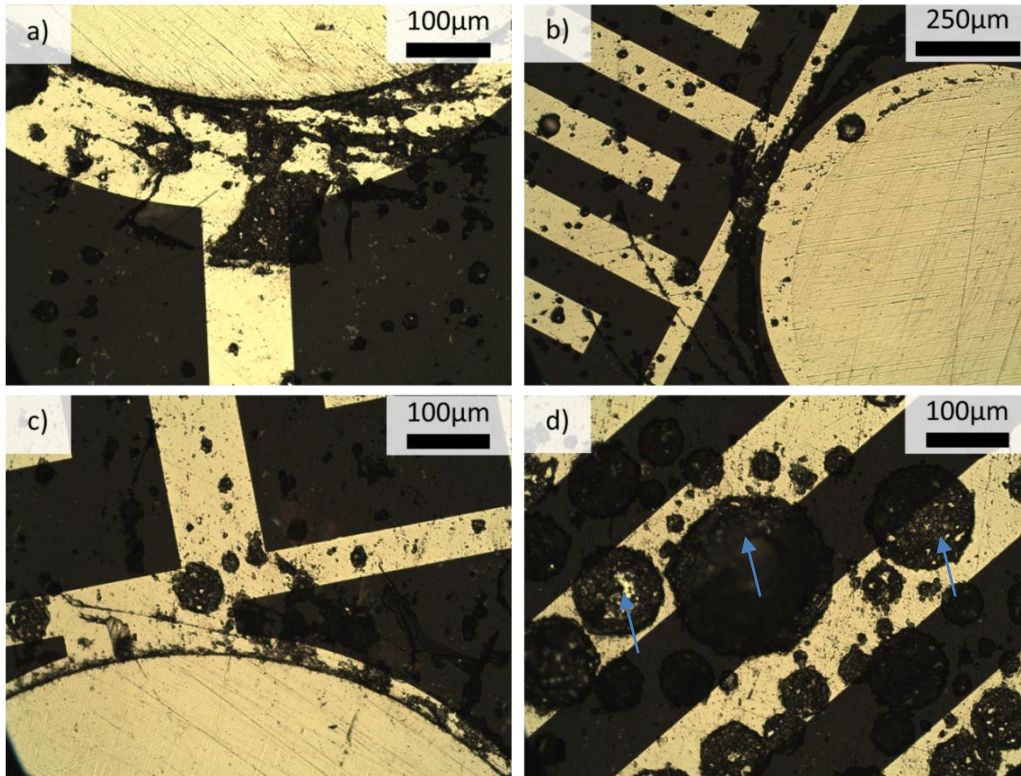


Figure 3.17: Optical micrographs of feedthroughs with chromium devices fabricated on them after surface treatment with Aremco silicone magnesia low melting point glass. Image d) shows three large defects mostly filled with glass and the rough texture of glass in the defect area.

### 3.4.3 Aremco LMP Glass

This glass was obtained after discussions with Aremco regarding the roughness observed inside of the filled defects. They then provided us with the same composition coatings but without the MgO filler material. They also provided a third coating that did not have the silicone binder material.

The composition of this glass material is shown in Table 3.1.

Table 3.1: Composition of Aremco low melting point glass as determined by XPS.

Glass constituent	Mol %
Bi <sub>2</sub> O <sub>3</sub>	36
ZnO	57
CaO	3
Na <sub>2</sub> O	4

The firing process recommended by Aremco involves a three step bake of 100°C for 30 minutes, 260°C for 30 minutes, and 538°C for 10 minutes followed by a slow cool

to room temperature. The maximum cure temperature of 538°C recommended by Aremco for melting the glass is significantly higher than the recommended operating range for the high pressure feedthrough substrate (427°C). Because of this temperature difference a set of three different maximum firing temperatures were explored of 450°C, 475°C, and 500°C. Three samples were prepared on glass slides and fired with the recommended firing times and temperatures except replacing the final temperature step with the three lower values. These samples are shown in Figure 3.18. All of the samples showed obvious signs of melting and adhered well to the glass slide surface after firing. The appearance of the glass changes significantly between the 450°C and 475°C firing temperature, becoming significantly smoother, denser and a second phase approximately 5µm in size becomes visible in the higher resolution micrographs of the 475°C sample that is also present in the 500°C sample. The sample melted at 450°C did not have any defects in it larger than 10µm in size and this temperature was determined to be acceptable for filling in the feedthrough defects.

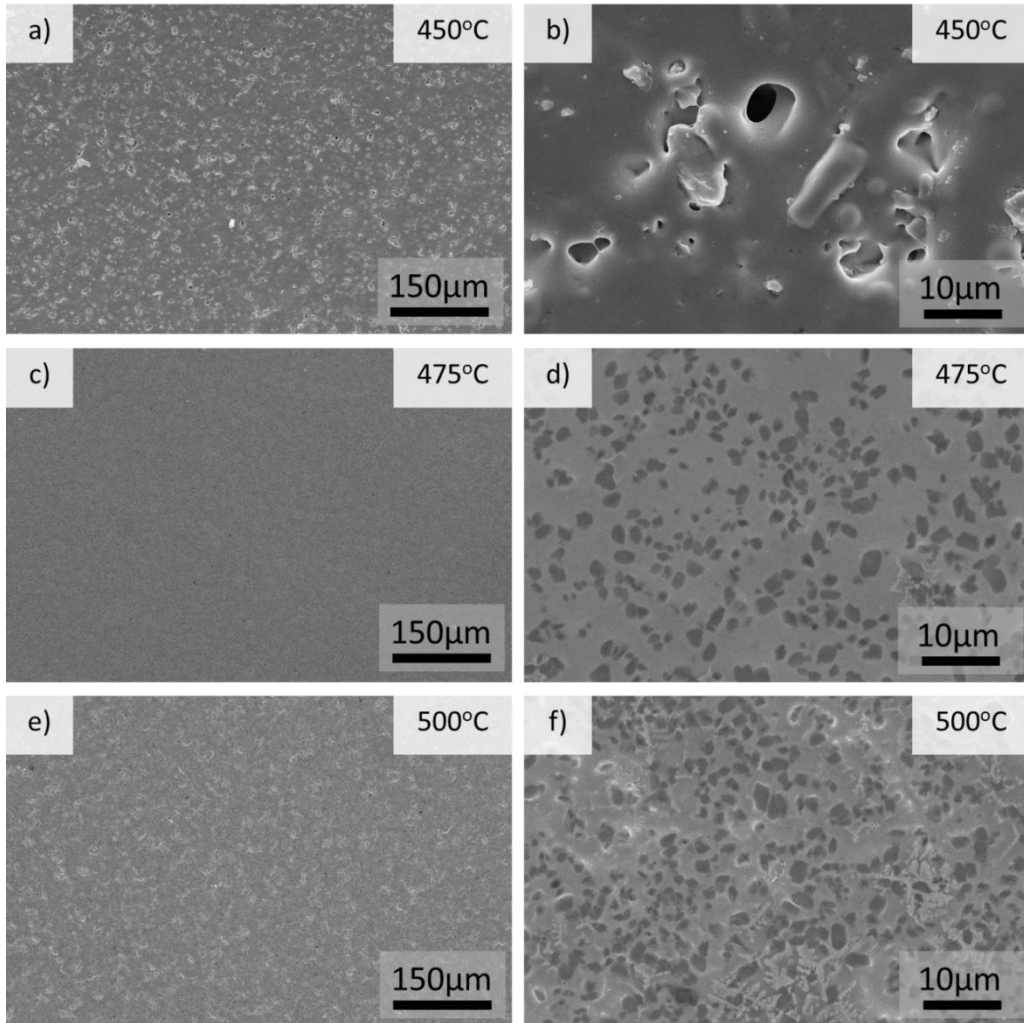


Figure 3.18: Low magnification SEM micrographs of Aremco low melting point glass melted on a glass slide at 450°C a), 475°C c) and 500°C e), and higher magnification images of the same in b), d), and f).

Initially thick coatings of the low melting point glass were applied to the feedthrough surface in an attempt to fill all of the defects in one processing step. These thick coatings all resulted in dramatic damage to the surface of the high pressure feedthrough involving “chip-out” of large flakes of glass and large cracks. This damage was initially thought to be caused by the high temperature of the firing being slightly above the operating temperature of the feedthrough but it was later found that uncoated feedthroughs did not crack at all when taken through the same temperature cycle. Diffusion between the thick glass coating and the feedthrough coating could cause expansion or contraction of the feedthrough glass leading to cracking. It was not evident from observation of the cracked glass whether or not the cracking was due to expansion or contraction of the feedthrough glass caused by diffusion.

After this discovery, only thin coatings of the low melting point glass were used for coating the feedthroughs. Figure 3.19 shows a feedthrough that was severely damaged by a thick coating of the glass and subsequent attempts to fix the damage using thin coatings of the low melting point glass. It demonstrates that the low melting point glass works quite well at filling large surface defects on the feedthrough surface filling in a millimeter dimensioned chip-out with two coatings. After the first coating (Figure 3.19a,c) a significant portion of the large defects are filled in. After the second coating (Figure 3.19b,d) the feedthrough is quite smooth and mostly repaired. Highlighted in Figure 3.19b is an inset that shows 10 $\mu$ m cracks and a 100 $\mu$ m sized pit completely filled in with low melting point glass. Thin coatings of this low melting point glass work well at filling in defects larger than 50 $\mu$ m in size. After two to three coat and fire steps, large surface defects can be completely repaired.

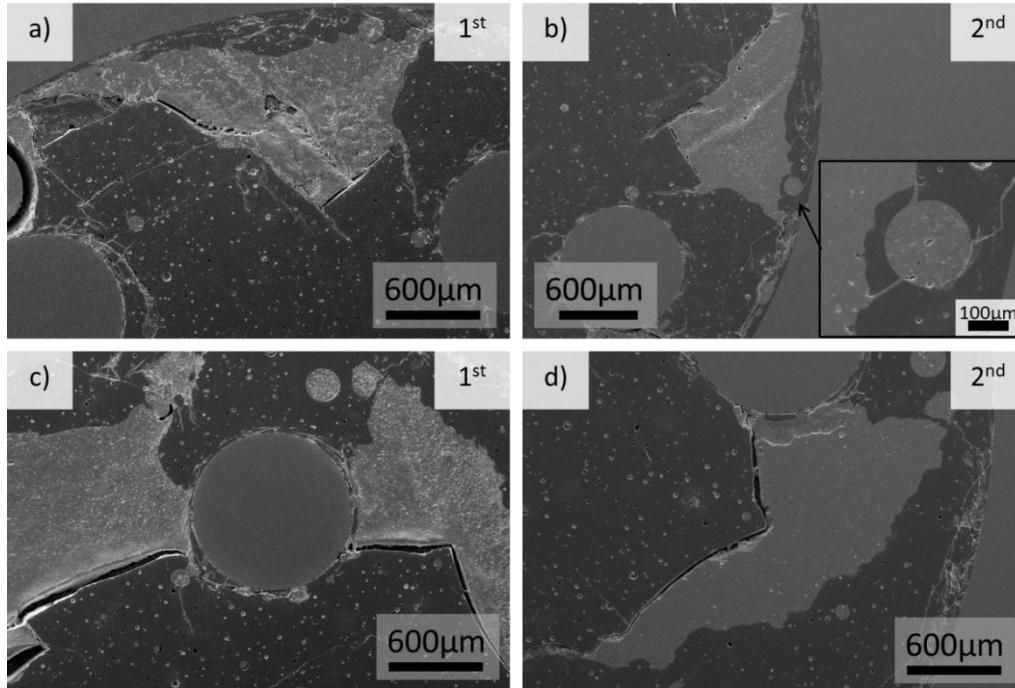


Figure 3.19: Very large defects successfully filled with low melting point glass after 1 coating in a) and c) and after two coatings in b) and d). Inset of b) shows a 100µm size feature perfectly filled with glass.

A final example of this process doing an excellent job of filling in large surface defect regions can be seen in Figure 3.20 where a poor surface quality feedthrough that was cut in a region between two glass frits has been mostly repaired by a low melting point glass surface treatment. Low magnification SEM shown in Figure 3.20 suggests that more than half of the defects between the size of 50µm and 500µm have been successfully filled.

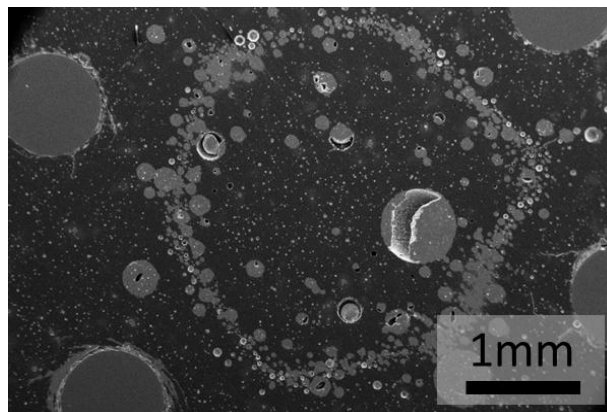


Figure 3.20: Low magnification scanning electron micrograph overview of a high pressure feedthrough with a large number of defects mostly corrected with a surface treatment with low melting point glass.

### 3.4.4 Lead Borate Solder Glass

Some feedthroughs were sent to a laboratory in Germany (Sensor Engineering) where a lead borate solder glass was melted onto the high pressure feedthrough surface. When the glass was melted on the surface of the feedthrough a rough vacuum was applied to the glass to help with the removal of bubbles in the glass. After cooling the feedthroughs were shipped back and then polished back to a smooth surface finish. A very thick layer of solder glass was applied (~500 $\mu$ m) and no damage was caused to the feedthrough as was seen with the thick layers of Aremco bismuth zinc oxide based glass. After polishing, the feedthrough surface appeared as shown in Figure 3.21b with many of the defects being nicely filled in but with the larger defects still having some small bubbles present inside of them. This treatment successfully reduced 25 $\mu$ m-100 $\mu$ m sized defects to 5 $\mu$ m size defects and filled well over half of the surface topography.

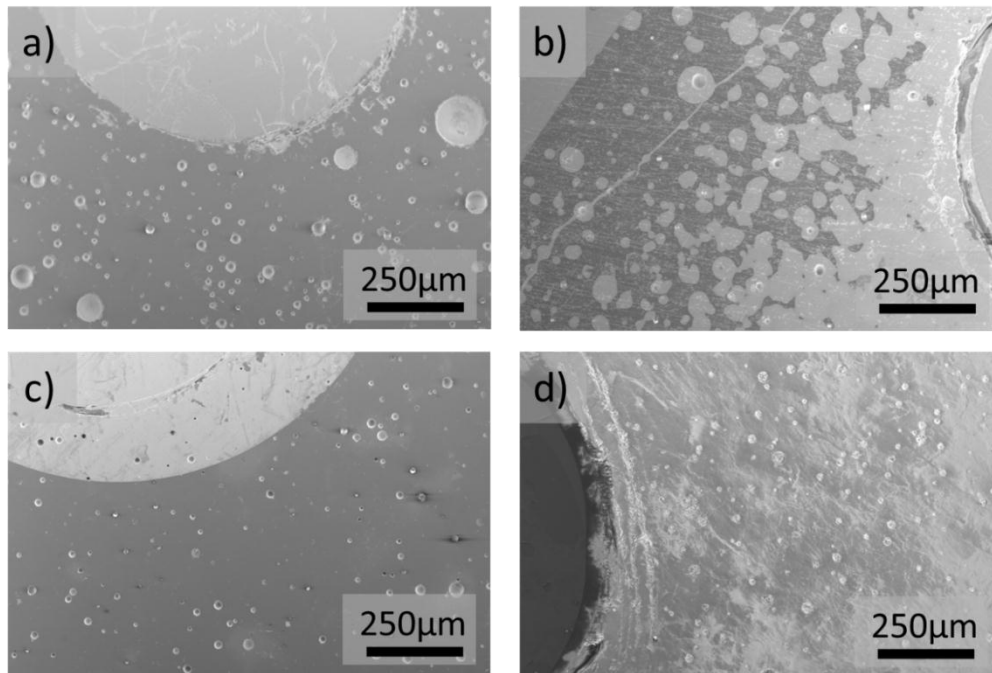


Figure 3.21: a) Cut and polished feedthrough b) PbO based glass melted then polished back c) Spin on glass coated and polished back d) Aremco coating covered and polished back.

### 3.4.5 Glass Coating Summary

The tested materials are briefly summarized in Table 3.2. Fox-25 spin on glass was found to do a good job of filling very small defects but could not be used to fill in larger defects because of its cracking tendency at larger thicknesses. The Aremco low melting point glass with MgO filler worked well but left a rough texture inside of the defects that it filled due to the non-melting filler material MgO. To improve the texture of the filled in defects a second low melting point glass without the MgO filler was used and was found to do an excellent job of filling in defects in the size

range of 20 $\mu$ m to 100 $\mu$ m and even showed some ability to fill in 1mm sized defects on the surface of the feedthrough. Also tested was a lead borate solder glass that showed good filling of defects but still contained some small pits in larger defects that it filled. Both the Lead Borate and bismuth zinc oxide based low melting point glass show promise for filling larger defects on the surface of the feedthrough. A good material for filling in smaller defects less than 20 $\mu$ m in size still needs to be found. Summary images of the different tested materials are shown in Figure 3.21 and Figure 3.22 where the spin on glass, lead borate, and MgO filled coatings are compared at two different magnifications.

**Table 3.2: Summary of tested planarization materials.**

Surface modification	Processing Temperature	Result
Fox-25 spin on glass	250°C-435°C	Thick = cracking Thin = can't fill large defects
Aremco MgO coating	450°C	Too coarse
PbO based low temp glass	< 500°C	Good coverage still bubbles in large defect sites
Aremco Bi <sub>2</sub> O <sub>3</sub> ZnO	450°C - 538°C	Good at filling defects ranging from 20µm to 100µm in size

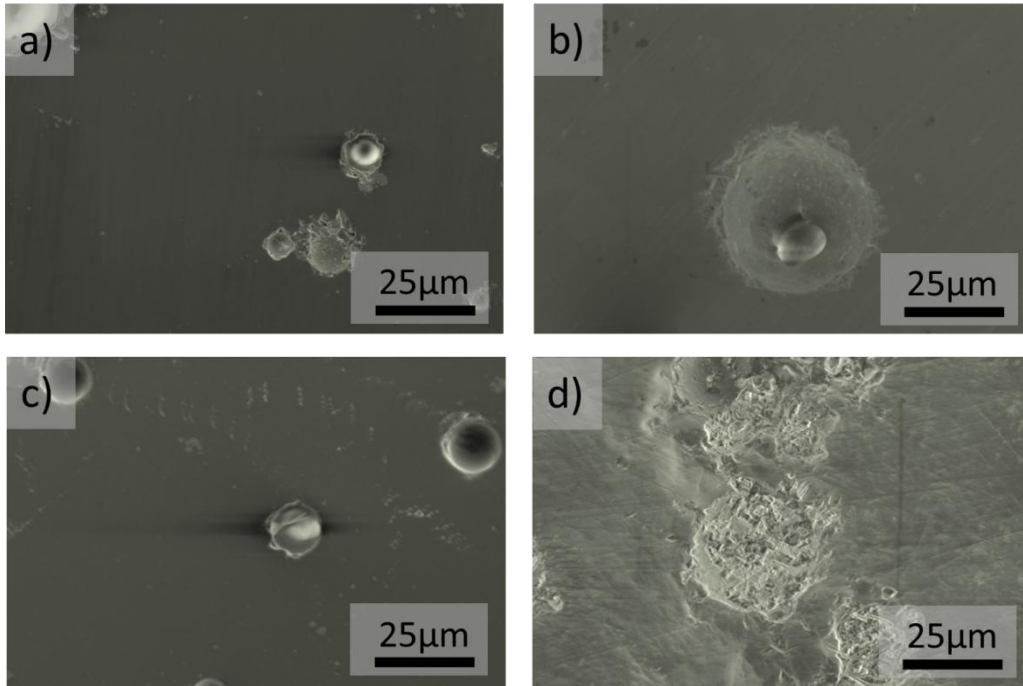


**Figure 3.22: a) Cut and polished feedthrough b) PbO based glass melted then polished back c) Spin on glass coated and polished back d) Aremco coating with MgO filler covered and polished back.**

### **3.5 Sensor Device Material Selection**

In active service the sensors developed for this project will be exposed to pressures up to 69MPa, temperatures up to 180°C, erosion from sand, and corrosive environments containing CO<sub>2</sub>, H<sub>2</sub>S, and salt water. Temperature stability was used as a first test to qualify the material that the sensors would be fabricated from.

In order to test the temperature stability of the devices, temperature cycling over the range of 20°C to 200°C was used. Creating devices that can survive more than one temperature cycle without failing or drifting was a significant unexpected challenge in this project. The different thermal expansion properties of the multiple components on the sensor surface cause stress in the metal film when the device temperature is changed. This stress can lead to device failure by delamination from the feedthrough, cracking and breaking of the micromachined devices. Sputtered chromium devices, while having excellent corrosion resistance, fail consistently when cycled in temperature from 20°C to 200°C. Over-plating was explored as a solution to these device failures as it is a technique that can easily deposit thicker metal layers and it is not affected by shadowing which creates thin sections in films deposited by sputter deposition.

#### ***3.5.1 Feedthrough device over-plating***

Both chromium and nickel were investigated for electroplating of the sensor devices in order to improve the robustness of the structures on the surface. Because of shadowing during sputtering, the deposition thickness in cracks and defects is expected to be thinner than that on the majority of the surface. By electroplating after forming devices using a sputtering and lift off technique, a thicker structure can be built-up in these thin regions and a more robust metallic structure formed.

#### ***3.5.2 Electroplating Chromium***

Chromium was tried first as an electroplating material as it is commonly electroplated and known to be corrosion resistant in downhole applications. Devices were first fabricated on the feedthrough surface from 300nm of sputtered chromium. These devices were then submerged in a custom electroplating cell and plated with the following conditions taken from Modern Electroplating[114].

Solution: 100mL H<sub>2</sub>O, 25g CrO<sub>3</sub>, 130uL of H<sub>2</sub>SO<sub>4</sub>

Temperature: 50°C

Stir speed: 200RPM

Current: -20mA

Anode: Pure Nickel

Cathode-Anode Spacing: 5mm

After plating for 100seconds the surface texture of the device was significantly different (Figure 3.23c) and a deposit is clearly formed on the chromium device. Significant sections of the device peeled from the substrate and the previously electrically continuous beam became open circuit. The second beam was plated for 10minutes to apply a significantly thicker chromium coating onto the device. In this case a significant portion of the device was completely removed from the surface of the feedthrough and only portions of the chromium coating were still visible with SEM. Chromium electroplating consistently resulted in delamination of the sputter coated devices from the surface of the feethrough. This is believed to be caused by high thin film stress in the electrodeposited films causing delamination of the underlying sputter deposited film of chromium.

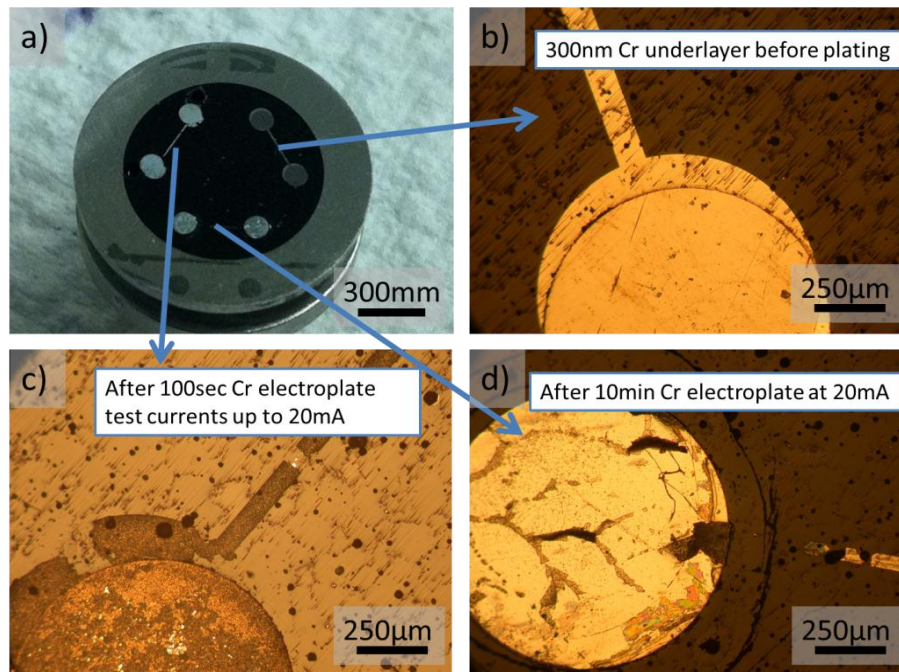


Figure 3.23: Results from first chromium electroplating test. a) The feedthrough after two of the beams were electroplated b) the appearance of the Cr under layer before deposition c) the appearance of the device after 100 seconds of electroplating at 20mA d) after extended electroplating for 10 min at 20mA, the surface stress resulted in the bulk of the chromium flaking off of the surface.

### 3.5.3 Electroplating Nickel

Nickel was tried second as an electroplating material because it is known that nickel electroplated from a sulfamate bath has extremely low thin film stress and can be plated to significant thickness without cracking or delaminating. First, a seed of 300nm of chromium is deposited as an electroplating seed layer. Second, the electroplating is conducted using a bath composition described in table 2.1 and a current density of  $0.4\text{mA}/\text{mm}^2$ . The resulting devices were very nicely coated and no additional delamination or breaking of the sputter deposited films was observed.

Figure 3.24 shows two images of a beams plated for 10minutes (a) and 20minutes(b) respectively. Pitting was observed in the deposits as can be seen in the figures, but the devices were functionally improved showing more consistent resistances from device to device, and better temperature cycling behavior. Adjusting of the concentration of added anti-pitter to the plating solution was found to dramatically reduce the number of pits in the plated devices.

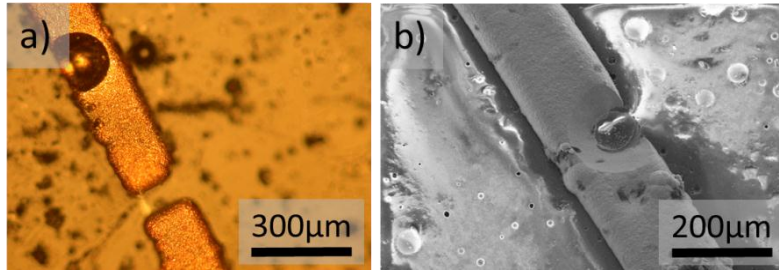


Figure 3.24: a) Optical micrograph of a beam electroplated with nickel for 10 minutes at 2mA b) SEM of a beam electroplated with nickel for 20 minutes at 2mA

By electroplating 5-10µm of nickel onto the feedthroughs we could prevent temperature cycling failures and stop the cracking and breaking of beam structure sensors. The nickel coated beams did not fail after 5 temperature cycles to 200°C and they had a monotonic and linear resistance vs temperature behavior. Unfortunately they also had a continuous positive drift in resistance when exposed to temperatures above 150°C. The room temperature resistance of a 100µm wide beam started at 80 Ω and drifted to 800 Ω after multiple temperature cycles.

### 3.6 Diffusion Barrier Coatings

#### 3.6.1.1 Chromium Oxide Coating

The problem of resistance drift was solved by coating the devices with a 1.2 µm thick chrome oxide layer. This layer prevented the oxidation of the beam structure sensors and resulted in a stable temperature sensor device that could be cycled several times to 180°C without any significant drift. The combination of a chromium device with thick nickel over-plating capped with a chromium oxide layer was stable over the temperature range of interest and did not fail after multiple temperature cycles. Chromium oxide is well known to be corrosion resistant in oil well applications. Inconel, which is frequently used in down hole sensor applications, naturally forms a chromium oxide passivation layer that provides excellent corrosion resistance. Because of the prevalence of Inconel already used in down hole applications it is expected that a chrome oxide protective layer on the micro sensor provides sufficient protection in the oil well environment.

The chromium oxide coating acts as a barrier layer and slows diffusion of oxygen to the nickel surface preventing further oxidation. The chromium oxide layer is also chemically stable and quite hard thus providing protection to the sensor from corrosion and erosion. The current process flow is outlined in Figure 3.25. Yield for

this process is quite good with a production run resulting in 14/15 sensor elements working on a batch of five feedthroughs.

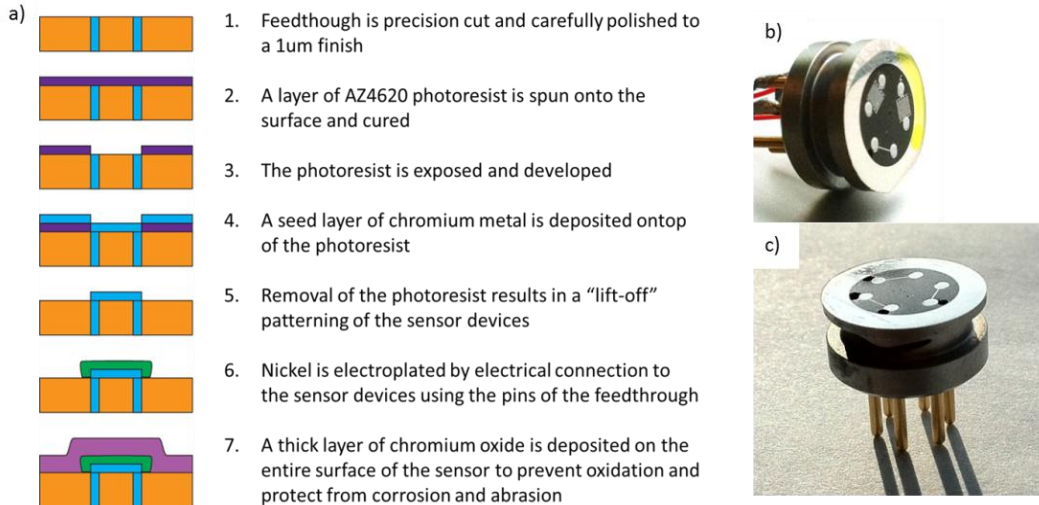


**Figure 3.25: Fabrication procedure for anchored devices on a high pressure feedthrough. b) finished feedthrough device with two comb structures and one beam structure. c) finished device with three beam structures.**

Figure 3.26 shows the temperature cycling data for three beam structures fabricated with 300nm of chromium as a base layer with 1um of nickel electroplated on the surface of the chromium. These beams were then sputter coated with 1.2 um of chromium oxide. The oxide coating prevented the beams from further oxidation and resulted in very little drift in the measurements with temperature cycling. This is a demonstration that the coated sensors physically work, have good performance as a temperature sensor with a significant linear increase in resistance with temperature, and can provide repeatable, stable measurements even after being exposed to a high temperature environment.

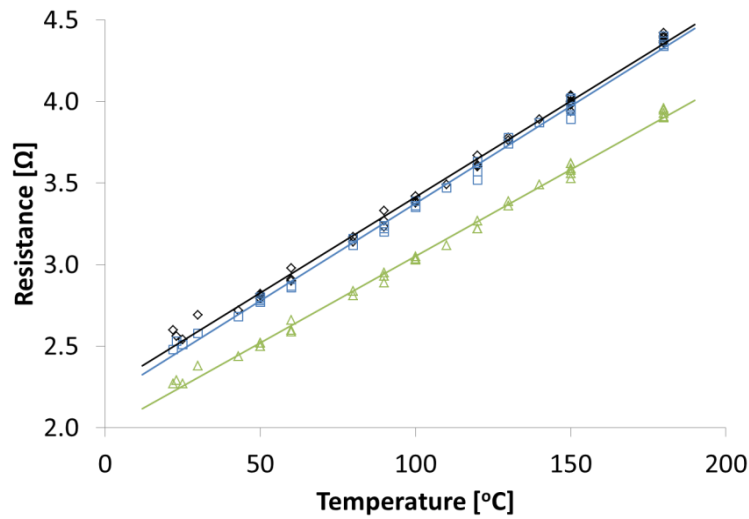


Figure 3.26: Resistance vs. Temperature calibration graph for a feedthrough with three beam structures. Furnace was heated and cooled three times with resistance and temperature measurements recorded during cycling.

It was possible to damage the chromium oxide coatings with gentle scraping and by tape tests. As a result other coatings were tried after proving that the diffusion barrier of chromium oxide prevented resistance drift of the metal devices. It is possible that further optimization of deposition parameters could improve adhesion characteristics of this film and improve its durability.

### 3.6.1.2 Parylene Coating

Parylene, the generic name for poly-para-xylenes, is a conformal and chemically resistant polymer coating. It is deposited via vapor deposition polymerization and forms linear, highly-crystalline polymers. There are various types of Parylene; C, N, D, SF, HT and AF-4 (SF, HT, and AF-4 being names of the same polymer). The chemical structure of these monomers is shown below in Figure 3.27.

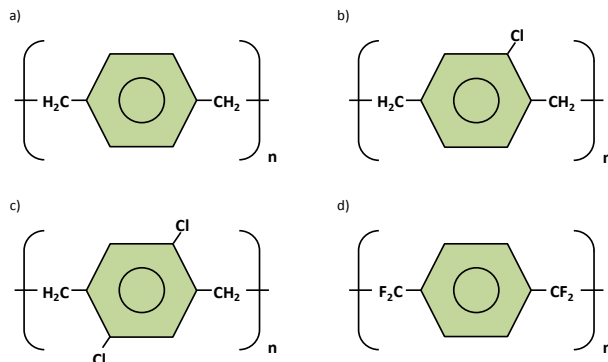


Figure 3.27: Monomers of the four types of Parylene: a) Parylene N. b) Parylene C. c) Parylene D. d) AF – 4, SF, HT[144]

Parylene N is a completely linear and highly crystalline material[144]. Crystallinity can range from 60% to 80% depending on deposition pressure and can be raised further to 100% with post annealing[145]. The Parylene C monomer is identical to that of Parylene N, except for the mono-chloro substitution. Parylene D has a di-chloro substitution, which enables it to withstand slightly higher operating temperatures when compared to the C and N variants. Parylene AF-4 has the  $\alpha$  – hydrogen replaced with fluorine; this version of Parylene is used in high temperature applications. It is interesting to note that Parylene AF-4 is a Teflon (polytetrafluoroethylene) analogue; both have the same aliphatic chemistry, the repeat unit – CF<sub>2</sub>–. The high temperature stability of Parylene AF-4 is due in part to the C – F bonds in the repeat units of the polymer.

A specially designed system is used to deposit Parylene. The dimer precursor is loaded into the system, which is held under vacuum. The dimer is then vaporized and the resulting gas is passed through a furnace. The dimer is cleaved at high temperatures (600 – 700°C) to form the reactive Parylene monomers. The reactive gaseous monomer is then passed into the deposition chamber, where polymerization occurs. The deposition chamber and the sample to be coated are held at room temperature. The reactive monomer disperses and polymerizes spontaneously once it comes into contact with the room temperature surfaces.

The Parylene polymer deposition takes place on the molecular level and there is little stress in the deposited film. Due to the monomers being in a gas phase prior to deposition, no surface tension effects exist during deposition and there are no risks of stiction. A dense and conformal polymer film is deposited on the sample. The final thickness of the Parylene coating is determined by the initial amount of precursor loaded into the system and coatings can range in thickness from 10nm to 30µm.

To determine if a Parylene coating would work for our application, a ~30 µm thick coating of Parylene C was deposited on a number of feedthroughs with functioning comb capacitors and beam structures. Some of the general properties and specifications of Parylene C are listed below in Table 3.3.

<b>Parylene C – Properties</b>		
	Value	ASTM Method
<b>General</b>		
Density [g/cm]	1.289	D1505
<b>Electrical</b>		
Dielectric strength (voltage breakdown) [volts/mil]	5,600	D149
Dielectric constant		D150
60 Hz	3.15	
1 kHz	3.10	
1 MHz	2.95	

Volume resistivity (@ 23°C, 50% RH) [ $\Omega$ ]	$8.8 \times 10^{16}$	D257
Surface resistivity (@ 23°C, 50% RH) [ $\Omega$ ]	$1 \times 10^{14}$	D257
<b>Mechanical</b>		
Tensile modulus [GPa]	3.2	D882
Tensile strength [MPa]	70	D882
Yield strength [MPa]	5.5	D882
Elongation to break [%]	200	D882
<b>Thermal</b>		
Melting point [°C]	290	
Glass transition [°C]	80-100	
Linear coefficient of expansion [ $10^{-5}/^{\circ}\text{C}$ ]	3.5	D696
Thermal conductivity (@ 25°C) [ $\text{Wm}^{-1}\text{K}^{-1}$ ]	0.082	C177

Table 3.3: Specifications and general properties of Parylene C[146].

Prior to deposition, an adhesion promotion step was carried out. The adhesion promoter is a mixture of IPA, deionized water (DI) and A-174 Silane; the ratios being 100:100:1, respectively. The three chemicals were added to a beaker and stirred for 30 sec. After mixing, the solution is left to sit for 2 hrs to fully react prior to immersing the samples. The samples are submerged for 30 mins, air dried for 30 mins, rinsed with IPA and then dried with  $\text{N}_2$ .

Parylene is resistant to many chemicals and is insoluble in most common organic solvents up to 150°C[147], which makes it an ideal candidate for coating our sensor devices. Parylene C is known to be stable in 10% HCl, 10%  $\text{H}_2\text{SO}_4$ , 10%  $\text{HNO}_3$ , 10% HF, 10% NaOH, 10%  $\text{NH}_4\text{OH}$ ,  $\text{H}_2\text{O}_2$ , n-Octane, toluene, monochlorobenzene, pyridine, 2-propanol (IPA) and acetone for 2 hour exposure times. The chemical resistance of our 30  $\mu\text{m}$  Parylene C coating was confirmed by exposing small samples of the polymer to various solvents for 24 hrs. Acetone, IPA, tap water, crude oil and 37% HCl were all tested. Weight gain/loss after exposure was measured; the results are shown below in Table 3.4. There was little change in the weight of the samples after treatments and the samples appeared identical before and after testing.

Solvent	Mass [mg]	
	Before	After
Acetone	2.35	2.40
IPA	2.16	2.16
Tap water	2.44	2.40
Crude oil	3.40	3.36
37% HCl	2.80	2.80

Table 3.4: Change in mass of Parylene C samples after exposure to various solvents for 24 hrs.

SEM images of the surface of the Parylene samples after exposure to various solutions are shown below in Figure 3.28, along with an image of an as-deposited

sample. The surface of the coating is very smooth and no change is evident after the solution treatments.

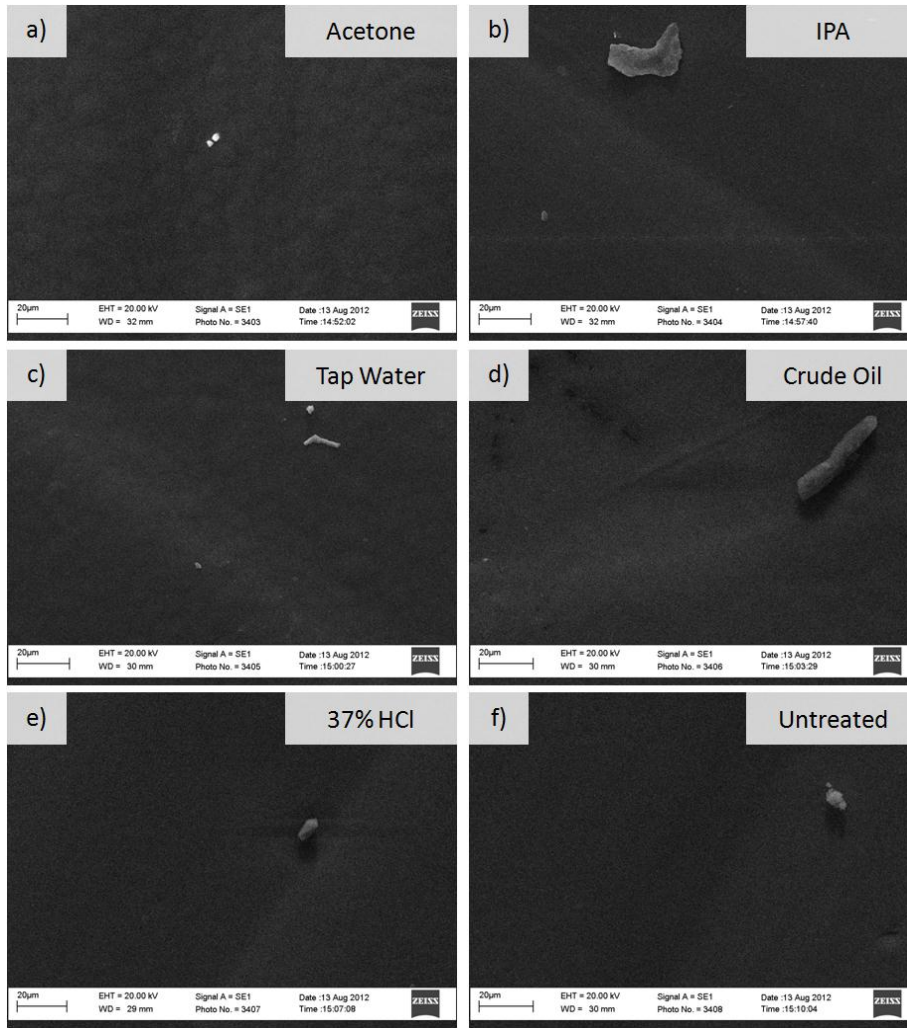


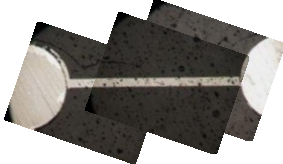
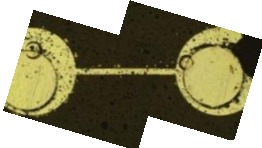
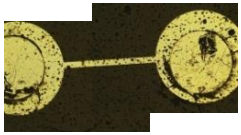
**Figure 3.28: Chemical stability of Parylene C at room temperature in various solvents. Time of exposure was ~60 hours. All samples were dried, coated with a thin layer of gold and imaged.**

Parylene C was tested in our lab and found to be an excellent and stable barrier coating. In the final implementation of the sensors it is expected that the higher temperature variant (Parylene HT) would be used. In discussions with the supplier Specialty Coating Systems it was found that they had significant experience providing coating services for down hole equipment and sensor elements exposed to the wellbore environment. They do not sell the equipment for depositing Parylene HT but do offer a coating service for a fee.

### 3.7 Final Implementation

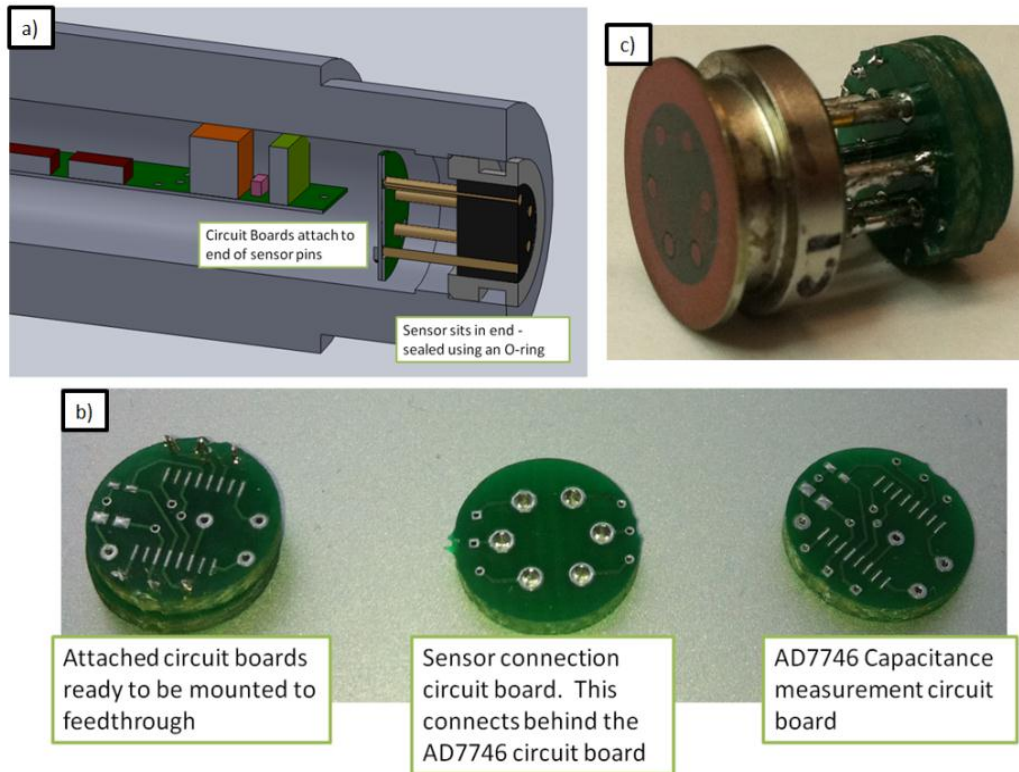
A summary of several tested material combinations for fabrication of a thermal sensing device is provided in Table 3.5 with the last entry being the solution that was decided on for the final implementation.

Table 3.5: Summary of sensor device material combinations.

Device material selection	Result summary
<b>300nm Cr</b> 	Beams are electrically connected but have a non-monotonic resistance vs temperature graph Thermal cycling to 200°C results in breaking of beams and an open circuit condition.
<b>500nm Cr</b>	Poor yield immediately after liftoff (open circuit beams)
<b>1um Cr</b> 	Poor yield immediately after liftoff (open circuit beams)
<b>300nm Cr with Chromium electroplating</b> 	All beams went open circuit and failed. Images showed that stress in the deposited film led to delamination from the substrate.
<b>300nm Cr with Nickel electroplating</b> 	All beams seemed to work and resistance varied from 0.3Ω to 80Ω depending on plating time. Thermal cycling to 200°C resulted in an upwards drift in the beam resistance making them unsuitable for temperature sensors.
<b>300nm Cr with nickel electroplate and Cr<sub>2</sub>O<sub>3</sub> protective coating</b> 	Five feedthroughs were manufactured using this material stack. Yield was good with 14/15 devices functioning. Thermal cycling showed nice temperature vs resistance results with 1% drift observed after 6 cycles to 180°C. Electrical isolation of beams from surroundings improved dramatically. Adhesion of the first Cr <sub>2</sub> O <sub>3</sub> coatings is not ideal and can be removed from the Inconel feedthrough surface with Tape/Scratching.
<b>50nm Cr 250nm Cu with 1um nickel electroplate and Parylene protective coating</b>	Nine feedthroughs were manufactured using this material stack and the resulting device yield was 100% with 27/27 devices functioning perfectly.

Electrical isolation of the comb capacitance structures worked perfectly allowing for repeatable and reliable capacitance measurements. Adhesion of the Parylene coating was excellent and the resulting coating was very durable resisting scratching/wiping/tape tests and assorted hot solvents.

The final design of the feedthroughs uses an Aremco bismuth zinc oxide LMP glass coating after cross sectioning to improve the surface finish of the feedthrough. After this coating lift off is used to pattern a sputter deposited seed layer consisting of 50nm chromium followed by 250nm copper. These seed devices are then plated with 1 $\mu$ m of nickel from a nickel sulfamate bath. This feedthrough is then electrically tested, pretreated, and coated with a parylene coating. Figure 3.29 shows a completed sensor element attached to the circuit board that contains the capacitance to digital measuring circuit. Figure 3.29a shows how the sensor element would be integrated into an oil well logging instrument with the sensor being pressed into an o-ring sealed seat and the electronics section protected by an Inconel housing. Figure 3.29b shows the two level circuit board adapter developed to integrate the feedthrough sensors with an Analog Devices AD7746 capacitance to digital converter. Once interfaced measurements of the capacitance of the microfabricated comb structures in different fluids could be conducted. And Figure 3.29c shows the sensor feedthrough soldered to the sensing circuit board in the final implementation of this sensor package.



**Figure 3.29: Implementation of the high pressure feedthrough in a down hole oil well tool. A) The integration of the feedthrough sensor in an inconel housing that surrounds the sensor circuit boards. b) Images of the fabricated circuit boards for interfacing an AD7746 capacitance to digital converter to the sensors. c) Photograph of the finished sensor device soldered to the measuring circuit board.**

### 3.8 Conclusion

Four different methods for cross sectioning high pressure feedthroughs were tested and compared. A method of cutting using a low speed gravity fed saw was found to cause the least amount of damage to the Inconel pin glass interface. Several coatings were tested and compared for planarization effectiveness including: Fox spin on glass, lead borate glass, and Aremco bismuth zinc oxide glass with and without a MgO filler. Spin on glass was found to work for filling very small defects on the surface of the feedthrough and all three of the other glasses were able to fill in defects larger than  $20\mu\text{m}$  in size with the bismuth zinc oxide LMP glass working the best. Sputtered chromium devices were found to not be stable during temperature cycling due to delamination from the substrate. Reliability during temperature cycling was considerably improved by using an electroplated nickel coating on the devices patterned with lift off and sputtering. The stability of the electrical resistance of the structures was dramatically improved with an oxygen diffusion barrier of either chromium oxide or parylene. Both of these coatings are expected to be corrosion resistant in the downhole environment. The finished materials system, implemented as an electrode platform for microfabrication onto

a high pressure feedthrough, enables a variety of sensor structures to be fabricated for use in the down hole oil well environment.

## 4 Fabrication 2: Phase Change Release Fabrication for Free Standing MEMS

The idea for fabricating cm scale released devices came from an electroplating experiment where very thick nickel plating was being tested on silicon wafers. One of the plated structures delaminated from the substrate and is pictured in Figure 4.1. This free standing nickel structure was surprisingly rugged and could be handled, moved and washed while freestanding without breaking. The entire structure was rigid and could be held from any edge without deforming or bending. This demonstration of the ruggedness of the nickel plated structure enabled the possibility of fabricating onto pins and creating an integrated freestanding sensor.

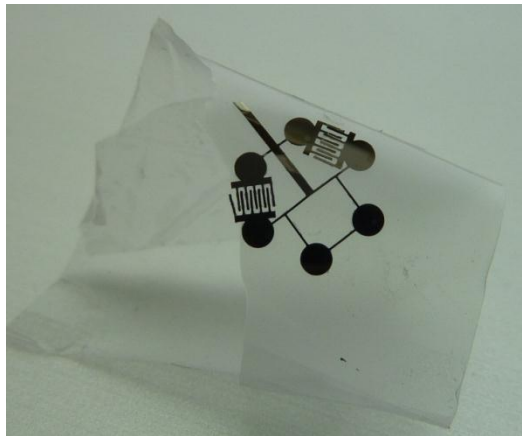


Figure 4.1: Free standing devices removed from silicon wafer using scotch tape. Devices were rigid and did not bend much when removed from the tape. This indicated that the devices could work well if fully released on pins.

### 4.1.1 Concept for free standing devices using a thick sacrificial layer

The proposed fabrication process for centimeter scale release of MEMS structures is shown in Figure 4.2. This process depends on finding a sacrificial material that can be used as a scaffolding support for the fabrication of microstructures onto a pin array. After the microstructures are fabricated the sacrificial material must be removable with high selectivity so that the microstructures are not damaged. The finding of a suitable sacrificial material will be outlined below.

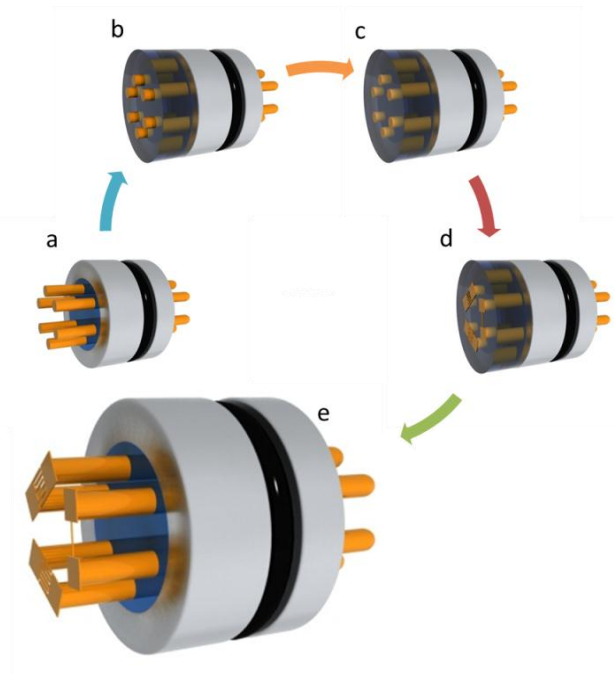
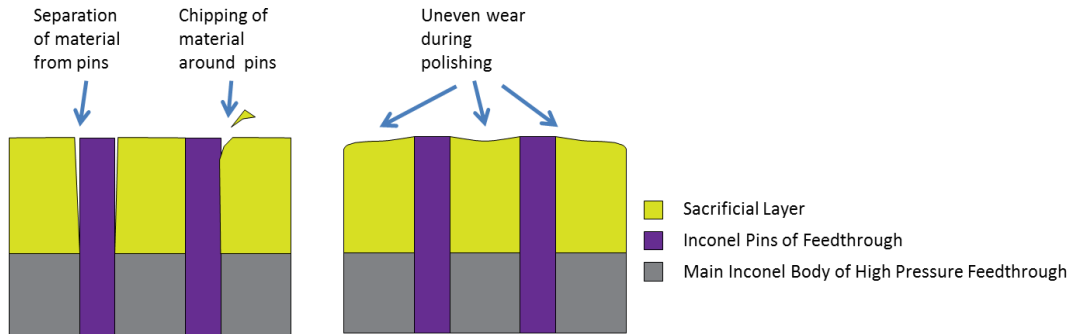


Figure 4.2: Process flow for fabrication of fully released devices. a) shows the starting high pressure feedthrough device b) shows filling of the space between the pins with a sacrificial material c) shows what the device looks like after being cut and polished d) After photolithographic patterning of devices. e) After removal of the sacrificial layer.

#### 4.1.2 Physical requirements for a sacrificial layer material

Several properties are required to make a sacrificial layer that can be used as described in Figure 4.2. These properties are outlined in this section.

The sacrificial layer material has to be a liquid (melted or uncured epoxy, melted metal) that solidifies around the pins of the feedthrough. This material must cure to be hard enough to allow for cutting and polishing. Adhesion to the pins during curing is important, as separation between the sacrificial material and pins would make fabrication impossible. If the material is brittle, vibrations during polishing will break the sacrificial layer in the areas surrounding the pins as shown in Figure 4.3. If the material is too soft it will wear away faster than the pins when polishing resulting in a surface that is not even as seen in the second part of Figure 4.3. Potting materials used for metallography prep meet both of these requirements and are designed to withstand cutting and polishing steps while strongly adhering to the sample embedded within them.



**Figure 4.3: Problems that can occur during the cutting and polishing step if material properties are not ideal for the sacrificial layer.**

The material must also be free from bubbles or voids that will limit the resolution of photolithography on the surface. Bubbles that cure in the body of the sacrificial material will be cross sectioned and revealed during the cutting and polishing steps. They result in a surface that is pockmarked with semispherical crater like defects. These defects limit the resolution of successful photolithography that can be done on the surface. If there are 10um sized craters in the surface then 50um resolution lithography should still work, but it would be difficult to get a good yield of 10um resolution devices on such a surface.

The material must be thermally stable up to 100°C as this is the baking temperature for most photoresists that are used to pattern the devices. The material must be chemically stable in acetone and IPA as the photoresist carrier solvent might attack the surface of the material and this would result in a failure during photolithography. Perfectly selective removal of the material after the devices are patterned must be possible. To meet these requirements several materials were tried as described below.

In conclusion the material must start as a liquid that can be poured into the pins of the feedthrough, it must then solidify into a mass that is stable enough to allow for cutting, polishing, lithography and metal deposition, and finally the material must be easily removed after processing leaving behind the microfabricated devices.

## 4.2 Material Selection

### 4.2.1 Material 1: Sample Mount Epoxy

Allied High Tech EpoxySet sample mount epoxy was used first because it meets all of the requirements for a sacrificial layer. It can be poured into the pins of the feedthrough and it cures to 89 Shore D hardness, which is excellent for polishing. It does not shrink when curing and adheres well to all surfaces of the feedthrough pins.

The epoxy was first mixed for five minutes in a 10:1 ratio of resin to hardener. This mixture was placed in a wide and shallow container and heated slightly to 40°C to aid in removal of bubbles from the mixture. This mixture was then carefully poured while still warm into a cup mold surrounding the pins of the feedthrough, trying not to introduce any bubbles. The feedthrough was then cycled twice to a rough vacuum and back to atmospheric pressure using a vacuum desiccator connected to a dry vacuum pump. This cycling helped to reduce the number of bubbles that cured in the epoxy. Interestingly, if the epoxy is cured under a constant vacuum it will foam and have significant porosity throughout. After curing for 12 hours the mold can be removed and the epoxy remains as a block encasing the pins of the feedthrough. This assembly is then mounted in a gravity-fed, slow-speed diamond saw and slowly cut over an hour. The resulting flat cross sectioned epoxy is interrupted by the now exposed pins of the feedthrough. This surface is then polished using silicon carbide sandpaper over the sequence of 1500, 2000, and 4000 grits. The feedthrough is then mounted into our thin film deposition magnetron sputtering machine where a 100nm layer of chromium is deposited over the epoxy encased pins and the prepared, polished surface. Photolithography is then done to pattern a 50um thick KMPR photoresist on this surface aligning the micro devices with the still visible pins on the prepared surface. This feedthrough is then placed into an electroplating bath and a 30um thick nickel plating is coated into the exposed areas in the photo resist making up the micro beams. At this point the feedthrough looked as it does in Figure 4.4.



**Figure 4.4: Feedthrough with sample mount epoxy sacrificial layer at process step before electroplating and after photolithography.**

The feedthrough was then placed in epoxy dissolver provided by Allied High Tech. The removal of the epoxy started off looking like it would be successful, with the thin chromium coating flaking off and leaving behind the thicker nickel MEMS (Figure 4.5a). However, after approximately 10 minutes the epoxy was visibly

swelled as seen in Figure 4.5b and after 15 minutes the nickel devices are physically pressed off of the surface as seen in Figure 4.5c.

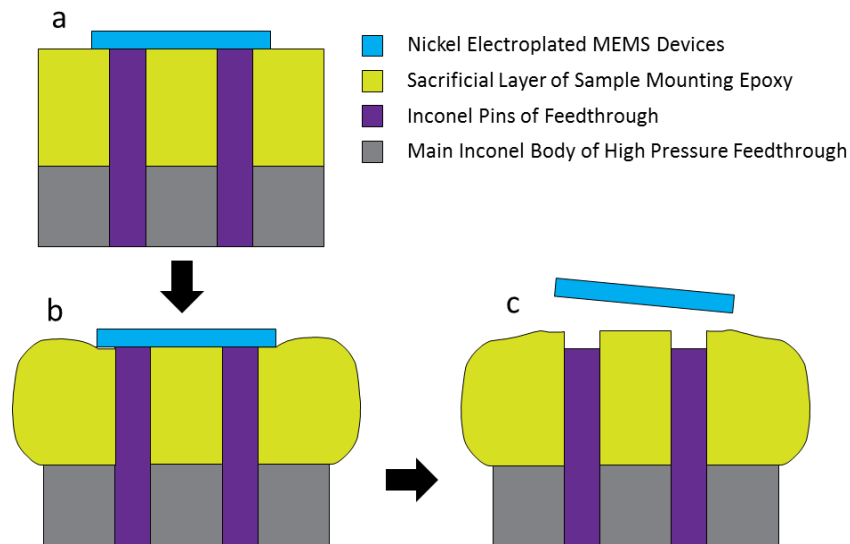


**Figure 4.5: Epoxy remover release issue:** a) shows the feedthrough with completed devices electroplated on the pins that is ready for release b) after the assembly is immersed into epoxy remover the epoxy starts to swell and this applies pressure on the electroplated devices c) the devices eventually pop off of the pins due to the swelling epoxy.

Finally the epoxy starts to decrepitate and fall apart but the devices are no longer attached to the pins of the feedthrough. This failure mode was found to be quite reproducible and at this point the sample mount epoxy was abandoned as a sacrificial support material for released MEMS Structures.

#### **4.2.2 Material 2: Crystal Bond**

Crystal Bond Adhesive from Pelco was tested as it is known to dissolve in acetone without any noticeable swelling and it technically does not melt until 120°C. The crystal bond was melted on a hot plate and the bubbles removed. It was then poured into the molds around the feedthrough pins in a similar fashion to the sample mount epoxy as shown in Figure 4.6.



**Figure 4.6:** Feedthrough with crystal bond melted into the space between the pins. The red plastic is a cup to hold the crystal bond in place as it cools and solidifies.

Upon cooling, it was found that the crystal bond was not hard enough to allow for effective cross sectioning of the feedthrough with a diamond saw. The crystal bond smeared instead of cutting leaving a very rough surface. It was also observed that at temperatures above 50°C the crystal bond is extremely soft and would not remain stable during lithography baking steps. At this point Crystal Bond was abandoned as a possible sacrificial layer.

#### **4.2.3 Material 3: Solder**

Tin based solder was identified as a possible sacrificial layer after the previous organic materials did not work. Molten metal casting is used in a large number of commercial products and is a good technique for rapidly fabricating parts with low requirements for dimensional precision. Often parts are cast first and then later machined to shape in areas that require high precision. Working with a molten metal instead of an epoxy required the use of a mild steel mold instead of the original plastic mold. The mold used is shown in Figure 4.7a. The feedthroughs are first pressed into the mold so that the tips of the pins are flush with the surface. Solder is then melted into the cavity, dripping from a height of 20cm. The added height results in a denser early distribution of solder around the pins of the feedthrough. Once the cavity is completely filled the assembly is inserted into a tube furnace and heated to 275°C under an argon atmosphere. Once at 275°C the atmosphere is cycled twice between atmospheric pressure and a rough vacuum to help remove trapped bubbles in the molten solder. The feedthrough is then cooled to 200°C and removed from the tube furnace while the solder is still molten. The feedthrough holder is tapped firmly on a surface to level the solder and allowed to cool quickly in air.

A vice and a die are used to push the feedthroughs out of the holder. The solid solder locks the feedthroughs into place and significant force is required to remove the feedthroughs from the mold. An image of the feedthrough with solder filling one end is shown in Figure 4.7b.



**Figure 4.7: a) Mild steel mold used to hold feedthroughs in place for molten solder to be poured over the pins. b) Feedthrough with a block of solid tin surrounding the pins with microfabricated devices on top.**

The feedthrough, now with solidified solder filling one side, is sectioned through the solder surrounded pins using a gravity fed slow speed diamond saw, as shown in Figure 4.8.

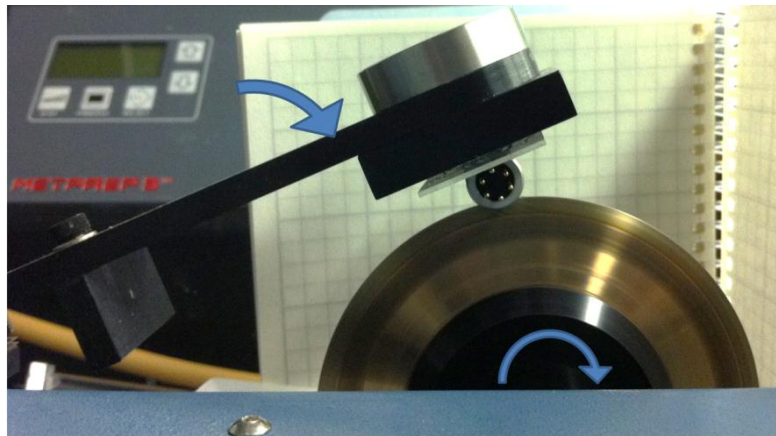


**Figure 4.8: Cutting step of preparing the feedthrough in a gravity fed slow speed diamond saw**

The cutting takes approximately one hour with the saw speed set to 6 and no counter weight. The remaining surface is quite smooth and requires only brief polishing using 2000 and 4000 grit silicon carbide paper before starting the lithography process. Photolithography is then done to pattern a 50 $\mu\text{m}$  thick KMPR photoresist on this surface aligning the micro devices with the still visible pins on the prepared surface. Next, the sides of the solder and feedthrough are masked off for the electroplating process using a thin layer of two-part epoxy. This feedthrough is then placed into an electroplating bath and a 30 $\mu\text{m}$  thick nickel plating is coated into the exposed areas in the photo resist making up the micro beams. At this point, the feedthrough looks similar to Figure 4.7b. The feedthrough is then placed into a bath of heated PG remover to remove the two part epoxy and the photo resist, giving the feedthrough (pictured in Figure 4.9a) with thick nickel devices on top of solder surrounded Inconel high pressure feedthrough pins. An SEM image of the electroplated nickel devices on top of the prepared solder surface is shown in Figure 4.9.

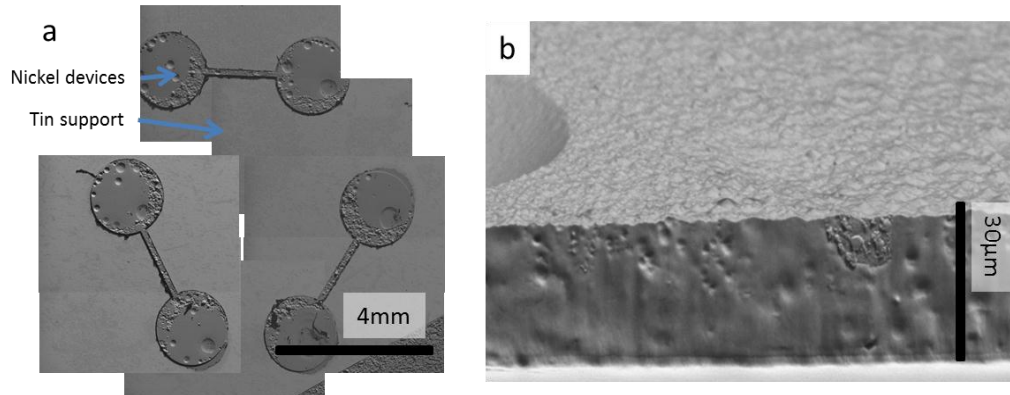


**Figure 4.9:** SEM images of the nickel electroplated structures on top of the prepared solder surface showing a) a top down view of the devices and b) a higher magnification at a high angle showing the thickness of the electroplated nickel.

The next step in the procedure is the removal of the sacrificial solder layer. This is done by submersing the feedthrough in a crucible of molten solder and letting it sit for 20 minutes to thermally equilibrate. Liquid solder has a high surface tension that makes it difficult to completely remove from the feedthrough since it clings inside of the space between the pins. This problem can be partially addressed by rapidly accelerating the feedthrough after removal from the liquid solder crucible. This physically removes most of the liquid solder leaving only a thin film of the solder remaining on the surface of the devices as seen in Figure 4.10a-b. At this point, the solder does not wet the nickel devices, but instead covers them with obvious air-gaps between the tin coating the nickel devices. In the bottom right of Figure 4.10b one of the nickel device pin contacts is not covered with tin after the phase change release. From the higher magnification image in Figure 4.10c one can see that there is a gap between the tin and the nickel and that the surface texture of the electroplated nickel, including electroplating pitting defects, is still intact. The tin did not wet the nickel surface making it quite easy to remove. Figure 4.10 d and e show the EDX maps of tin and nickel for the enlarged area shown in c. It is clear that the tin only coats the bottom and the beam structure in the image and that the nickel pad contains very little residual tin.

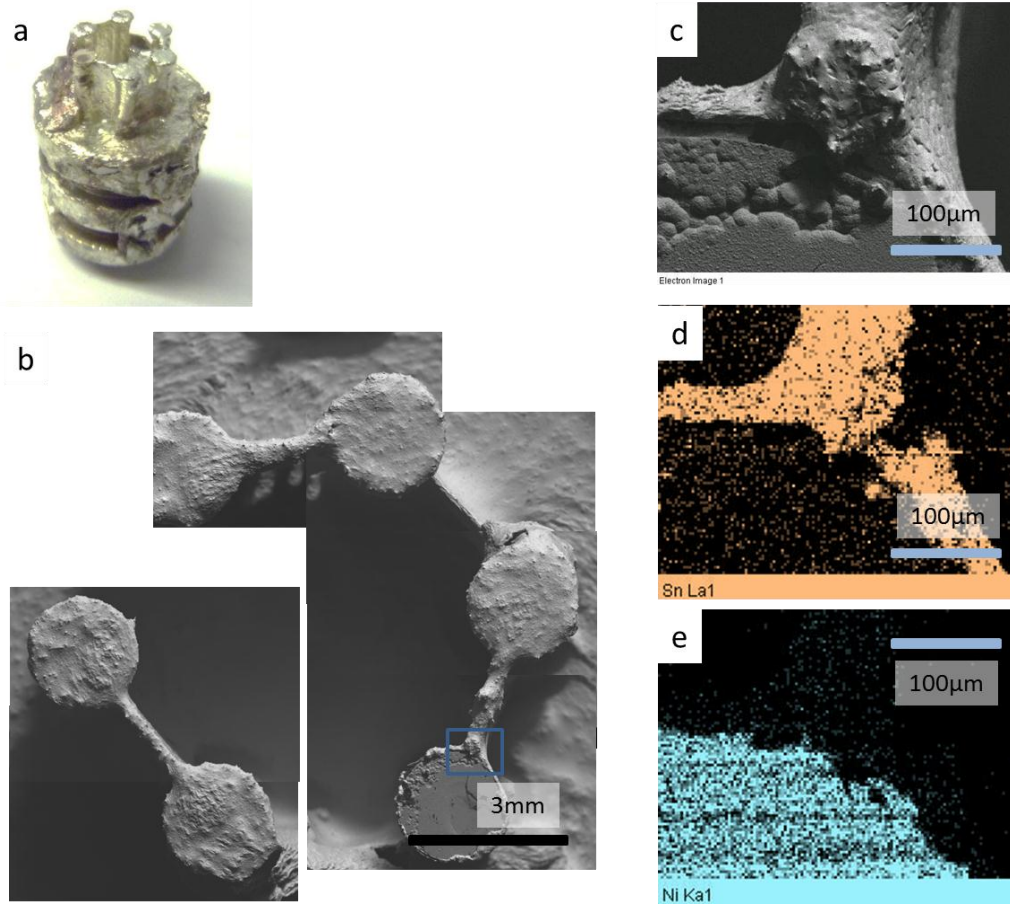


**Figure 4.10:** a) Photo of feedthrough after the majority of the solder has been removed. b) Top down SEM image of the devices coated with a thin layer of solder. c) Magnified section of b showing a section that is partially free from tin. d) EDAX map of tin in for the magnified area e) EDAX map of nickel for the magnified area.

The remaining thin tin coating is removed in the final step. Initially a chemical etch recipe that was reported (Haruta et al. [148]) to be highly selective for tin over nickel was tried. A 100mL solution was prepared with 10g Sodium M-nitrobenzenesulfonate, 10g glycolic acid, 1g sodium chloride, 40mL HNO<sub>3</sub> and water. The etch rapidly removed the tin coating in approximately 2 minutes, but immediately after the tin was removed from the beam structures, the nickel devices themselves were attacked. After 150 seconds, most of the nickel structures were removed and the devices appeared as pictured in Figure 4.11.

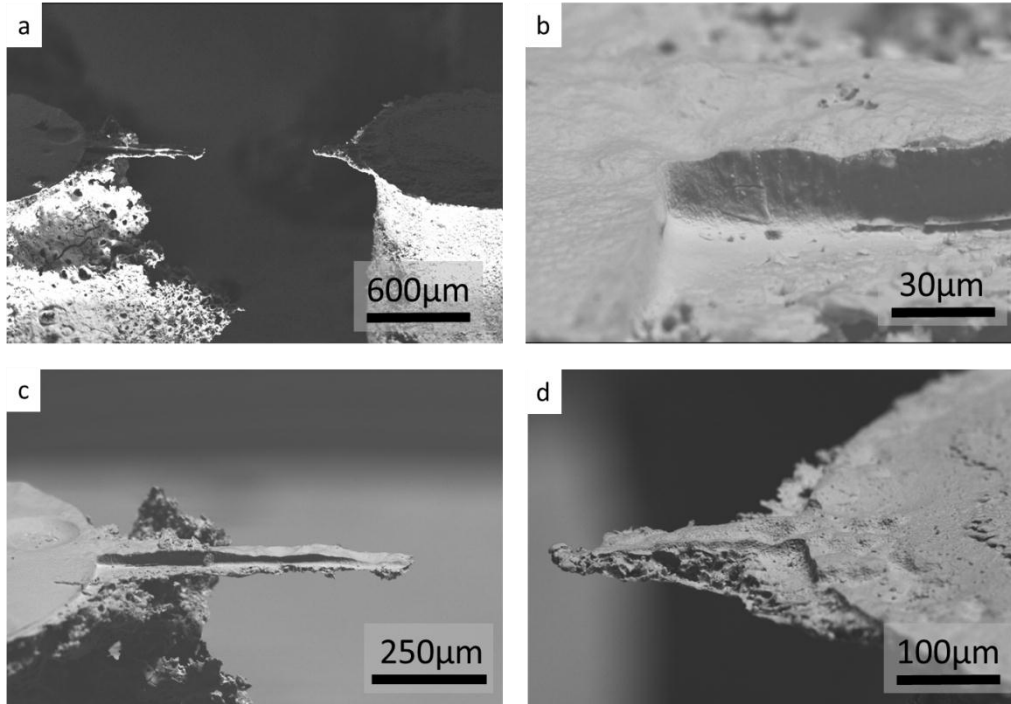


**Figure 4.11:** SEM Images of a nickel device fabricated onto a high pressure feedthrough after a failed etching attempt to remove the remaining tin coating the devices.

An exciting aspect of the images shown in Figure 4.11a,c,d is that after this etch there were partially dissolved beams that were still attached to the ends of the pins. These structures, although severely etched, were free standing and released. They resemble singly clamped “diving board” like cantilevers. The beam shown in Figure 4.11c is over 300µm long, 50µm wide and less than 20µm thick. It is not curved or curled as is common in released metal MEMS Structures[149]. This is a good indication that there is not a significant stress gradient throughout the thickness of the nickel devices. Accomplishing these released, cantilever-like structures was quite encouraging as it suggested that if the selective etching could be overcome, significantly high-aspect-ratio single-clamped beam devices could be fabricated.

#### **4.2.4 Selective Electrochemical Etching of Tin**

Sodium hydroxide was chosen as a potential candidate for selective etching of tin. Pure nickel tubing and containers are suggested for industrial applications involving sodium hydroxide. This was an early indicator that this etchant would work well as a possible selective etch. Ideally no nickel would be dissolved at all over the whole sacrificial layer removal step. Looking at the Pourbaix diagrams for nickel and tin shown in Figure 4.12, an area can be identified where tin corrodes freely while nickel passivates or is immune. This region is between 13 and 14pH over the potential range from -0.9V to 1.2V and is highlighted in green on the nickel diagram and red on the tin diagram. In acidic environments Nickel corrodes freely within the stability

region of water. This suggests that acidic etches might not be the best candidates for selectively removing tin.

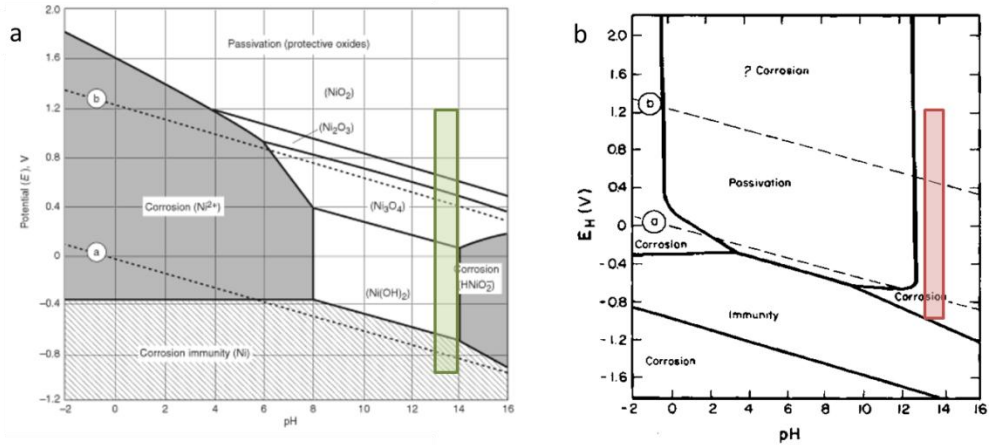


Figure 4.12: Pourbaix diagrams for nickel (a) and tin (b) in water[150].

Sodium hydroxide is known to attack tin at a rate of 0.24mm/year when the concentration is as low as 0.25%[151]. Choosing sodium hydroxide as the etchant, initial tests were conducted to check the etch rate of nickel and tin in concentrated solution. It was found that nickel showed no mass loss in an overnight test and tin was extremely slowly attacked. As etching in NaOH was too slow, anodic biasing was explored as a way to speed up the etching rate. This has already been shown to allow for rapid dissolution of tin in a NaOH environment to form nanostructures[152]. In Figure 4.13 the Cyclic Voltammetry (CV) and Linear Sweep Voltammetry (LSV) results of a pure tin electrode in 4M NaOH shows that tin rapidly dissolves in the potential region around -1.4V vs. Mercury Sulfate Electrode (MSE). In Figure 4.13b two peaks labeled E and H correspond with the formation of Sn(II) and Sn(IV) species, respectively. This plot shows that if you hold a tin electrode at a potential of -1.4V vs. MSE there will be a significant current related to the dissolution of tin.

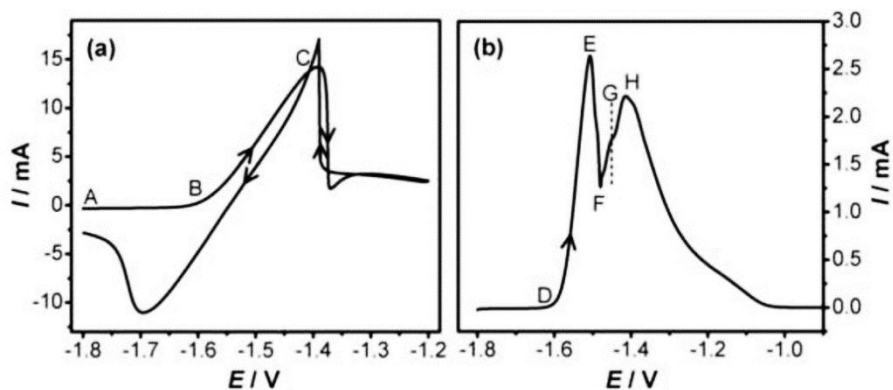


Figure 4.13: CV at 100mV/s and linear sweep voltammetry at 2mV/s for the Sn electrode in 4M NaOH. Potential is shown vs. MSE and the electrode is 2mm in diameter[152].

Yang et al. showed that when the potential is held at -1.44Volts vs MSE the current is high, but also oscillates between 9 and 0.5mA. These oscillations are due to the alternating formation and then dissolution of passive tin oxides and are shown in Figure 4.14.

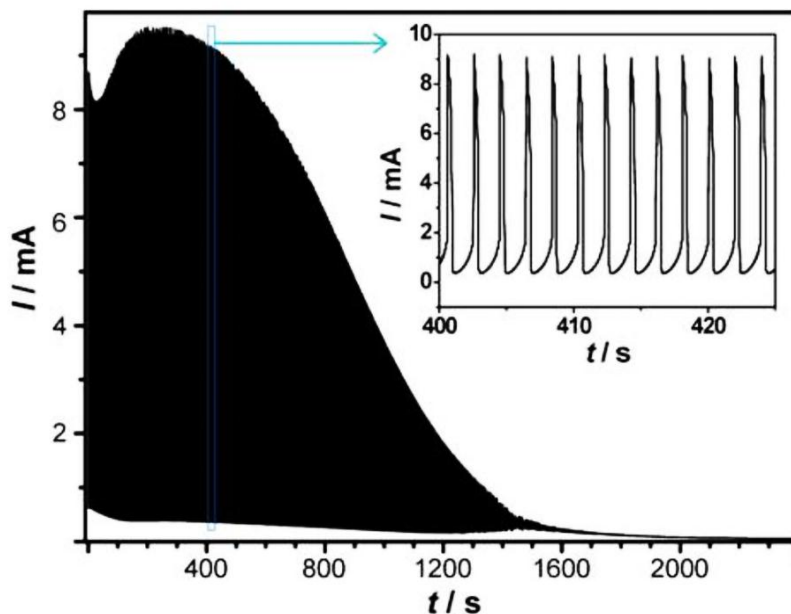


Figure 4.14: Shows the current response with time as the electrode is held at -1.44V vs. MSE for 2000 seconds in 4M NaOH solution. The transient behavior in a shorter time scale is shown as an inset. The electrode is 2mm in diameter[152].

While the current density seen in Yang et al.'s work reaches  $0.29A/cm^2$  (8mA with a 2mm diameter electrode at -1.44V vs. MSE) for the corrosion of tin in 4M sodium

hydroxide, nickel under similar conditions (2.5M and 1M sodium hydroxide) shows less than  $1\text{mA}/\text{cm}^2$  and  $0.1\text{mA}/\text{cm}^2$  current respectively at this potential[153, 154]. Figure 4.15 shows the baseline work of Krstajic et al. who conducted CV of a pure nickel electrode in 1M NaOH. It can be clearly seen that there is very little current in the voltage range between  $-1.3\text{V}$  and  $0\text{V}$  vs SCE; in this region nickel is quite stable in NaOH and undergoes little or no reaction. At above  $0\text{V}$  vs SCE a clear peak for the oxidation of the surface of nickel is visible at point c in Figure 4.15 and the reduction of this oxide at  $c'$ . Peak a is ascribed to the formation of  $\alpha\text{-Ni}(\text{OH})_2$  and peak  $a'$  results from the reduction of this hydroxide back to metallic Ni[153].

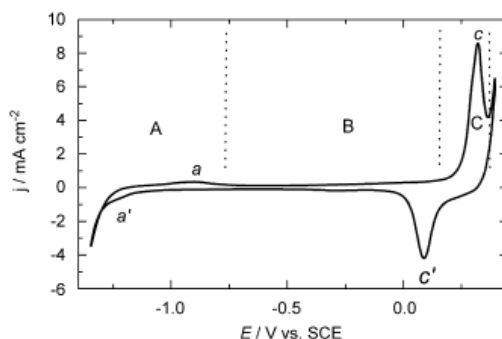
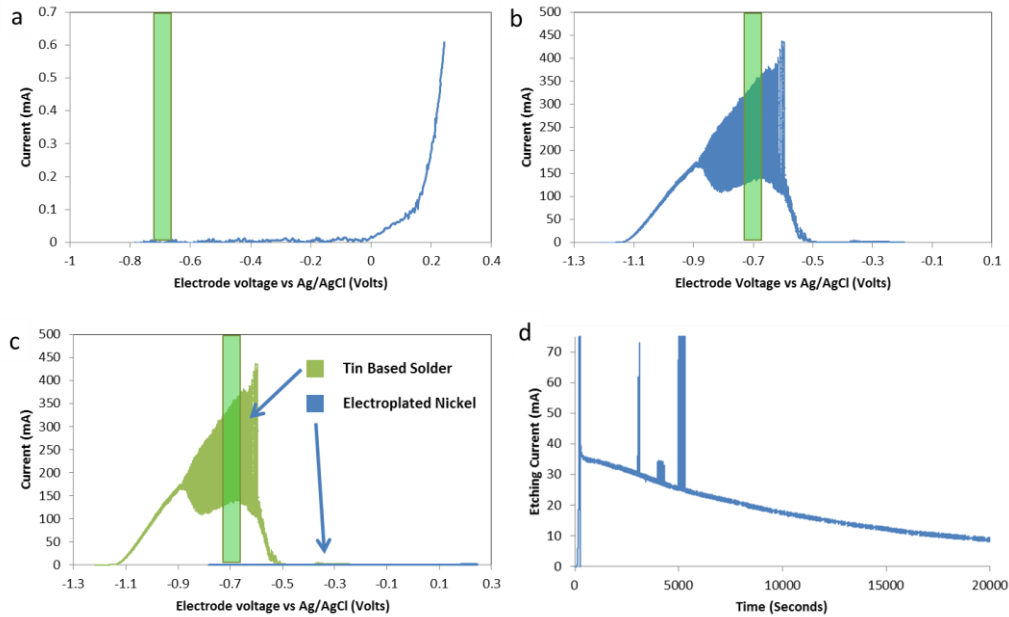


Figure 4.15: CV recorded at a sweep rate of  $10\text{mV}/\text{s}$  in  $1\text{M NaOH}$  at  $25^\circ\text{C}$  for a nickel mesh electrode[153].

In the region below  $-1\text{V}$  vs SCE hydrogen evolution starts to happen and this is accompanied by hydrogen absorption into the metallic nickel[153]. When cycling nickel devices in this potential range, hydrogen bubbles would form on the surface at  $-0.7\text{V}$  vs. SCE when doing an anodic sweep starting at  $-1.1\text{V}$  vs. SCE ( $-0.7\text{V}$  vs. SCE is well above the expected hydrogen evolution potential). This would be due to desorbing of absorbed hydrogen in the nickel. As a result of this effect Linear Sweep Voltammetry (LSV) results for nickel start at only slightly below the open circuit potential to limit hydrogen absorption into the nickel and the subsequent desorbing. Results of LSV in  $2\text{M NaOH}$  are shown in Figure 4.16a-c. Current remains quite small for a nickel electrode scanning from the open circuit voltage ( $-0.8\text{V}$  vs  $\text{Ag}/\text{AgCl}$ ) to  $0.2\text{V}$  in  $2\text{M NaOH}$  (Figure 4.16a). At  $0.2\text{V}$  the current starts to increase rapidly as a result of the oxidation of the nickel surface. In contrast to this low current for nickel, tin shows an extremely high current in the region between  $-1.1\text{V}$  and  $-0.5\text{V}$  vs.  $\text{Ag}/\text{AgCl}$ . The two distinct peaks seen at  $-0.9\text{V}$  and  $-0.65\text{V}$  can be ascribed to formation of  $\text{Sn}(\text{II})$  and  $\text{Sn}(\text{IV})$  species, respectively[152]. The two graphs are overlaid in Figure 4.16c showing the dramatic difference in corrosion currents for these two materials in  $2\text{M NaOH}$ . These results show that  $2\text{M NaOH}$  and an electrode potential of  $-0.7\text{V}$  vs  $\text{Ag}/\text{AgCl}$  will result in excellent selectivity for etching tin and not nickel. These conditions were used for the selective removal of the remaining tin on the high pressure feedthroughs, after the melting release, shown in Figure 4.10a.



**Figure 4.16:** Linear Sweep Voltammetry conducted in 2M NaOH all potentials reported vs Ag/AgCl reference electrode. A) shows a sweep from -0.8V to 0.2V for pure nickel. B) shows a sweep from -1.2V to -0.2V for tin based solder. C) Shows a and b plotted on the same scale showing the dramatically lower currents seen for nickel. Highlighted in all is the selected voltage region for selective electrochemical etching. D) The current drop during a long term electrochemical etch of tin based solder covered nickel devices.

A long term selective electrochemical etch was conducted on the high pressure feedthrough that contained nickel MEMS devices surrounded with a thin layer of tin based solder shown in Figure 4.10. The current over time recorded during this etch at -0.7V vs Ag/AgCl is shown in Figure 4.16d. This etch was completed after 20,000 seconds or approximately 5.5hours. At this point the high pressure feedthrough appeared as shown in Figure 4.17. Figure 4.17a and b show low magnification images of the high pressure feedthrough in SEM. It can be seen that the all three beams are fully released and only coated with a thin discontinuous and rough layer of tin with some copper. EDX analysis in Figure 4.17c,d,e shows that some areas are completely free of Tin and other areas still have some tin coverage. A separate copper map shown in green in Figure 4.17c confirms that some of the Cu in the solder is left behind in a porous and rough coating. Ultrasonic agitation conducted after these images were taken removed a significant amount of the rough tin coating seen in these images.

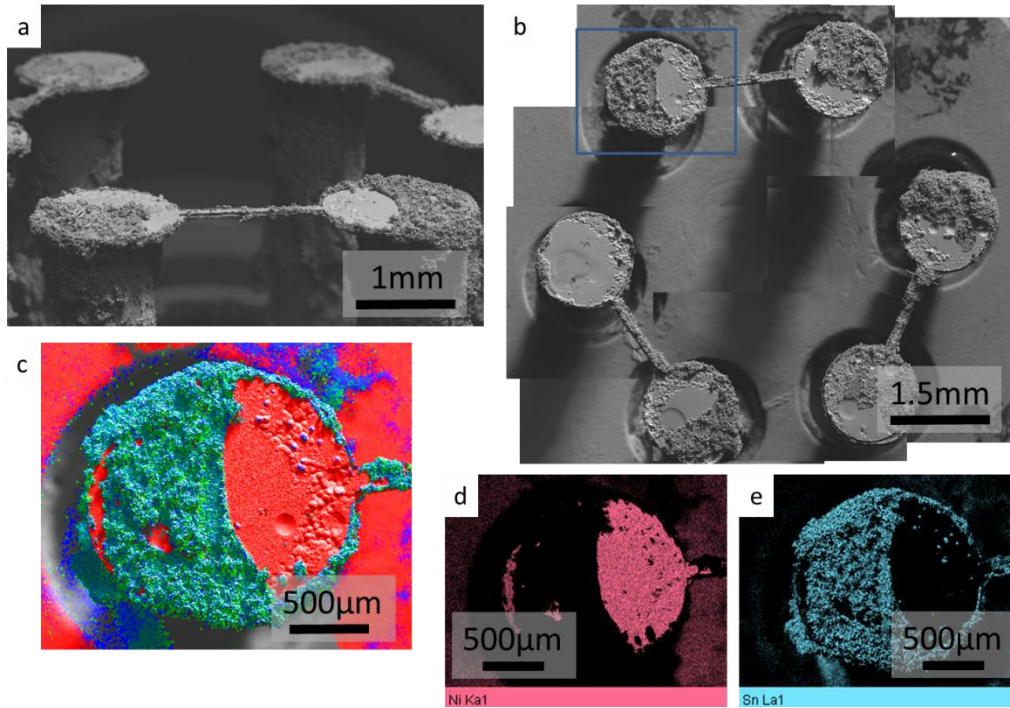


Figure 4.17: a) high angle SEM of feedthrough after 5.5hour etch b) top down view of same feedthrough c) combined EDX map of partially covered pin red is Ni, blue is Sn, green is Cu. d) EDX map for Ni e) EDX map for Sn

The second processed device was electrochemically etched for 24 hours in 2M NaOH at -0.7V vs Ag/AgCl and then ultrasonically cleaned immediately after removal from the etchant. This second device is pictured in Figure 4.18 and it is apparent that most of the tin coating is removed and the devices are completely clean.

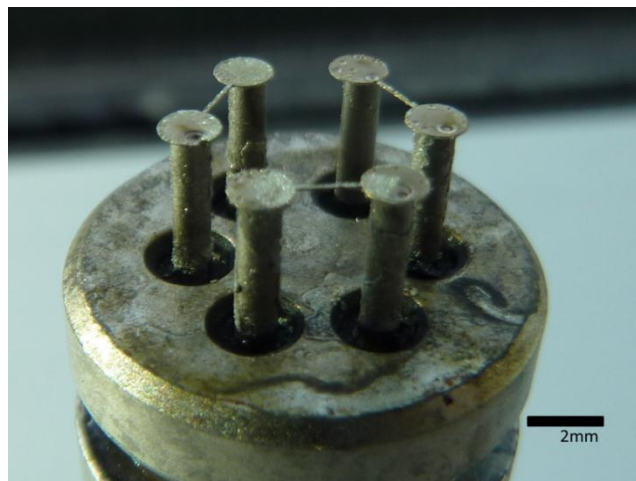


Figure 4.18: Photograph of a feedthrough etched overnight at -0.7V vs. Ag/AgCl in 2M NaOH until the current reached zero.

#### **4.2.5 Material 4: Indium**

Another candidate for a phase change release is Indium. It has not yet been tested, but seems to be a good candidate for a release material. Indium possesses the correct electrochemical properties for selective dissolution and melts at a low temperature of 156°C. Indium is amphoteric, dissolves in alkaline and acidic environments, and has a Pourbaix diagram similar to Tin but with a smaller potential range for the passive region[150]. Indium passivates in alkaline media such as NaOH and KOH and does not dissolve as rapidly as tin[155, 156]. However, in HClO<sub>4</sub> Indium dissolves rapidly via a one electron process and Nickel is not dissolved at this same potential[157, 158]. Further testing could be conducted in order to characterize Indium as a possible sacrificial layer.

#### **4.2.6 Material 5: Pressed Pure Tin**

During the etch of the solder, as shown in Figure 4.17, it was found that the trace elements led to an imperfect etch, and so pure tin was tested as a replacement for solder. The first technique tested involved filling the feedthrough pins with loose powder and heating under hydrogen to 400°C. This process did not work as the tin remained in powder form and did not form a continuous liquid phase. It is possible but not proven that the tin oxide around the powder tin particles prevented agglomeration during heating even under a pure hydrogen environment. While working with the tin powder, it was found that by pressing the powder at 35MPa using a pellet press it was possible to turn the dull gray powdered tin into shiny dense tin pellets. This process was then extrapolated for production on feedthroughs by attempting to directly press the powdered tin into a solid substrate on the feedthrough pins. Using the hydraulic press to compress the tin powder, a dense solid tin puck was formed around the pins of the feedthrough that could be cut and polished and would work for the fabrication steps. Unfortunately the melting behaviour of this puck was unpredictable when immersed in a molten tin bath. Often a portion of the puck would not melt completely and turn to a solid dark tin oxide containing mass that could not be melted and easily removed. This technique holds promise as it does not require a high temperature melting step for forming the tin sacrificial scaffolding for microfabrication. This process could be used to fabricate MEMS devices on plastic connector structures or pin arrays directly mounted on a circuit board if coupled with a purely electrochemical release step. Increasing the pressing pressure could potentially improve the tin melting behaviour but this was not further explored.

#### **4.2.7 Material 6: Melt Cast Pure Tin**

The final procedure that was decided on was to return to the use of molten tin being poured into the mold, similar to the solder method, but using pure molten tin, instead of “dirty” solder. This pure tin was created by melting pellets pressed from the pure tin powder (~100µm particle size), as the tin powder did not melt without

pressing due to oxidation. (It was later found that larger quantities of pure tin could be produced by reducing the tin powder at 800°C under hydrogen.) This pure tin was made molten by a hotplate at 450°C, and poured onto the feedthroughs in the mold, which was also heated to approximately 200°C (measured by the thermocouple in contact with the mold) by the same hotplate. If the feedthroughs and mold were not heated to 200°C the tin rapidly solidifies during pouring and large bubbles would be trapped in the pin area. When the mold was kept hot, the tin remained liquid during the pouring and a dense and bubble free block of tin was formed around the pins. This process was repeatable and consistent, resulting in a dense template of solid tin formed around the feedthrough pins.

The substrates prepared in this fashion worked by far the best during the release step as the tin did not appear to wet the Inconel pins or the nickel plated devices. This resulted in a very clean melt release step with only a very small quantity of tin remaining that needed to be electrochemically etched.

The final electrochemical etch worked very well to remove the remaining tin that was not removed by the melt release. Similar etching conditions were used as for the solder release layer, but the two substrates displayed significantly different etch currents. The solder, because there was significantly more remaining on the feedthrough, displayed higher currents, reaching as high as 400mA while the pure tin samples only showed etching currents below 40mA. The major difference between the pure tin and solder etching, was the fact that the current would oscillate significantly at higher currents for solder Figure 4.16d and not for pure tin. The complete etching of the remaining solder generally took approximately 24hours to lower to a current near 5mA and an additional 24 to 48 hours to reach zero. The etch was often stopped after the first 24hours and sonication was used to remove any remaining material, since this was believed to be mainly the trace elements and easily fell off with sonication. This behavior was not observed in the pure tin, where only small currents of approximately 20mA were observed with relatively stable curves (no pulsing to high current) and the tin remained shiny throughout the etch. This etch generally reached a complete (zero current) endpoint in less than a day, with the pins being extremely clean after etching and not requiring a sonication step to remove residue.

#### **4.2.8 Adhesion of metal devices to Inconel pins**

After fabricating several freestanding Nickel microdevices using the above procedure it was identified that the weakest point of the fabricated structures was the interface between the electroplated devices and the inconel pins. Almost every failure observed involved the nickel devices being physically removed from the inconel pins and in most cases the thin nickel beam remained intact. Because of this observation, several methods were explored to help improve the adhesion of the nickel microfabricated devices to the inconel pins.

#### **4.2.8.1 HF Etch**

The first technique that was attempted to improve the adhesion of the electroplated devices to the pins was the use of an HF etch prior to electroplating. It was designed to remove the passive chrome oxide layer that naturally forms on the surface of the Inconel pins, thus allowing plating directly onto the Inconel. It was performed directly before the substrate was immersed in the electroplating bath, so as to minimize the time for the passivation layer to reform. For this process, two different etch times were tested: a quick 2-3 second dip and a longer (approximately) 10 second soak. It was found that, while both times improved the adhesion, the short dip was more effective. One problem with this technique was that the inconel pins are attacked much more slowly than the surrounding Tin. If etching longer than 10 seconds was done, the tin was severely attacked and subsequent nickel plating results in very rough devices.

#### **4.2.8.2 Nickel Strike**

Another technique tried was the use of an Acid-Nickel Chloride strike, prior to electroplating in the Nickel Sulfamate solution. The choice of this technique was based on ASTM B558-79: Standard Practice for Preparation of Nickel Alloys for Electroplating[159], which specifies the standard treatment to use for Inconel 750, which the pins are made of. The plating solution used in this technique was comprised of 240g  $\text{NiCl}_2 \cdot 6\text{H}_2\text{O}$  and 31ml of 31.45 mass% HCl per 1L of solution. In this solution, the substrate underwent first an anodic treatment for 2 minutes at  $3\text{A}/\text{dm}^2$  and then a cathodic treatment for 6 minutes at the same current. These treatments were performed in the same bath at room temperature, with nickel being used as the counter electrode in both cases. Using these initial trial parameters, significantly rougher plated layers were observed with even worse adhesion. In an attempt to remedy the failure, slight variations on the time and current density of the strike were attempted, but little improvement was seen. Again the problem with this technique is that the tin material dissolves much faster and preferentially to the inconel and the anodic treatments result in a rapid dissolution of tin and little effect to the inconel pins.

Following a similar idea to the nickel strike, an anodic treatment in the standard nickel sulfamate bath was attempted. Again nickel was used as the counter electrode, and a short 5 second anodic treatment at  $3\text{mA}/\text{dm}^2$  was performed. This, like the strike, resulted in worse adhesion and yield than the previous procedure.

#### **4.2.8.3 Sputtered Adhesion Layers**

Since many of the techniques involving modification of the pins seemed to fail, a new approach was used where an adhesion layer was deposited by magnetron sputter deposition. Two different layers were tried: Ti-Ni and Cr-Cu. For all these layers, the basic procedure involved a secondary masking of the substrate using sharpie, followed by deposition, and then removal of the material on the sharpie mask by wiping in acetone.

#### **4.2.8.4 Titanium-Nickel**

The first layer combination attempted was a 10nm Ti adhesion layer, followed by a 100nm Ni seed layer. This combination was chosen because Ti is a known adhesion layer for oxide substrates, while the Ni base layer should readily adhere with the electro-deposited nickel devices. Electroplating was performed very shortly after the substrates were removed from vacuum, so as to minimize the time for a passivating oxide layer to form on the nickel; but even still this combination of metals proved ineffective as an adhesion layer. In fact, some of the layer even fell off while gently wiping with a q-tip to remove the sharpie mask.

#### **4.2.8.5 RF Back-Sputter**

For the next adhesion layers, as well as the sputtered devices (discussed later), a 50W RF back-sputter was performed on the substrate prior to film deposition. The goal of this additional step was to sputter off any passivation layers or other contaminants that may negatively affect adhesion. A variety of times were tried, ranging from 10 minutes to 1 hour, with the best results being found with shorter times. On the longer times, it was found that excessive sputtering from the substrate had occurred. Because the tin substrate has a low melting point and is softer than the Inconel pins, the tin was etched significantly more than the pins and was much rougher. This led to visible differences in surface roughness, which resulted in a poor transition, and thus poor adhesion, between the deposited metals on the pins and the tin. This effect was significantly less at shorter times (15minutes was found to be the best), and no problems with the transition between the pins and tin substrate were observed.

#### **4.2.8.6 Chrome-Copper**

The other layer combination tested to date was a 50nm Cr adhesion layer, followed by a 150nm Cu seed layer. This combination was chosen, like the Ti-Ni, because of the good adhesion of Cr and the ability to easily plate on Cu. This layer successfully survived removal of the sharpie mask, but failed when the melt release was performed. After submerging two different feedthroughs, only one beam successfully survived the release; one other pad did survive the release, but it readily flaked off when gently brushed. After failure, the deposited copper layer was clearly still visible on the pins, suggesting that it was the electro-deposited nickel that failed to adhere to the copper seed layer. This suggests that the choice of a chrome adhesion layer was successful, but that there is either a problem with the electro-deposition or a different seed layer is needed. In order to further test the failure of electro-deposition, devices deposited purely by sputtering were tested, and future tests are planned to investigate alternative seed layers with a chrome adhesion layer.

### **4.2.9 Sputtered Devices**

#### **4.2.9.1 Copper**

In an attempt to completely eliminate the electroplating step from the procedure, devices deposited solely by magnetron sputtering were attempted. The first devices

attempted were made using a 50nm Cr adhesion layer, followed by a 2 $\mu$ m Cu device layer. After removal of the photoresist, these devices looked quite good, although they clearly suffered from some discontinuities between the pin and surrounding pad due to excessive back-sputtering. When the melt release was performed, the beams were completely destroyed, but the copper layer was still visible on the end of the pins. This suggests that beams were destroyed by the melt release, likely due to accidental contact with either the bottom of the beaker or chunks of tin oxide that had not melted. This suggested that a better technique for the melt release may help, but because of the fragility of a 2 $\mu$ m beam, and the potential for copper dissolution in tin (copper was used primarily as a test) these devices were modified to 5 $\mu$ m Copper-Hafnium.

#### **4.2.9.2 Copper<sub>80</sub>-Hafnium<sub>20</sub>**

After the failure to release the thin copper beams, more robust devices were attempted. These devices were made from a 50nm Cr adhesion layer, followed by a 5 $\mu$ m Cu<sub>80</sub>Hf<sub>20</sub> metallic glass layer, and finally a 50nm Cr cap layer to improve corrosion resistance. Cu<sub>80</sub>Hf<sub>20</sub> is known to be an excellent candidate for the fabrication of freestanding MEMS Structures[96]. The results of our first tests with this process have yielded only one possible surviving device and multiple surviving contact pad structures; however, this failure is believed to be due to contact with tin oxide during the melt release. Future testing is planned with this composition using a larger, cleaner molten tin bath for the release in hopes that greater success can be achieved.

#### **4.2.10 Nickel Over-Plate**

One experiment was conducted with released beam structures involving a ~10 $\mu$ m thick over-plate that involved electroplating nickel onto the bare released structures. Figure 4.19 shows the resulting structure with the thin coating of nickel shown in green conformally coating the entire released structure. The beam structures were found to be much better attached to the inconel pins in this case. Unfortunately, the thicker released beam structures had a poor thermal response due to the released beams being significantly thicker and rougher as a result of the over-plate. The roughness was potentially due to the devices not being completely clean of residue as a result of the tin release. A future implementation with, cleaner beam structures, and a thinner over plate would improve the effectiveness of this technique. Also possible would be the use of epoxy to mask off the beam part of the structure and only electroplate on the pin/pad interface shown in Figure 4.19c.

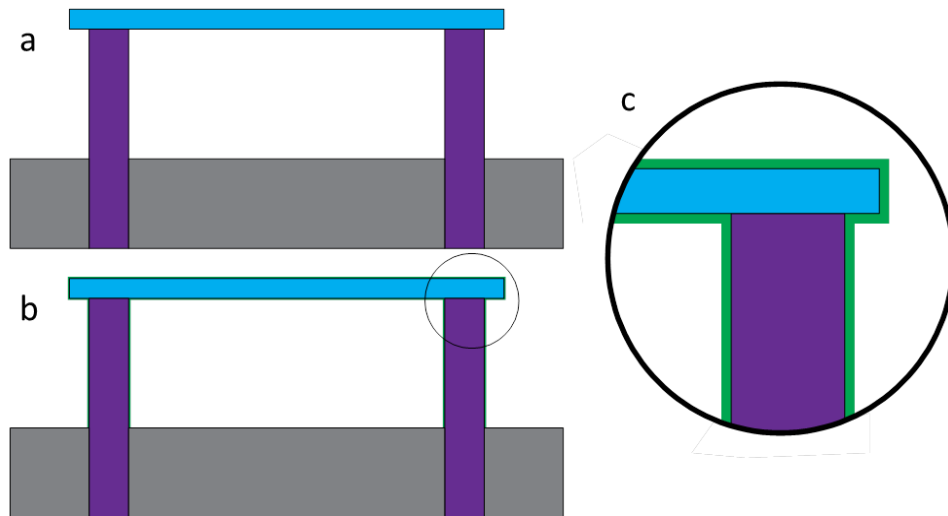


Figure 4.19: Diagram of the over-plating process. a) The devices after being released and cleaned showing in light blue the released beam and in purple the inconel pins. b) The same device but coated with a thin nickel over-plate (green). c) A magnified view showing the nickel over-plate attaching the beam structure to the Inconel pins.

### 4.3 Final Implementation

The finalized procedure is outlined in Figure 4.20. First the feedthrough is placed into a mild steel mold and heated to a temperature of 200°C. Molten tin is then poured into the top of the mold over the end of the feedthrough and around the feedthrough pins. The tin should stay liquid when in the mold to ensure that no bubbles are present in the melt. The feedthrough is then slowly cooled to allow the tin to solidify.(Figure 4.20b) The feedthrough is then pressed out of the mold using a die and vice and cut with a high speed diamond saw to reveal a flat surface with the feedthrough pins exposed and surrounded by tin. This surface is then polished to a P-4000 grade sandpaper.(Figure 4.20c) A thick photoresist is coated and patterned on the surface aligning the sensor pads to the inconel pins on the surface. (Figure 4.20d) The sides of the feedthrough are then masked with epoxy(Figure 4.20e), and nickel is electroplated into the photoresist mold. (Figure 4.20f) After electroplating is completed the photoresist and epoxy are removed in an acetone ultrasonic bath. This leaves a structure as shown in Figure 4.20g. This is then placed in a heated beaker filled with liquid tin and the tin support is melted away. The feedthrough is then rapidly lifted resulting in most of the tin being removed from the surface of the MEMS devices (Figure 4.20h). Finally the devices are immersed in a NaOH bath while electrically biased to -0.7 V vs. Ag/AgCl to remove the remaining tin surrounding the devices. A final ultrasonic bath after the electrochemical etching current reaches 0mA leaves clean and released MEMS devices suspended on inconel high pressure feedthrough pins as shown in Figure 4.20i.

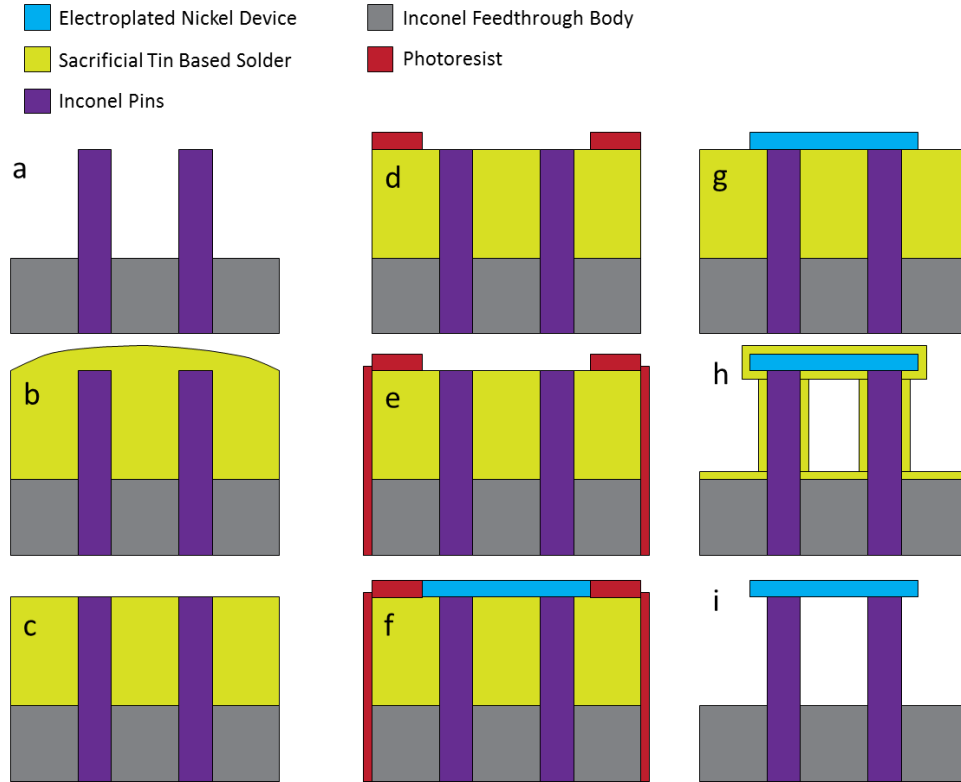


Figure 4.20: Finalized fabrication procedure for producing cm scale released Nickel MEMS structures.

#### 4.4 Conclusion

A final production procedure was developed for fabricating centimeter scale released metallic MEMS devices. Several potential sacrificial layers were investigated and a best candidate was found to be pure tin. An extremely selective electrochemical etching technique was developed to remove leftover tin material from the released nickel MEMS devices based upon a sodium hydroxide etching bath. Several techniques were tested for improving the adhesion of the nickel devices to inconel pins and further work is still required to improve this aspect of the finished devices. An over-plating method was shown to be quite effective at firmly anchoring fabricated devices to the pin structure. The finished implementation demonstrates the technique with three freestanding beam structures  $30\mu\text{m}$  thick,  $100\mu\text{m}$  wide and 2mm long. This is the first demonstration of microfabricated structures being released by approximately 1cm from a surface that does not use a bonding or transfer technique.

## 5 Results and Discussion: Sensor Testing for Oil Well Logging Applications

The motivation for fabricating these integrated sensor elements onto high pressure feedthroughs was to make a smaller oil well production logging tool capable of measuring multiple fluid properties at a single location in the wellbore. Current tools successfully measure multiple oil well fluid properties but at different locations in the well bore with each sensor only measuring a single parameter at a single location. The existing technology for detecting fluid properties to distinguish oil water and gas in a producing oil well has been established for nearly 25 years and has been focused on using a combination of dielectric constant measurement with differential pressure density. Techniques using optical and acoustic density are relatively new being developed in the last five years in order to address needs for fluid identification in highly deviated and horizontal wells.

In this work the capacitance method is used for distinguishing the difference between oil water and gas and also implemented is an additional technique for distinguishing these three phases based on thermal conductivity. The capacitance sensor will be covered in less detail because it is already established in the field for successfully detecting water cut in production logging. The thermal conductivity sensor will be covered more extensively as it has not yet been used in oil well logging equipment. Data gathered for thermal conductivity as well as for dielectric constant measurement will be discussed below in two sections.

### 5.1 Thermal Conductivity Sensor Characterization

The sensors fabricated in this work were entirely made from nickel and were 2000 $\mu\text{m}$  long, 50 $\mu\text{m}$  wide, and 20 $\mu\text{m}$  thick with an estimated thermal mass of 9.6 $\mu\text{J}/\text{K}$ . These sensors were electrically heated with a Keithley sourcemeter which applied a constant current and measured the voltage response.

#### 5.1.1 Materials Selection for Thermal Sensing

The reason that a metal beam structure can be used as both a heating element and a temperature sensor is due to the fact that the resistance of a metal increases as it is heated. This increase in resistance is often quite linear and can be described by equation 5.1 where  $T$  is the temperature in  $^{\circ}\text{C}$ ,  $\rho$  is the resistance in  $\Omega$  and the Temperature Coefficient of Resistance (TCR) is  $\alpha_0$  in  $^{\circ}\text{C}^{-1}$  and for a metal is defined as the slope of resistance vs temperature graph shown in equation 5.2.

$$\rho(T) = \rho_0[1 + \alpha_0(T - T_0)] \quad \text{Eq. 5.1}$$

where

$$\alpha_0 = \frac{1}{\rho_0} \left[ \frac{\delta \rho}{\delta T} \right]_{T=T_0} \quad \text{Eq. 5.2}$$

The higher the TCR of the material, the larger the change in resistance for a given change in temperature. Given an electrical circuit with limited resolution for measuring a resistance, a higher TCR will result in a temperature sensor with greater sensitivity. Table 5.1 outlines a number of different common pure materials that could be used as candidates for making a resistance based temperature sensor. For each material a TCR measured for the bulk material is listed as well as a TCR for a thin film of that material.

**Table 5.1: Temperature Coefficient of Resistance for several metals as bulk measurements and measurements of thin films deposited by sputtering and evaporation[160].**

<b>Metal</b>	<b>Bulk Metal TCR (0-100°C) x 10<sup>-4</sup></b>	<b>Thin Film TCR x 10<sup>-4</sup></b>
Au	34	28
Pt	39	25
Ir	40	18
Rh	46	20
Pd	37	23
Ni	64	50
Cr	30	6
Ti	54	7
Zr	44	<1
Mo	33	2
Ta	31	<1
W	48	<1
Al	43	28

As can be seen in the table the thin film TCR values are all lower than the expected bulk metal TCR values and that for a number of easily oxidized materials the TCR is extremely low. Of the materials listed in the table Nickel is the best candidate for a thin film sensor due to its high TCR value. It is also one of the materials that has a thin film TCR that is quite close to the expected bulk TCR value.

Another aspect that is important for building a thermal sensor from a metallic thin film is the material oxidation properties. Belser demonstrated that only platinum gold and iridium thin film samples could be held at 600°C in air without being damaged. Belser showed in Figure 5.1a that nickel thin films cycled in air significantly increased in resistance at temperatures above 250°C due to oxidation of the nickel. Their data showed that in the range from 20°C-200°C the resistance verses temperature graph showed a slightly curved and significant slope shown in Figure 5.1b. This behavior is excellent for a temperature sensor that does not need

to operate above 200°C[160]. Nickel is an excellent candidate for a resistance based temperature sensor as it has one of the highest TCRs of readily available metals, providing significant electrical signal with temperature change and does not significantly oxidize in air at temperatures below 200°C.

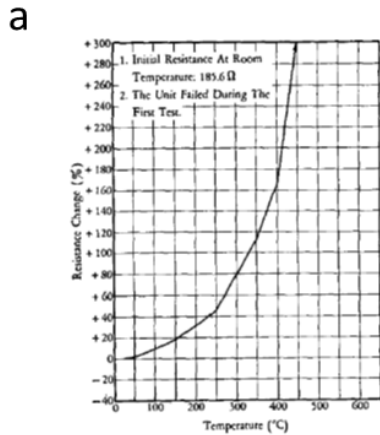


FIG. 5. Resistance-versus-temperature characteristics of a sputtered nickel film temperature cycled in air. Rapid resistance increase above 250°C denotes oxidation.

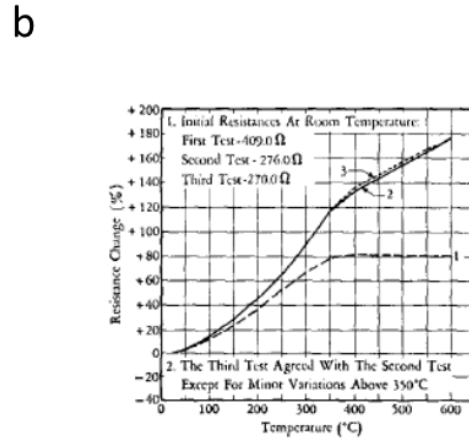
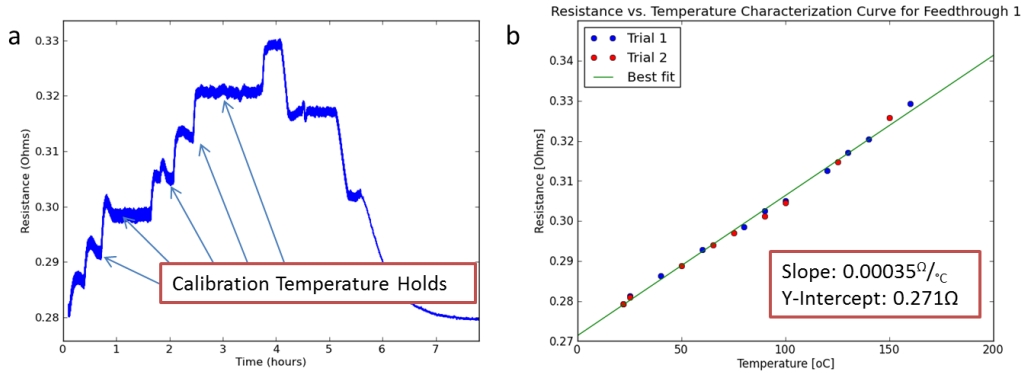


FIG. 6. Resistance-versus-temperature characteristics of a sputtered nickel film deposited on a hot (350°C) substrate, coated with silicon monoxide and temperature cycled in argon.

Figure 5.1: Resistance vs. temperature graphs for a sputtered nickel thin film cycled in air (a) and capped by SiO in argon (b)[160].

### 5.1.2 Thermal characterization of a fully released nickel beam structure

In order to find the relationship between temperature and the resistivity of the test beam a calibration was conducted where the sensor was held in a temperature controlled thermal bath and the resistivity of the wire was measured as the bath temperature was changed. The bath was heated in 20°C steps up to 180°C and then cooled in 20°C steps while the resistance was measured throughout. The calibration data showing the resistance with time is shown in Figure 5.2a and the resulting calibration curve for a beam is shown in Figure 5.2b. The slope of the temperature vs resistance curve is the measured TCR. The slope and intercept of the temperature calibration were  $3.5 \times 10^{-4} \Omega/K$  and  $0.271 \Omega$  respectively. These give a TCR for this feedthrough ( $\rho_0 = 0.271 \Omega$ ) of  $12.9 \times 10^{-4}/K$ , significantly different than the expected  $50-64 \times 10^{-4}/K$ . Possible explanations for a reduction in TCR for the microfabricated beam could include: Impact of contact resistance at the Inconel pin nickel pad interface, resistance of the inconel pins, resistance of the solder connections, and oxidation of the beam outer surface. The TCR is still easily measured using a source meter and results in an accurate sensor with little drift or hysteresis in the 20-200°C range. Heating and cooling results were perfectly in line and no hysteresis existed that would suggest that the feedthrough was oxidizing or annealing at the temperatures under test.



**Figure 5.2:** a) Resistance with time recorded for the feedthrough as the oil bath temperature was adjusted to 10 different set temperatures. b) Plot of two successive calibrations of the same beam of temperature vs. beam resistance.

Using the calibration between temperature and resistance of the beam the current through the beam can be adjusted to control its temperature. Additional current results in electrical heating of the beam and the resistance rises. By raising the current until a desired resistance (temperature) is reached the temperature of the beam can be precisely controlled. For the purpose of measuring thermal conductivity of the fluid in contact with the sensor a square wave of current was used with a high current pulse of 800mA and a low current pulse of 100mA. When the current through the beam was 800mA the beam quickly heated and the resistance was shown to rise. When the current was dropped to 100mA the beam cooled and the resistance dropped. A typical response in the resistivity of a beam when a square wave of current is applied is shown in Figure 5.3. The curvature and the amplitude of the change are useful in describing the thermal characteristics of the fluid in contact with the thin beam.

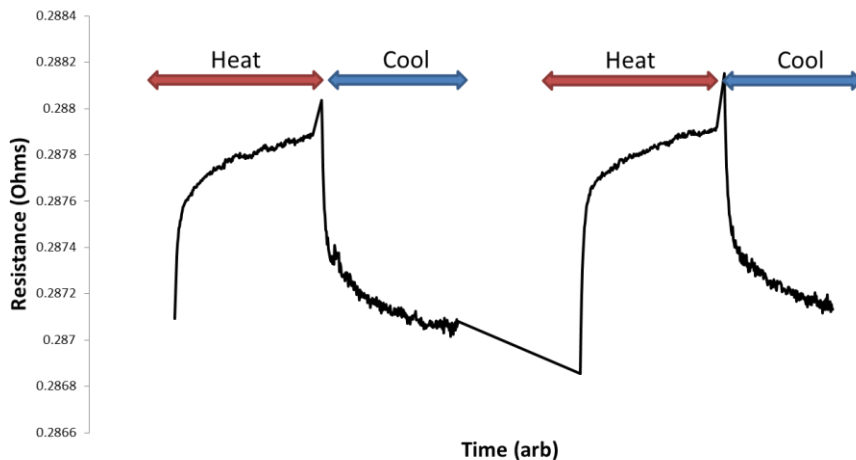


**Figure 5.3:** Resistance of a released beam vs. time as the current pulsed through the beam is pulsed to a high value then to a low value in a square wave pattern. High current corresponds to the heat section and low current corresponds to the cool section.

A computer controlled linear actuator was used to slowly move the sensor device between the three test fluids: Air, Water and Oil. The speed and distance travelled of the linear actuator can be controlled by a simple C# computer program. The speed of the stirring and the temperature of the liquids under test can be controlled using a heated stir plate. The linear actuator and the beaker filled with the three test fluids is shown in Figure 5.4a and b.

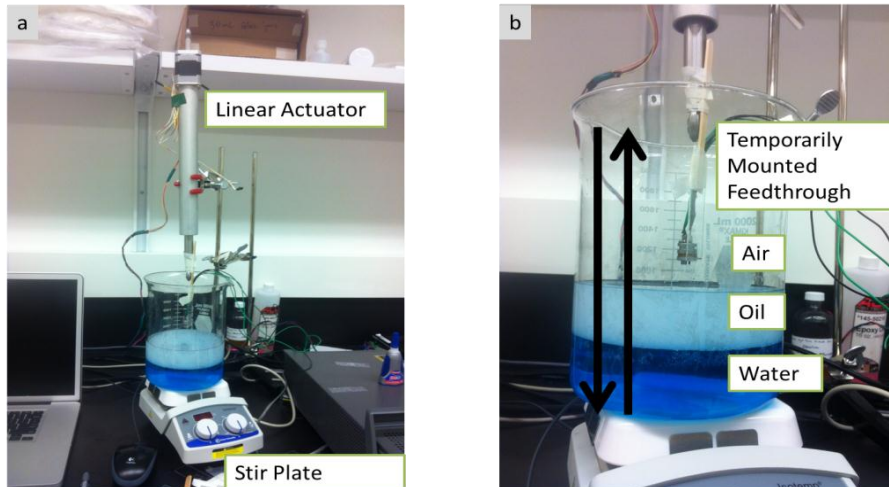


**Figure 5.4:** Photographs of the experimental setup to test transitions between air, oil and water. A computer controlled linear actuator sets the position and speed of the feedthrough and a hotplate controls the fluid flow and temperature.

A control program was created to interface with a Keithley 2611 source meter with a four wire electrical connection to the beam sensor. All electrical connections were soldered to ensure a low resistivity and reliable electrical connection to the beam. Figure 5.5 shows the raw data from the pulsed current beam as it travels from air to oil to water to oil and then back to air. The amplitude of the temperature change reduces significantly as the sensor is moved through the three liquids, with water more efficiently removing heat from the wire than oil or air. This measurement very clearly shows a difference between these three fluids.

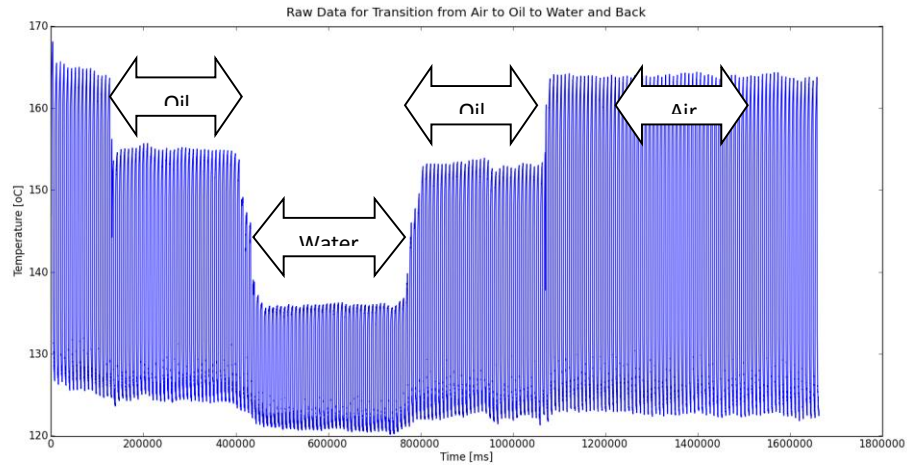


**Figure 5.5: Figure of beam temperature vs. time with a square wave current. The transition sequence is air, oil, water, oil, air.**

A simple algorithm was used to measure the amplitude of the temperature cycling that takes the last ten resistance measurements on a heating cycle and averages them and then takes the last ten resistance measurements on a cooling cycle and averages these. The difference between these two averages gives a temperature difference measurement that is shown in Figure 5.6. The green arrow shows the amplitude used to generate an amplitude difference graph shown in Figure 5.7. Figure 5.6 shows a typical transition from oil to water where the amplitude shown in orange is measured while the sensor is in oil and the amplitude shown in green is in water. The inset (Figure 5.6b) shows as a blue bar where the average is taken using the last 10 data points from the 100 points that are measured during a heating or cooling cycle. The cycle time used of approximately 0.5 seconds does not allow for the beam to equilibrate or reach a limiting temperature in the fluid. If the cycles were longer the amplitude of the heating and cooling waveform would be larger.

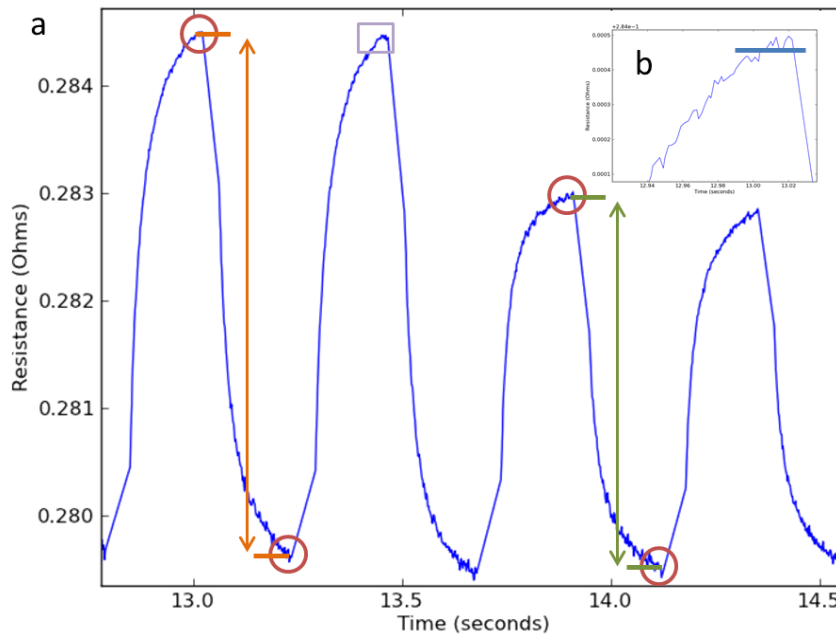


**Figure 5.6:** a) magnified section of an oil to water transition of the sensor. Resistance of the beam is plotted vs time as the beam is pulsed with a square wave current. The orange amplitude is in oil and the green amplitude is in water. Inset (b) shows the last 10 point in a cycle and a thick blue line denoting the value achieved when taking the average of the last ten acquired data points used in deriving the temperature amplitude.

This temperature swing shows a very clear distinction between air, oil, and water. An exciting aspect of this measurement is that the sensor responds quickly to a change in environment and does not show a significant lag as it is moved between the three fluids. This lag was further explored by varying the speed the sensor was moved through the three fluids by the linear actuator.

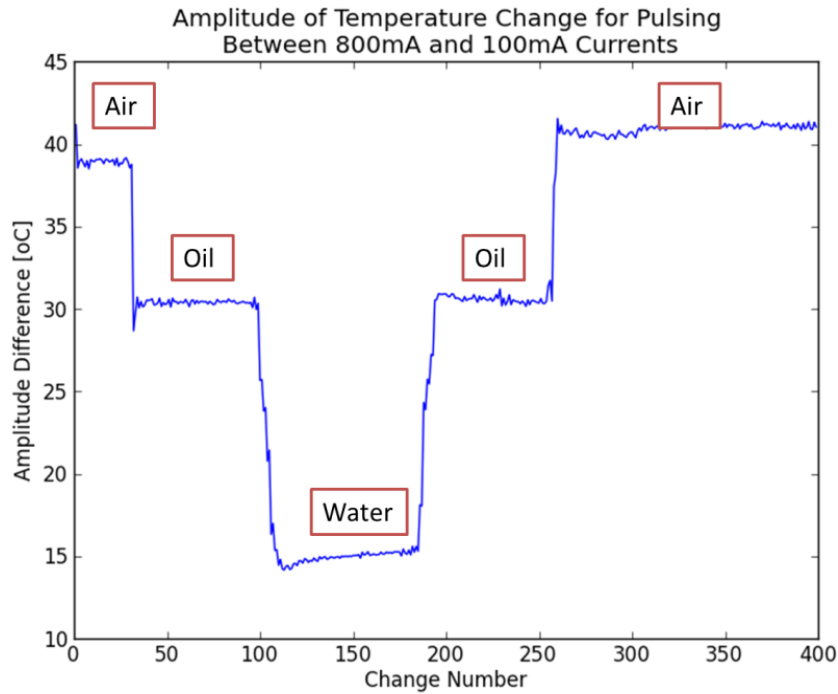
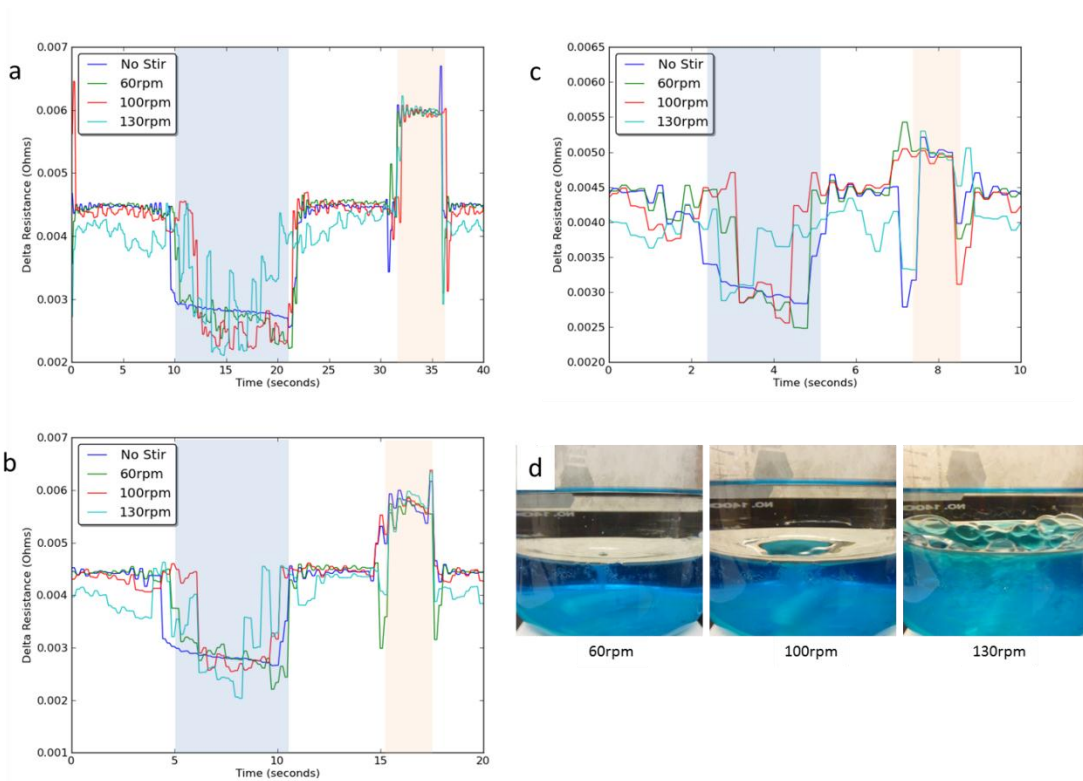


Figure 5.7: The calculated amplitude vs cycle number from the data in figure 5.5. The amplitude changes significantly for the three fluids tested.

In the above test the sensor was moved very slowly (1mm/s) through the three different media spending approximately a full minute in each medium. This allowed for multiple data points to be gathered as the sensor punctured through from one media to the next. It was clearly visible during the testing that surface tension at the interfaces resulted in the sensor pushing this interface slightly as it moved through. Especially on the oil/water transitions it can be seen that multiple cycles are included in this transition time and result in intermediate amplitude readings while the beam is held in this interface region. Figure 5.8 shows the results retrieved at significantly higher movement speeds for the sensor. Figure 5.8a,b,c show the sensor moving at speeds of 3,6,12mm/sec respectively. Four lines are shown where the test fluid is stirred at four different speeds. The separated structure of the oil sitting on top of the water was maintained at stirring speeds of 60 and 100rpm. At 130 rpm the interface between the water and oil started to mix and large bubbles were apparent at the surface of the water. This behavior can be seen in the photographs seen in Figure 5.8d. At the sensor movement speed of 3mm/second the three different fluids are very easy to observe on the delta resistance graph. At the highest stir speed there is some noise in the water oil transition that could be caused by the passing of larger bubbles of oil suspended in the water. And in the oil region there is some indication of water passing by the beam. At the faster speed of 6mm/second the distinction between the three phases is not as clear especially when the fluid is being stirred at 130 rpm, although all three phases are still quite distinct in the graph. At the speed of 12mm/second there is significant noise and

only a couple of instrument cycles between hot and cold happen in each fluid. Here the data looks moderately clear in an unstirred solution but becomes much less clear in the stirred cases.



**Figure 5.8:** a) amplitude vs time for the sensor as it moves through the fluids at 3mm/sec. Three stirring speeds and still fluid are plotted. b,c) same plot at a speed of 6mm/sec and 12mm/sec respectively. d) photograph of the fluid stack at each of the three stirring speeds.

This set of tests gives some understanding of the response time of the sensor. It takes approximately 2 seconds for the sensor to register a transition, and if the fluid transition is for duration of less than this time limit than the transition is not evident. In this case phase transitions could be observed if the residence time of the fluid is longer than 2-3 seconds. When conducting production logging in a real oil well, logging speeds range from 0-200ft/min and fluid speeds range up to 600ft/min. The sensor with a 2 second response time should have approximately a 6 ft spatial resolution with fluid speeds of 200ft/min. When the sensor was moving at 3mm/second the stirring speed did not seem to have a significant effect on the response time of the sensor.

### 5.1.3 Thermal characterization of an anchored nickel beam structure

This same test was conducted with a beam that was not released but anchored to the feedthrough surface as discussed in chapter 3. Because this wire was attached to the glass substrate heat loss becomes a combination of loss to the support and to the test fluid. The signal to noise ratio of the sensor was still good and the sensor

was able to distinguish between phases quite well. An interesting effect occurred with this sensor as shown in Figure 5.9 where the sensor was cycled through air, oil, water, oil, and then air three times. The water sections did not show clearly for two of the three cycles. The interface between the two phases shows up as a “ringing” of the signal but the amplitude difference did not significantly change between oil and water. This was caused by the surface of the sensor maintaining a thin coating of oil while traveling through the water. In the third cycle this oil layer was broken and water was able to come in contact with the beam structure and a clear change in the thermal response was visible. High flow past the sensor surface would help alleviate this problem of surface masking. It is well known for large capacitance tools used in oil well logging that high flow rates are required for accurate capacitance measurements due to surface wetting effects on the sensor[1].

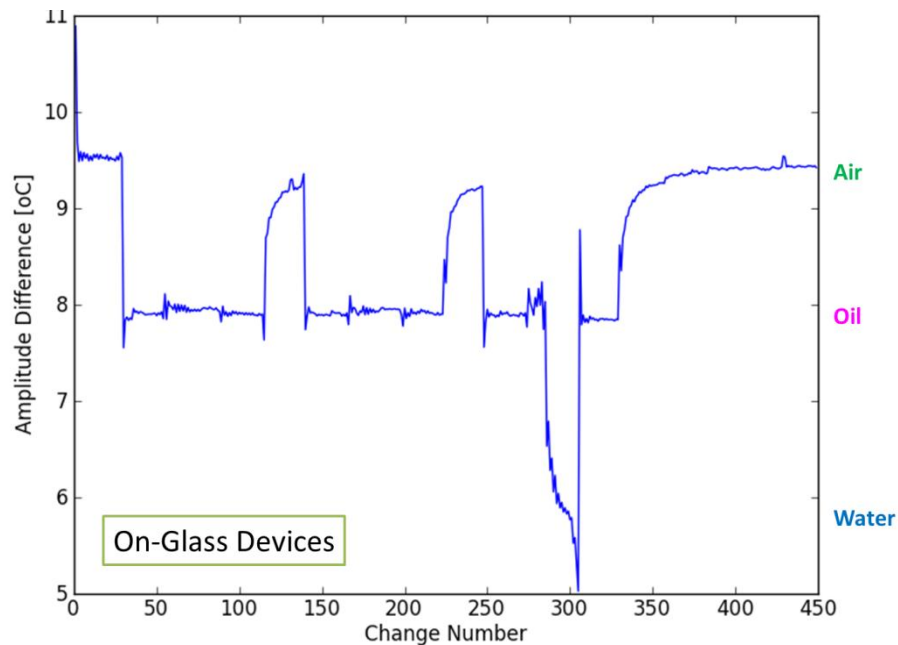


Figure 5.9: Temperature amplitude vs cycle number for three transitions from air to oil to water to oil to air for an anchored nickel beam. On the last transition water was detected as the oil film on the sensor surface broke.

#### 5.1.4 Thermal Conductivity Measurement with Miscible fluids

After showing a clear distinction between water, oil and air, a further exploration of fluid mixtures was undertaken. The first step taken was to take two liquids with significantly different heat capacities and thermal conductivities (water and IPA) and prepare several different mixtures of the two. When in pure IPA the temperature swing seen was approximately 12°C and when in pure water the temperature swing seen was approximately 6°C. The results of conducting this experiment three times with the same beam are shown in Figure 5.10. The three trials agreed nicely with one another all showing a gradual increase in the temperature delta as the IPA concentration increased. The shaded area in the graph approximates the error in

the measurement and suggests that using this technique the concentration of the IPA/water can be determined with an error of  $\sim \pm 5\%$  measured as the width of 2 standard deviation range shown in Figure 5.10.

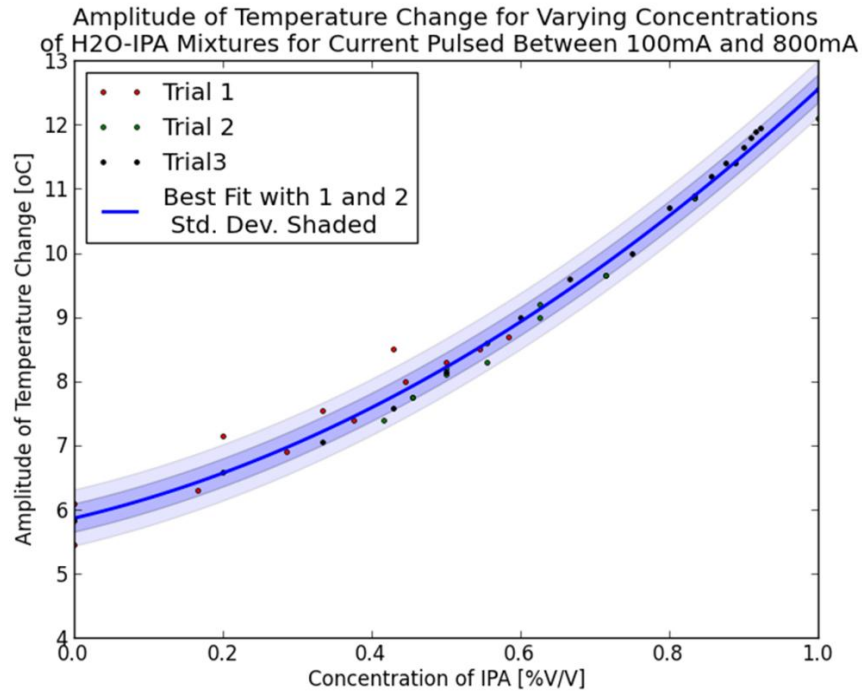


Figure 5.10: Amplitude of heating and cooling waveform in several different mixtures of IPA and Water tested in three separate trials plotted on the same figure.

**IPA**

Density: 0.786 g/cm<sup>3</sup>  
 Viscosity: 1.96cP at 25°C  
 Heat Capacity: 2.68 J/gK at 20-25°C  
 Thermal conductivity: 0.14W/mK

**Water**

Density: 1g/cm<sup>3</sup>  
 Viscosity: 0.89cP at 25°C  
 Heat Capacity: 4.18 J/gK at 25°C  
 Thermal conductivity: 0.6W/mK

**Mineral Oil**

Density: 0.8g/cm<sup>3</sup>  
 Viscosity: 22cP at 25°C  
 Heat Capacity: 1.67J/gK at 25°C  
 Thermal conductivity: 0.126W/mK

### 5.1.5 Thermal Conductivity Measurement with emulsion stabilization

A sequence of emulsions of oil and water were prepared using oil, triton surfactant, water and urea. These emulsions would remain stable for over 30 seconds after being mixed and allowed for a thermal measurement to be taken with the sensor. The variation in the measurements is believed to be more a function of the stability of the emulsion than the stability of the measuring technique. The data from testing the amplitude of the pulse heated wire are shown in Figure 5.11. The data has significantly more spread than what was observed using the IPA/Water mixtures but shows a similar trend with the amplitude of the thermal cycling increasing as more oil is present in the emulsion. In an oil well it is expected that water and oil would be present simultaneously and would be well mixed in a high flow rate well. The ratio of oil to water could potentially be determined with this technique.

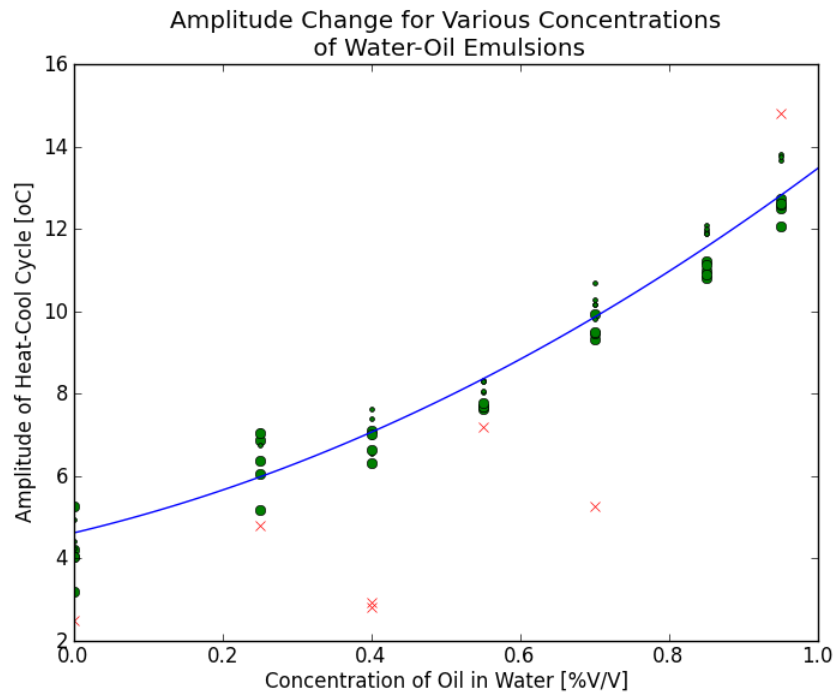


Figure 5.11: Amplitude of heating and cooling waveform in eight different mixtures of partially stabilized emulsions of oil and water. The red x symbols are data points that were removed from the best fit calculation according to Chauvenet's Criterion.

The effect of heat capacity and thermal conductivity on the response of a current square wave pulse heated sensor was characterized by Ernst et al. The device that they used incorporated a germanium thermistor for sensing the temperature and a chromium wire as a heating element. These two devices were incorporated in close proximity on a silicon nitride membrane. They showed that there is a non-linear relationship between the amplitude of the thermal response waveform and the thermal conductivity of the fluid. They tested six different known fluids and

measured the response amplitude and time constant in each. They found that the response amplitude for their sensor followed a relationship of  $\text{Amplitude} = 3.8896 * \lambda^{0.6438}$ , [23] where  $\lambda$  is the thermal conductivity. Using this relationship they were able to calculate the thermal conductivity of fluids given their thermal response. They claimed that their thermal sensor had a resolution of  $2 \times 10^{-6} \text{W/Km}$  for thermal conductivity and a resolution of around  $1 \times 10^{-3} \text{J/KgK}$  for specific heat capacity.

An extensive characterization of the effect of frequency of pulsing, pulse duty cycle and the effect of wire thickness on the thermal response of a pulse heated wire was conducted by Al-Salaymeh et al for application in flow measurement. They fabricated a flow meter based upon a suspended  $12.5 \mu\text{m}$  diameter and 5mm long platinum wire. They used a pulse excitation instead of the traditional constant temperature hot wire anemometer method for measuring flow. They showed that the excitation frequency of the heated wire should be tuned to match the diameter of the sensing wire showing that 100Hz should be used for extremely thin wires about  $5 \mu\text{m}$  in diameter and 6.7Hz should be used for thicker wires with a diameter of  $25 \mu\text{m}$ . This wide range in frequency response for a change in wire diameter of only  $20 \mu\text{m}$  highlights the need for a small wire to achieve a fast sensor response using thermal techniques[27].

#### **5.1.6 Effect of current and duty cycle time on heating and cooling behavior**

The optimal heating and cooling parameters for a thin beam in air were found using a matrix of testing conditions. A number of currents for both the heating and cooling steps and different pulse durations were tested. Low current testing points included 1,10,20,50,100mA; high current testing points included 200,350,500,650,800mA, and three durations included 2,4,10seconds. All combinations of these currents and pulse times can be seen in Figure 5.12b. In Figure 5.12e and f, a magnified section of the last sequence of steps is shown where the three pulse durations can be clearly seen. The resulting data gave significant insight into the behavior of both the test equipment and the thin test beam. When currents less than 20mA are used during the cooling step the voltage across the  $\sim 0.3 \Omega$  beam is expected to be less than 6mV. At this low voltage the source meter shifts measurement ranges and does not give results for resistance that make sense during the cooling section of the current pulse. This is the reason for the resistance measurements that are clipped off in the first two sequences of steps shown in Figure 5.12 c and d. Using cooling currents of 50mA and 100mA gave the clearest results, clearly showing the curvature of the cooling curve high resolution data over the duration. When the heating current used is higher, the temperature swing of the beam is higher and gives a larger resistance change. This change is more easily measured by an electronic analog to digital converter.

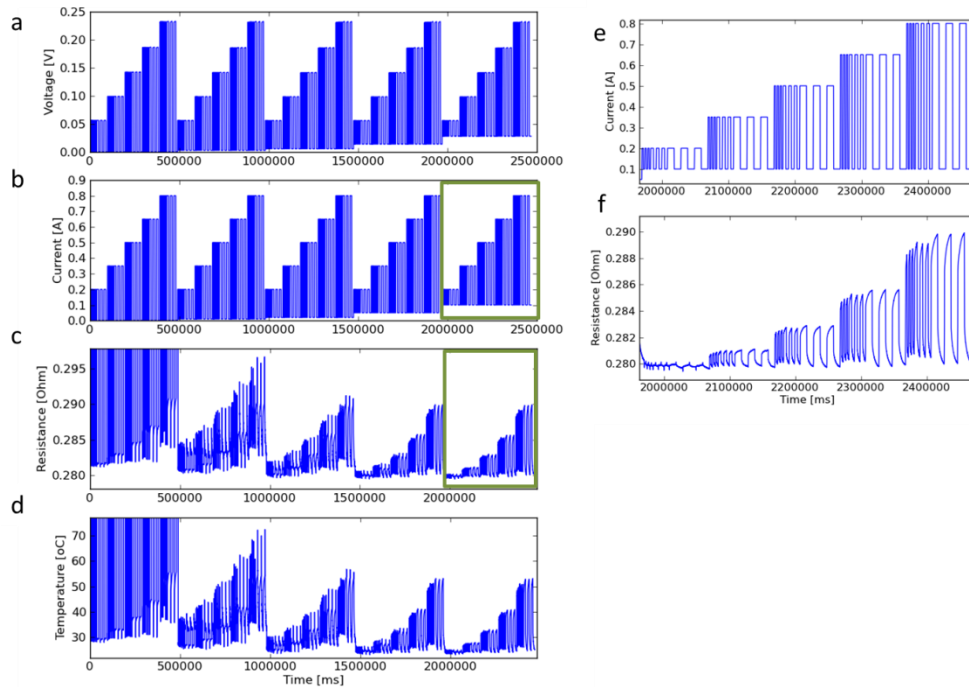


**Figure 5.12:** Test data from a released nickel beam tested in a matrix of five different high currents, five different low currents, and three different pulsing times. a) Measured voltage vs time. b) Set current vs time. c) Measured resistance vs time. d) Calibrated temperature vs. time. E) Magnified section of current vs. time (b). f) Magnified section of resistance vs. time (c) measurements with the lowest currents resulted in source meter giving incorrect resistance measurements resulting in off scale measurements for resistance and temperature in some plots.

Good clean data was available using heating and cooling currents that were above 350mA and 50mA respectively. An overlay of the heating and cooling curves using 800mA and 100mA are shown in Figure 5.13a,b. In this example a very clear increase in temperature is visible during the heating pulse. The shape of the heating temperature response is similar for the three different durations with the longer duration heating curve seeming to approach a limit where the temperature change with time is very small. When a heating time of 2 seconds is used it is clear that the beam is still increasing in temperature at the end of the pulse. In Figure 5.13 c,d an example at the lower currents of 350mA heating and 50mA cooling is shown. In this case the smaller temperature swing observed resulted in a smaller measured voltage signal and the noise in the measurement instrument is visible. During the 10 second duration heating cycle it appears that the beam is in fact reaching a steady state temperature, longer cycle times would have the same voltage response amplitude.

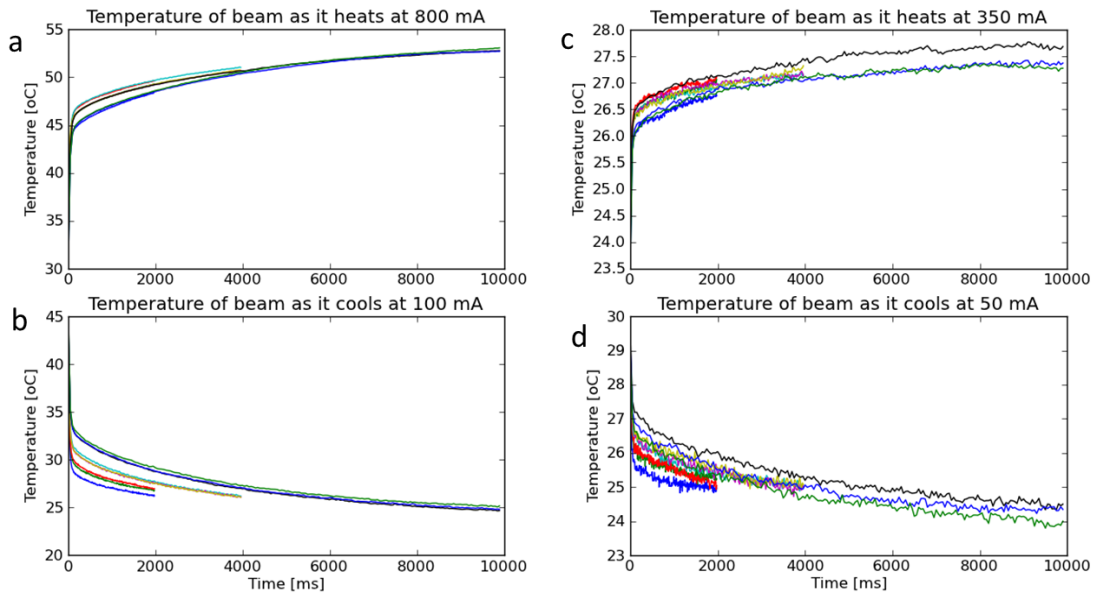


**Figure 5.13: Response overlays of wire at different currents. a) heating at 800mA after cooling at 100mA. b) Cooling at 100mA after Heating at 800mA. c) heating at 350mA after cooling at 50mA and d) Cooling at 50mA after heating at 350mA.**

As the frequency is increased the amplitude of the temperature swing starts to decrease until the heating frequency is significantly faster than the thermal constant of the beam and no fluctuation in the beam temperature happens between the on and off cycles. Some of this effect is shown in Figure 5.14a and in Figure 5.14 b where it is clear that the amplitude of the temperature response is less for the higher frequency pulsing.

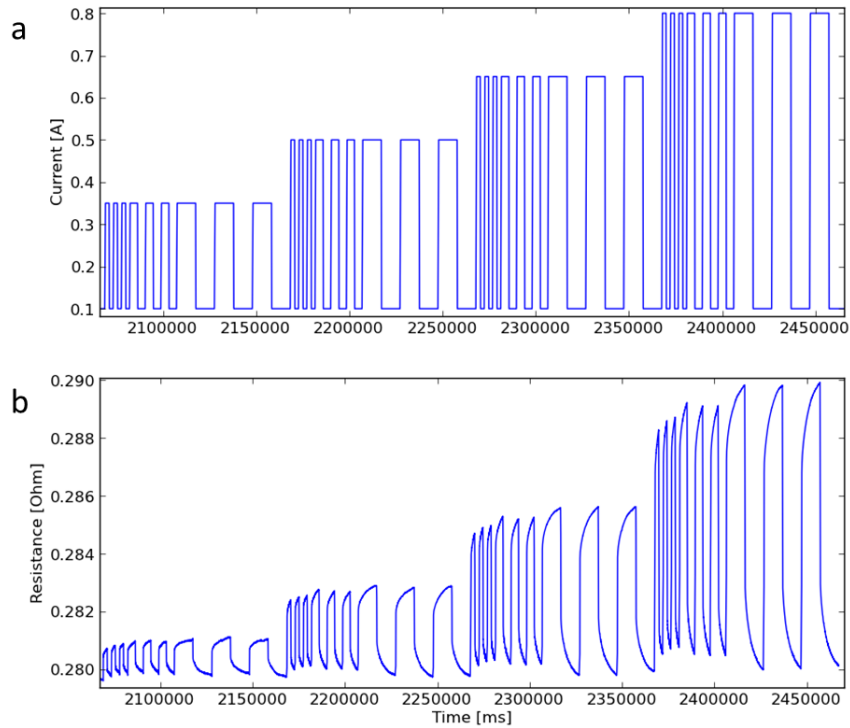


**Figure 5.14: a) pulsing current current used to heat and cool a released nickel beam structure. b) the response of that beam resistance to the stimulus current.**

Plotting amplitude of the waveform vs pulsing frequency gives a graph as shown by Ernst et al. and clearly shows the frequency thermal response of the sensor[23]. Ernst showed that this response can be modified by different fluids with different thermal conductivities and multiple thin layers of fluids above the sensor[161]. This technique was used to characterize the thermal response of the two sensors developed in this work and an additional wire wrapped sensor for comparison to a non-microfabricated device. The pulsing frequency was gradually changed from 20ms per heat/cool cycle to 100 seconds per heat/cool cycle and multiple cycles were obtained at each chosen frequency. The resulting response of the freestanding device in air, oil, and water is shown in Figure 5.15. It is clearly visible that the amplitude of the heating and cooling waveform increases as the frequency of pulsing decreases for each fluid.

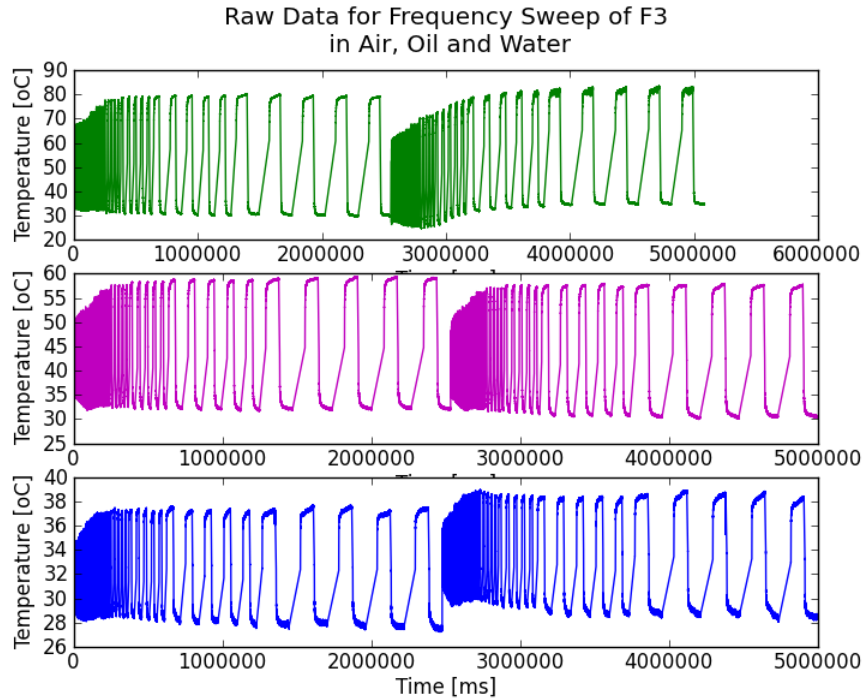


**Figure 5.15:** Raw data for the a frequency sweep from pulse times of 20ms to 100seconds of a released nickel beam in Air (green), Oil (purple), and water (blue).

For each frequency the amplitude of the waveform was measured as described in 5.1.2 and shown in Figure 5.6. The resulting data is plotted in Figure 5.16 which shows the temperature change of the pulsed sensing wire vs the pulsing period used. At high frequencies the sensor does not respond fast enough to significantly heat and cool during each cycle. This behavior is similar to that of an incandescent light bulb heated with a 60Hz power source; the wire response is slow enough that the light does not cool significantly and the strobe effect is small during the low cycles. As the frequency decreases, the amplitude of heating and cooling starts to significantly increase. Also the difference observed between oil, water, and gas increases. This analysis helps to better describe the thermal response of the sensor and allow for the optimum pulsing frequency to be selected for a sensor's thermal characteristics.

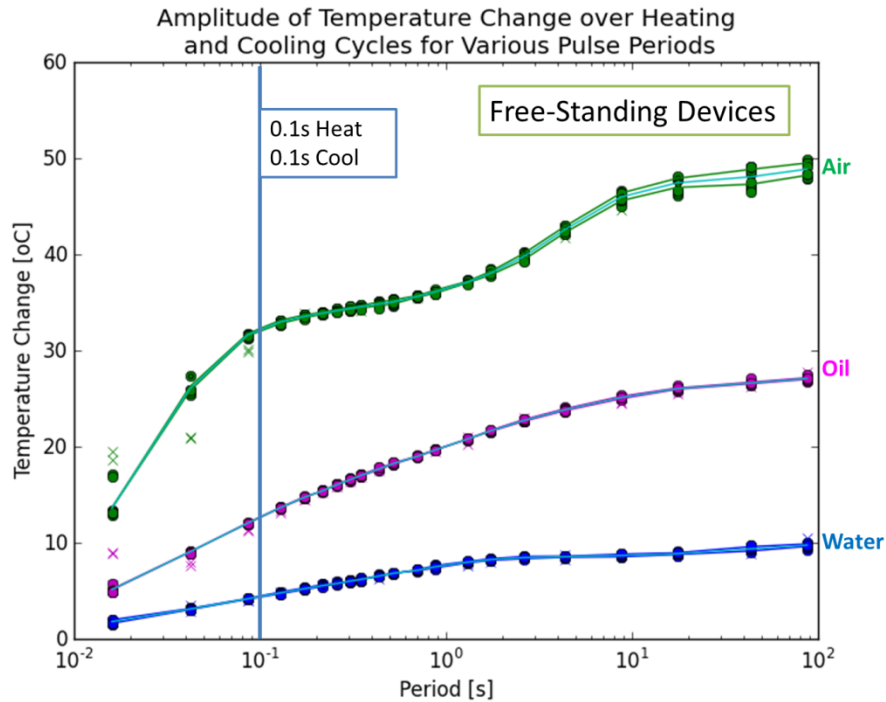
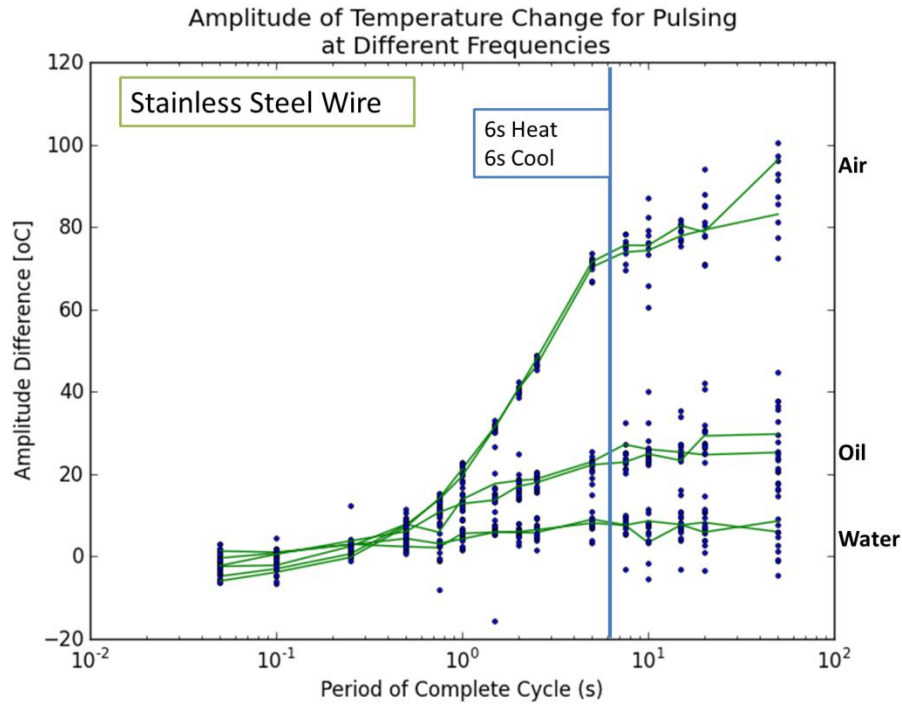


Figure 5.16: Processed data showing the amplitude of the temperature swing vs pulse period for a released nickel beam in air, oil, and water.

This same analysis was conducted for a simple hot wire anemometer constructed of a 200 $\mu$ m diameter 316 Stainless Steel wire suspended between two gold coated pins held 5mm apart. The results of the frequency analysis are shown in Figure 5.17. This device is similar in structure to the released beam design sensor but does not require any microfabrication techniques to fabricate. It has three disadvantages: The electrical contact between the wire and the pins is interrupted by the native oxide on the 316Stainless steel, the TCR of the stainless steel is significantly less than that of nickel, and the thermal mass vs surface area of the 200 $\mu$ m diameter wire is larger than the 20 $\mu$ m thick, 100 $\mu$ m wide released beam. The lower TCR results in significantly more noise in the measured electrical signal; the resistance of the wire is not changing as much as a result of temperature change. The larger ratio of thermal mass to surface area of the wire results in a significant increase in the time constant of the sensor. Pulsing periods of 6 seconds allowed for clear distinction of air, but the distinction of water and oil was not very clear.



**Figure 5.17:** The amplitude of the temperature swing vs pulse period for 200µm diameter 2mm long 316 stainless steel wire in air, oil, and water.

The anchored devices discussed in chapter 3 were also characterized using this technique. It was found that these sensors did a great job of distinguishing the three phases of air oil and water. The thermal response was very repeatable from run to run. The optimal pulse period was found to be around 2 seconds. It is expected that the thermal response of the anchored devices would be slower than the freestanding beams due to the increase thermal load of the glass support underneath the beam. It is interesting that the three different liquids can still be clearly distinguished even though the thermal path to the supporting glass in the feedthrough is significant. The resulting thermal frequency response is shown in Figure 5.18.

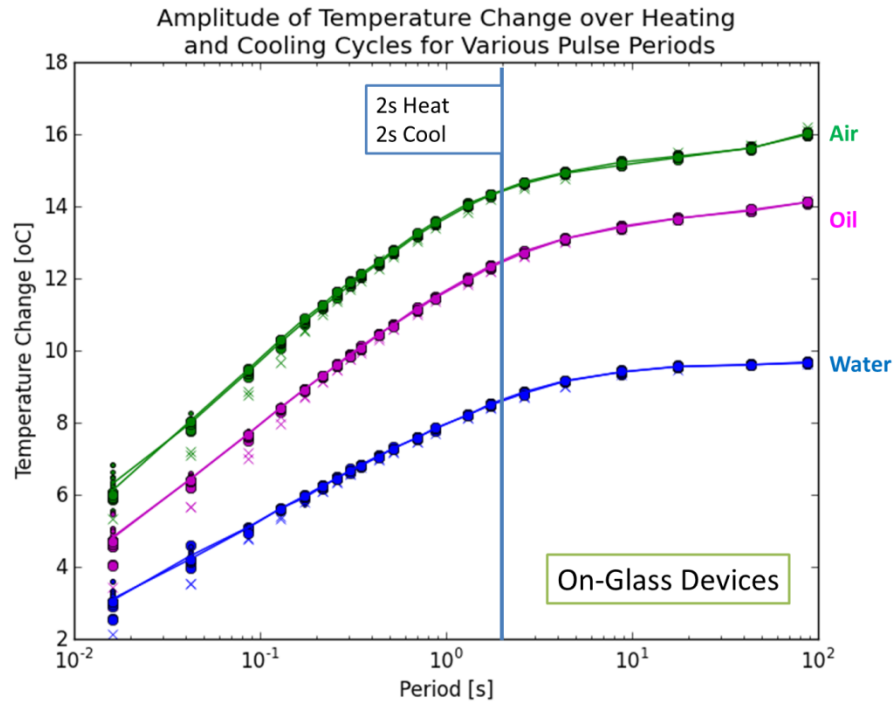


Figure 5.18: The amplitude of the temperature swing vs pulse period for an anchored on feedthrough nickel beam in air, oil, and water.

We tested an anchored device with a 30 $\mu$ m thick parylene coating as well to see if this device could also distinguish between the three different phases. This result shown in Figure 5.19 is quite interesting as the liquids are no longer in direct contact with the electrically heated beam as it is covered over by a thick dielectric layer. The thermal response of this completely isolated thin beam is fundamentally different from the previous three devices because there is no distinguishable difference between the three fluids at high frequencies. The differences only become evident at longer pulsing periods. This effect is mentioned by Nagasaka et al. who used a 10 $\mu$ m thick layer of polyester to coat a 50 $\mu$ m thick platinum wire in order to use the pulsed hot wire technique to measure the thermal conductivity of electrically conducting liquids[162]. If the time of heating is long enough the thermal effect of the thin insulating coating is negligible[25].

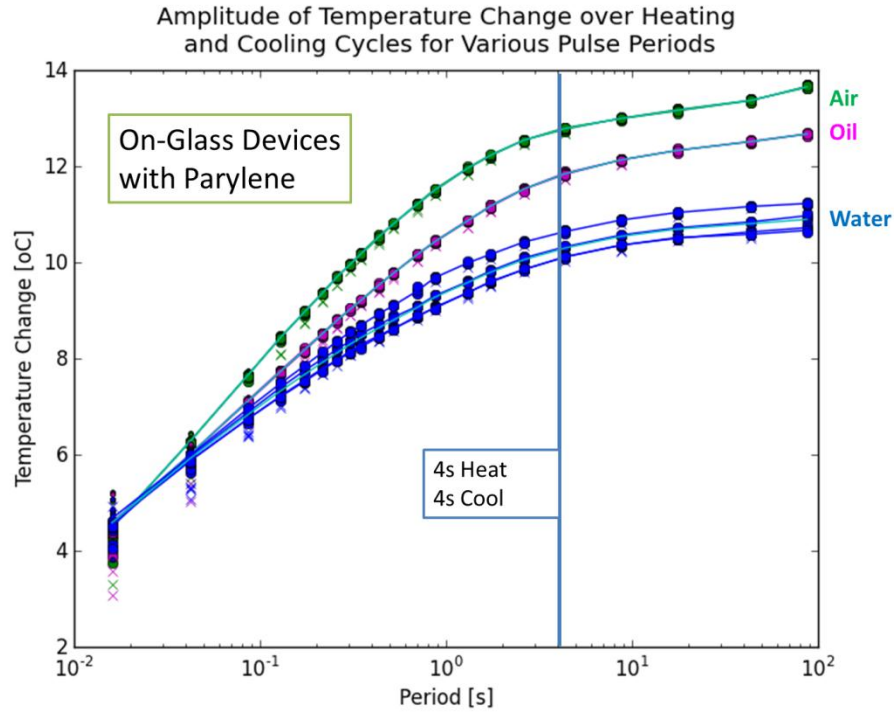


Figure 5.19: The amplitude of the temperature swing vs pulse period for an anchored on feedthrough nickel beam coated with 30um of Parylene in air, oil, and water.

A schematic diagram of the four geometries of thermal sensor tested is shown in Figure 5.20. Two geometries of suspended wires completely surrounded by the test fluid were tested. The 100x20 $\mu$ m beam had the fastest thermal response and showed the most sensitivity to changes in the surrounding fluid. The 200  $\mu$ m diameter stainless steel wire had the slowest thermal response and showed the poorest distinguishing capability between the three test fluids. Two anchored sensors were tested that were sitting directly on the high pressure feedthrough glass surface, one was exposed to the test fluid and the other was coated with a 30  $\mu$ m thick parylene coating. Both of these sensor structures were able to distinguish between oil water and gas with the uncoated sensor having the most sensitivity.

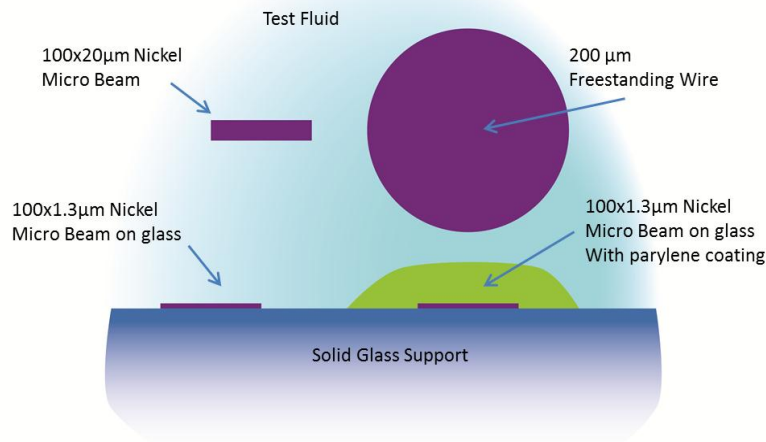


Figure 5.20: Diagram of the different geometries tested for thermal response to current pulsing in this work.

### 5.1.7 Sensor Resistance Components

The total resistance of the sensor is made up of four parts: resistance of the sensing beam  $R_B$ , a contact resistance between the nickel beam and the inconel pin  $R_C$ , the resistance of the inconel pin  $R_p$ , and the resistance of the solder contacts. The total resistance observed for the systems studied with  $20\mu\text{m}$  thick beams that are  $100\mu\text{m}$  wide and  $2\text{mm}$  long is usually close to  $0.3\Omega$ . This resistance is the total resistance of the system and includes all of the separate parts.

The resistance expected of a nickel beam with these dimensions assuming a resistivity for bulk nickel of  $69\text{n}\Omega\text{m}$  can be found with the equation for resistance of a rod.

$$Resistance = \rho \frac{L}{A}$$

Where  $\rho$  is the resistivity of the material,  $L$  is the length of the rod, and  $A$  is the cross sectional area. The expected resistance for the  $2\text{mm}$  long nickel beam is approximately  $0.0693\Omega$ . Using a probe station to measure the resistance of the beam by itself after detaching from the feedthrough, two beams were measured to have resistances of  $0.080\Omega$  and  $0.082\Omega$ . The resistance of the beam is significantly smaller than the  $R_T$  measured of  $0.3\Omega$  for the whole system.

Figure 5.21 shows a drawing of the sensor structure and the location of the various resistances expected to be connected in series between the four point connections of the source meter leads. The inconel pins are expected to have a resistance of approximately  $30\text{m}\Omega$  each leading to an approximately  $60\text{m}\Omega$  resistor in series with the sensor beam. Inconel has a low temperature coefficient of resistance compared to pure nickel. A reference from Oakridge National Lab presented data giving a TCR

0.00011 K<sup>-1</sup>[163]. The inconel beams are expected to be coated with a thin native oxide that will separate the pins from the electroplated nickel beams and this oxide should be quite thin (1-5nm) but would be composed of a high resistance chromium oxide[164]. A value of resistivity for chromia of  $\sim 55\Omega\text{m}$  taken from Park and Natesan[165] would give this layer a resistance of between 0.072-0.359  $\Omega$  per pin surface with 1mm diameter. This value suggests that this contact resistance is quite significant. Several studies regarding the contact resistance of nickel based superalloys have been conducted for application in solid oxide fuel cells. Inconel 718 after being oxidized for 100 hours at 800°C will grow an oxide with an Area Specific Resistance (ASR) of 0.1 $\Omega\text{cm}^2$ [166]. The inconel pin surface used in this work has only been exposed to 120°C during lithography after being cut and would be expected to have a ASR significantly lower than the values proposed in this fuel cell work. If oxidized inconel was used this resistance would dominate the system at  $\sim 12\Omega$  per pin.

Also in series with the beam is the resistance of the soldered connection of the source meter leads to the inconel pins. Lead free solder has a low resistivity 10-15 $\mu\Omega\text{cm}$ , a low TCR of 0.00029, and has a quite large cross sectional area and short length. The solder contribution to the series resistance is expected to range from 10-20 $\mu\Omega$  and is low because the cross sectional area of the solder joints is quite large.

Each of these components is expected to have its own response to a change in overall sensor temperature, but in the case of electrical heating of the wire the pins and solder connection do not heat significantly. Because of this difference in uniform heating vs non-uniform electrical heating, the calibration conducted using an isothermal oil bath cannot be used directly to extrapolate the temperature of the beam when electrically heated. The problem is somewhat improved because the inconel pins and the solder used have small TCR values. By making the beam thinner and therefore increasing  $R_B$  in relation to the other resistances this effect can be minimized. A beam that is only 20 $\mu\text{m}$  across and 20 $\mu\text{m}$  thick would have an estimated resistance of 0.35 $\Omega$  and contact resistances and the resistances of the inconel pins would be smaller in comparison. This would improve the sensor as a whole as the resistive behavior of the sensor would be dominated by the beam structure and the thermal mass of the beam would also be reduced allowing for a faster thermal response.

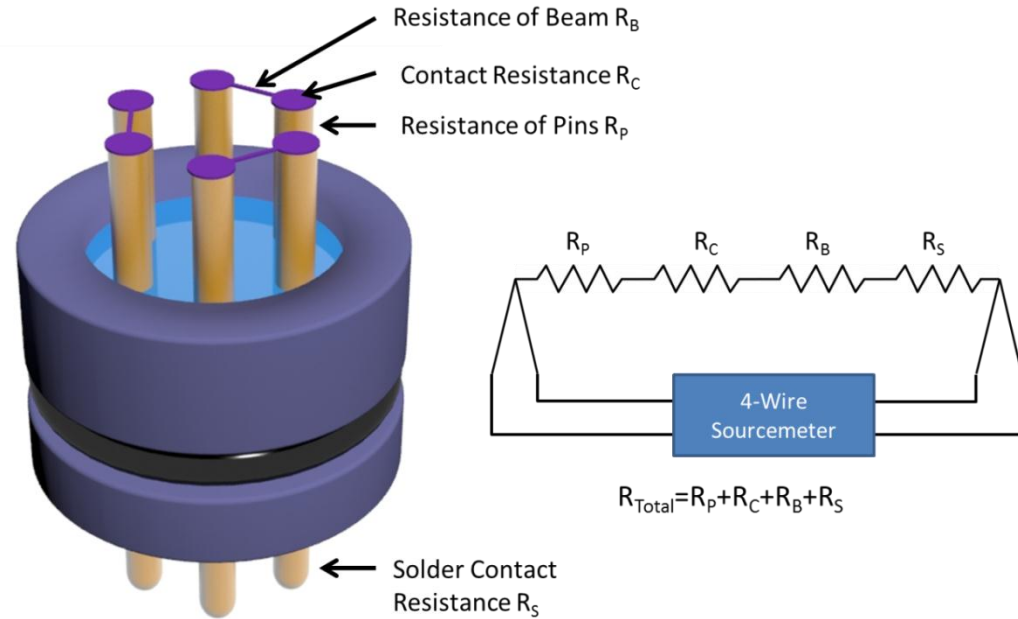


Figure 5.21: 3D drawing of the fabricated released nickel beam structures showing the different resistances that are measured by the attached 4-wire source meter.

### 5.1.8 Thermal Transient Response of Sensor

Because the sensor is made up from three distinct geometries with significantly different length scales it is not expected to heat up in a uniform fashion when exposed to temperature transients. When immersed in a high temperature bath, the 20 $\mu$ m thin exposed nickel beam structure will heat up significantly faster than the 1mm diameter inconel pins which will in turn heat up faster than the larger 1.25cm diameter full feedthrough. We conducted a series of high temperature shock and low temperature quench experiments in an effort to show that this sensor responds faster to thermal transients than a conventional 1/8" diameter RTD or thermocouple probe. In our testing we found that our sensor responds very quickly to temperature transients, it also has a distinct transient response caused by the different size scales of the sensor device. The thin beam equilibrates very quickly but the full sensor takes a significantly longer time to reach a steady state resistance as the rest of the feedthrough slowly reaches thermal equilibrium. Incorpora et al. in the textbook "Introduction to Heat Transfer" showed that the transient thermal response of a solid body can be approximated using the "Lumped Capacitance Method" that neglects temperature gradients within the solid and uses an energy balance to approximate the temperature rise/fall in the solid. The first law of thermodynamics states that the total energy of a system is conserved. Setting the rate of energy transfer into a control volume to equal the rate of increase of energy stored within a control volume gives the following equation[30].

$$\frac{dE_{St}}{dt} = -\frac{dE_{Out}}{dt} \quad \text{or} \quad \rho V c \frac{dT}{dt} = -h A_s (T - T_{\infty})$$

Where  $\frac{dE_{st}}{dt}$  is the rate of increase of energy stored within a control volume,  $\frac{dE_{out}}{dt}$  is rate of energy transfer out of a control volume,  $\rho$  is the mass density in  $\text{Kg/m}^3$ ,  $V$  is the volume,  $c$  is the specific heat capacity in  $\text{J/Kg}$ ,  $\frac{dT}{dt}$  is the change in temperature with time,  $h$  is the convection coefficient in  $\text{W/M}^2$ ,  $A_s$  is the surface area,  $T$  is the temperature of the immersed body, and  $T_\infty$  is the temperature of the bath that the body is immersed in.

By substituting in the variable  $\theta$  such that  $\theta = T - T_\infty$ , with  $T_\infty$  remaining constant then the equation becomes:

$$\frac{\rho V c}{h A_s} \frac{d\theta}{dt} = -\theta$$

Separating the variables and integrating gives the relationship

$$\frac{\rho V c}{h A_s} \int_{\theta_i}^{\theta} \frac{d\theta}{\theta} = - \int_0^t dt$$

$$\frac{\rho V c}{h A_s} \ln \left( \frac{\theta_i}{\theta} \right) = t$$

And solving for the change in temperature gives the equation that describes the rise/fall in temperature of a body when immersed in a bath with a different temperature.

$$\frac{\theta}{\theta_i} = e^{-\frac{h A_s t}{\rho V c}}$$

Graphing this equation using values of  $A_s$  and  $V$  from the thin beams of the sensor and for the inconel pins in the sensor gives the result shown in Figure 5.22. ( $h$  was set to the value of  $100\text{W/m}^2$ ,  $\rho$  was set to  $8908\text{kg/m}^3$  and  $c$  was set at  $540\text{J/kg}\cdot\text{K}$ ). The response of the thin beam is significantly faster than that of the inconel pins. The beam heats in less than 1 second where the pins take over 30 seconds when the convection coefficient is fixed at  $100\text{W/m}^2$ .

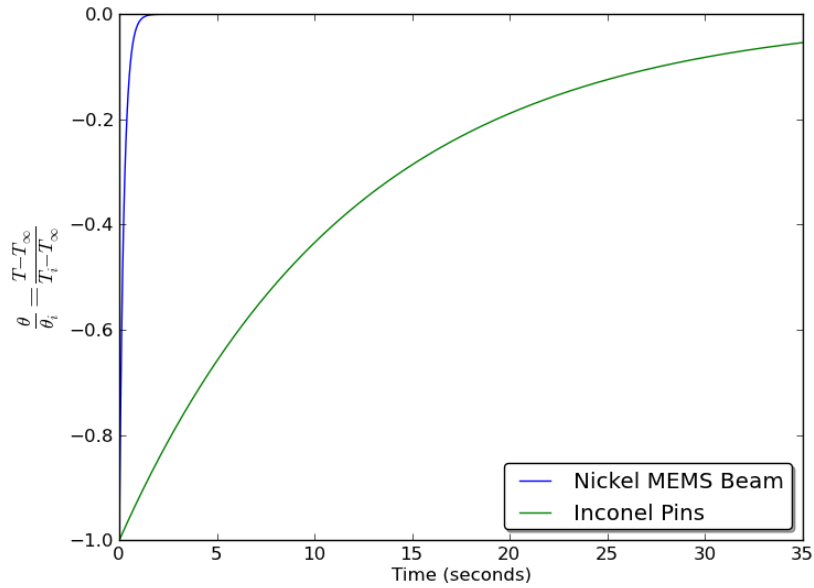


Figure 5.22: Calculated thermal response of nickel MEMS beams and larger inconel pins when immersed in a high temperature fluid. When  $\theta / \theta_1$  is -1 the beams/pins are at their initial temperature. When  $\theta / \theta_1$  reaches 0 they have reached equilibrium with the bath temperature.

This dramatic difference in thermal time constant is a possible explanation for the thermal response of the sensors shown below in Figure 5.23 where the resistance rapidly rises then starts to slowly increase with significant instability and then reach a steady and stable value when shock heated to 170°C.

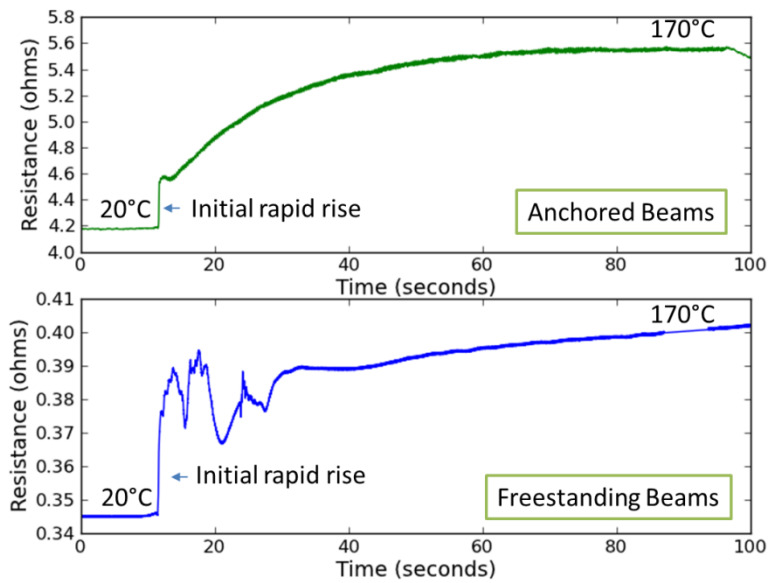
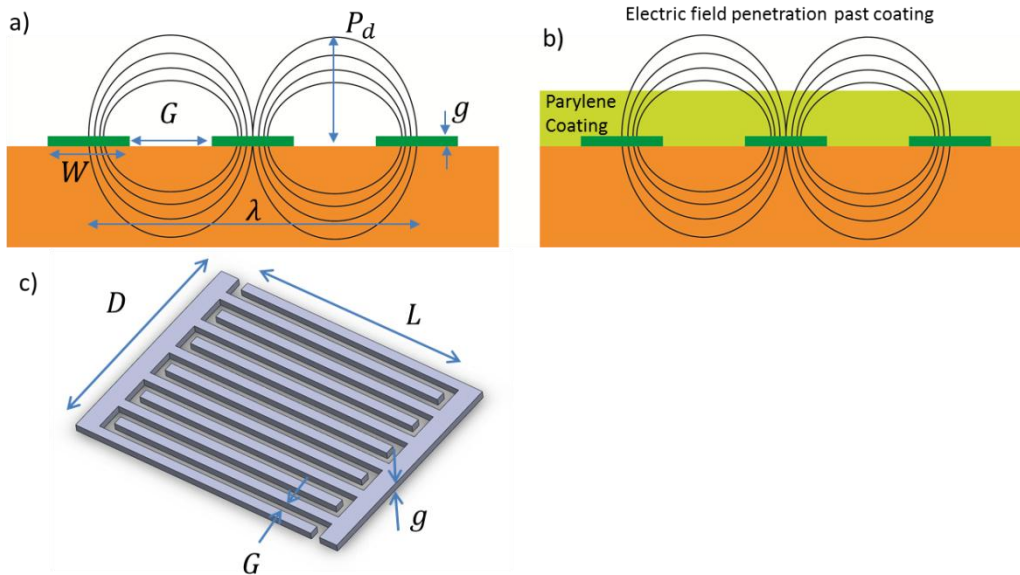


Figure 5.23: Resistance response of anchored and freestanding devices when rapidly plunged into 170°C oil.

This effect could also be responsible for the double plateau seen in the frequency response of the free standing beams in air seen in Figure 5.16. The resistance of the sensor during a temperature change is a combination of the increase in resistance of the beam and the pins. If the resistance of the beam is significantly larger than that of the pins then the beam thermal response will dominate the total resistance measurement. If the pin resistance is larger than the pin thermal response would dominate the measurement. In our case the two resistances are similar and a combination of the two responses results in the observed transient response of the sensor. Further modification to implement a thinner beam with a higher resistance will dramatically improve the transient response of the sensor with the rapid initial rise accounting for greater than 90% of the response.

## 5.2 Dielectric constant measurements with a comb style capacitor

For measurements of fluid dielectric constant comb structures were used. The structures were  $1.3\mu\text{m}$  thick ( $g$ ) having teeth ( $W$ ) that were  $100\mu\text{m}$  wide and spacings between teeth ( $G$ ) of  $100\mu\text{m}$ . The comb array is  $2\text{mm}$  wide ( $D$ ) x  $1.5\text{mm}$  long ( $L$ ) consisting of ten interwoven teeth. The basic structure of the comb is shown in Figure 5.24c and a cross section diagram is shown in Figure 5.24a. A detailed discussion of the derivation of the capacitance of a comb capacitor and an approximation of the electric field penetration depth above the comb array ( $P_d$ ) has been done by Starzyk. He found that the penetration depth was equal to approximately  $\frac{G+W}{\pi}$  [167]. In the case of the devices tested in this work, the penetration depth would be approximately  $60\mu\text{m}$ . Testing with uncoated comb arrays resulted in unpredictable results as electrically conducting water would interfere with the measurements. The measurements were found to depend more on the electrical conductivity (cleanliness) of the water than dielectric constant. Salt water would result in anonymously high capacitance measurements. Coating the sensor elements with parylene and electrically isolating the electrodes from the solution resulted in repeatable and predictable measurements. The coating used was approximately  $30\mu\text{m}$  thick which was less than the predicted  $60\mu\text{m}$  penetration depth of the electric field. Figure 5.24b shows a parylene coating that is less than the predicted electric field penetration depth.



**Figure 5.24:** a) Cross section of the comb capacitor showing the interdigitated teeth, the expected electric field and the critical dimensions of the comb capacitor. b) A figure showing a coating that is thinner than the expected penetration depth of the electric field. c) A 3D model of the comb capacitor showing the overall dimensions.

Measurements with this comb capacitor were made using an Analog Devices AD7746 capacitance to digital converter electrically connected to the comb electrodes with short and rigid electrical connections. Longer electrical contacts would result in poor repeatability of measurements due to the wiring having a significant effect on the total measured capacitance. The results of a test of several mixtures of IPA and water are shown in Figure 5.25. The graph shows the sensor being exposed to each mixture in sequence starting with pure water and being dried in-between exposures. The inset graph shows the average of the capacitance measurements for each step plotted against the volume percent of water. IPA has a dielectric constant of 18.3 while water has a much higher dielectric constant of 80.4. As water is added to IPA the dielectric constant of the mixture is expected to increase significantly resulting in a larger capacitance measurement by the comb capacitor. Because the sensor is on a glass substrate and coated by parylene, the total capacitance is affected by the dielectric constant of all three materials and the capacitance shift due to a changing the fluid in contact with the parylene is quite small. Figure 5.24b shows the three materials that affect the capacitor response and a rough drawing of the electric field penetration depth above and below the comb elements. The response is quite high for low concentrations of water and seems to saturate at higher concentrations. A similar sensor response has been seen in kerosene water mixtures tested with a capacitance probe by western atlas[1]. The results of this analysis suggest that low concentrations of water can be detected with significant resolution providing sub 2% quantification, but at higher concentrations the sensor saturates and cannot provide good quantification above 60% water by volume.

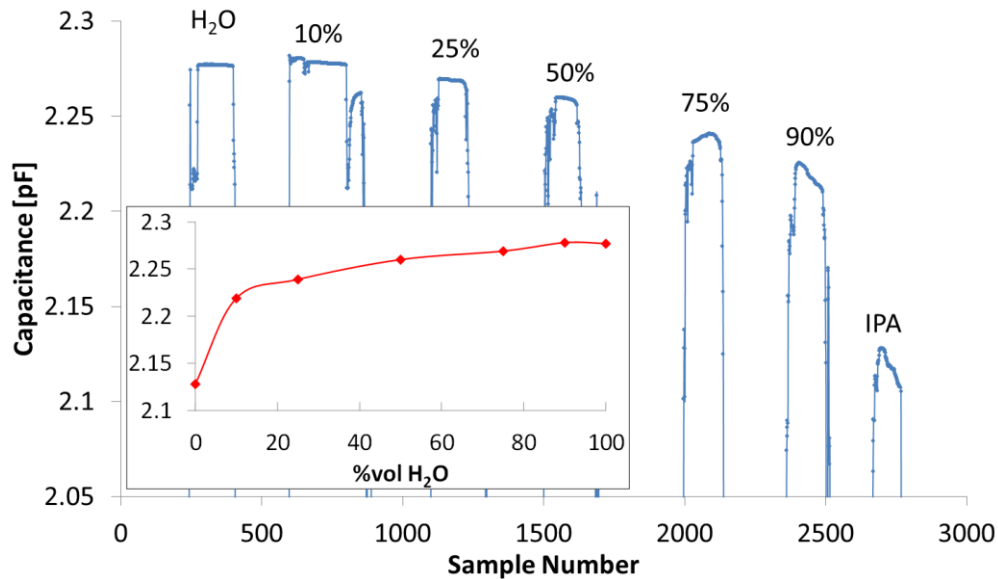


Figure 5.25: The response of the comb capacitor coated with 30um of Parylene to several different mixtures of IPA and water in sequence. The inset is the generated calibration curve of capacitance vs. water content.

### 5.3 Conclusion

Dielectric constant and thermal conductivity phase identification techniques were explored using the microfabricated sensor platforms developed in chapters 3 and 4. Thermal measurements were conducted using four different sensor geometries including free standing and anchored heating elements. The effect of a parylene coating on the thermal response was explored. Good distinction between oil water and gas was found using the different sensor geometries, with the freestanding microfabricated beams having the best performance and a non-microfabricated stainless steel wire having the poorest performance. IPA water mixture compositions could be determined with an accuracy of  $\sim\pm 5\%$  using the free standing wires and oil water emulsions could be determined with an accuracy of  $\sim\pm 10\%$ . Transitions between oil water and gas were tested using a linear stage to move between the three fluids and rapid response to fluid transitions was seen with the free standing beams. The anchored devices did not work as well transitioning between fluids and were found to be masked by a thin film of oil when being transferred from oil to water. Dielectric constant measurements using comb electrodes covered with parylene worked well showing a good sensitivity in IPA rich mixtures but the sensor response saturated at higher water concentrations.

The sensors demonstrated in this work are the smallest available that can be operated at temperatures up to 180°C and pressures above 10,000psi. The ability to integrate three microfabricated sensors onto a single high pressure feedthrough allows for three different measurements to be conducted in essentially the same

location in an oil-well. When deployed as an array, this will allow for dramatically improved data quality compared to currently available technology.

The use of thermal conductivity to distinguish between oil water and gas has not been incorporated into a down-hole tool commercially. One of the major limiting factors for conducting thermal conductivity tests with larger structures is the thermal time constant and low electrical resistance of the sensor. Microfabrication allows for a dramatic reduction of this time constant which results in a faster response of the sensor and allows for smaller higher resistance structures to be fabricated. In short, microfabrication is required to do this type of measurement in this application and the reported sensors in this work are the first of their kind in the field of production logging.

## 6 Electrocatalytic Hydrogenation of 2-cyclohexen-1-one in a High Sulfur Environment Using a Carbon-supported Nanostructured Tungsten Sulfide Catalyst<sup>1</sup>

### 6.1 Abstract

Vitreous-carbon supported tungsten sulfide (WS<sub>2</sub>) nanoparticle catalysts were synthesized by fully sulfiding thin films of W. This support-catalyst combination was shown to be successful at hydrogenating 2-cyclohexen-1-one in the presence of sulfur. A well-known hydrogenation catalyst consisting of a nickel film, used as a baseline, was found to be completely ineffective in an identical solution. Catalyst samples with a nominal W thickness of 2nm, produced the largest hydrogenation product yields with the highest efficiencies. SEM and XPS analysis confirms that this nominal thickness corresponds to a dense distribution of nano-scale WS<sub>2</sub> particles templated on the carbon substrate. We envision the WS<sub>2</sub>-carbon system becoming a catalyst of choice for electrocatalytic hydrogenation in a sulfur-rich environment.

### 6.2 Introduction

A major environmental and economic cost of refining heavy crude oil is the hydrotreating of the distillate fractions to hydrogenate olefins and polyaromatics, and to remove sulfur and nitrogen as hydrogen sulfide and ammonia. The carbon dioxide from the hydrogen plants is a major source of greenhouse gas emissions. The challenge for a greener technology is to substantially reduce the carbon footprint of refining without compromising the quality of the products. One approach is to avoid the use of high-pressure natural gas for processing of distillate fractions to improve their quality. Electrocatalytic hydrogenation may achieve these goals with a much lower carbon impact, with recent work showing facile synthesis of a variety of molecules e.g. [168-171].

The hydrogenation of organic compounds, such as olefins and aromatics, can be achieved at ambient pressure by electrocatalytic hydrogenation. At the cathode, active hydrogen is generated from protons in solution. The relevant compounds converted by electrocatalysis include 2-cyclohexen-1-one [168], benzene [172], phenanthrene [173], thiophenol [174, 175] and olefins [176, 177]. If the formation of elemental hydrogen (H<sub>2</sub>) is avoided by controlling the electrode potential, then the conversion of protons into active hydrogen can exceed 75% [172].

Workers utilize several combinations of electrode materials for electrocatalytic hydrogenation. Roughly, these can be separated into three categories: noble metal-based, pure nickel, or iron-based catalysts. A 1992 review by Moutet covers the

---

<sup>1</sup> Material in this chapter has been published in:  
CMB Holt, S Murphy, MR Gray and D Mitlin, *Catalysis Communications*, 12 (2010) 314-317

pertinent cathode/anode materials combinations [178], though many of these have now evolved to possess a nano-scale microstructure. Unfortunately, due to the high sulfur content of heavy oil, electrocatalytic hydrogenation of materials with a high sulfur content has not been achieved. This is because “conventional” electrocatalysts rapidly and irreversibly deactivate in that environment. The recent advances in achieving nano-scale catalyst microstructures have not improved this issue at all.

In this study we demonstrate a proof-of-principle electrohydrogenation of 2-cyclohexen-1-one in a high sulfur (0.1 vol.% thiophene) environment using a nano-scale WS<sub>2</sub> catalyst supported on an electrically conductive vitreous carbon substrate. To our knowledge, electrocatalytic hydrogenation has not been achieved under sulfur-rich conditions. The geometry/size of the sulfide (tungsten and molybdenum) nanoparticles is known to influence the conventional hydrogenation properties [179-182]. In this study we investigate this effect indirectly, by varying the nominal thickness of the initial pre-sulfided tungsten layer.

### 6.3 Experimental

In order to achieve uniform current density and to minimize the resistive losses, a small batch reactor was custom designed and fabricated out of glass. A schematic of the cell is shown in Figure 1. It had opposing symmetrical round electrodes, as well as a reference electrode positioned adjacent to the cathode. The cell consisted of a single glass cylinder with an ultra fine porous glass frit (pore size 0.9 - 1.4 μm) in the center. The cell consisted of two tubular compartments that would hold a volume of 50mL each. The diameter of the cell was just large enough to fit the 31.75mm diameter electrode discs. At the top of the cell, there were two sealable openings that functioned as a means of filling the cell with the electrolyte solution as well as a location for the reference electrode to be inserted. Two titanium rods 25.4mm in diameter were used to make electrical connections to the electrodes. The glassy carbon disks, which were used both as a working and counter electrodes, were 2mm thick, and 31.75mm in diameter, with a 3.6mm diameter countersunk hole in the center. The disks were Sigradur G vitreous carbon commercially available from HTW Hochtemperatur-Werkstoffe GmbH of Germany. The electrodes were attached to the rods by electrically insulating alumina screws. A Ag/AgCl KCl(sat'd) reference electrode was inserted in the cathode compartment and sealed with a rubber o-ring and a plastic screw cap. The reference electrode was positioned such that the tip was as close as possible to the cathode surface. All electrochemical testing and measurements were performed using a Princeton Applied Research VSP multichannel potentiostat and Bio-Logic EC-Lab software package.

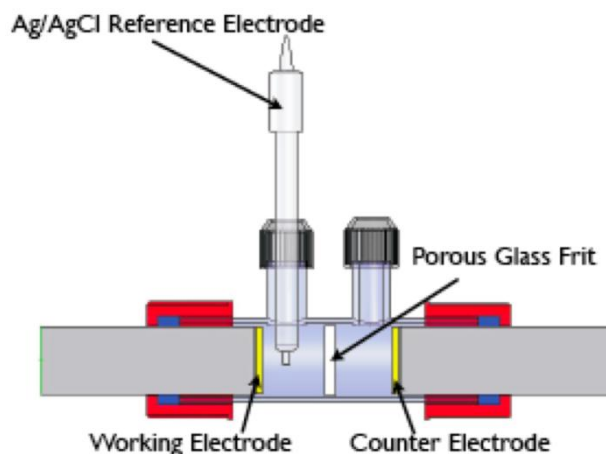


**Figure 6.1:** Cross-section schematic of the symmetric opposing electrode electrochemical reactor used for the experiments.

The catalysts were deposited on the vitreous carbon disc that was used as the working electrode (cathode). The surface of the vitreous carbon was polished using a 0.5  $\mu\text{m}$  grit diamond lapping film. The vitreous carbon discs were then cleaned by sonic bath in acetone followed by isopropanol. The counter electrode glassy carbon disk was cleaned but not polished. Afterwards all discs were thoroughly dried with nitrogen.

Pure metallic tungsten and nickel films were magnetron sputtered (AJA International) onto the vitreous carbon held nominally at ambient temperature. Deposition rates were determined using a quartz crystal microbalance positioned exactly at the substrate plane. Additionally, ex-situ rate calibration was also used to confirm the in-situ data. For the ex-situ calibration, the rate was measured at 5 separate powers, and fit to a linear slope using linear regression. This data was then used to determine the sputter rates for a given power. A base pressure of  $5 \times 10^{-8}$  mTorr was achieved in the sputtering chamber before all depositions. Argon pressure was maintained at 4.0 mTorr, with a flow rate of 10 sccm throughout. The W films were deposited with thicknesses of 0.5 to 10 nanometers. A low deposition rate of 0.3  $\text{\AA}/\text{sec}$  was used to ensure thickness accuracy. After deposition the films were sulfided through exposure to a flowing hydrogen -  $\text{H}_2\text{S}$  environment in a dedicated sulfiding tube furnace. Prior to sulfidation the tube furnace was purged using nitrogen gas to remove oxygen in the tube. The tube furnace was then heated under  $\text{N}_2$  gas flow until the sulfiding temperature (600°C) was reached. The samples were held at that temperature for 4 hours. After the sulfidation temperature had been reached the gas flow was switched from  $\text{N}_2$  to the  $\text{H}_2/\text{H}_2\text{S}$  mixture. A flow rate of 60 mL/min of  $\text{H}_2/\text{H}_2\text{S}$  mixture was used. The gas had an  $\text{H}_2\text{S}$  concentration of 5000 ppm. Baseline Ni films were deposited to a thickness of 10 nm. At that thickness the films were continuous and adherent with the carbon substrate.

Solutions were prepared in glass beakers and then transferred to the reaction cell.

The volumes of water and methanol for the hydrogenation reaction were measured with pipettes and mixed in a beaker. The electrolyte salt was then measured by weight and added to the solution. The solution was manually stirred with a glass rod to facilitate the dissolution of the salt. After transferring the solution to the reaction cell, the substrate was measured with a pipette and added to the cell. The solution was again stirred with a glass rod. The solution consisted of 8 mL of 99.9% methyl alcohol, 32 mL of water, 2 mL of 2-cyclohexen-1-one, and 0.3088g of  $(\text{NH}_4^+)(\text{CH}_3\text{COO}^-)$ . Thiophene (>99% purity) was added at a concentration of 0.1 vol% (12 mM) as a representative sulfur compound. The water was purified using a Gradient A10 Milli-Q system from Millipore and had 4 ppb content of total organic carbon and 18.2 M $\Omega$ -cm resistivity at 25 °C. The 2mL of 2-cyclohexen-1-one was added to the solution in the working electrode compartment of the cell just prior to reaction. Reaction was carried out under a constant applied potential of -1.3V versus Ag/AgCl, KCl (sat'd) across the working electrode-solution interface. During reaction, the cathode compartment was stirred magnetically at 600rpm using a magnetic stir bar. Samples were taken and analyzed after 90 minutes of reaction.

Two gas chromatographs with identical columns were used for identification and quantification of hydrogenation reaction products. Reaction products were identified by comparing their retention times with the retention times obtained from chromatography of pure compounds. Pure reagents of 2-cyclohexen-1-one, cyclohexanone, and cyclohexanol were obtained from Sigma Aldrich. The other possible hydrogenation product, 2-cyclohexen-1-ol, was not detected. Agilent 5790 gas chromatographs were used and equipped with Agilent DB-1 columns and flame ionization detectors. Helium gas was used as the mobile phase. Toluene was added as an internal standard in order to quantify the results. Electrode surface analysis was performed with a AXIS Ultra photospectrometer using an Al K $\alpha$  x-ray source. All survey scans were performed with a binding energy step size of 1 eV from 0 to 1200 eV. High-resolution scans were performed on binding energy ranges containing peaks from elements of interest with a step size of 0.1 eV. Morphology of catalysts was studied using scanning electron microscopy (SEM). All analysis was performed on a Hitachi S4800 high resolution electron microscope. The microscope was used in secondary electron mode with an accelerating voltage of 20.0kV.

The electrochemical efficiency of the electrocatalytic hydrogenation reactions was determined by calculating the ratio of electrons used for hydrogenation to the total number of electrons consumed in the process. Here the major competing reaction is the hydrogen evolution reaction (HER), which uses 2 electrons per H<sub>2</sub> molecule. The current-time curves from the chronoamperometry scans were integrated to give the total amount of charge passed, and then total number of electrons consumed was calculated. The number of electrons required for the quantity of observed reaction products was then calculated (2 mols of electrons per 1 mol of cyclohexanone for hydrogenation of the double bond and 4 mols of electrons per 1 mol of cyclohexanol for hydrogenation of the double bond and reduction of the

ketone to an alcohol). Conversion of cyclohexanone was calculated from its initial concentration in solution and the total concentration of the hydrogenation products, cyclohexanone and cyclohexanol.

#### 6.4 Results and Discussion

The pre- and post-sulfided W catalyst surfaces were analyzed using x-ray photoelectron spectroscopy (XPS). Figure 2A shows an XPS scan of the pre-sulfided 2 nm thick catalyst in the binding energy range of W 4f orbital electrons. The binding energies observed for the two peaks are shifted from those expected for pure W due to bonding with oxygen in the form of a  $WO_3$  native oxide. Comparing the pre-sulfided and post-sulfided spectra, it is clear that we have tungsten in the state analogous to  $WS_2$ . The electron binding energies observed in the post-sulfided sample agree with those attributed to W in +4 (as in  $WS_2$ ) with doublet peaks at 33.0 and 35.2eV [183]. Conversely, the pre-sulfided sample electron binding energies observed for W agree with those attributed to W in a +6 (as in  $WO_3$ ) oxidation with doublet peaks at 35.6 and 37.8eV [183]. The S atom electron binding energies in the sulfided sample are also in agreement with those observed for S 2p electrons in a  $WS_2$  electronic environment (162.4, 163.6eV) [183], illustrated in Figure 2B.

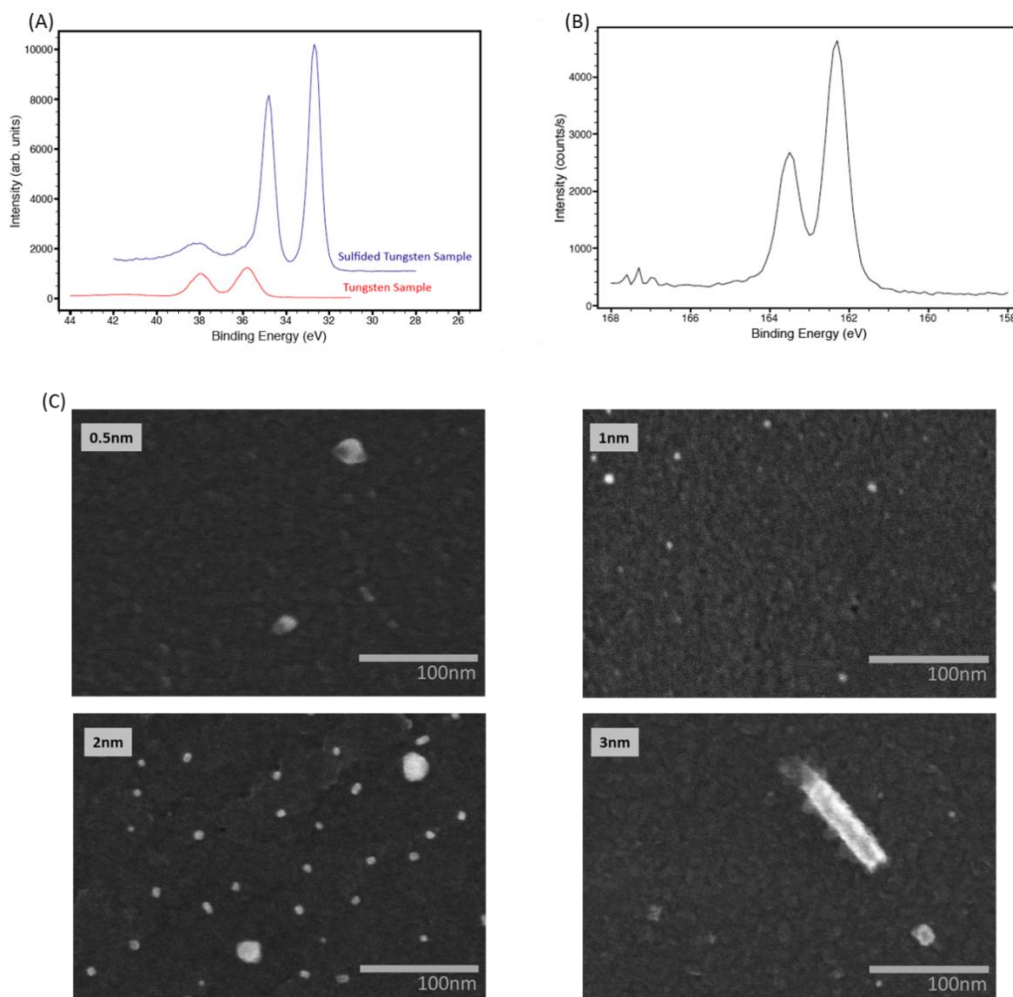


**Figure 6.2: A) XPS scans of pre- and post-sulfided electrodes in tungsten binding energy range. B) XPS scan of post-sulfided electrodes in sulfur binding energy range. C) SEM images of various thicknesses of W catalyst on vitreous carbon, after complete sulfiding.**

Figure 2C shows the representative surfaces of the glassy carbon covered by 0.5, 1, 2, and 3 nanometers of W and then sulfided. High resolution SEM analysis of the sulfided films with a nominal W thickness of 0.5 nm cannot clearly resolve the sulfide layer. The sulfide particles synthesized from the 2 nm W layer had the optimum combination of a fine nano-scale and a dense distribution. An example of such distribution is shown in the Figure, with the bright particles being the sulfide. Analysis performed on the 1 nm W layer showed sulfide particles of similar sizes, but were more coarsely distributed. Analysis of the 3 nm W layer showed a sparse distribution of sulfide particles that were significantly larger in scale than in the 2 nm sample. We believe that in the 3 nm layer many of the sulfide particles actually separated from the substrate prior to the SEM analysis, most likely shortly after the sulfiding process. At even higher thicknesses, such as at 4 nm (not shown) and beyond, the vast majority of the  $WS_2$  clearly separated from the substrate. When we examined the 4nm post-sulfided samples in the SEM, only bare glassy carbon

was observed. Those samples also appeared as bare carbon in XPS analysis, and yielded a negligible electrocatalytic yield.

The performance of the cell was tested with Ni on a glassy carbon electrode (10 nm film). Conversion of 2-cyclohexen-1-one to cyclohexanone (in the absence of thiophene) was 0.9% after 2 h of hydrogenation. However, when we attempted the same reaction but with thiophene present in the system, no hydrogenation product was detected at all. Also, a negative control reaction was performed with a bare vitreous carbon disc as a catalyst. No hydrogenation was observed with vitreous carbon.

Reaction over the W-S composite catalyst produced both cyclohexanone and cyclohexanol, the final hydrogenation product. The yields of reaction products were measured by gas chromatography after 90 minutes of applied voltage. The results, plotted as a function of the nominal W film thickness, are shown in Figure 3. The yield of the hydrogenation reaction increases with W layer thickness until 2nm, and then decreases again. At nominal thicknesses of 4nm and above, the catalyst delaminated from the vitreous carbon support, resulting in negligible hydrogenation. The efficiencies of the hydrogenation reactions also varied with the W thicknesses. At W thickness of 0.5 nm, the electrochemical efficiency was 35%, at 1 nm the efficiency was 66%, at 2 nm the efficiency was 77%, and at 3 nm the efficiency was 42%. Most likely the balance of the current is utilized for the generation of hydrogen gas as a side reaction.

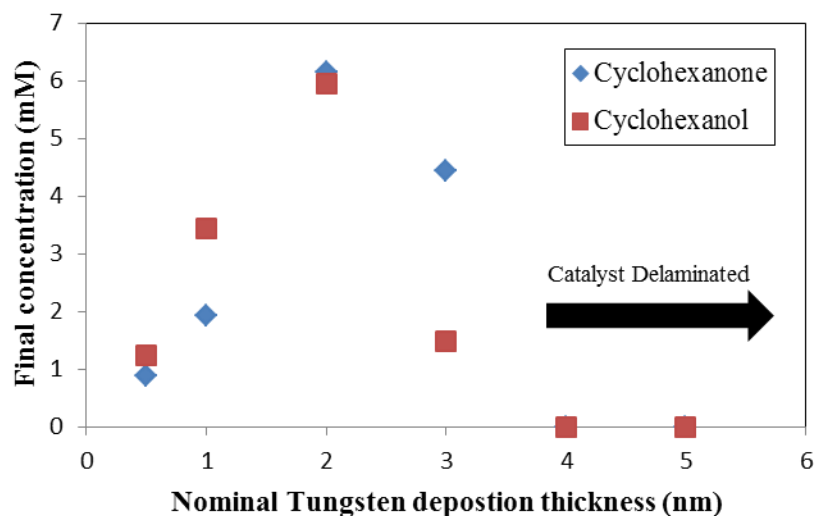


Figure 6.3: Product yield of cyclohexanone and cyclohexanol versus nominal catalyst thickness after a 90 minute hydrogenation of 2-cyclohexen-1-one under applied potential of - 1.3V versus Ag/AgCl(sat'd).

In order to explore the application of these electrodes to electrocatalytic hydrogenation of petroleum fractions, several requirements must be met. First, the solubility of the target compounds in the electrolyte solution must be addressed. We selected the combination of 2-cyclohexen-1-one and water-methanol as a convenient system. Actual sulfur, nitrogen and poly-nuclear aromatic compounds of interest would not be soluble in such an electrolyte. Second, the active area of the electrode must be significantly increased, possibly by the use of porous or powdered carbon materials as supports. Finally, the ability of electrocatalytic hydrogenation to remove sulfur and nitrogen as hydrogen sulfide and ammonia must be demonstrated. Hydrogenation is thermodynamically favored at low temperature, but the breakage of carbon-sulfur and carbon-nitrogen bonds may require higher temperatures.

## 6.5 Conclusions

Vitreous carbon-supported tungsten sulfide nanoparticle catalysts have been shown to be successful at hydrogenating 2-cyclohexen-1-one in the presence of sulfur, demonstrating a resistance to being poisoned by 0.1 vol.% thiophene. The catalytic activity and efficiency of these particles is highly dependent on their dispersion on the substrate material. Catalyst samples with a nominal deposition thickness of 2nm produced the highest yields of hydrogenation products with the highest current efficiencies. A nickel catalyst film, used as a baseline, is poisoned by sulfur.

## 7 Nickel Iron MEMS and NEMS Fabrication<sup>2</sup>

### 7.1 Introduction

Magnetic materials find use in MEMS devices as electromagnetically actuated MEMS have better stability in high force, large actuation gap applications[184]. Using magnetic actuation enables large deflections of devices of over 1mm both parallel and perpendicular to the substrate plane[185]. The magnetic field can be introduced externally by a coil allowing for remote control of the microfabricated devices[185]. For example, a demonstration of a magnetically actuated micro manipulator was controlled simply by varying the distance between the device and a permanent magnet[186]. Another device used a permalloy coated silicon membrane as a microfluidic valve[187]. Permalloy has been used extensively for magnetic MEMS devices because it has high saturation flux density, high relative permeability, low coercivity and near zero magnetostriction[188]. Davis et al. showed that a nanofabricated permalloy cantilever could be selectively actuated to resonate in a single torsional mode using an alternating magnetic field which was impossible using piezoelectric actuation[189]. Bhaskaran et al. made a ferromagnetic cantilever structure that could be actuated with an external alternating magnetic field and the deflection could be measured by the piezoresistance of the of cantilever material. This allowed for a very simple fabrication process to make a very sensitive resonating sensor structure[190].

The processing and deposition options for permalloy are well developed. Permalloy can be deposited by electro-deposition[184, 191], sputtering[122], or evaporation[192] and can be etched easily and cleanly with a dilute HF/HNO<sub>3</sub> acid mixture[122]. A major application for permalloy in microfabricated devices has been in the magnetic recording heads of computer hard drives[193] but currently other alloys and multilayer materials are used for this application. Thin film stress and differential stress across the thickness of deposited magnetic material is a major limitation for application in MEMS devices and significant work has been done to control the stress of deposited permalloy thin films[184, 193]. In a recent study, the composition of an electroplated permalloy film was controlled by current density and plating bath composition showing a modification in the crystal structure from a BCC iron phase to an FCC nickel phase with increasing nickel content. Grain size, coercivity and hardness were found to vary significantly with composition [194]. Unfortunately, in this study the deposition rate varied by four times in the different compositions tested and this could be the reason instead of composition for variations in coercivity, grain size, and crystal structure. The study of effect of deposition parameters and composition in Ni-Fe thin films has been reviewed by

---

<sup>2</sup> This chapter includes work done by Chris Holt to create devices for this publication: J Losby, JAJ Burgess, CMB Holt, JN Westwood, D Mitlin, WK Hiebert and MR Freeman, *Journal of Applied Physics*, 108 (2010) 123910.

Freedman showing the relationship between coercivity and composition, grain size and deposition temperature[195].

Recent work by the Freeman group has demonstrated the exceptional sensitivity of thin film NEMS integrated with permalloy for studying the magnetism of single nanoscale magnetic objects. [122, 189, 192] Smaller features of a torsion resonator results in higher sensitivity[189]. Developing techniques to fabricate micro and nanoscale devices from permalloy thin films is important to realizing better sensitivity in these sensors. Previous work has mostly been conducted using thin films deposited on silicon[192], or silicon nitride[189] supports that do not contribute to the magnetic sensitivity and only provide support. By removing these supports and fabricating devices entirely from permalloy sensitivity could be significantly improved. Very little work has been done in fabricating unsupported all metal permalloy NEMS devices as demonstrated in this work.

A method for manufacturing permalloy based MEMS and NEMS is useful for conducting micro-magnetic experiments and investigating the interaction and coupling between mechanical motion and magnetic behaviour at the nanoscale. The binary nickel-iron alloy system spans a range of magnetic properties from hard to soft. By tuning the composition and deposition parameters it is possible to manipulate the magnetic behavior, mechanical properties and stress in the thin films deposited[154, 196]. Using magnetron co-sputtering the composition of a deposited thin film can be precisely controlled. In this study a range of nickel-iron compositions was deposited and the crystal structure, surface morphology, thin film stress and magnetic properties were measured over a range from pure nickel to 40at.% iron. MEMS and NEMS devices were then fabricated using optical and electron beam lithography and the resonant properties of NEMS singly clamped cantilever devices were characterized.

## 7.2 Experimental

Single crystal silicon <100> wafers were cleaned using a H<sub>2</sub>O<sub>2</sub>:H<sub>2</sub>SO<sub>4</sub> solution and rinsed using deionized water prior to depositions. For the sub-micrometer scale devices a thermal oxide was grown on the silicon wafers by thermally oxidizing in a quartz tube furnace for 2 hours at 1000°C in a wet nitrogen environment prepared by bubbling the feed gas through 95°C water at 40sccm.

All thin films fabricated in this study were deposited using magnetron co-sputtering. (AJA Orion 8) Prior to all depositions the base pressure of the sputtering chamber was pumped to below 5x10<sup>-8</sup> Torr. During depositions, the flow rate of Argon (99.999% Purity, Praxair) was held at 10sccm and the sputtering pressure in the chamber was maintained at 4 mTorr. Two pure targets of Nickel (99.99% Plasmaterials) and Iron (99.99% Plasmaterials) were used as deposition sources.

Rate testing was done with an in-plane quartz crystal microbalance to find the relationship between deposition rate and sputtering power for each material. The composition of the co-sputtered films was adjusted by setting the required powers for each deposition source using the calibration data. A thin 5nm thick chromium adhesion layer was used for the thicker micro devices but no adhesion layer was used for the thinner sub-micrometer scale devices fabricated. The iron deposition rate was from 0 to 5.7 nm/min and the nickel rate was fixed at 7.9 nm/min in order to achieve the range of compositions tested.

For fabrication of the micrometer scale devices, after thin film depositions a  $\sim 1 \mu\text{m}$  thick, HPR 504 photoresist was patterned using photolithography and the NiFe film was etched using an etching solution consisting of a mixture of 1HF:1HNO<sub>3</sub>:5H<sub>2</sub>O by volume. After etching the photoresist was rinsed off with acetone, IPA and water in sequence. The patterned devices were then released using a XeF<sub>2</sub> dry etch. The process flow for the fabrication of these devices is shown in Figure 7.1.

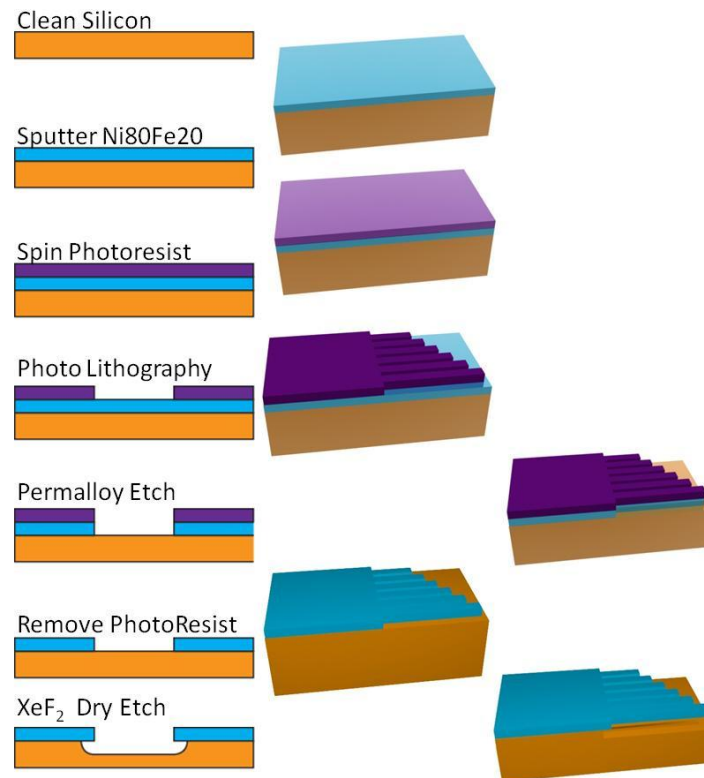


**Figure 7.1: Process flow for fabrication of micrometer scale devices. Sputtered permalloy is patterned with a HPR 504 photomask and a chemical etch and the patterned devices are released using a XeF<sub>2</sub> dry etch.**

For the sub-micrometer scale devices, electron beam lithography was conducted to pattern a double layer positive resist consisting of Poly(methyl meth-acrylate) (PMMA) 950 and 495 that was 360nm thick in total on the oxidized silicon wafers. After patterning, the desired NiFe composition was sputtered onto the samples without an adhesion layer. A simple lift-off procedure was conducted to remove the

PMMA and photoresist and the NiFe film on top of the resist. First the sample was soaked in acetone for 2 hours, rinsed with acetone, isopropyl alcohol, and deionized water. The sample was then placed in an acetone bath that was ultrasonically agitated for 30 seconds and re-rinsed with acetone, isopropyl alcohol and deionized water and dried using compressed nitrogen.

The release was conducted with a 20 minute etch in an iron chloride containing Buffered Oxide Etch (BOE) solution (200mL BOE and 3 grams FeCl<sub>2</sub>). The iron chloride helps reduce the etching rate of the nickel-iron devices during the release. The sample was then quickly transferred to a large beaker filled with water. In order to prevent stiction of the released devices, in this wet etch process the sample was slowly transferred to a lower surface tension solution of isopropyl alcohol and then finally to a solution of pentane before drying. This was accomplished by preparing 3 solutions of successive dilutions to transfer from water to IPA and 3 more solutions of successive dilution to transfer from IPA to Pentane. The sample was quickly transferred through the set of solutions spending 60seconds in each solution with care not to let the sample dry between transfers. The sample was then transferred to a hotplate set to 150°C to dry quickly. This process was adapted from Raccurt et al. who showed that stiction was dramatically reduced by transfer to a lower surface tension solution before drying released MEMS cantilevers. The surface tension of IPA and Pentane are significantly lower than water as shown in Table 7.1 from Raccurt’s paper discussing this technique for preventing stiction as an alternative to critical point drying[197].

**Table 7.1: Comparison of the surface tensions of water, isopropyl alcohol, and pentane as reported by Raccurt[197].**

Liquid	Water	Isopropyl Alcohol	Pentane
Surface Tension(10 <sup>-3</sup> Nm <sup>-1</sup> )	73.05	21.7	13.72

The full process flow for the fabrication of the sub-micrometer devices is shown in Figure 7.2.

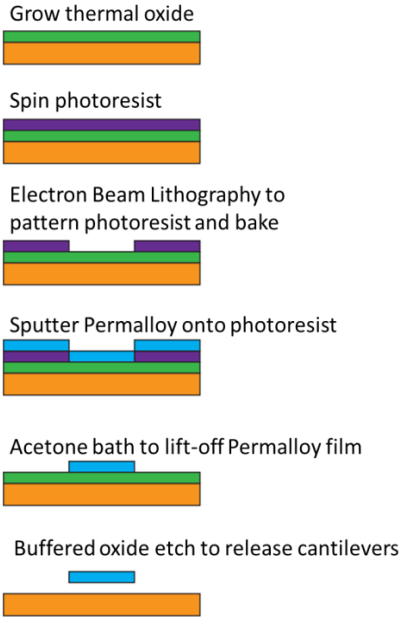


**Figure 7.2:** Process flow for fabrication of submicrometer scale devices. Sputtered permalloy is patterned with a dual layer PMMA photoresist in a lift off process and then the devices are released using a FeCl saturated BOE solution and a pentane solution transfer.

X-ray diffraction analysis was conducted in a Bruker AXS D8 Discover diffractometer with a GADDS area detector and a Cu K $\alpha$  source. Scanning electron microscopy was conducted in a Hitachi S-4800 scanning electron microscope with a field emission source. Compositions were confirmed using an EDS system mounted on a Hitachi S3000N SEM. Film stress measurements were done with an in-situ Multi-beam Optical Stress Sensor attached to the sputtering chamber using viewports in the chamber to observe the substrate curvature during depositions.

The resonance frequency of an array of singly clamped beams was measured using the experimental apparatus shown in Figure 7.3. A network analyzer (HP8752C) was used to drive a piezo-electric element mounted under a chip containing the NEMS cantilever beams. Optical detection of the movement of the cantilever beams was done using a helium neon laser ( $\lambda=632.8\text{nm}$ ) which sensed small changes in the reflected optical power, where the contrast was from interference between light reflected from top of the cantilever beam and the silicon substrate. The cantilevers were held at a vacuum of approximately  $10^{-5}$  torr during resonance testing.

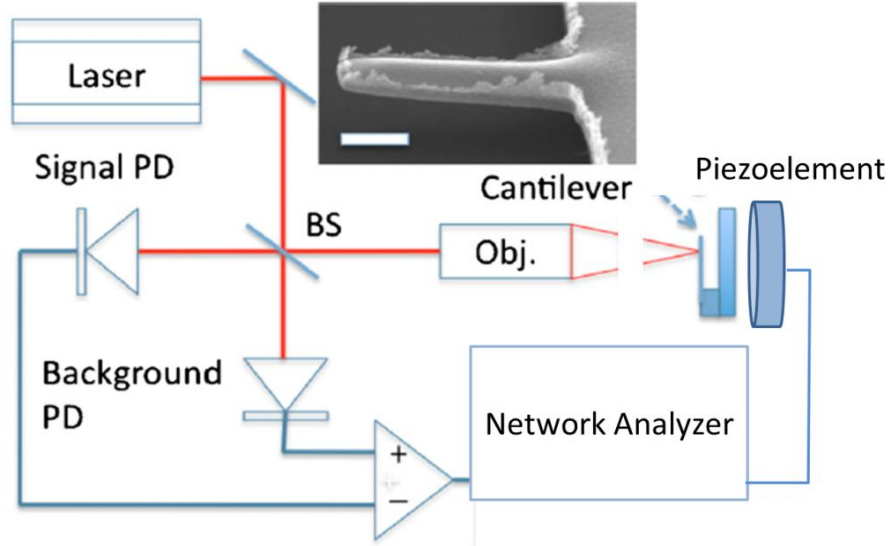


Figure 7.3: System used for resonant testing of the NEMS cantilever structures. The inset is a scanning electron micrograph of a released beam 300nm wide and 2 $\mu$ m long. Scale bar is 500nm.

## 7.3 Results

### 7.3.1 XRD

Figure 7.5a shows the XRD scans for 200nm thick films deposited on silicon wafers at room temperature with the compositions Ni, Ni-10at.% Fe, Ni-20at.% Fe, Ni-30at.% Fe and Ni-40at.% Fe. The phase diagram for Ni-Fe is shown in Figure 7.4. At equilibrium a body centered cubic (bcc)  $\alpha$ Fe phase is expected at compositions below 3% Ni, a mixture of bcc and fcc phases is expected from 3-75%, there is a region where the FeNi<sub>3</sub> phase is expected from 75% to 90%, and a face centered cubic (fcc) phase is expected above 95%. In experiments (not equilibrium) with slowly cooled melts, the fcc phase is obtained in compositions above 30% Ni[198]. A study by Kaloshkin et al. preparing different NiFe compositions through mechanical alloying did not find an FeNi<sub>3</sub> phase and showed that an FCC phase is obtained from 30-100% nickel, a mixed bcc + fcc region from 20-30% and a bcc phase below 20%[199, 200].

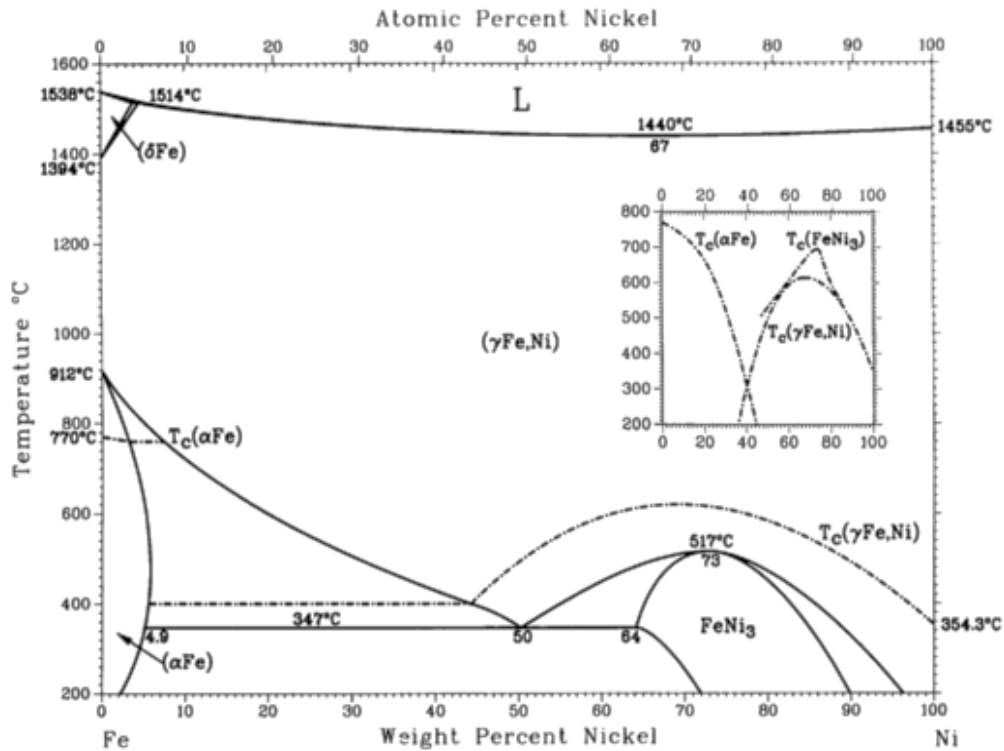


Figure 7.4: Phase diagram for the Ni-Fe System[201].

All of the films deposited in this work show peaks in the positions expected for the (111), (200), and (220) of Nickel showing that all of the deposited films are FCC phase which is expected for compositions above 30% nickel. As additional iron is added to the film the peaks broaden showing a reduction in grain size. The peaks also slightly shift to lower  $2\theta$  positions showing an increase in lattice spacing with additional iron. The films deposited at 200°C shown in Figure 7.5b have sharper peaks indicating a larger grain size in the deposited films. Scherrer analysis of the (111) peak gave grain sizes of 15nm, 13nm, 11nm, and 8nm for the 200°C deposited Ni-10at.% Fe, Ni-20at.% Fe, Ni-30at.% Fe and Ni-40at.% Fe films respectively. And grain sizes of 12nm, 10nm, 9nm, 8nm, and 8nm were obtained for the 20°C deposited Ni, Ni-10at.% Fe, Ni-20at.% Fe, Ni-30at.% Fe and Ni-40at.% Fe films respectively. This analysis confirms the reduction in grain size with addition of iron and the finer grains seen in the lower temperature deposition films.

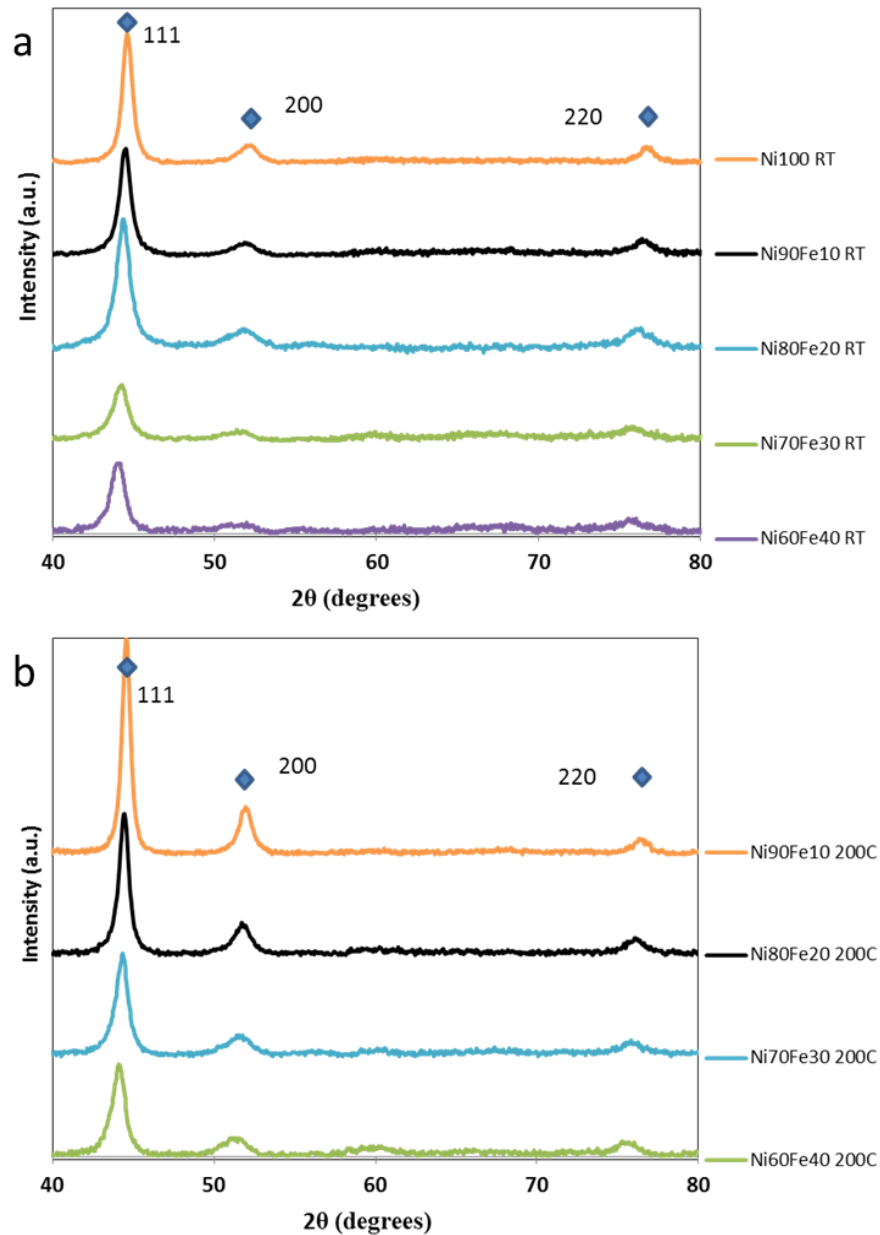


Figure 7.5: X-ray diffraction of 200nm thick co-sputtered Ni-Fe thin films deposited at a) room temperature and b) 200°C. Indexed peaks are for face centered cubic nickel

### 7.3.2 Average Film Stress

A Multi-beam Optical Stress Sensor was used to measure the change in curvature of the silicon wafers as the thin films were being deposited. An array of parallel laser beams was projected onto the wafer and observed using a CCD camera. The spacing between the beams changes when the wafer bends giving a way of finding the stress in the deposited film. The average stress was found using the difference in curvature of the silicon wafer before and after the thin film deposition. Figure 7.6 shows the

results from different compositions of NiFe at the temperatures of 25°C and 200°C. It is clear that the films deposited at 200°C have significantly lower average tensile stress than the films deposited at 25°C. Also visible is an increase in stress as additional Fe is added to NiFe during the 200°C depositions.

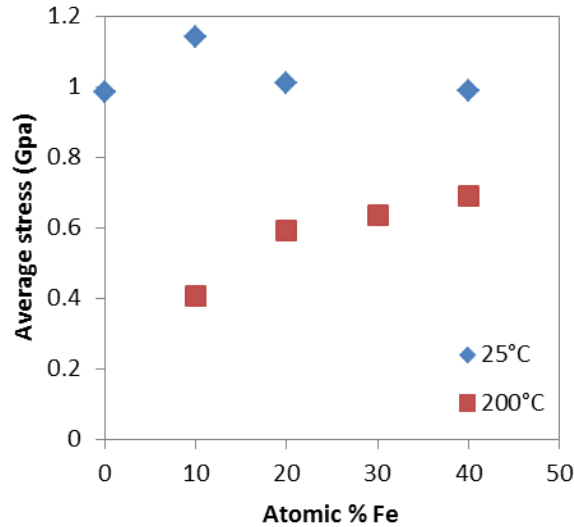


Figure 7.6: Average thin film stress for 200nm thick co-sputtered Ni-Fe thin films measured by an in-situ Multi-beam Optical Stress Sensor.

### 7.3.3 Magnetic Properties

Magneto-Optic Kerr Effect (MOKE) was used to produce magnetic hysteresis curves for each of the deposited alloys to characterize the magnetic behaviour of the deposited films. The results are shown in Figure 7.7a for films deposited at room temperature and in Figure 7.7b for films deposited at 200°C. The coercivity is higher for the compositions deposited at room temperature than the samples deposited at 200°C. And for each set of depositions the composition Ni-30a.t.% Fe was the one with the lowest coercivity. Grain size has a significant effect on the coercivity of Ni-Fe thin films[202]. Smaller grain sizes are expected to correlate with smaller coercivity values. Increased stress in a thin film can result in increased coercivity as seen in literature[203, 204]. The larger grain sizes observed from the XRD results for the 200°C deposition films do not correlate with the observed lower coercivity, but the significantly lower stress in these films does correlate with the expected trend of lower coercivity. All of the films were shown to be ferromagnetic materials with well-defined hysteresis loops. The coercivity of these films is higher than that reported for bulk permalloy. At this point the composition of Ni-20a.t.% Fe was chosen for further analysis for application as a metal for MEMS fabrication.

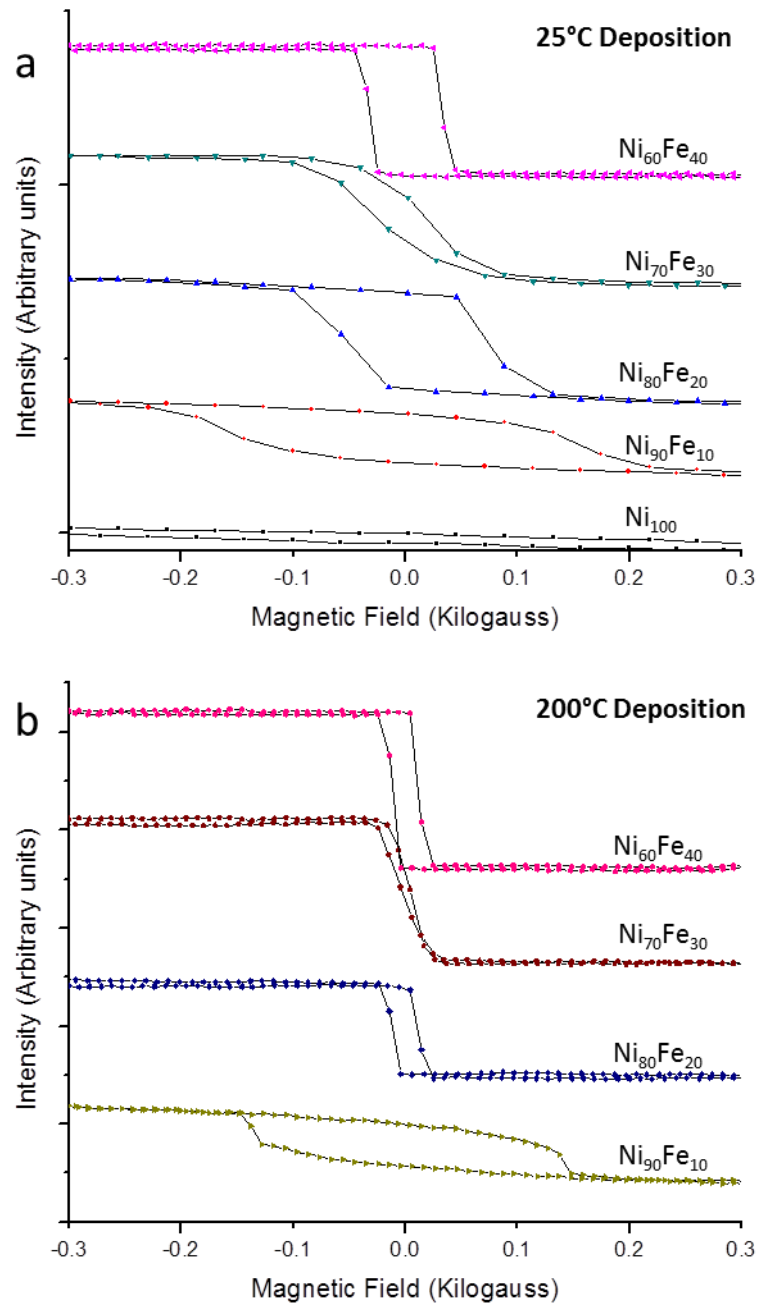


Figure 7.7: Magnetic hysteresis loops acquired using MOKE of Ni-Fe thin films deposited at a) room temperature and b) 200°C .

### 7.3.4 Surface Morphology

From the magnetic characterization it was found that the best magnetic performance could be found in films that were deposited at higher temperature. Lift-off was the best way to undertake patterning the permalloy thin films for sub-micrometer devices as etching resulted in significant undercutting of the photoresist and limited the resolution of possible fabricated devices. Because lift-off of a PMMA Electron Beam Lithography resist was used to pattern the nanostructured devices,

we were limited in the temperature of the substrate during deposition, and 200°C was considered too high for lift-off with these materials. At high temperatures in high vacuum the photoresist is expected to off-gas in the deposition chamber. Also possible is that the photoresist will undergo a chemical change that makes it difficult to remove using acetone during the release step. For this reason a series of experiments was done to assess the possibility of annealing the devices after patterning but before the release step. By annealing the grain size was expected to increase and the stress gradient through the thin film was expected to decrease. Two annealing temperatures were used: 200°C and 300°C in an argon atmosphere with 5°C/min heating and 5°C/min cooling and an annealing time of 2 hours. The SEM of the thin films after this treatment is shown in Figure 7.8c, d, and e. The feature size in the film deposited at 20°C shown in Figure 7.8b is significantly smaller than that shown in Figure 7.8a deposited at 200°C. Both films appear to be quite smooth and uniform over their surface. After annealing the 20°C deposited film at 200°C small cracks begin to appear on the surface of the film (Figure 7.8d). The cracks are approximately 10nm across and 30-100nm in length. In the sample annealed at 300°C the cracks were significantly larger being 15nm across and 50-150nm in length. This cracking is assumed to be caused by the significant thermal expansion mismatch between the silicon wafer and the NiFe film. Nickel iron has a significant variation in thermal expansion depending on the composition ranging from  $2 \times 10^{-6}/^{\circ}\text{C}$  -  $12 \times 10^{-6}/^{\circ}\text{C}$  with a minimum around Ni-60a.t.% Fe and a value of  $12 \times 10^{-6}/^{\circ}\text{C}$  at Ni-20a.t.% Fe[198]. Silicon has a thermal expansion coefficient of  $3 \times 10^{-6}/^{\circ}\text{C}$  which is significantly lower than what is expected for the permalloy film on its surface. This would result in the film shrinking more than the silicon wafer as the system is cooled from the annealing temperature and could be the cause of the cracks observed in the films. Figure 7.8e shows a crack that formed at a clamping location for a micro-beam fabricated from a film annealed at 200°C showing that the film fails along these cracks that are shown on the surface. These results suggested that post patterning annealing introduced cracking even at 200°C and this technique was not used to try to modify the grain size in the fabricated MEMS/NEMS devices.

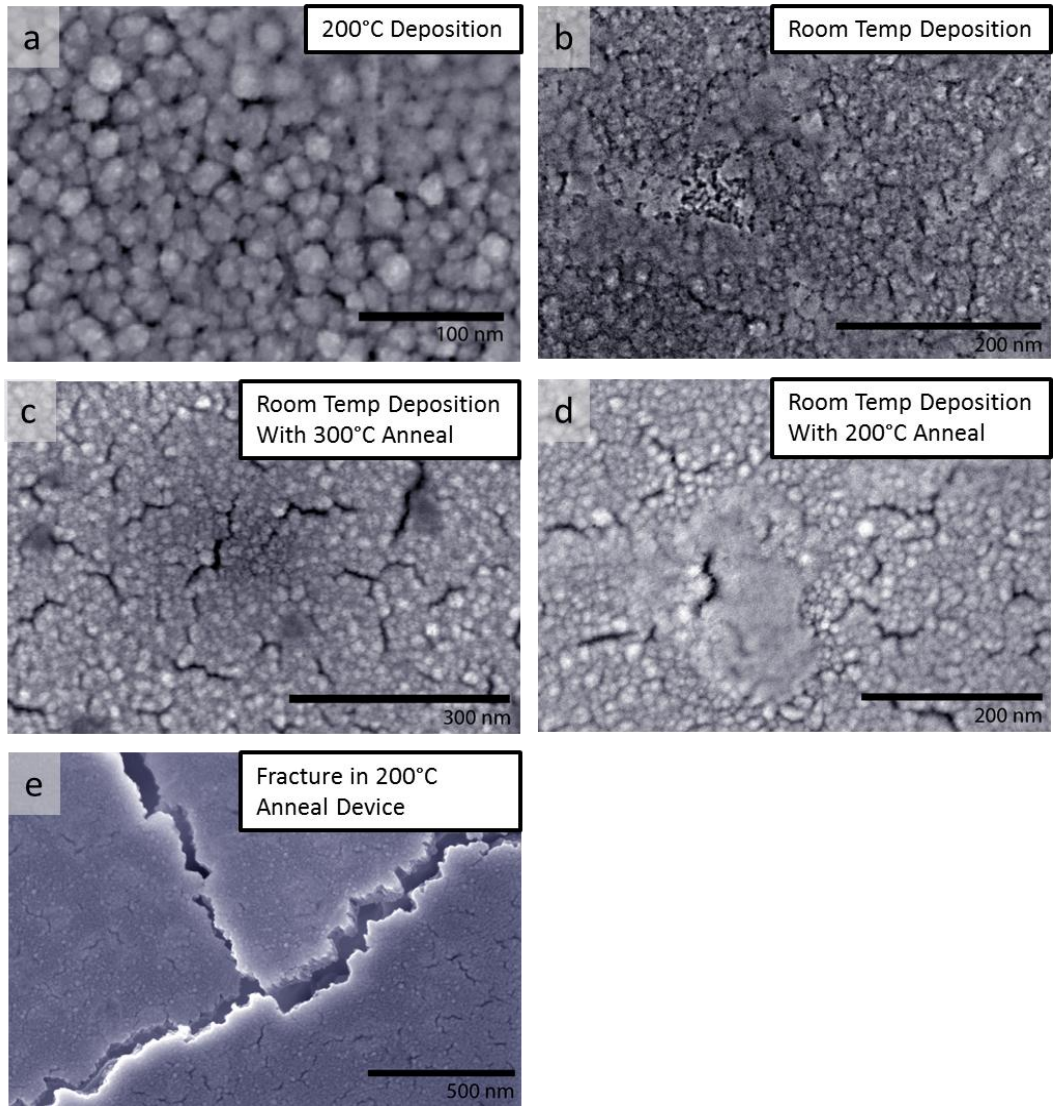


Figure 7.8: Scanning electron micrographs of a 200nm thick  $Ni_{80}Fe_{20}$  thin film with different thermal treatments. a) Film deposited onto a 200°C heated substrate, b) Film deposited onto a room temperature substrate, and c), d) room temperature deposition followed by a 300°C and 200°C two hour anneal respectively. e) A magnified section of a fracture in a 200°C annealed device after release.

## 7.4 Discussion

### 7.4.1 NiFe MEMS Fabrication

The stress is not constant throughout the thickness of a thin film. A difference in the stress  $\sigma$  through the film can cause beams made from this film to bend. The following formula can be used to describe the uniaxial residual stress field in a thin film[205].

$$\sigma_{total} = \sum_{k=0}^{\infty} \sigma_k \left(\frac{y}{h/2}\right)^k \quad \text{Eq. 7.1}$$

Where  $y \in (-\frac{h}{2}, \frac{h}{2})$  and is the coordinate over the thickness  $h$  with the zero chosen at the middle of the thin film. Taking the first two terms from this equation produces the approximation [205]

$$\sigma_{total} \approx \sigma_0 + \sigma_1 \left(\frac{y}{h/2}\right) \quad \text{Eq. 7.2}$$

where  $\sigma_0$  accounts for the effect of the symmetric polynomial terms in equation 2.1 and  $\sigma_1$  accounts for the effect of the anti-symmetric terms. A diagram of a simple stress that can be approximated by this model is shown in Figure 7.9 where the addition of a uniform stress is added to a gradient stress. The stress gradient across a thin film is what causes curvature in released singly clamped beam structures[205, 206]. Uniform compressive stress leads to buckling of clamped-clamped beam structures[207, 208].

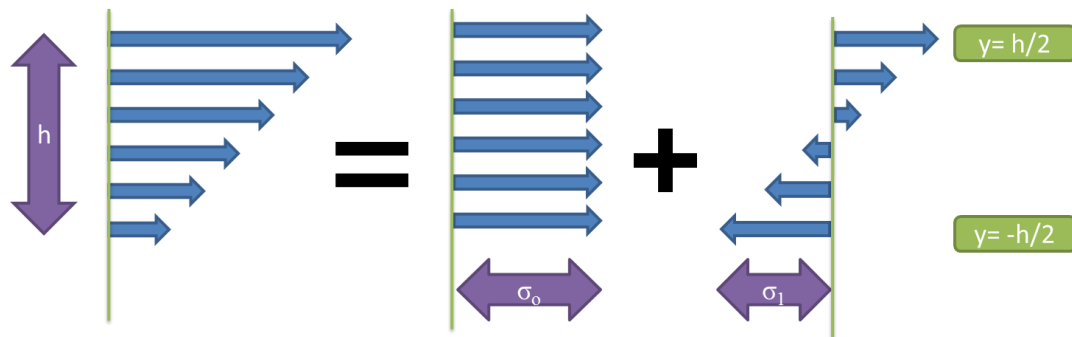


Figure 7.9: Stress model in a thin film including the first two terms of equation 2.1.

The aspect ratio of the released structure and the support geometry decide the direction that the released structures bend. Figure 7.10 shows several MEMS structures that have not been completely released and are bending along the length of the support instead of the length of the beam as shown in Figure 7.11. The curvature of the films varies significantly between the 25°C deposition (b) and the 200°C deposition (a).

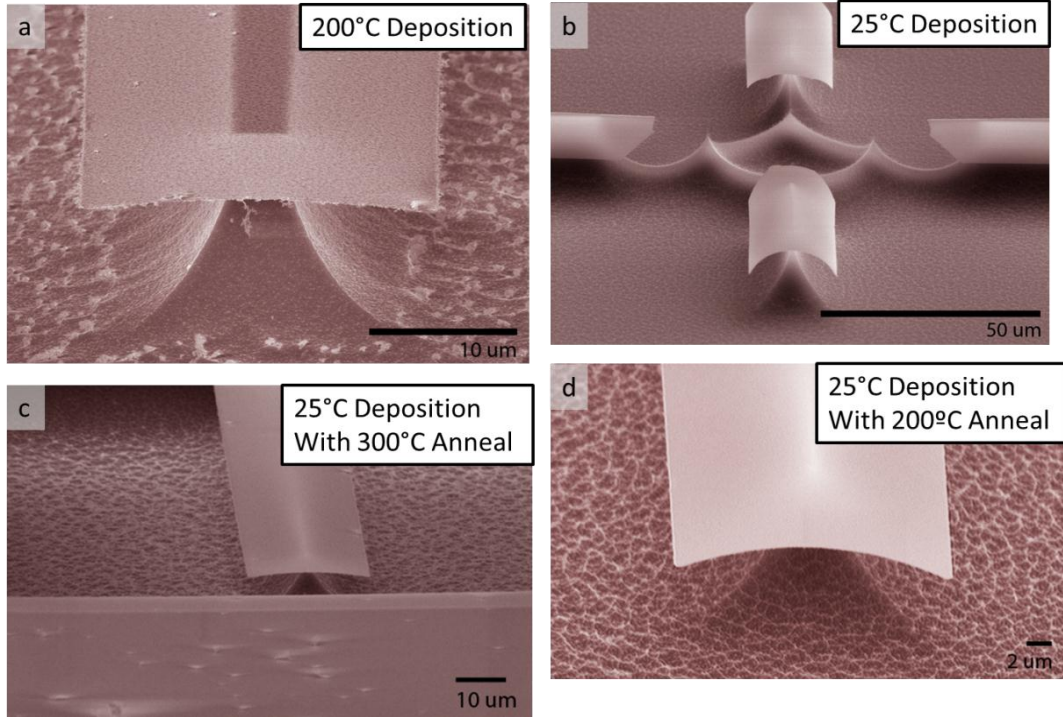
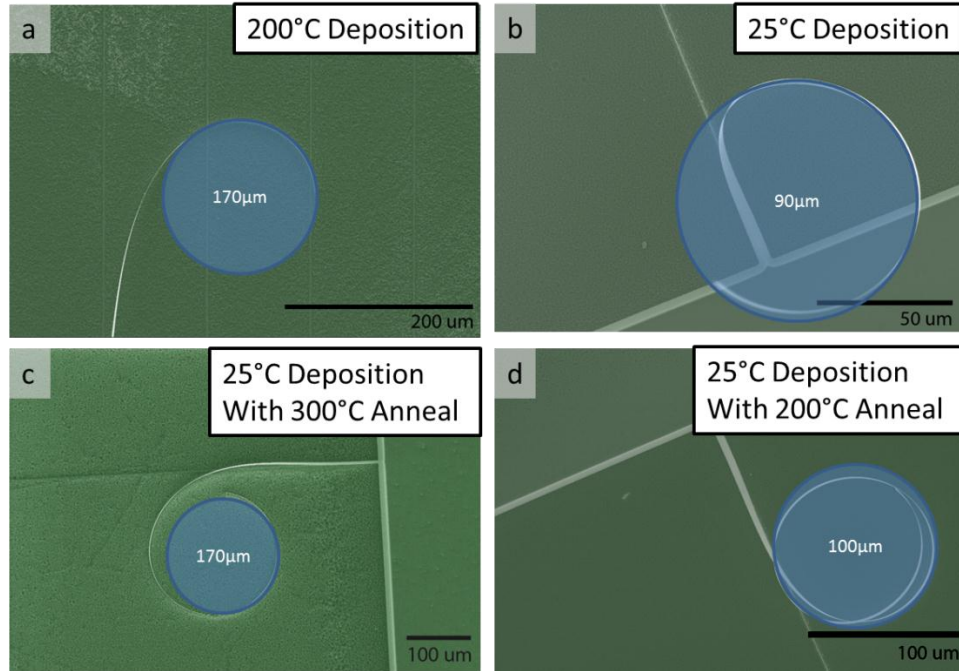


Figure 7.10: End of cantilever images of 200nm thick  $\text{Ni}_{80}\text{Fe}_{20}$  structures released with  $\text{XeF}_2$  deposited at a) 200°C, b) 25°C and annealed at 300°C (c) and 200°C (d).

For a beam structure the peak value of the gradient stress can be recovered from the radius of curvature of the beam using the following equation[205].

$$\sigma_1 = \frac{Eh}{D}$$

Where  $D$  is the diameter of curvature,  $h$  is the thickness of the beam, and  $E$  is the elastic modulus of the material. An elastic modulus of 100GPa for permalloy was used for the calculations of  $\sigma_1$  as this was used in literature for films that were both electroplated and sputtered[209, 210]. Using this relationship with the curl radius of micro-beams 100nm thick and 5um wide made from  $\text{Ni}_{80}\text{Fe}_{20}$  deposited at 25°C and 200°C, and also deposited at room temperature and annealed at 200°C and at 300°C. The images of the curled beams are shown in Figure 7.11 and the resulting  $\sigma_1$  values are 110MPa and 59MPa for the 25°C (b) and 200°C (a) depositions and 100MPa and 59MPa for the 200°C (d) and 300°C (c) annealed samples, respectively.



**Figure 7.11:** Released singly clamped cantilever structures fabricated from 200nm thick Ni<sub>80</sub>Fe<sub>20</sub>. Blue circles are drawn to match the radius of curvature of the released structures. These beams curled and then fell over onto the substrate during the release process.

This thin film gradient stress causes long cantilevers (>100µm in length) to bend significantly, while in shorter beam structures the bending amount is much less pronounced. Figure 7.12 shows three different magnifications of a section of a 170 µm diameter circle. Figure 7.12b shows that at length scales of approximately 10µm the curvature observed is quite slight. In Figure 7.12c it is shown quite clearly that at length scales below 1 µm that the curvature is almost imperceptible. When making devices with critical dimensions less than 1µm, all of the deposited films studied in this set will result in devices with very little noticeable curvature. Gradient stress approximately an order of magnitude higher would be required in order to result in failed singly clamped devices. Mitlin group published a paper on Ni-Mo metallic glass based nanometer scale devices [95] that were claimed to be “stress-free”. In the paper the devices imaged had lengths less than 2µm and with this low length of measured beam it would be difficult to discern small stress gradients in the films. A figure from a paper by Lubber et al. is shown in Figure 7.12d showing a very straight nanoscale cantilever. Below, in Figure 7.12e is a figure of the same Ni<sub>56</sub>Mo<sub>46</sub> amorphous material that was deposited 250nm thick and patterned using a mask for long (>100µm in length) cantilevers. The curvature at the longer length scale is significant (~200µm) and is a similar length scale to that seen with the Ni<sub>80</sub>Fe<sub>20</sub> films deposited in this study.

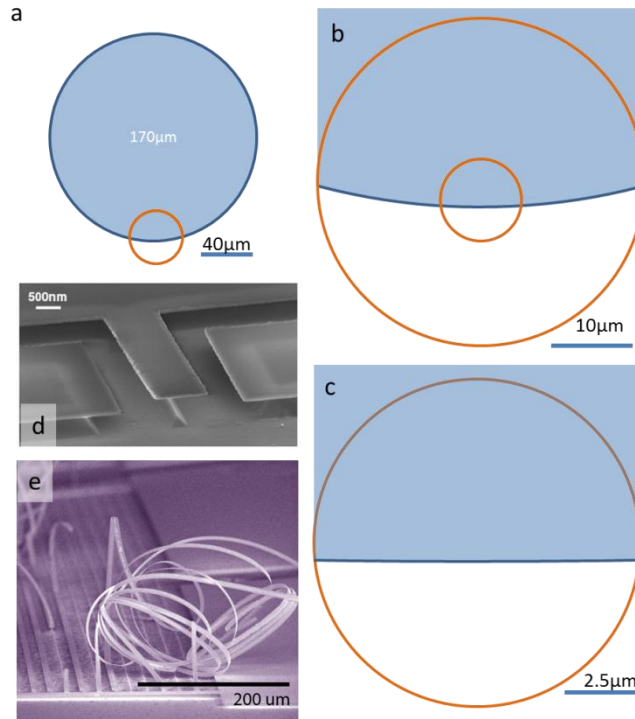


**Figure 7.12:** Sequence of magnifications of a circle (a,b,c) showing that a large curl radius is hard to notice on a small length scale. d) A thin NiMo beam that is only a few micrometers long showing very little curvature. e) 500 μm long beams made from the same material showing significant curvature.

Figure 7.13a shows three singly clamped beams fabricated from 100nm thick 200°C deposited  $\text{Ni}_{80}\text{Fe}_{20}$  on silicon. The length scale of these beams is significantly less than 100μm and the curvature is noticeable. The shortest beam just barely touches the substrate surface after release. It would be expected that beams shorter than this 50μm long beam would be fully released and not touch the substrate. Figure 7.13b shows a paddle like structure with a suspended cross having arms that are approximately 20μm long. These arms are completely released and do not curl enough to touch the substrate, demonstrating smaller devices that show very little curvature. These devices are in the scale range shown in Figure 7.12b where slight curvature is noticeable. In the sub-μm length devices this curvature will be extremely small and difficult to detect using scanning electron microscopy.

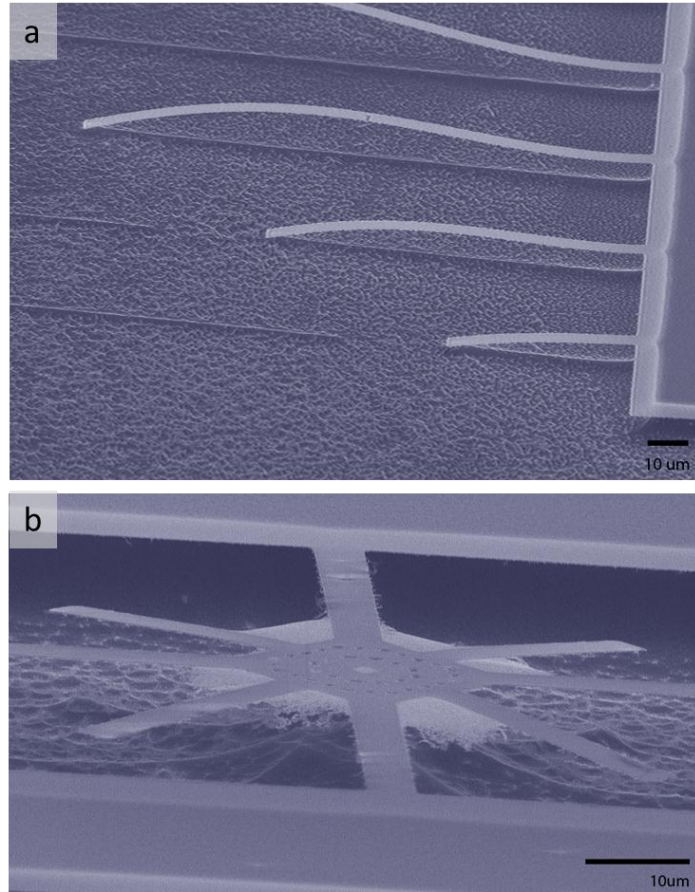


Figure 7.13: Released Ni<sub>80</sub>Fe<sub>20</sub> structures showing a) longer curved beams touching the substrate and beams less than 50μm long (b) showing very little curvature.

#### 7.4.2 NiFe NEMS Fabrication

With these results it was concluded that it would be possible to create sub-micrometer scale devices from these NiFe based thin films that would not have significant curvature and would have the desirable soft magnetic properties required for conducting nanoscale magnetic experiments. The fabrication process for these devices is slightly different in that it uses a thermally grown silicon oxide layer, removed in a FeCl saturated BOE solution, as a sacrificial layer instead of silicon (removed using XeF<sub>2</sub>). The resist used for lift off was a PMMA based dual layer resist and it was exposed using electron beam lithography. The deposition parameters for the permalloy thin films were kept the same as those used for the MEMS scale devices. The process flow for the fabrication of NiFe NEMS is shown in Figure 7.2.

Some of the resulting successfully fabricated NiFe devices are shown in Figure 7.14. Figure 7.14a shows a doubly clamped beam that is 1.5μm long and less than 100nm across, Figure 7.14b shows a 4μm long singly clamped beam that is less than 100nm across. Shadowing from the deposition process into the EBL resist resulted in the thickness of deposited NiFe being thinner in the small features than in the larger pad

features. It is expected that the thickness of the beams is significantly less than the 100nm nominal deposition thickness. The cantilevers shown in Figure 7.14b and the inset of Figure 7.3 make it clear that the thickness of the beam is significantly less than the thickness of the base where shadowing would have no effect because of the larger feature size. Roughness observed on the edges of the base in b are caused by the lift off process and result from a thin metal coating of the photoresist side wall not being completely removed during the lift off. Figure 7.14c shows a low magnification overview of the array of clamped-clamped beams and singly clamped cantilevers fabricated. The large structure in the forefront is a broken wire-bond attachment that would be used to electrostatically actuate the nanostructured devices.

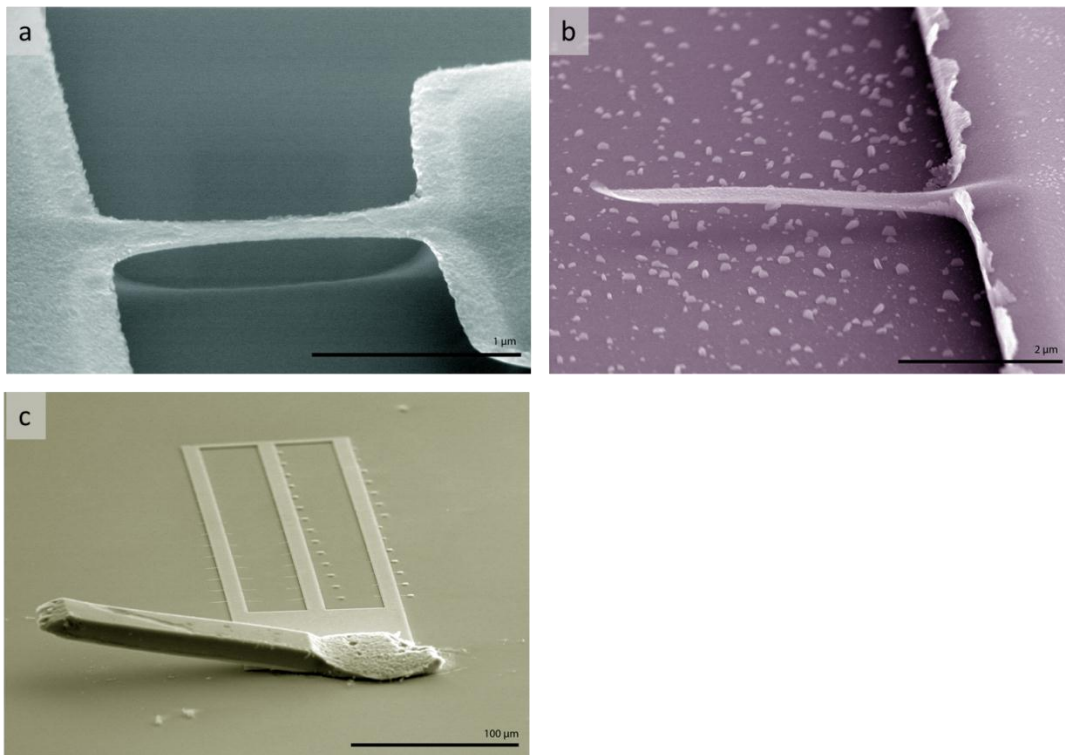


**Figure 7.14:** NEMS devices fabricated from nickel iron thin films. a) A doubly clamped beam, b) a singly clamped cantilever, and c) a lower magnification view of the array of NEMS structures. The structure in the forefront is a wirebond used to electrostatically actuate the devices.

### **7.4.3 NEMS Resonant Properties**

The results from the resonant frequency testing are shown in Figure 7.15 from a paper published by Losby et. al. using the same devices[122]. The equation governing the relationship between the length of a singly clamped beam and the resonance frequency for the first fundamental out of plane flexural mode is as follows[122]:

$$f_{res}^{-1/2} = \sqrt{\frac{2\pi}{3.516}} \left(\frac{\rho A}{EI}\right)^{1/4} L \quad \text{Eq. 7.3}$$

Where  $\rho$  is the density of the material,  $E$  is the effective Young's Modulus,  $I$  is the moment of inertia,  $L$  is the length of the beam, and  $A$  is the cross sectional area of the cantilever[122]. The slope from the devices tested was equal to  $0.17 \pm 0.01$   $\text{MHz}^{-1/2}/\mu\text{m}$ . Because the beams are thinner than the nominal deposited thickness due to shadowing effects during deposition there is considerable error in determining the thickness of the cantilevers used in this experiment. Using the measured slope from Figure 7.15 and equation 7.3 one can calculate the range in the expected elastic modulus: 255GPa if the beam is 40nm thick to 113GPa if the beam is 60nm thick. The shape of the cross section in the tested beams is not a perfect rectangle and has a slight arch from shadowing that would reduce the accuracy of the measurement. The sensitivity of this method to changes in the cantilever thickness make the uncertainty in thickness from shadowing in the NEMS cantilever a very large contributor to the error in the modulus measurement. The inset of Figure 7.15 shows the frequency response of a  $5\mu\text{m}$  long cantilever and its comparison to a Lorentzian curve fit. The curve fit gives a quality factor of 880. This is similar to the results from other metallic cantilevers of this size in vacuum and at room temperature. Other nano-scale all metallic resonators have shown similar Q factors such as Al-32%Mo resonators 20nm thick with Qs ranging from 30 to 245[94], another Al-32%Mo cantilever that is  $5\mu\text{m}$  long 20nm thick with a Q factor of 482[211] and Au-5at.%Ta cantilevers that were 50nm thick with Qs ranging from 304-640 [212].

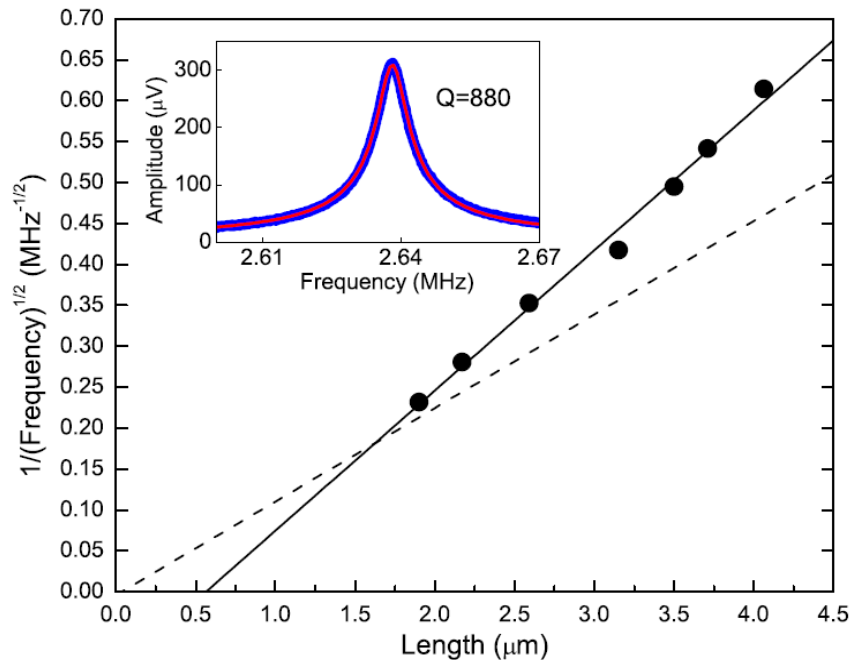


Figure 7.15: Resonant frequency of an array of singly clamped beams ranging from  $4\mu\text{m}$  to  $2\mu\text{m}$  in length. Inset is the frequency response of a  $5\mu\text{m}$  long beam.

## 7.5 Conclusion

A range of compositions of co-sputtered permalloy thin films was explored for application as a material for building magnetic resonant cantilevers. Compositions ranging from pure nickel to Ni-40a.t.%Fe were deposited and tested for average film stress using a MOSS technique, films deposited at 200°C were found to have a significantly lower average tensile stress than those deposited at 25°C. Microfabricated devices were fabricated out of Ni-20a.t.%Fe composition films deposited at 25°C and 200°C and also of films deposited at 25°C and annealed at 200°C and 300°C. Differential film stress was found to be lowest in the 300°C annealed sample and the sample deposited at 200°C but was found to be low enough to allow for fabrication of extremely straight and uncurled sub micrometer scale devices. An array of different length cantilever beams ranging from 2-5 $\mu$ m long and 300nm wide were fabricated using electron beam lithography and shown to resonate as expected with a quality factor of 880 found for a 5 $\mu$ m long beam.

## 8 Conclusion and Future Work

Thin film techniques and methods span many different length scales and applications. In this work thin film deposition was used to fabricate nanometer thick catalysts for oil upgrading, centimeter scale devices for sensing oil in water, and micrometer scale devices for exploring micro magnetic effects. All of these challenges were met with a similar set of obstacles involving thin film adhesion, substrate film interaction, and film stress management. These challenges were overcome through material design. Each challenge required different deposition techniques in order to achieve the required outcome. Magnetron sputtering worked well for depositing the metals required for micrometer scale cantilevers. Thin film stresses in these deposited films prohibited making larger devices as beams longer than 10um in length were significantly curved. By fabricating larger devices from electroplated nickel these stress issues were resolved and mm length devices were successfully fabricated without any noticeable bending or buckling. The ductility and thickness of electroplated nickel made fabrication on high pressure feedthroughs possible where sputtered thin films consistently failed due to either oxidation or broken electrical contact due to thermal expansion mismatch causing cracking in the deposited films. This same effect of thin film stresses caused ultra thin deposited tungsten films to delaminate during sulfidation and limited the thickness of deposited catalyst films to less than 4 nm in the work related to hydrogenation of model compounds. The ability to select and design a thin film deposition method for a specific application enables the fabrication of a large variety of sensors, devices, or functional materials. This work demonstrated this process for a wide range of applications ranging from oil upgrading (hydrogenation) to analysis (phase identification), and from sensor development for hostile oil well environments (released and anchored sensors) to high vacuum laboratory experiments (NiFe Cantilevers).

The focus of this thesis is on the development of two platforms for integrating microfabricated sensors with high pressure feedthroughs for application in hostile high temperature high pressure environments. A specific application in oil well production logging is explored and two sensors were implemented with these developed platforms for application in an oil well.

Production logging is a global oil-services industry where down-hole information (such as temperature, pressure, phase identification, and fluid flow) is gathered from already producing wells to assess their health and condition[1, 2]. Data gathered from a well can be used to make important decisions on well maintenance and modifications to improve production[3]. Micro-machined technology is almost ubiquitous in modern society, comprising many of the core sensors in automobiles, aerospace, home entertainment and biomedical applications. However, such technology has achieved almost no ingress into down-hole sensing. This is due to the inability of conventional micro-machined materials to survive the extremely

harsh well environment which combines high temperatures (up to 180 °C), high pressures (up to 100 MPa), and corrosive fluid media. Traditional packaging of MEMS devices using wirebonding is not compatible with this hostile environment and typical MEMS plastic encapsulation techniques are also not suitable. This work outlines a platform for integrating MEMS sensors into a down-hole environment and represents a major revolution in down hole logging technology.

Fabricating multiple MEMS sensor elements onto high pressure feedthroughs enables a smaller oil well production logging tool capable of measuring multiple fluid properties at a single location in the wellbore. Current tools successfully measure multiple oil well fluid properties but at different locations in the well bore with each sensor only measuring a single parameter at a single location. By integrating sensors directly into a high pressure feedthrough, electrical connections in the hostile oil well environment can be avoided and the electrical sensing circuits can be more closely integrated with the sensor elements themselves. This tight integration and the increase in sensor durability and decrease in sensor size was accomplished by microfabricating sensors directly onto a high pressure feedthrough. The two solutions shown from Schlumberger and NASA for integrating MEMS sensors with a high pressure feedthrough are either extremely complicated and delicate (Schlumberger) or not capable of operating at oil well pressures (NASA). No other wirebond free solutions for MEMS integration with a high pressure feedthrough exist. This work demonstrates a solution that provides a wirebond free IBM SLT like platform for MEMS sensor integration with a high pressure feedthrough that is simple and robust.

The freestanding devices developed in this work use a sacrificial tin scaffolding surrounding an array of pins instead of a traditional substrate for supporting MEMS devices. Creating a new substrate with a sacrificial layer on a surface that ordinarily would prohibit lithography based fabrication is demonstrated in this work.

The first platform developed, involving microfabrication on a cut and polished feedthrough, is more robust than the wire bonded silicon die technique used for MEMS integration in pressure sensors and therefore allows for direct interface of a microfabricated sensor with a fluid environment which is not currently possible. The platform developed within has been pressure tested to 10,000psi and temperature cycled several times from 20°C to 200°C. This platform enables electronics integration with a variety of electrical and thermal based sensors within the oil well environment.

The second platform developed, involving free space fabrication of nickel microfabricated devices onto an array of pins, enables for the very first time microfabricated metal MEMS that are released by distances of 1cm from their substrate. With sub 50um features and heights of 1cm the structures fabricated in this work are unique.

The released MEMS sensor process flow allows for fabrication to be done on any pin array substrate regardless of surface quality. By fabricating a new surface the problem of MEMS substrate selection is avoided. Being able to place released MEMS sensors directly onto traditional style circuit boards, ceramic circuit boards, electrical connectors, ribbon cables, pin headers, or high pressure feedthroughs greatly improves the variety of possible applications and reduces fabrication costs.

These two developed platforms were then used to fabricate thermal conductivity sensors that showed excellent performance for distinguishing between oil, water, and gas phases. Thermal conductivity sensors are not currently used for phase identification in an oil well, making these sensors unique in the production logging field. Larger macro machined sensors do not respond quickly enough to be used in a flowing environment and use a significant amount of electrical power to heat making their implementation in oil well production logging impossible. Microfabrication enables application of this type of sensor by improving response time and reducing power consumption. Testing was conducted with the two platforms at various flow rates and performance of the released platform was shown to be better than the performance seen in the anchored sensors while both platforms were significantly better than a simply fabricated wrapped wire sensor. The anchored platform was also used to demonstrate a traditional capacitance based fluid dielectric sensor which was found to work similarly to conventional commercial capacitance probes while being significantly smaller in size.

This research will continue over the next two years and the following aspects will be addressed in future developments related to the microfabricated sensors. Testing of a protective coating made from the most resistant and high temperature Parylene HT will be conducted to ensure proper operation of this sensor in an oil well. Further electronics development will be undertaken to integrate these sensors into a data acquisition system that does not require bench top equipment for taking measurements. The fully released sensors could be further developed to improve adhesion of the inconel pins to the electroplated devices. There is significant opportunity in expanding these high pressure feedthrough integrated sensors into other hostile environment sensing applications where high pressure and high temperature fluid property measurement provides valuable information.

# Bibliography

- [1] J. J. Smolen, *Cased Hole and Production Log Evaluation*: PennWell Books, 1996.
- [2] B. H. Incorporated, *Interpretive Methods for Production Well Logs*: Baker Hughes Incorporated, 2000.
- [3] A. D. Hill, *Production Logging: Theoretical and Interpretive Elements*: Henry L. Doherty Memorial Fund of AIME, Society of Petroleum Engineers, 1990.
- [4] T. R. Hsu, *Mems Packaging*: The Institution of Engineering and Technology, 2004.
- [5] J. H. Lau, *et al.*, *Advanced MEMS Packaging*: McGraw-Hill, 2009.
- [6] K. Gilleo, *MEMS/MOEM Packaging*: McGraw-Hill, 2005.
- [7] A. T. Goodwin, *et al.*, "Fluid property sensors," US Patent US 2002/0194906 A1, 2002.
- [8] A. R. H. Goodwin, *et al.*, "A vibrating plate fabricated by the methods of microelectromechanical systems (MEMS) for the simultaneous measurement of density and viscosity: Results for argon at temperatures between 323 and 423K at pressures up to 68 MPa," *International Journal of Thermophysics*, vol. 27, pp. 1650-1676, Nov 2006.
- [9] C. Harrison, *et al.*, "Protective barriers for small devices," US Patent US 7673679, 2010.
- [10] M. E. Kandil, *et al.*, "Determination of the Relative Permittivity,  $\epsilon'$ , of Methylbenzene at Temperatures between (290 and 406) K and Pressures below 20 MPa with a Radio Frequency Re-Entrant Cavity and Evaluation of a MEMS Capacitor for the Measurement of  $\epsilon'$ ," *Journal of Chemical & Engineering Data*, vol. 53, pp. 1056-1065, 2008/05/01 2008.
- [11] A. R. H. Goodwin, *et al.*, "A Vibrating Edge Supported Plate, Fabricated by the Methods of Micro Electro Mechanical System for the Simultaneous Measurement of Density and Viscosity: Results for Methylbenzene and Octane at Temperatures between (323 and 423) K and Pressures in the Range (0.1 to 68) MPa," *Journal of Chemical & Engineering Data*, vol. 51, pp. 190-208, 2006/01/01 2005.
- [12] A. Chikenji, *et al.*, "Apparatus for downhole fluids analysis utilizing micro electro mechanical system (MEMS) or other sensors," US Patent US 7392697, 2008.
- [13] E. P. Donzier, "Method and apparatus for optically discriminating between the phases of a three-phase fluid," ed: Google Patents, 1999.

- [14] P. S. Waggoner and H. G. Craighead, "Micro- and nanomechanical sensors for environmental, chemical, and biological detection," *Lab on a Chip*, vol. 7, pp. 1238-1255, 2007.
- [15] S. Systems. (2012, August 21, 2012). *Cased Hole Logging Production Logging Instrumentation*. Available: [http://www.sparteksystems.com/siteimages/Brochures/Flyer\\_Production\\_Logging\\_Instrumentation.pdf](http://www.sparteksystems.com/siteimages/Brochures/Flyer_Production_Logging_Instrumentation.pdf)
- [16] G. O. Gas. (2012). *Fluid Density Inertial (FDI) Production Logging Tool*. Available: [http://www.ge-energy.com/content/multimedia/files/downloads/GEA17988D\\_FDI.pdf](http://www.ge-energy.com/content/multimedia/files/downloads/GEA17988D_FDI.pdf)
- [17] K. Brueckner, *et al.*, "Electromechanical resonances of SiC and AlN beams under ambient conditions," in *Gallium Arsenide and Other Semiconductor Application Symposium, 2005. EGAAS 2005. European, 2005*, pp. 585-588.
- [18] R. Lundstrum, *et al.*, "Measurement of the Viscosity and Density of Two Reference Fluids, with Nominal Viscosities at T = 298 K and p = 0.1 MPa of (16 and 29) mPa·s, at Temperatures between (298 and 393) K and Pressures below 55 MPa," *Journal of Chemical & Engineering Data*, vol. 50, pp. 1377-1388, 2005/07/01 2005.
- [19] F. Ordway, "TECHNIQUES FOR GROWING AND MOUNTING SMALL SINGLE CRYSTALS OF REFRACTORY COMPOUNDS," *Journal of Research of the National Bureau of Standards*, vol. 48, pp. 152-158, 1952.
- [20] J. H. Welch, "A simple microscope attachment for observing high-temperature phenomena," *Journal of Scientific Instruments*, vol. 31, p. 458, 1954.
- [21] T. E. Pochapsky, "Determination of Heat Capacity by Pulse Heating," *Review of Scientific Instruments*, vol. 25, pp. 238-242, 1954.
- [22] O. Sandberg, *et al.*, "HEAT-CAPACITY AND THERMAL-CONDUCTIVITY FROM PULSED WIRE PROBE MEASUREMENTS UNDER PRESSURE," *Journal of Physics E-Scientific Instruments*, vol. 10, pp. 474-477, 1977.
- [23] H. Ernst, *et al.*, "Dynamic thermal sensor - principles in MEMS for fluid characterization," *Sensors Journal, IEEE*, vol. 1, pp. 361-367, 2001.
- [24] E. Zhuravlev and C. Schick, "Fast scanning power compensated differential scanning nano-calorimeter: 1. The device," *Thermochimica Acta*, vol. 505, pp. 1-13, 2010.
- [25] X. Lu, *et al.*, "Thermal and electrical conductivity of monolithic carbon aerogels," *Journal of Applied Physics*, vol. 73, pp. 581-584, 1993.
- [26] N. M. Kharalkar, *et al.*, "Pulse-power integrated-decay technique for the measurement of thermal conductivity," *Measurement Science and Technology*, vol. 19, p. 075104, 2008.
- [27] A. Al-Salaymeh and F. Durst, "Development and testing of a novel single-wire sensor for wide range flow velocity measurements," *Measurement Science and Technology*, vol. 15, p. 777, 2004.

- [28] F. Durst, *et al.*, "Theoretical and experimental investigations of a wide-range thermal velocity sensor," *Measurement Science and Technology*, vol. 12, p. 223, 2001.
- [29] H. Berthet, *et al.*, "Time-of-flight thermal flowrate sensor for lab-on-chip applications," *Lab on a Chip*, vol. 11, pp. 215-223, 2011.
- [30] F. P. Incropera and D. P. DeWitt, *Introduction to Heat Transfer*: John Wiley & Sons, 2000.
- [31] A. Greve, *et al.*, "Micro-calorimetric sensor for vapour phase explosive detection with optimized heat profile," in *Sensors, 2009 IEEE*, 2009, pp. 723-726.
- [32] E. W. Backer, *et al.*, "Production of separation-nozzle systems for uranium enrichment by a combination of X-ray lithography and galvanoplastics," *Naturwissenschaften*, vol. 69, pp. 520-523, 1982.
- [33] C. K. Malek and V. Saile, "Applications of LIGA technology to precision manufacturing of high-aspect-ratio micro-components and-systems: a review," *Microelectronics Journal*, vol. 35, pp. 131-143, 2004.
- [34] V. Saile, *et al.*, *LIGA and its Applications*: Wiley, 2009.
- [35] A. M. Morales, *et al.*, "Microstructure and mechanical properties of nickel microparts electroformed in replicated LIGA molds," in *Micromachining and Microfabrication*, 2003, pp. 440-447.
- [36] L. Jian, *et al.*, "SU-8 based deep x-ray lithography/LIGA," in *Micromachining and Microfabrication*, 2003, pp. 394-401.
- [37] I. Song and P. K. Ajmera, "Use of a photoresist sacrificial layer with SU-8 electroplating mould in MEMS fabrication," *Journal of Micromechanics and Microengineering*, vol. 13, p. 816, 2003.
- [38] Synova. (2012). *Technology Comparison between laser curing and Laser MicroJet*. Available: <http://www.synova.ch/technology/comparison/>
- [39] J. McGeough, *Micromachining of Engineering Materials*: Marcel Dekker, 2002.
- [40] A. Bertsch, *et al.*, "Combining microstereolithography and thick resist UV lithography for 3D microfabrication," in *Micro Electro Mechanical Systems, 1998. MEMS 98. Proceedings., The Eleventh Annual International Workshop on*, 1998, pp. 18-23.
- [41] C. N. LaFratta, *et al.*, "Soft-lithographic replication of 3D microstructures with closed loops," *Proceedings of the National Academy of Sciences*, vol. 103, pp. 8589-8594, 2006.
- [42] F. Perennes, *et al.*, "Sharp beveled tip hollow microneedle arrays fabricated by LIGA and 3D soft lithography with polyvinyl alcohol," *Journal of Micromechanics and Microengineering*, vol. 16, p. 473, 2006.
- [43] H. Mekar, *et al.*, "Development of three dimensional LIGA process to fabricate spiral microcoil," *Japanese journal of applied physics*, vol. 44, p. 5749, 2005.
- [44] H. Mekar, *et al.*, "Fabrication of a spiral microcoil using a 3D-LIGA process," *Microsystem Technologies*, vol. 13, pp. 393-402, 2007.

- [45] M. C. Wanke, *et al.*, "Laser rapid prototyping of photonic band-gap microstructures," *Science*, vol. 275, pp. 1284-1286, 1997.
- [46] B. Bhattacharyya, *et al.*, "Advancement in electrochemical micro-machining," *International Journal of Machine Tools and Manufacture*, vol. 44, pp. 1577-1589, 2004.
- [47] P. Meyer, *et al.*, "Why you will use the deep X-ray LIG (A) technology to produce MEMS?," *Microsystem Technologies*, vol. 14, pp. 1491-1497, 2008.
- [48] C. H. Robinson and R. Wood, "Ultra-miniature, monolithic, mechanical safety-and-ariming (S&A) device for projected munitions," ed: Google Patents, 2001.
- [49] C. Robinson, *et al.*, "Development of inexpensive, ultra-miniature MEMS-based safety and ariming (S&A) device for small-caliber munition fuzes," *US Army Tank Automotive Command (TACOM) Armament Research Development and Engineering Center Fuze Division*, 2002.
- [50] W. Wang, *et al.*, "A MEMS Safe and Arm Device for Spin Stabilized Ammunition Fuze," *Advanced Materials Research*, vol. 403, pp. 4593-4597, 2012.
- [51] L. Fan, *et al.*, "SLIGA based underwater weapon safety and ariming system," *Microsystem Technologies*, vol. 4, pp. 168-171, 1998.
- [52] K. Birkelund, *et al.*, "New approaches to atomic force microscope lithography on silicon," *Journal of Vacuum Science & Technology B: Microelectronics and Nanometer Structures*, vol. 15, pp. 2912-2915, 1997.
- [53] A. Chand, *et al.*, "Microfabricated small metal cantilevers with silicon tip for atomic force microscopy," *Microelectromechanical Systems, Journal of*, vol. 9, pp. 112-116, 2000.
- [54] J. Zou, *et al.*, "A mould-and-transfer technology for fabricating scanning probe microscopy probes," *Journal of Micromechanics and Microengineering*, vol. 14, p. 204, 2003.
- [55] B. Fernandez Rocha, "Design, fabrication and characterization of high-stroke high-aspect ratio micro electro mechanical systems deformable mirrors for adaptive optics," 2011.
- [56] A. Cowen, *et al.*, "MetalMUMPs design handbook," *MEMSCAP Inc., Durham*, 2002.
- [57] L. Almeida, *et al.*, "Study of the electrical contact resistance of multi-contact MEMS relays fabricated using the MetalMUMPs process," *Journal of Micromechanics and Microengineering*, vol. 16, p. 1189, 2006.
- [58] R. I. Shakoor, *et al.*, "Electrothermally actuated resonant rate gyroscope fabricated using the MetalMUMPs," *Microelectronics Journal*, vol. 42, pp. 585-593, 2011.
- [59] L. Li and D. Uttamchandani, "Monolithic RF MEMS inductor using silicon MEMS foundry process," *Micro and Nano Letters*, vol. 1, pp. 5-8, 2006.
- [60] I. Zine-El-Abidine and M. Okoniewski, "A tunable radio frequency MEMS inductor using MetalMUMPs," *Journal of Micromechanics and Microengineering*, vol. 17, p. 2280, 2007.

- [61] M. Bakri-Kassem and R. R. Mansour, "Two movable-plate nitride-loaded MEMS variable capacitor," *Microwave Theory and Techniques, IEEE Transactions on*, vol. 52, pp. 831-837, 2004.
- [62] L. Li and D. Uttamchandani, "Design and implementation of MEMS Cockcroft-Walton voltage multiplier," *Electronics Letters*, vol. 45, pp. 36-37, 2009.
- [63] S. He, *et al.*, "Characterization of Young's modulus and residual stress gradient of MetalMUMPs electroplated nickel film," *Sensors and Actuators A: Physical*, vol. 154, pp. 149-156, 2009.
- [64] S. E. Alper, *et al.*, "Ultrathick and high-aspect-ratio nickel microgyroscope using EFAB multilayer additive electroforming," *Microelectromechanical Systems, Journal of*, vol. 16, pp. 1025-1035, 2007.
- [65] A. Cohen, *et al.*, "EFAB: rapid, low-cost desktop micromachining of high aspect ratio true 3-D MEMS," in *Micro Electro Mechanical Systems, 1999. MEMS'99. Twelfth IEEE International Conference on*, 1999, pp. 244-251.
- [66] A. L. Cohen, "Medical devices and EFAB methods and apparatus for producing them," ed: Google Patents, 2003.
- [67] A. Sharon, *et al.*, "Manufacturing of 3D microstructures using novel UPSAMS process (ultra precision manufacturing of self-assembled micro systems)," in *Micro Electro Mechanical Systems, 2003. MEMS-03 Kyoto. IEEE The Sixteenth Annual International Conference on*, 2003, pp. 542-545.
- [68] D. W. Sherrer and J. J. Fisher, "Coaxial waveguide microstructures and methods of formation thereof," ed: Google Patents, 2006.
- [69] E. D. Cullens, *et al.*, "Micro-Fabricated 130&#x2013;180 GHz Frequency Scanning Waveguide Arrays," *Antennas and Propagation, IEEE Transactions on*, vol. 60, pp. 3647-3653, 2012.
- [70] FormFactor, "FormFactor Announces MicroProbe Acquisition Financial Presentation," ed. [www.formfactor.com](http://www.formfactor.com), 2012.
- [71] I. Y. Khandros, "Method of manufacturing electrical contacts, using a sacrificial member," 5,476,211, 1995.
- [72] B. N. Eldridge, *et al.*, "Electronic components with terminals and spring contact elements extending from areas which are remote from the terminals," 6043563, 2000.
- [73] I. Y. Khandros, *et al.*, "FABRICATING INTERCONNECTS AND TIPS USING SACRIFICIAL SUBSTRATES," 2005.
- [74] B. H. Kim, *et al.*, "A highly manufacturable large area array MEMS probe card using electroplating and flipchip bonding," *Industrial Electronics, IEEE Transactions on*, vol. 56, pp. 1079-1085, 2009.
- [75] K. Kataoka, *et al.*, "Low contact-force and compliant MEMS probe card utilizing fritting contact," in *Micro Electro Mechanical Systems, 2002. The Fifteenth IEEE International Conference on*, 2002, pp. 364-367.
- [76] F. Wang, *et al.*, "A MEMS probe card with 2D dense-arrayed'hoe'-shaped metal tips," *Journal of Micromechanics and Microengineering*, vol. 18, p. 055008, 2008.

- [77] B. H. Kim, *et al.*, "A vertically guided MEMS probe card with deeply recessed trench-type cantilever," in *Micro Electro Mechanical Systems, 2005. MEMS 2005. 18th IEEE International Conference on*, 2005, pp. 271-274.
- [78] D. I. Kim, *et al.*, "Micro cantilever style contact pin structure for wafer probing," ed: Google Patents, 2002.
- [79] X. Jing, *et al.*, "Design and fabrication of a micromachined bilayer cantilever probe card," *Journal of Micro/Nanolithography, MEMS, and MOEMS*, vol. 9, pp. 043005-043005-7, 2010.
- [80] D. Lee, *et al.*, "Fabrication of BeCu module probe array using heating and fusing currents," in *Sensors, 2011 IEEE*, 2011, pp. 1732-1735.
- [81] J. Luo, *et al.*, "Young's modulus of electroplated Ni thin film for MEMS applications," *Materials Letters*, vol. 58, pp. 2306-2309, 2004.
- [82] D. Son, *et al.*, "Tensile properties and fatigue crack growth in LIGA nickel MEMS structures," *Materials Science and Engineering: A*, vol. 406, pp. 274-278, 2005.
- [83] J. Lou, *et al.*, "An investigation of the effects of thickness on mechanical properties of LIGA nickel MEMS structures," *Journal of Materials Science*, vol. 38, pp. 4129-4135, 2003.
- [84] M. Haj-Taieb, *et al.*, "Thermal stability of electrodeposited LIGA Ni-W alloys for high temperature MEMS applications," *Microsystem Technologies*, vol. 14, pp. 1531-1536, 2008.
- [85] H. Wang, *et al.*, "A study on utilizing a chloride bath to electroform MEMS devices with high aspect ratio structures," *Journal of Micromechanics and Microengineering*, vol. 20, p. 115024, 2010.
- [86] G. Liu, *et al.*, "Fabricating HARMS by using megasonic assisted electroforming," *Microsystem Technologies*, vol. 14, pp. 1223-1226, 2008.
- [87] W. Merlijn van Spengen, "MEMS reliability from a failure mechanisms perspective," *Microelectronics Reliability*, vol. 43, pp. 1049-1060, 2003.
- [88] M. R. Douglass, "Lifetime estimates and unique failure mechanisms of the digital micromirror device (DMD)," in *Reliability Physics Symposium Proceedings, 1998. 36th Annual. 1998 IEEE International*, 1998, pp. 9-16.
- [89] C. Dyck, *et al.*, "Si-Based RF MEMS Components."
- [90] M. Okandan, *et al.*, "High Speed (GHz), Ultra-high Pressure (GPa) Sensor Array Fabricated in Integrated CMOS+ MEMS process," in *Micro Electro Mechanical Systems, 2009. MEMS 2009. IEEE 22nd International Conference on*, 2009, pp. 845-847.
- [91] S. Y. Lin, *et al.*, "Three-dimensional photonic-crystal emitter for thermal photovoltaic power generation," *Applied Physics Letters*, vol. 83, pp. 380-382, 2003.
- [92] G. Kumar, *et al.*, "Nanomoulding with amorphous metals," *Nature*, vol. 457, pp. 868-872, 2009.
- [93] G. Kumar, *et al.*, "Bulk metallic glass: the smaller the better," *Advanced Materials*, vol. 23, pp. 461-476, 2010.

- [94] C. Ophus, *et al.*, "Resonance properties and microstructure of ultracompliant metallic nanoelectromechanical systems resonators synthesized from Al-32 at. %Mo amorphous-nanocrystalline metallic composites," *Applied Physics Letters*, vol. 92, pp. 123108-3, 2008.
- [95] E. Luber, *et al.*, "Tailoring the microstructure and surface morphology of metal thin films for nano-electro-mechanical systems applications," *Nanotechnology*, vol. 19, p. 125705, 2008.
- [96] E. J. Luber, *et al.*, "All-metal AFM probes fabricated from microstructurally tailored Cu-Hf thin films," *Nanotechnology*, vol. 20, p. 345703, 2009.
- [97] P. Totta and R. Sopher, "SLT device metallurgy and its monolithic extension," *IBM Journal of Research and Development*, vol. 13, pp. 226-238, 1969.
- [98] D. Seraphim and I. Feinberg, "Electronic packaging evolution in IBM," *IBM Journal of Research and Development*, vol. 25, pp. 617-630, 1981.
- [99] "System 360 from computers to computer systems," 2012.
- [100] (2012). *Erich Bloch Biography*. Available: <http://www.computerhistory.org/fellowawards/hall/bios/Erich,Bloch/>
- [101] R. Okojie, *et al.*, "Improved reliability of SiC pressure sensors for long term high temperature applications," in *Solid-State Sensors, Actuators and Microsystems Conference (TRANSDUCERS), 2011 16th International*, 2011, pp. 2875-2878.
- [102] G. W. Hunter, *et al.*, "Development and application of high-temperature sensors and electronics for propulsion applications," in *Defense and Security Symposium*, 2006, pp. 622209-622209-12.
- [103] A. Maciossek, *et al.*, "GALVANOPLATING AND SACRIFICIAL LAYERS FOR SURFACE MICROMACHINING," *Microelectronic Engineering*, vol. 27, pp. 503-508, Feb 1995.
- [104] Z. Cui and R. A. Lawes, "A new sacrificial layer process for the fabrication of micromechanical systems," *Journal of Micromechanics and Microengineering*, vol. 7, pp. 128-130, Sep 1997.
- [105] Y. Kim, *et al.*, "New release technique of a thick sacrificial layer and residue effects on novel half-coaxial transmission line filters," *Journal of Micromechanics and Microengineering*, vol. 19, May 2009.
- [106] K. R. Williams, *et al.*, "Etch rates for micromachining processing-Part II," *Microelectromechanical Systems, Journal of*, vol. 12, pp. 761-778, 2003.
- [107] K. Isamoto, *et al.*, "A 5-V operated MEMS variable optical attenuator by SOI bulk micromachining," *Selected Topics in Quantum Electronics, IEEE Journal of*, vol. 10, pp. 570-578, 2004.
- [108] T. K. Tang, *et al.*, "A packaged silicon MEMS vibratory gyroscope for microspacecraft," in *Micro Electro Mechanical Systems, 1997. MEMS '97, Proceedings, IEEE., Tenth Annual International Workshop on*, 1997, pp. 500-505.
- [109] P. Merz, *et al.*, "A novel micromachining technology for structuring borosilicate glass substrates," in *TRANSDUCERS, Solid-State Sensors*,

- Actuators and Microsystems, 12th International Conference on, 2003, 2003,* pp. 258-261 vol.1.
- [110] M. Mehregany and C. A. Zorman, "SiC MEMS: opportunities and challenges for applications in harsh environments," *Thin Solid Films*, vol. 355–356, pp. 518-524, 1999.
- [111] P. Cong and D. J. Young, "Single crystal 6H-SiC MEMS fabrication based on smart-cut technique," *Journal of Micromechanics and Microengineering*, vol. 15, p. 2243, 2005.
- [112] M. F. Aimi, *et al.*, "High-aspect-ratio bulk micromachining of titanium," *Nat Mater*, vol. 3, pp. 103-105, 2004.
- [113] O. J. A. Schueller, *et al.*, "Fabrication of glassy carbon microstructures by soft lithography," *Sensors and Actuators A: Physical*, vol. 72, pp. 125-139, 1999.
- [114] P. D. Mordechay Schlesinger, *Modern Electroplating: John Wiley & Sons*, 2010.
- [115] P. J. Kelly and R. D. Arnell, "Magnetron sputtering: a review of recent developments and applications," *Vacuum*, vol. 56, pp. 159-172, 2000.
- [116] L. Zhang, *et al.*, "Oxygen reduction reaction activity and electrochemical stability of thin-film bilayer systems of platinum on niobium oxide," *Journal of Physical Chemistry C*, vol. 114, pp. 16463-16474, 2010.
- [117] I. Safi, "Recent aspects concerning DC reactive magnetron sputtering of thin films: a review," *Surface and Coatings Technology*, vol. 127, pp. 203-218, 2000.
- [118] T. Ito and S. Okazaki, "Pushing the limits of lithography," *Nature*, vol. 406, pp. 1027-1031, 2000.
- [119] S. A. Campbell, *The Science and Engineering of Microelectronic Fabrication: Oxford University Press, USA*, 2001.
- [120] D. J. Elliott, *Microlithography: process technology for IC fabrication: McGraw-Hill*, 1986.
- [121] G. R. Brewer and J. P. Ballantyne, *Electron-beam technology in microelectronic fabrication: Academic Press*, 1980.
- [122] J. Losby, *et al.*, "Nanomechanical torque magnetometry of permalloy cantilevers," *Journal of Applied Physics*, vol. 108, pp. 123910-5, 2010.
- [123] Z. Lee, *et al.*, "Metallic NEMS components fabricated from nanocomposite Al-Mo films," *Nanotechnology*, vol. 17, pp. 3063-3070, Jun 2006.
- [124] L. Zhang, *et al.*, "Oxygen Reduction Reaction Activity and Electrochemical Stability of Thin-Film Bilayer Systems of Platinum on Niobium Oxide," *Journal of Physical Chemistry C*, vol. 114, pp. 16463-16474, Oct 2010.
- [125] C. H. Lee and K. Jiang, "Fabrication of thick electroforming micro mould using a KMPR negative tone photoresist," *Journal of Micromechanics and Microengineering*, vol. 18, 2008.
- [126] D. McMullan, "Scanning electron microscopy 1928–1965," *Scanning*, vol. 17, pp. 175-185, 1995.
- [127] R. F. Egerton, *Physical Principles of Electron Microscopy: An Introduction to TEM, SEM, and AEM: Springer*, 2005.

- [128] R. Van Grieken and A. Markowicz, *Handbook of X-Ray Spectrometry, Second Edition*: Taylor & Francis, 2001.
- [129] W. Osten, *Optical Inspection of Microsystems*: Taylor & Francis, 2006.
- [130] M. Birkholz, *Thin Film Analysis by X-Ray Scattering*: John Wiley & Sons, 2006.
- [131] I. W. Donald, *Glass-To-Metal Seals*: Society of Glass Technology, 2009.
- [132] A. H. Industries. (2009). *Hermetically Sealed Interconnects for Ultra Harsh Environments* [Catalog]. Available: [www.hccindustries.com/files/HTHeader-Durock.pdf](http://www.hccindustries.com/files/HTHeader-Durock.pdf)
- [133] A. C. Adams and C. D. Capiro, "PLANARIZATION OF PHOSPHORUS-DOPED SILICON DIOXIDE," *Journal of the Electrochemical Society*, vol. 128, pp. 423-429, 1981.
- [134] J. A. Amick, *et al.*, "DEPOSITION TECHNIQUES FOR DIELECTRIC FILMS ON SEMICONDUCTOR-DEVICES," *Journal of Vacuum Science & Technology*, vol. 14, pp. 1053-1063, 1977.
- [135] R. Ghodssi and P. Lin, *MEMS Materials and Processes Handbook*: Springer, 2011.
- [136] L. E. Stillwagon and R. G. Larson, "Fundamentals of topographic substrate leveling," *Journal of Applied Physics*, vol. 63, pp. 5251-5258, 1988.
- [137] L. E. Stillwagon and R. G. Larson, "Leveling of thin films over uneven substrates during spin coating," *Physics of Fluids A*, vol. 2, pp. 1937-1944, 1990.
- [138] D. Widmann, *et al.*, *Technology of Integrated Circuits*: Springer, 2000.
- [139] K. A. Defriend and A. R. Barron, "Surface repair of porous and damaged alumina bodies using carboxylate-alumoxane nanoparticles," *Journal of Materials Science*, vol. 37, pp. 2909-2916, 2002.
- [140] A. Azzam Yasseen, *et al.*, "Thick glass film technology for polysilicon surface micromachining," *Microelectromechanical Systems, Journal of*, vol. 8, pp. 172-179, 1999.
- [141] S. Hollar, *et al.*, "Robot Leg Motion in a Planarized-SOI, Two-Layer Poly-Si Process," *Microelectromechanical Systems, Journal of*, vol. 14, pp. 725-740, 2005.
- [142] Y. K. Siew, *et al.*, "Thermal Curing of Hydrogen Silsesquioxane," *Journal of the Electrochemical Society*, vol. 147, pp. 335-339, 2000.
- [143] C.-C. Yang and W.-C. Chen, "The structures and properties of hydrogen silsesquioxane (HSQ) films produced by thermal curing," *Journal of Materials Chemistry*, vol. 12, pp. 1138-1141, 2002.
- [144] S. C. Systems. (2012). *SCS Parylene Properties*. Available: [http://scscoatings.com/what\\_is\\_parylene/parylene\\_properties.aspx](http://scscoatings.com/what_is_parylene/parylene_properties.aspx)
- [145] X. Zhang, *et al.*, "Crystallinity properties of parylene-n affecting its use as an ILD in submicron integrated circuit technology," *Thin Solid Films*, vol. 270, pp. 508-511, 1995.
- [146] P. Engineering. (2010). *Typical Specifications of Parylene C*. Available: [http://www.paryleneengineering.com/specifications\\_parylene\\_c\\_astm.html](http://www.paryleneengineering.com/specifications_parylene_c_astm.html)

- [147] P. Engineering. (2010). *Solvent Resistance of Parylene*. Available: [http://www.paryleneengineering.com/solvent\\_resistance.html](http://www.paryleneengineering.com/solvent_resistance.html)
- [148] T. Haruta, *et al.*, "Process for removing tin and tin-lead alloy from copper substrates," 5035749 1991.
- [149] K. Kataoka, *et al.*, "Electroplating Ni micro-cantilevers for low contact-force IC probing," *Sensors and Actuators A: Physical*, vol. 103, pp. 116-121, 2003.
- [150] M. Pourbaix, *Atlas of electrochemical equilibria in aqueous solutions*: National Association of Corrosion Engineers, 1974.
- [151] S. D. Cramer, *et al.*, *ASM Handbook: Corrosion : materials*: ASM International, 2005.
- [152] Y. Yang, *et al.*, "Fabrication of pompon-like and flower-like SnO microspheres comprised of layered nanoflakes by anodic electrocrystallization," *Electrochimica Acta*.
- [153] N. V. Krstajić, *et al.*, "Electrodeposition of Ni-Mo alloy coatings and their characterization as cathodes for hydrogen evolution in sodium hydroxide solution," *International Journal of Hydrogen Energy*, vol. 33, pp. 3676-3687, 2008.
- [154] L. Wang, *et al.*, "Grain size effect in corrosion behavior of electrodeposited nanocrystalline Ni coatings in alkaline solution," *Scripta Materialia*, vol. 55, pp. 657-660, 2006.
- [155] S. B. Saidman, *et al.*, "Stationary and non-stationary electrochemical response of polycrystalline indium in alkaline media," *Electrochimica Acta*, vol. 35, pp. 329-338, 1990.
- [156] A. Sayed, *et al.*, "Electrochemical behaviour of an indium electrode in concentrated KOH solutions at different temperatures," *Monatshefte für Chemie / Chemical Monthly*, vol. 122, pp. 1019-1027, 1991.
- [157] F. Zucchi, *et al.*, "Corrosion and corrosion inhibition of nickel in HClO<sub>4</sub> solutions using the EQCM technique," *Journal of Applied Electrochemistry*, vol. 29, pp. 347-353, 1999.
- [158] B. Miller and R. E. Visco, "Ring-Disk Amperometry: A Study of Indium Dissolution," *Journal of the Electrochemical Society*, vol. 115, pp. 251-258, 1968.
- [159] A. International, "Standard Practice for Preparation of Nickel Alloys for Electroplating," ed, 2008.
- [160] R. B. Belser and W. H. Hicklin, "Temperature coefficients of resistance of metallic films in the temperature range 25°to 600°C," *Journal of Applied Physics*, vol. 30, pp. 313-322, 1959.
- [161] H. Ernst, "High-resolution thermal measurements in fluids," Institut für Mikrosystemtechnik 2001.
- [162] Y. Nagasaka and A. Nagashima, "ABSOLUTE MEASUREMENT OF THE THERMAL-CONDUCTIVITY OF ELECTRICALLY CONDUCTING LIQUIDS BY THE TRANSIENT HOT-WIRE METHOD," *Journal of Physics E-Scientific Instruments*, vol. 14, pp. 1435-1440, 1981.

- [163] R. E. Pawel and R. K. Williams, "Survey of physical property data for several alloys. [Nitronic 33; copper C10400; copper C17510]," ORNL/TM-9616; Other: ON: DE85018138, 1985.
- [164] J. B. Bult, *et al.*, "Passivation oxide controlled selective carbon nanotube growth on metal substrates," *Nanotechnology*, vol. 20, Feb 2009.
- [165] J. H. Park and K. Natesan, "Electronic transport in thermally grown C<sub>2</sub>O<sub>3</sub>," *Oxidation of Metals*, vol. 33, pp. 31-54, 1990.
- [166] D. M. England and A. V. Virkar, "Oxidation Kinetics of Some Nickel-Based Superalloy Foils in Humidified Hydrogen and Electronic Resistance of the Oxide Scale Formed Part II," *Journal of the Electrochemical Society*, vol. 148, pp. A330-A338, January 1, 2001 2001.
- [167] F. Starzyk, "Parametrisation of interdigit comb capacitor for dielectric impedance spectroscopy," *Archives of Materials Science and Engineering*, vol. 34, pp. 31-34, 2008.
- [168] C. Kim and H. Lee, "Shape effect of Pt nanocrystals on electrocatalytic hydrogenation," *Catalysis Communications*, vol. 11, pp. 7-10, 2009.
- [169] M. Hasnat, *et al.*, "Electrocatalytic ammonia synthesis: Role of cathode materials and reactor configuration," *Catalysis Communications*, vol. 10, pp. 1975-1979, 2009.
- [170] M. Hasnat, *et al.*, "Different reaction routes in electrocatalytic nitrate/nitrite reduction using an H<sup>+</sup>-conducting solid polymer electrolyte," *Catalysis Communications*, vol. 10, pp. 1132-1135, 2009.
- [171] C. M. Cirtiu, *et al.*, "Comparative study of catalytic and electrocatalytic hydrogenation of benzophenone," *Catalysis Communications*, vol. 8, pp. 751-754, 2007.
- [172] P. Pintauro and J. Bontha, "The role of supporting electrolyte during the electrocatalytic hydrogenation of aromatic compounds," *Journal of applied electrochemistry*, vol. 21, pp. 799-804, 1991.
- [173] R. Menini, *et al.*, "The electrocatalytic hydrogenation of phenanthrene at Raney nickel electrodes: the influence of an inert gas pressure," *Electrochimica acta*, vol. 43, pp. 1697-1703, 1998.
- [174] B. G. Bravo, *et al.*, "Reversible redox, hydrodesulfurization and anodic oxidation of chemisorbed thiophenols: a comparison at platinum and gold electrodes," *Journal of electroanalytical chemistry and interfacial electrochemistry*, vol. 241, pp. 199-210, 1988.
- [175] M. E. Bothwell and M. P. Soriaga, "Reversible redox chemistry, hydrodesulfurization, and anodic oxidation of thiophenols chemisorbed at smooth polycrystalline iridium electrodes," *Journal of electroanalytical chemistry and interfacial electrochemistry*, vol. 295, pp. 123-138, 1990.
- [176] A. P. da Silva, *et al.*, "Homogeneous electro-mediated reduction of unsaturated compounds using Ni and Fe as mediators in DMF," *Tetrahedron*, vol. 62, pp. 5435-5440, 2006.

- [177] D. S. Santana, *et al.*, "Electrocatalytic hydrogenation of organic compounds using a nickel sacrificial anode," *Journal of Electroanalytical Chemistry*, vol. 569, pp. 71-78, 2004.
- [178] J. C. Moutet, "ELECTROCATALYTIC HYDROGENATION ON HYDROGEN-ACTIVE ELECTRODES. A REVIEW," *Organic preparations and procedures international*, vol. 24, pp. 309-325, 1992.
- [179] M. Brorson, *et al.*, "The morphology of MoS<sub>2</sub>, WS<sub>2</sub>, Co-Mo-S, Ni-Mo-S and Ni-W-S nanoclusters in hydrodesulfurization catalysts revealed by HAADF-STEM," *Catalysis today*, vol. 123, pp. 31-36, 2007.
- [180] H. Topsøe, *et al.*, "The role of reaction pathways and support interactions in the development of high activity hydrotreating catalysts," *Catalysis today*, vol. 107, pp. 12-22, 2005.
- [181] F. Besenbacher, *et al.*, "Recent STM, DFT and HAADF-STEM studies of sulfide-based hydrotreating catalysts: Insight into mechanistic, structural and particle size effects," *Catalysis today*, vol. 130, pp. 86-96, 2008.
- [182] J. V. Lauritsen, *et al.*, "Size-dependent structure of MoS<sub>2</sub> nanocrystals," *Nature nanotechnology*, vol. 2, pp. 53-58, 2007.
- [183] I. Martin-Litas, *et al.*, "Characterisation of rf sputtered tungsten disulfide and oxysulfide thin films," *Thin Solid Films*, vol. 416, pp. 1-9, 2002.
- [184] Y. Zhang, *et al.*, "Electroplating of low stress permalloy for MEMS," *Materials characterization*, vol. 57, pp. 121-126, 2006.
- [185] J. W. Judy and R. S. Muller, "Magnetically actuated, addressable microstructures," *Microelectromechanical Systems, Journal of*, vol. 6, pp. 249-256, 1997.
- [186] J. Cao, *et al.*, "Magnetically actuated micro-manipulators for biological and biomedical applications," in *Nano/Micro Engineered and Molecular Systems, 2008. NEMS 2008. 3rd IEEE International Conference on*, 2008, pp. 708-711.
- [187] D. J. Sadler, *et al.*, "Prototype microvalve using a new magnetic microactuator," in *Micromachining and Microfabrication*, 1998, pp. 46-52.
- [188] D. Niarchos, "Magnetic MEMS: key issues and some applications," *Sensors and Actuators A: Physical*, vol. 109, pp. 166-173, 2003.
- [189] J. Davis, *et al.*, "Nanotorsional resonator torque magnetometry," *Applied Physics Letters*, vol. 96, pp. 072513-072513-3, 2010.
- [190] H. Bhaskaran, *et al.*, "Active microcantilevers based on piezoresistive ferromagnetic thin films," *Applied Physics Letters*, vol. 98, pp. 013502-013502-3, 2011.
- [191] A. Sanaty-Zadeh, *et al.*, "Properties of nanocrystalline iron-nickel alloys fabricated by galvanostatic electrodeposition," *Journal of Alloys and Compounds*, vol. 485, pp. 402-407, 2009.
- [192] J. Losby, *et al.*, "Thermo-mechanical sensitivity calibration of nanotorsional magnetometers," *Journal of Applied Physics*, vol. 111, pp. 07D305-07D305-3, 2012.

- [193] N. V. Myung, *et al.*, "Development of electroplated magnetic materials for MEMS," *Journal of magnetism and magnetic materials*, vol. 265, pp. 189-198, 2003.
- [194] G. Pavithra and A. C. Hegde, "Magnetic property and corrosion resistance of electrodeposited nano crystalline iron-nickel alloys," *Applied Surface Science*, 2012.
- [195] J. Freedman, "Soft magnetic thin-film memory materials," *Magnetics, IEEE Transactions on*, vol. 5, pp. 752-764, 1969.
- [196] Y. Zhang, *et al.*, "Low-stress permalloy for magnetic MEMS switches," *Magnetics, IEEE Transactions on*, vol. 42, pp. 51-55, 2006.
- [197] O. Raccurt, *et al.*, "Influence of liquid surface tension on stiction of SOI MEMS," *Journal of Micromechanics and Microengineering*, vol. 14, p. 1083, 2004.
- [198] E. P. Wohlfarth, *Ferromagnetic materials*. 2. Amsterdam [u.a.]: North-Holland, 1999.
- [199] S. Kaloshkin, *et al.*, "Phase transformations in Fe–Ni system at mechanical alloying and consequent annealing of elemental powder mixtures," *Physica B: Condensed Matter*, vol. 299, pp. 236-241, 2001.
- [200] V. Tcherdyntsev, *et al.*, "Formation of iron-nickel nanocrystalline alloy by mechanical alloying," *Nanostructured Materials*, vol. 12, pp. 139-142, 1999.
- [201] H. Baker and H. Okamoto, "ASM Handbook, Volume 03 - Alloy Phase Diagrams," ed: ASM International.
- [202] H. L. Seet, *et al.*, "Effect of deposition methods on the magnetic properties of nanocrystalline permalloy," *Journal of Alloys and Compounds*, vol. 449, pp. 284-287, 2008.
- [203] D. Ozkaya, *et al.*, "Effect of Ga implantation on the magnetic properties of permalloy thin films," *Journal of Applied Physics*, vol. 91, pp. 9937-9942, Jun 2002.
- [204] L. J. Gao, *et al.*, "Characterization of permalloy thin films electrodeposited on Si(111) surfaces," *Journal of Applied Physics*, vol. 81, pp. 7595-7599, Jun 1997.
- [205] W. Fang and J. A. Wickert, "Determining mean and gradient residual stresses in thin films using micromachined cantilevers," *Journal of Micromechanics and Microengineering*, vol. 6, p. 301, 1996.
- [206] W. H. Chu and M. Mehregany, "A study of residual stress distribution through the thickness of  $p^+$  silicon films [thermal oxidation effects]," *Electron Devices, IEEE Transactions on*, vol. 40, pp. 1245-1250, 1993.
- [207] H. Guckel, *et al.*, "A simple technique for the determination of mechanical strain in thin films with applications to polysilicon," *Journal of Applied Physics*, vol. 57, pp. 1671-1675, 1985.
- [208] W. Fang and J. A. Wickert, "Post buckling of micromachined beams," *Journal of Micromechanics and Microengineering*, vol. 4, p. 116, 1994.
- [209] X. Li, *et al.*, "Micromechanical characterization of electroplated permalloy films for MEMS," *Microsystem Technologies*, vol. 14, pp. 131-134, 2008.

- [210] D. Hong, *et al.*, "Comparison of mechanical and tribological properties of permalloy and high moment FeTaN thin films for tape recording heads," *Magnetics, IEEE Transactions on*, vol. 32, pp. 3702-3704, 1996.
- [211] Z. Lee, *et al.*, "Metallic NEMS components fabricated from nanocomposite Al–Mo films," *Nanotechnology*, vol. 17, p. 3063, 2006.
- [212] N. Nelson-Fitzpatrick, *et al.*, "Synthesis and characterization of Au–Ta nanocomposites for nanomechanical cantilever devices," *Nanotechnology*, vol. 18, p. 355303, 2007.